Photometric and Spectroscopic Analysis of Classical Novae: An Examination of Their Observational Characteristics and Greater Astronomical Impact

A DISSERTATION
SUBMITTED TO THE FACULTY OF THE GRADUATE SCHOOL
OF THE UNIVERSITY OF MINNESOTA
BY

Lorren Andrew Helton

IN PARTIAL FULFILLMENT OF THE REQUIREMENTS
FOR THE DEGREE OF
Doctor Of Philosophy

December, 2010

Acknowledgements

There are many people that have earned my gratitude for their contribution to my graduate school experience.

The first people I would like to thank are my advisors, Bob Gehrz and Chick Woodward. Bob was always happy to answer my questions and provide support when I needed it most. I couldn't have done this without him. Chick provided me with the challenges that helped me develop into the researcher that I am today. The rest of the astronomy faculty also played an important role in my graduate experience. I owe a tremendous debt to Roberta Humphreys. She provided me with knowledge, advice, and a pleasant little office in which to work that I will miss dearly. Much of my observing knowledge I gained from Terry Jones. Evan Skillman also deserves my thanks. He provided me not only with summer support, but also enlightening discussion about the most curious aspects of academia. Thanks also to Kris Davidson for the many enlightening discussions.

I greatly appreciate all of the effort that John Marchetti and Al Knutson put into keeping the old observatories alive. The times I have been able to spend with them are some of my best experiences as a grad student. A big thanks to Al for all of the help that he has given me over the years. Thanks to John for all of the time that he spent observing with me and for all of our long afternoon conversations. I have enjoyed every minute.

As part of my thesis work, I have collaborated with numerous talented researchers. I would like to thank Greg Schwarz for the many instructive conversations, without which my understanding of classical novae would be notably

diminished. I thank Nye Evans, who was most generous in allowing an upstart graduate student lay claim to some of his most interesting data. I also appreciate Karen Vanlandingham for taking the time to help me learn Cloudy, one of the most obtuse routines used to model astronomical data.

As all of the grad students are aware, the ladies in the astronomy office keep the whole department running. Terry Thibeault deserves a big thank-you for all of the help that she has given me and all of the bureaucracy that she has waded through on my behalf. I also want to thank Corinne Komor for being a friend and always being straight with me when I needed it. And I thank Stephanie Rose for having my back when I forgot to file paperwork that a certain future employer needed in order to interview me.

I could not have made it through graduate school without the friends that I made along the way. Thanks to Mike Kelley and Gerry Ruch for their support and assistance in helping me learn how to do SCIENCE!, to Simon Strasser, Sean O'Neill, and the HARG crew for all of the good times we have shared, to Martha Boyer for being a terrific roommate and a wonderful friend, to Geoff Lawrence for keeping me active and sane, to Chelsea Tiffany for all of the great reading suggestions, and to Amy Fisher for all of her help and support throughout the entire graduate school endeavor. I expect you all to visit!

A big thank-you goes to my sister, Lori Helton, who challenged me enough as a child to make me want to explore on my own and who provided ever present support as an adult. She is always willing to listen and give advice, whether I'm too stubborn to listen or not.

Finally, I would like to extend a special thanks to Danielle Berg. She put up with me for months at a time as I was putting in far too much time working and far too little time with her. Her support and encouragement has been invaluable.

This work is based in part on observations made with the *Spitzer* Space Telescope, which is operated by the Jet Propulsion Laboratory, California Institute of Technology, under NASA contract 1407.

This work is also based on observations obtained at the Gemini Observatory, which is operated by the Association of Universities for Research in Astronomy, Inc., under a cooperative agreement with the NSF on behalf of the Gemini partnership: the National Science Foundation (United States), the Science and Technology Facilities Council (United Kingdom), the National Research Council (Canada), CONICYT (Chile), the Australian Research Council (Australia), Ministèrio da Ciència e Tecnologia (Brazil) and Ministerio de Ciencia, Tecnologìa e Innovacièon Productiva (Argentina).

Stony Brook University's initial participation in the SMARTS consortium was made possible by generous contributions from the Dean of Arts and Sciences, the Provost, and the Vice President for Research of Stony Brook University.

This work was also supported by the UK STFC, and various NASA Swift Grants to the investigators.

L.A. Helton was supported in part by NASA/JPL *Spitzer* grants 1289430, 1314757, 1267992, 1256406 and 1215746 to the University of Minnesota as well as various National Science Foundation grants.

We acknowledge with thanks the variable star observations from the AAVSO International Database contributed by observers worldwide and used in this research. We also thank our anonymous referee for multiple suggestions and comments that resulted in notable improvements to the manuscript.

We also thank Dennis Means and Geno Bechetti for all of their work as telescope operators at the Bok 90".

Dedication

This work is dedicated to my parents, Lorren & Becky Helton. During my childhood, they allowed me the freedom to explore and, as I grew up, they supported me in even my most random endeavors. I could not have done this without them.

Abstract

Classical novae (CNe) are violent thermonuclear explosions arising on the surface of white dwarfs in binary systems and are contributors to the chemical evolution of the interstellar medium through the production and ejection of copious amounts of metal-rich material. Observations and modeling of CNe eruptions illuminate numerous fundamental processes of astrophysical interest, including non-equilibrium thermonuclear runaway, radiative processes in dynamic nebular environments, binary star interaction, as well as dust condensation and grain growth. Here I summarize key findings from selected Galactic CNe observed as part of a 5 year, panchromatic optical/infrared observing campaign using Spitzer, Gemini, and other ground based optical facilities.

In particular, I present detailed analysis of nova V1065 Centauri, including photoionization analysis of the emission lines, which enabled the derivation of abundances in the ejecta, and radiative transport modeling of the dust emission features, which allowed determination of the composition and characteristics of the dust in this system. I present analysis of three novae, V1974 Cygni, V382 Velorum, and V1494 Aquilae, observed from $4.4-15.5$ years after outburst, discuss the characteristics of the nebulae at these late times, and estimate the abundances in their ejecta. In the case of V1494 Aql, I also report the first detection of neon. Finally, I present observations of three novae, DZ Crucis, V2361 Cygni, and V2362 Cygni, that exhibited unidentified infrared (UIR) features in their mid-infrared spectra, which exhibited unusual characteristics. I relate these features to other dusty novae in which features with similar characteristics were observed, and

discuss possible sources for the UIR carriers.

Analysis of the data obtained in the CNe monitoring campaign presented here highlights the need for synoptic observations obtained with broad wavelength coverage. Observations of V1065 Cen, which exhibited spectra rich in metals (e.g O, Ne, Mg, S, Ar, and Fe) produced during the thermonuclear runaway and through dredge up from the surface layers of the underlying WD, yielded robust estimates of WD composition, ejecta mass, and absolute abundances in the ejecta. Dusty novae such as V1065 Cen, V2362 Cyg, and V2361 Cyg, produced a variety of grain types as revealed by emission features characteristic of silicates, hydrogenated amorphous carbon dust, and PAH-like molecules, often in the same system. This data set is exceptional in that observations of many targets commenced immediately after eruption and followed the development for hundreds of days post-outburst providing unique insight into the evolution of conditions within the ejecta including the complete cycle of growth, processing, and dissipation of dust grains.

Contents

List of Tables

List of Figures

Chapter 1

Introduction

A classical nova (CN - singular; CNe - plural) is a thermonuclear explosion on the surface of a white dwarf (WD) star in a binary system. The explosion arises in an envelope of material that was accreted onto the WD surface from its companion and results in the system increasing in brightness by many orders of magnitude. Due to the extreme brightness increase, CNe may be observed even in other galaxies in the local group. The explosion jettisons material from the WD surface into the surrounding interstellar medium (ISM) at velocities up to a few thousand km s^{-1}. The majority of the ejected material is hydrogen (H), but there are also substantial quantities of metals produced by explosive nucleosynthesis and dredged up from the underlying WD and mixed into the ejecta. Hence, the ejecta of classical novae may have a considerable impact on the local chemical evolution of the ISM.

1.1 What is a Classical Nova?

A WD, the end state of evolution of a star with an initial mass between 0.5 and 10 solar masses ($M_{\odot}$), is the remnant core left behind after the progenitor star exhausted the available light elements (e.g., H, He, C) required for core nuclear

burning and subsequently shed its outer, hydrogen-rich envelope. The WD composition is determined by the initial mass of the progenitor, which determines the amount of nuclear processing that will be completed before depletion of the star's fuel reserves. The temperatures in the stellar interior of a star between 0.5 and 8 $M_\odot$ are high enough ($\sim 10^6 - 10^7$ K) initially to fuse hydrogen (H) to helium (He) and, later in its evolution, He into carbon (C) and oxygen (O). The remnant WD in a system such as this will be composed primarily of C and O, i.e., a CO WD. If the progenitor was larger, between 8 and 10 $M_\odot$, then the core reaches higher temperatures allowing the production of heavier metals through the fusion of C into O, neon (Ne) and magnesium (Mg), leading to a ONe WD remnant. In rare instances, the progenitor star may lose a substantial portion of its mass through binary mass exchange before it completes its main sequence (MS) lifetime, leaving behind a low mass He WD. Unlike stars, which are supported against gravitational collapse by radiation pressure, WDs are supported by electron degeneracy pressure, the quantum mechanical resistance of electrons against compression into the same energy states, as described by the Pauli exclusion principle. Observations of CN outbursts allow exploration of the composition and masses of WDs through abundance patterns observed in the ejecta and the energetics of the eruptions.

In CNe, the WD accretes matter from its companion through a process called Roche-lobe overflow. The Roche-lobe is the region of space surrounding a star in which orbiting material remains gravitationally bound. In a binary system, the Roche-lobes of the two objects are tear-drop shaped, meeting at their respective peaks, the L_1 Lagrangian equipotential point. As the secondary star evolves, its envelope gradually fills its Roche-lobe allowing material to escape through the L_1 point and fall into orbit around the WD primary. A typical CN system has mass transfer rates ranging from $10^{-9} - 10^{-8}$ $M_\odot$ yr^{-1} (Iben & Fujimoto 2008). Due to conservation of angular momentum, the infalling material forms an accretion disk.

The accretion of matter onto the WD surface produces a layer of semi-degenerate

material. Normally as the temperature of a plasma increases, the associated thermal pressure will cause the gas to expand and cool. In a degenerate fluid, however, the pressure (and density) is determined by the Pauli exclusion principle and is independent of temperature. Hence, as the accreted material becomes degenerate in the lower layers, the temperature is able to rise as the density continues to increase. Eventually, the temperature and pressure are high enough to initiate thermonuclear fusion in the accreted envelope (of order 10^7 K and $\sim 10^{20}$ dyne cm^{-2}; Starrfield et al. 2008). The ignition of fusion leads to thermonuclear runaway (TNR). As the TNR progresses, the temperature increases leading to increased reaction rates, but due to the degenerate nature of the accreted shell, the system cannot equilibrate. Eventually, the luminosity exceeds the Eddington limit, i.e. the luminosity at which the outwards force due to radiation pressure exceeds the inward force of gravity, resulting in the ejection of much of the accreted material. The TNR injects a tremendous amount of kinetic energy into the envelope resulting in the ejection of $10^{-5} - 10^{-4}$ M$_\odot$ of material at velocities ranging from $\sim 500 - 5000$ km s^{-1}.

The energetics of the eruption, including the speed and mass of the ejecta, as well as the ejecta composition, are determined by the mass of the underlying WD and the mass accretion rate, $\dot{\mathrm{M}}$. For a uniform $\dot{\mathrm{M}}$, the more massive the WD, the less mass must be accumulated before the accreted material reaches the temperature and pressure required to initiate TNR. Likewise, for a uniform WD mass, an increase in the accretion rate results in eruption at a lower accumulated mass (Iben & Fujimoto 2008, and references therein). Observational characteristics of the photometric light curve and the elemental abundances observed spectroscopically in the ejecta provide clues to the properties of the WD and the pre-eruption mass accretion rate.

Furthermore, the TNR may cause turbulent instabilities in the boundary between the accreted material and the WD leading to mixing of the WD material with the accreted envelope. This process of "dredge-up" can have a significant impact on the evolution of the TNR and the subsequent development of the ejecta

(Starrfield et al. 2008, and references therein). The heavy elements injected into the envelope can influence the reaction rates in the TNR, act as efficient coolants through nebular line emission as the ejecta expand, and be trapped in condensibles such as molecules and dust. Spectroscopic observations of the ejecta illuminate the process of dredge-up and reveal how this material influences the subsequent development of the system.

In the most simplistic model of the eruption, the ejection event is discrete with a relatively brief (hours to days) period of time between the initial mass loss and termination. This results in an expanding shell of material that produces the observed emission. More complicated models, and likely more physically realistic, suggest that there is an initial, relatively brief stage of heavy mass loss followed by a longer duration stage of low mass loss resembling a stellar wind. In either case, it is the observations of these ejecta that forms the basis of our understanding of CNe.

1.2 Observational Characteristics

Based upon the observational characteristics of the CN eruption, it is possible to understand the nebular environment and derive fundamental properties of the system. The following discussion provides an overview of the development of CNe along with their observed characteristics at each stage in the optical, infrared (IR), ultraviolet (UV), and X-ray regimes. A basic understanding of these phenomenological developments and the processes by which we glean information from them is crucial since these concepts will be referred to extensively throughout the rest of this thesis.

1.2.1 The Optical Light Curve

The first systematic studies of CNe were limited to the characterization of their optical light curves, i.e., the observed brightness as the system aged. Observations

of this photometric development revealed a surprising diversity in light curve evolution (Gaposchkin 1957).

The rise to maximum can take as little as 1-3 days and may correspond to an amplitude of $8 \lesssim \Delta m_V \lesssim 14 - 15$ magnitudes in the photometric V-band (Warner 2008). During these initial stages, the ejecta are optically thick due to the high densities ($\rho > 10^{12}$ cm^{-3}) and, near maximum light, mimic the appearance of an F-type stellar photosphere. The expansion of this "pseudophotosphere" causes the rapid increase to maximum brightness.

After maximum, optical luminosity declines as the ejecta cool and become optically thin. The optically thick surface recedes into deeper layers of the ejecta, where the temperatures are much higher. This recession of the pseudophotosphere results in a shift of the peak emission away from the optical and into the UV, and consequently, the observed decline in the light curve. During the early stages of development, the system radiates at a nearly constant bolometric luminosity (L_{bol}) that can exceed the Eddington luminosity of the system (Warner 2008). As the system evolves, the shape of the light curve is increasingly influenced by the presence of free-free emission and atomic emission lines (e.g., V1500 Cyg and V1065 Cen; Ennis et al. 1977; Helton et al. 2010b, respectively).

The speed at which the light curve decays is quantified by the nova's t_2 and t_3 times, i.e., the time it takes for the light curve to decline by 2 or 3 magnitudes, respectively. The "speed class" of a nova is determined by these values (Gaposchkin 1957). Fast novae such as V1974 Centauri, with t_2 times ranging from 11-25 days, typically have smooth light curves (Figure 1.1). In contrast, the light curves of slow novae, such as V723 Cas, with t_2 times of 81-150 days, often exhibit strong brightness variations of a few magnitudes (Figure 1.2). The fundamental determinant of the nova speed class is the mass of the underlying WD, however, the extreme variation in observed light curve behaviors implies that there are other physical parameters involved.

Observations of extragalactic novae of known distance have been used to generate accurate maximum magnitude-rate of decline (MMRD) relationships for CNe.

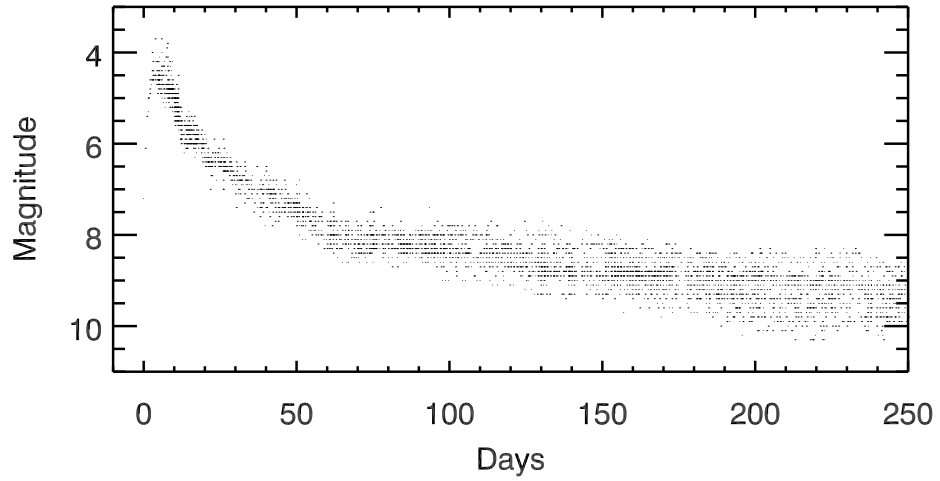

Figure 1.1: American Association of Variable Star Observers (AAVSO) light curve[2] of the fast nova V1974 Cyg.

The luminosities of CNe are typically greater than those of Cepheid variable stars enabling them to be observed well outside of the Local Group (e.g., SN2010U, which was observed at a distance of ~ 3.2 Mpc and misclassified as a supernova; Humphreys et al. 2010). Further, since CNe occur at a much higher frequency than supernovae (SNe), they have the potential to be useful as standard candles, i.e. cosmological distance indicators, if a reliable and accurate relationship can be derived between the t_2 time and the absolute magnitude (M_V) at maximum (Bode 2010). Unfortunately, there is a surprising degree of variation in the absolute magnitude of CNe and their light curve behaviors, particularly among fast, ONe novae (Del Pozzo 2005; Shafter 2008). Consequently, the accuracy of MMRD relations and their utility for use as standard candles is suspect, thus limiting their current usage to estimation of the distances to Galactic CNe.

1.2.2 Optical and Infrared Spectroscopic Development

Most novae go through a common sequence of spectroscopic developmental stages from initial outburst through their eventual return to a quiescent state. Although

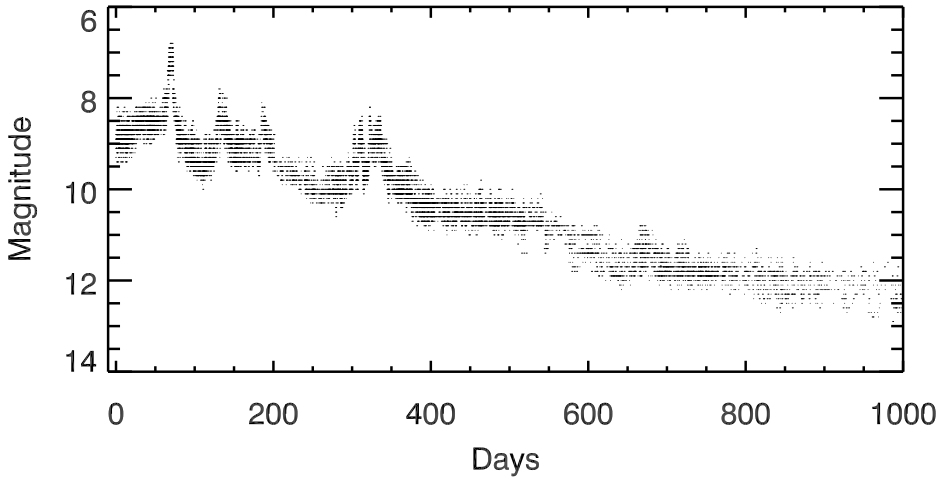

Figure 1.2: AAVSO light curve of the slow nova V723 Cas.

the general development is consistent amongst the majority of novae, including principal, diffuse-enhanced, and nebular stages (Gaposchkin 1957; Hack et al. 1993), individual objects display a striking dissimilarity in their detailed emission characteristics.

During the initial pre-maximum rise, the ejecta appear optically thick and exhibit spectroscopic characteristics very much like an F-type stellar photosphere. This stage is called the "fireball" stage due to its similarity to the early expansion of terrestrial nuclear explosions (Gehrz 1988). The spectra typically show absorption lines, the most prominent of which are from the Balmer sequence of hydrogen. The width of the absorption features provides a good approximation of the expansion velocity of the ejecta (Gaposchkin 1957; Warner 2008). At maximum light, emission lines of C, N, and O appear in the optical and infrared (IR), often with the characteristic P-Cygni absorption profiles. This "principal spectrum" can exhibit absorption profiles with multiple components blue-shifted by around -100 to -1300 km s^{-1}, providing clues to the structure of the ejecta at these early times (McLaughlin 1960). Some novae become rapidly dominated by permitted Fe II emission at this stage, followed by forbidden emission from [O I],

[N II], and [O III] (Williams 1992).

The P-Cyg components seen in the principal spectrum can be enhanced by the appearance of additional broad absorption components at even higher velocities (> 1500 km s^{-1}). This is called the "diffuse enhanced" spectrum. During this period, many novae have been observed to undergo an "O I flash" (Warner 2008)in which O I lines at 8446 Å and 1.1287 μm can become the brightest lines in the spectrum, in many cases exceeding the brightness of Hα (e.g., V1065 Cen, Helton et al. 2010b, and references therein).

During the principal and diffuse enhanced stages of optical development, the near- and mid-IR spectra show very weak absorption systems and much stronger emission lines. Most of the transitions observed during this stage are from the Humphreys, Brackett, and Paschen hydrogen recombination sequences, helium recombination lines, as well as various permitted transitions of C I, N I, O I, Fe II, and in some cases Na I (e.g., V705 Cas; Evans et al. 1996). Detection of the Na I lines is important for testing models of the thermonuclear runaway, which predict the production of substantial quantities of ^{22}Na (Starrfield et al. 2000; Gehrz et al. 1998b).

As the ejecta expand and the densities decline, the absorption components disappear due to the decreasing optical depth in the emission lines. During this nebular stage, the densities are low enough that forbidden lines are no longer collisionally de-excited and in most cases the observed spectra become dominated by nebular lines of [N II] λ5755, $\lambda\lambda$6548, 6583 Å, [O III] λ4363, $\lambda\lambda$4959, 5007 Å, [O II] λ3727 Å, and [Ne III] $\lambda\lambda$3869, 3968 Å(Williams et al. 1991, 1994). Some CNe spectra go through a coronal stage, in which the spectra exhibit emission lines of very highly ionized species such as [Ne V] $\lambda\lambda$3346, 3426 Å, [Fe VI] λ Å [Fe VII] λ5721, λ6087 Å, and even [Fe X] λ6375 Å. A more detailed overview of CNe optical spectral evolution is provided in Warner (2008), Williams (1992), and references therein.

At IR wavelengths, the spectra during the nebular stages are dominated by forbidden lines of a variety of metals including [N I] λ1.04 and λ4.65 μm, [Ne II]

λ12.81 μm, [Ne III] λ15.56 μm, [Ar II] λ6.99 μm, and [Ar III] λ8.99 μm, to name a few. During the later nebular and coronal stages more highly ionized species, such as [Ne V] λ14.32, λ24.30 μm, [Ne VI] λ7.61 μm, [Mg V] λ 5.61 μm, [Mg VII] λ5.50 μm, [Si VI] λ1.96 μm, and [Si VII] λ2.47 μm, among others, are often observed. The IR coronal lines are characterized by low excitation temperatures ($T < 10^5$ K), high critical densities ($n_{crit} > 10^6$), and ionization potentials $\geq$ 100 eV (Greenhouse et al. 1993; Woodward et al. 1995). [O IV] λ25.91 μm emission is frequently observed throughout the nebular stages of evolution (see Gehrz et al. 1998b, for additional discussion). Besides having complete isoelectronic[3] sequences available (Greenhouse et al. 1990), the IR wavelengths are less sensitive to reddening allowing for more accurate measurement of emission line fluxes. Thus, the IR regime is very useful in constraining the abundances of a variety of metal species during the nebular stages (Schwarz et al. 2007b; Helton et al. 2010b). Observations of CNe in the IR regime are crucial to developing a comprehensive picture of system dynamics, abundance values, and dust characteristics (Gehrz 1998a; Gehrz et al. 1998b).

In addition, various molecular species such as carbon monoxide (CO) and complex hydrocarbons such as polycyclic aromatic hydrocarbons (PAHs) (Evans et al. 1996) emit in the IR regime. The continuum at IR wavelengths can also be dominated by dust emission from amorphous carbon (AC) and may include solid state features arising from silicon carbide (SiC) and silicates (Gehrz 2008b, and see §1.3 below).

The emission lines observed during the nebular stages are determined primarily by the underlying radiation field from the WD, the ejecta densities and density inhomogeneities, and the abundances of elemental species within the ejecta. Hence, careful modeling of the observed emission lines can reveal the physical conditions (e.g., temperatures and densities) and elemental abundances in the ejecta (Helton et al. 2010b; Vanlandingham et al. 2005). Further, the shape of

[3] i.e. a sequence of elements having the same electron configuration and, in consequence, exhibiting similar chemical behavior

the emission lines can be used to estimate the dynamics and geometry of the ejecta (Lynch et al. 2006a; Kamath et al. 2005; Gill & O'Brien 1999).

1.3 Dust Production in CNe

Many CNe produce dust in their ejecta. The dust condensation event is signaled by a rapid decline in the optical light curve due to extinction (Figure 1.3) with a corresponding rise in the IR luminosity due to thermal emission from the dust (Gehrz 1988). Models of the spectral energy distribution (SED) in these systems suggest that the condensation event yields relatively large dust grains with radii up to ~ 1 μm (Gehrz 2008b). It is commonly assumed that the production of substantial quantities of dust, as demonstrated by deep optical extinction events, occurs primarily in CO systems (Retter 2004; Gehrz 2008b). However, Helton et al. (2010b) demonstrated that significant quantities of dust can be produced in ONe novae (e.g., V1065 Cen) as well. This emphasizes the need for high sensitivity mid-IR observations to accurately characterize dust production in CNe.

A prerequisite for grain formation is the presence of molecular nucleation sites, often thought to be large hydrocarbon molecules (Evans & Rawlings 2008). The precursors of nucleation sites are simple molecules such as CO, CN, CH, and C_2. Though CN was one of the first molecules detected in a nova (in DQ Her; Wilson & Merrill 1935), it has been found in very few other CNe. In contrast, a number of dust forming novae have revealed the presence of a transient population of CO in their ejecta prior to the onset of dust condensation (e.g., V705 Cas; Evans et al. 1996).

The formation of these nucleation sites is suppressed in regions of the ejecta in which carbon has been ionized. This suppression occurs because the most efficient chemical pathways for molecular formation of basic molecules (e.g., CO, CH, C_2), which precede the formation of more complex hydrocarbons, involve reactions with H_2, which is easily photodissociated in the carbon-ionized zone

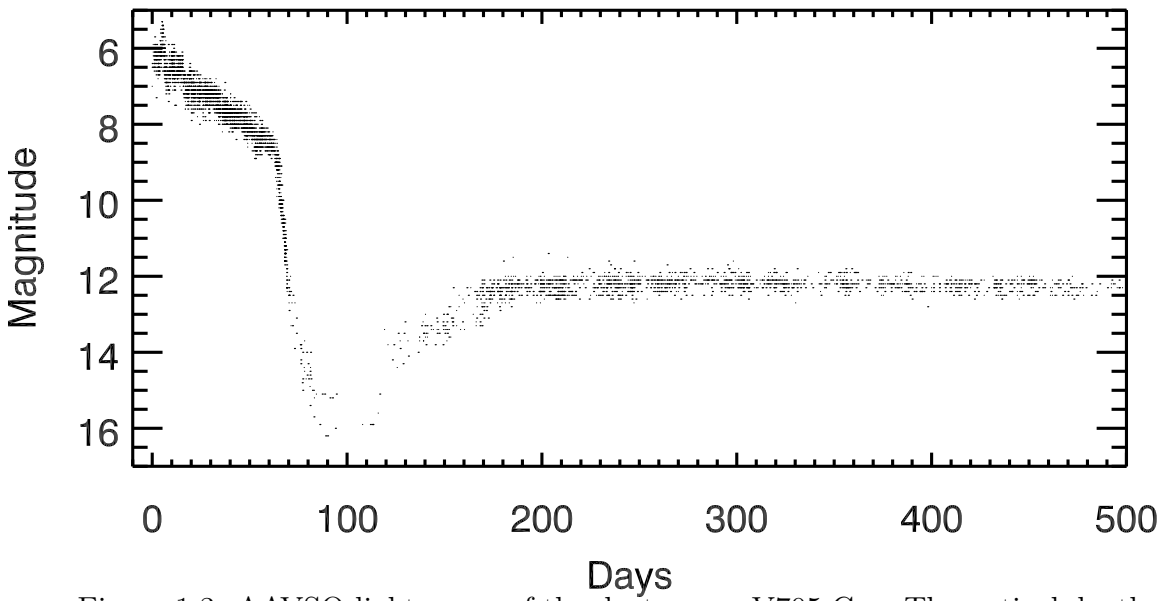

Figure 1.3: AAVSO light curve of the dusty nova V705 Cas. The optical depth of the extinction event was $\tau_V \sim 5.5$ magnitudes.

(Evans & Rawlings 2008). Further, the presence of oxygen in the ejecta is believed to inhibit the formation of nucleation sites due to neutral exchange reactions. Recent models have been been relatively successful at generating sufficient nucleation sites to allow grain growth even in the presence of gas phase oxygen (Pontefract & Rawlings 2004). These models have also successfully reproduced the observed CO abundances in novae ejecta.

The mechanism by which the dust grains condense and grow is not well understood. Simple models suggest that as the pseudophotosphere recedes, the ejecta are exposed to an increasingly hard radiation field, which ionizes the ejecta. If the gas temperature declines to the condensation temperatures of the dust (of order 1200-1400 K; Ebel 2000) before the ionization front reaches it and the local densities are high enough for frequent collisional interactions, then dust will be able to form (Evans & Rawlings 2008). Alternatively, Shore & Gehrz (2004) proposed that grain growth is not inhibited by the hard radiation field in the CN

environment, but rather photoionization may be required to explain the rapidity with which nova dust forms. In this model, photoionization increases the reaction cross section of grains and consequently yields higher growth rates. Optical and IR spectroscopic observations during the dust condensation stage may help elucidate the role of photoionization in dust formation by revealing the state of ionization of the system as dust condensation and grain growth progresses (see Chapter 3).

The complexity of the dust condensation process in CNe is made evident by the observational characteristics of the dust observed in CNe. Unlike most astronomical sources of dust, novae have been observed to produce both carbon rich and oxygen rich dust species in the same eruption (e.g., Gehrz et al. 1992c). Evans & Rawlings (2008) suggest that the chemical dichotomy observed in CNe may be explained by incomplete carbon monoxide formation in the ejecta (see also Pontefract & Rawlings 2004). If CO does not form to saturation, then neither carbon nor oxygen will be entirely bound up in CO, leaving both available for dust production. Alternatively, abundance gradients in the ejecta or a globally inhomogeneous abundance distribution could result in the production of different dust species.

Dust emission in CNe exhibits characteristics distinct from that in other astronomical sources. Observations soon after dust formation suggest that the dust can condense at extremely high temperatures (T $\sim$ 1400 K; Lynch et al. 2008b). The silicate features present in CNe appear to be more broad and have highly variable peak wavelengths and relative strengths between the 9.7 and 18 μm features (V705 Cas, Nova Aql 1982, and V1065 Cen; Evans et al. 1997; Smith et al. 1995; Helton et al. 2010b, respectively). Some novae also exhibit emission features associated with hydrocarbon molecules (e.g., V705 Cas and V842 Cen; Evans et al. 1997; Hyland & McGregor 1989, respectively).

1.3.1 X-ray and UV Emission

Throughout the early development of CNe, the excitation of the ejecta is due to illumination by the hot pseudophotosphere. As the pseudophotosphere recedes, hotter layers are revealed until the photospheric surface approaches that of the WD. This recession results in a transition of the peak emission into the UV and X-ray regimes.

Recent observations of CNe have confirmed that many undergo an extended period of super-soft source (SSS) X-ray emission (e.g., Ness et al. 2007a). This emission does not correspond to steady accretion of H-rich material onto the WD surface as in other SSSs (Kahabka & van den Heuvel 1997). Instead, the SSS emission arises from nuclear burning of the material left over from the mass ejection event. The duration of the SSS stage reflects the amount of H-rich material left behind on the WD surface after the mass ejection event. This, in turn is related to the mass of the WD progenitor as well as the mass accretion rate and WD temperature (Yaron et al. 2005). Predictions of the SSS duration based upon the amount of material predicted to be left behind after the CN eruption can be $> 10^3$ years (Hernanz & Sala 2002). In contrast, ROSAT observations suggested that most novae turn off within 10 years after outburst (Orio et al. 2001) and more recent observations indicate that the duration of the SSS phase in Galactic CNe is typically rather short, of order 2-3 years (Ness et al. 2007a). The orders of magnitude discrepancy between theoretical and observed turnoff times likely indicates higher than expected mass loss during the eruption though the theoretical explanation for this high mass loss is not yet understood (Hernanz & Sala 2010).

While in the SSS phase, the ejecta are subjected to an intense flux of high photons (0.5-10 keV) that can have a significant impact on the observed spectroscopic characteristics of the emission lines and the dust. By coordinating observations using the *Swift* telescope with optical monitoring efforts, it is possible to determine the connection between optical and IR observational characteristics and X-ray behavior. This may result in a general prescription for associating a class of optical spectral features with a general state of X-ray emission. For example,

initial results seem to indicate that the optical signature of [Fe X] λ6375 Å may be a good indicator that a CN is in a SSS state. These X-ray and UV data also reveal the connection between energetic radiation and dust processing.

1.4 Extant Questions, Broad Implications, and Thesis Goals

Though the general development of CNe is relatively well established, many important questions remain unanswered regarding both the evolution of CNe themselves as well as their applicability to broad areas of astrophysical importance.

The extreme overabundances of heavy elements (e.g., C, N, O, Ne, Ar, Mg, S) in the ejecta of CNe are due to convective dredge-up from the surface layers of the WD during the TNR. However, recent models of the TNR suggest that in some cases, it is possible for the runaway to undergo "breakout" from the hot CNO cycle allowing enhancements of the heavier elements (Glasner & Truran 2009). Isolating the abundance contribution from dredge-up relative to abundance enhancement from the TNR is complicated and requires careful abundance estimates, based upon broad wavelength, high cadence spectroscopic observations, for comparison to theoretical models (Vanlandingham et al. 2005; Helton et al. 2010b).

Theoretical models of the TNR suggest that an order of magnitude less material is ejected in the eruption than is measured observationally (Starrfield et al. 1998). Indeed, as the physics behind the models improves, (e.g., with improved reaction rates; Iliadis et al. 2002), and with the advent of 3-D simulations, the discrepancies seem to increase. Is this due to problems with the TNR models themselves or with the observational mass estimates? If the observationally determined ejecta masses are correct, then the relatively high rate of nova explosions in the Galaxy (i.e. 34^{+15}_{-12} yr^{-1}; Darnley et al. 2006) combined with the extreme elemental enhancements found in the ejecta of many novae would imply a significant contribution to chemical evolution of the interstellar medium (ISM), possibly

comparable to SNe.

Likewise, models predict that substantial quantities of ^{22}Na will be produced in the TNR. This isotope of sodium is unstable and has a relatively short half-life ($\tau_{1/2} \sim 2.6$ years). It decays into ^{22}Ne with the release of a 1.275 MeV γ-ray. Yet, the only detections of this emission signature have had very low significance, and this in spite of the fact that the observed ejecta masses in CNe are much higher than predicted by models (Iyudin et al. 2001). Though Na emission has been observed in some systems, (e.g., V705 Cas; Evans et al. 1996), it is seen only rarely.

Modeling of the ejecta of CNe often assumes that they are spherically symmetric. Indeed, historically it has been necessary to wait many years, perhaps decades, before the ejecta could be directly imaged. Recent observations on 8-meter class telescopes are able to reveal the structure of CNe much earlier (e.g., V1280 Sco and V445 Pup; Chesneau et al. 2008; Woudt et al. 2009, respectively) allowing more accurate modeling of the ejecta (Moraes & Diaz 2009). To date, however, too few novae have been observed to allow any meaningful connection to be drawn between light curve and spectroscopic behavior and ejecta morphology. Further, the processes that act to sculpt the ejecta distribution, e.g., the common envelope phase or asymmetric TNR, are also poorly understood.

A consistent, well defined model for the CN outburst is required to understand the photometric behavior of a CN and to develop a well defined MMRD relationship. Yet spectroscopic observations of CNe over broad wavelengths reveal a surprising degree of diversity in their observational characteristics (Williams et al. 1991, 1994). Current models do not well constrain the bright end of the relation. Without such constraint, it is not possible to use CNe as reliable distance indicators on local cosmological scales. Further, a well calibrated MMRD relation would allow distances to Galactic CN to be quickly determined and applied to subsequent analysis. Though deriving a robust relation for novae of all types has proven to be difficult, it may be possible to isolate a distinct class of CNe that are particularly self-consistent facilitating their use as standard candles (Bode 2010).

X-ray observations of CNe in the SSS phase also illuminate new questions that need to be addressed. The persistent nature of the SSS phase seems to indicate that the duration of the constant L_{bol} phase may be longer than originally believed. If correct, this might have severe implications for our understanding of the TNR, mass ejection during the outburst, and the processes of accretion and reestablishment of the accretion disk. Unfortunately, it is sometimes difficult to procure observing time on X-ray capable observatories. It would be useful then to identify an alternative means by which one can determine whether CNe are in a SSS state in cases where X-ray observations are unavailable. For example, is [Fe X] λ6375 Å emission always an indicator of an underlying SSS? Finally, what role does the underlying X-ray and UV source of illumination play on the processing of dust in the ejecta?

Much closer to home, CN are thought to have played a role in seeding the pre-solar nebula with metals dredged up from the WD and processed by the TNR (José et al. 2004; Pepin et al. 2010). Presolar SiC grains isolated from meteoric inclusions have been identified as originating in the outbursts of massive ONe CNe. Some of these grains have been found to have low $^{12}C/^{13}C$ and $^{14}N/^{15}N$ ratios with high $^{26}Al/^{27}Al$ ratios matching predictions for CNe (Amari et al. 2001). Analysis of other inclusions have found isotopic $^{12}C/^{13}C$, $^{14}N/^{15}N$, and $^{20}Ne/^{22}Ne$ ratios that are more consistent with a CO nova origin (Heck et al. 2007). Though a recent study has called into question the attribution of these grains to CNe (Nittler & Hoppe 2005), it seems likely that CNe were at least a secondary contributor to the metal and dust content of the presolar nebula.

This problem is closely associated with the questions surrounding dust formation in CNe. Observationally, CNe are known to produce many varieties of dust in their ejecta. Due to the rapid rate of condensation (of order hours to days) and the relatively short timescales on which the dust is subsequently processed and disseminated into the surrounding ISM (months to years), studies of dusty CNe provide insight into each stage of dust formation and processing in real time. They are effectively live science laboratories in which we can explore dust physics

under astronomical conditions. Conducting detailed observations of dusty novae throughout their evolution leads to a better understanding of molecule formation and the subsequent formation of nucleation sites and processes of grain condensation. Diligently following the evolution of the dust reveals the processes by which the dust is modified by the ambient radiation field and allows an estimation of the CNe contribution of dust grains to the ISM and presolar nebula.

This thesis seeks to answer some of the above questions about CNe evolution and physics, dust condensation and distribution, and the application of CNe to other, broadly ranging areas of astrophysics through an explorative examination of CNe during multiple stages in their outburst in the optical and IR regimes. In Chapter 2, I provide a brief overview of our CNe observational campaigns undertaken in the IR with both the *Spitzer Space Telescope* and the Gemini Observatories, and in the optical with the 90" Bok Telescope. I also briefly mention the other collaborative observational projects in which our research group is participating. In Chapter 3 I present detailed analysis of the classical nova V1065 Centauri (Nova Cen 2007). The data presented encompass nearly all stages of evolution discussed above and rely heavily upon observations in the optical (SMARTS) and infrared (*Spitzer* and Gemini), supplemented by X-ray and UV observations (*Swift*). In Chapter 4, I examine the spectra of old novae taking advantage of the high sensitivity and spectral resolution of the *Spitzer Space Telescope* to explore questions surrounding the late stages of CNe evolution, many years after eruption. In Chapter 5, I present analysis of the dusty nova DZ Cru along with initial analysis of V2362 Cyg and V2361 Cyg observed with *Spitzer*. These targets have been found to exhibit highly atypical dust features. I examine their IR spectroscopic characteristics in detail and attempt to identify the nature of the carrier for the emission. Finally, in Chapter 6, I summarize the results of the work presented in this thesis. I also provide a short discussion of ongoing projects involving the extensive observational data set obtained as part of my thesis work and discuss future observational strategies to explore remaining questions.

Chapter 2

The UMN Nova Program

2.1 Program Overview

Our understanding of CNe eruptions is limited by access to time resolved, panchromatic spectra. Without adequate temporal and spectral coverage, it is impossible to accurately assess the dynamical evolution of the TNR, the changing structure of the ejected shell, or the processes of dust grain growth and destruction. In order to achieve the thesis goals outlined in Chapter 1 above, I have been involved in a long-term, multiwavelength observational campaign using the *Spitzer Space Telescope*, the Gemini observatories, the Bok 90" (2.29-m) optical telescope, and the *Swift GRB* telescope. I have also actively collaborated with the The Stony Brook / SMARTS Spectroscopic Atlas of Southern Hemisphere Novae initiative. Other collaborators have obtained data at the Lick Observatory and the IRTF.

The data obtained as part of this project allows a detailed examination of the CN phenomenon. Analysis of changing emission line structure and relative strengths provide important clues to the distribution, temperature, density, and dynamics of the expanding ejecta, which can be modeled using the Cloudy07 photoionization code (Ferland et al. 1998). Early hydrogen recombination line spectra reveal the initial ionization state of the shell while later observations of nebular

and coronal lines prominent in the mid-IR, such as Ne, Ar, and S, give ejecta temperatures, densities, and relative abundances. The individual line profiles exhibit the ejecta geometry and degree of clumpiness (Shore et al. 2003; Woodward et al. 1995). IR observations provide insight into the dust production in the ejecta. Since silicates and PAH-like molecules have prominent emission features from $8 - 13$ μm and hot, optically thick dust emits a blackbody-like continuum that initially appears in the near-IR, modeling of the IR spectral energy distribution (SED) using the DUSTY radiative transfer code (Ivezić et al. 1999) provides constraints to the dust composition, grain size distribution, dust temperature, and mass.

As part of this campaign, we have observed nearly 59 different novae in the optical and the infrared. Five targets were not detected. Of the objects observed in our sample, there were 49 classical novae, 6 recurrent novae, 3 dwarf novae, and 2 symbiotic novae. At least one object, GK Per, has exhibited eruptions characteristic of both a classical nova and a dwarf nova. This thesis only discusses the classical novae sample.

The classical novae in the sample encompassed a variety of classes, fast and slow, dusty and dust free, throughout many different stages of development. Of the novae observed, 13 fell into the "very fast" speed class of Gaposchkin (1957), 15 were "fast," 5 were "moderately fast," 2 were "slow," and 14 were of unknown speed class. The lack of speed classification in these latter objects was due to poor sampling of their light curves or to their relative youth at the time of this writing. Further, 16 novae in our sample showed clear indications of dust formation, and of those, 5 also exhibited UIR emission features. Only 5 objects, including V2671 Oph, V2615 Oph, V496 Sct, NQ Vul, and V705 Cas, were observed to produce CO in their ejecta. Caution should be exercised when drawing conclusions from the number of objects in our sample that were observed to produced CO or dust in their ejecta. Since the onset of dust condensation varies from a few days to nearly 100 days after outburst and since dust formation often coincides with a precipitous drop in the optical light curve, it is likely that many targets in our

sample either have not yet produced dust but will, or produced dust that was not detected. Similarly, the stage of formation of CO is often short and was probably overlooked in some targets.

This program has been highly successful. To date, the *Spitzer* and optical data have contributed to nearly 10 refereed publications including detailed analysis of the 2008 eruption of the recurrent nova RS Ophiuchi (Evans et al. 2007a,b; Ness et al. 2007b), examination of the CO nova V1186 Scorpii (Schwarz et al. 2007b), late stage evolutionary analysis of nova QU Vulpeculae (Gehrz et al. 2008a), and examination of UIR features in CNe such as V2362 Cygni and DZ Crucis (Lynch et al. 2008b; Evans et al. 2010b, respectively). Many targets were observed very early after outburst revealing time sensitive clues to the nature of their evolution. These observations have led to the publication of numerous circulars intended to notify the greater CNe observing community of critical developments in these systems. The circulars resulting from this program include publications on V2491 Cyg (Helton et al. 2008a), V2671 Oph (Helton et al. 2008b), V2670 Oph (Helton et al. 2008c), V1721 Aql (Helton et al. 2008d; Hounsell et al. 2010b), V1280 Sco (Ness et al. 2009), V2468 Cyg (Schwarz et al. 2009), and V5586 Sgr (Helton et al. 2010a).

A brief summary of the observations obtained as part of this program is provided here. The log of *Spitzer* observations is given in Table 2.1 and optical observations in Table 2.2. Table 2.3 provides basic properties of all targets in the observational program derived from the literature and from our observations.

2.2 Infrared Observational Program

The core of our infrared observational program consisted of data obtained with the *Spitzer* Space Telescope (Werner et al. 2004; Gehrz et al. 2007). *Spitzer* data acquisition was conducted using two observational strategies, one a Target-of-Opportunity (ToO) program and the other a monitoring program. These data were supported by supplementary observations using the Gemini Telescopes and

the Large Binocular Telescope (LBT).

Early mid-IR studies of CNe relied primarily on narrow band photometry, which approximated very low resolution spectra. Though critical for the development of our understanding of the IR behavior of CNe, these observations failed to reveal weak emission lines or to provide information about emission line structure Gehrz (2008b). A key advancement in our understanding of the IR development of CNe was obtained through a coordinated observational campaign using the Infrared Space Observatory (ISO; Kessler et al. 1996). ISO allowed spectroscopic observations to be made from 2.4 to ~ 200 μm with relatively high spectral resolution, $R = \Delta\lambda/\lambda$ ranging from ~ 200 to $\sim 35,000$ depending upon the instrumental setup used (Clegg et al. 1996; de Graauw et al. 1996). The ISO CNe observations provided fresh insight into the development of conditions in the ejecta during the nebular and coronal stages (e.g., Gehrz et al. 1997; Lyke et al. 2001), allowed new, more accurate determination of CNe abundances (Lyke et al. 2001, 2003a), and revealed the critical importance of using panchromatic observations to constrain abundance models of the ejecta (Lyke 2003b). Unfortunately, due in part to poor target availability, fewer than 10 CNe were able to be observed using ISO and most of these observations had poor temporal coverage amounting only to snapshots of the IR development (e.g., Lyke 2003b). Further, there was a surprising dearth of dust producing sources observed as part of the ISO campaign (Salama et al. 1998).

Our *Spitzer* CNe ToO and monitoring campaigns are the next step in our effort to develop a comprehensive understanding of the CN outburst and its impact on its local environment. In contrast to previous observational efforts, the Infrared Spectrograph (IRS) on board *Spitzer* obtained data with mJy sensitivity at moderate resolution (up to $R \sim 600$) allowing the examination of weak emission lines as well as emission line structure in targets both young (a few 10s of days) and old (10+ years). Many objects in the program were observed from initial outburst through the late stages of their development with semi-regular coverage for over 3-4 years. The data obtained in our *Spitzer* CNe ToO and monitoring campaigns

amounts to the most comprehensive, quality mid-IR data set obtained on CNe to date. Taken as a whole, these data provide a uniform basis for a statistical examination of the IR development of CNe. A summary of the *Spitzer* data obtained as part of this program is provided in Table 2.1. Full details of the data acquisition and reduction for the individual targets presented in this thesis are provided in subsequent chapters.

Details of the observations varied by target, by epoch, and by observational program. Targets were observed using the short wavelength ($5.2 - 14.5$ μm), low-resolution module (SL), the long wavelength ($14 - 38.5$ μm), low-resolution module (LL), short wavelength ($9.9 - 19.5$ μm), high-resolution module (SH), and the long wavelength ($18.7 - 37.2$ μm), high resolution module (LH). The resolution of the low resolution modules ranged from $R = \lambda/\Delta\lambda \sim 60 - 128$. The high resolution modules had $R \sim 600$. In most cases, the target was acquired using the peak-up array. Upon acquisition in the peak-up array, the centroid of the source was calculated and the source was offset into position within the slit. For some observations, the source was too faint to use peak-up array positioning. In these cases, the targets were positioned in the slit using the raw pointing of the telescope. In all cases, the target was nodded along the slit. In the case of the low-resolution modules, this allowed the sky to be removed through a simple subtraction of the two nod positions. The PSF nearly filled the high-resolution slits, preventing sky subtraction of the high resolution data using the different not positions alone. Instead, for most of the high resolution observations, separate follow-on sky frames were obtained of a field near to the source. These frames were median combined and subtracted from the on-source data. In addition, to the problems with sky subtraction, nodding of the high resolution modules resulted in partial flux losses preventing rigorous absolute flux calibration of these data.

The details of the data reduction varied by source. The general procedure was as follows. Bad pixels in the IRS Basic Calibrated Data (BCD) products were identified using bad pixel masks provided in the calibration data sets and were corrected using a linear interpolation scheme. The data were nod subtracted (low

resolution) or sky subtracted (high resolution) to remove the background flux. The spectra were then extracted using Spice program, provided by the Spitzer Science Center, using the default point source extraction widths. The extracted spectra were then combined using a weighted mean. In some cases, data were cleaned visually and defringed if needed.

A log of the *Spitzer* observations is provided in Table 2.1 below.

Table 2.1: *Spitzer* Target Details

Target	PID[a]	Date (UT)	AOR[b]	Modules[c]
V723 Cas	30076	2006 Sep 17	17732608/7728	SL,SH,LH/LH
	40060	2007 Sep 04	22268416/8672	SL,SH,LL,LH/SH,LH
GK Per	00124	2004 Mar 01	5028608	SL,SH,LH
V574 Pup	02333	2005 Mar 20	10274560/5072	SL,SH,LH/SH,LH
	02333	2005 Apr 16	10276096/6864	SL,SH,LH/SH,LH
	02333	2005 Nov 15	10276352/7120	SL,SH,LH/SH,LH
	20262	2006 Apr 16	14475776/7056	SL,SH,LL,LH/SH,LH
	20262	2006 May 14	14476032	SL,SH,LL,LH
	20262	2006 May 25	14476288	SL,SH,LL,LH
	30076	2007 May 03	17731328/6448	SL,SH,LH/LH
	30076	2007 Dec 07	17731584/6704	SL,SH,LH/LH
	40060	2007 Dec 17	22267136/7392	SL,SH,LH/SH,LH
	30076	2008 Apr 25	17731840/6960	SL,SH,LH/LH
V382 Vel	00122	2004 Feb 21	5021696	SL,SH,LH
	30076	2007 Mar 26	17733120/8240	SL,SH,LH/LH
	40060	2008 Feb 25	22269440/9696	SL,SH,LL,LH/SH,LH
V1065 Cen	30007	2007 Mar 08	17677568/7824	SL,SH,LL,LH/SH,LH
	30007	2007 Mar 18	1768080/8336	SL,SH,LL,LH/SH,LH
	30007	2007 Mar 26	17679616/9872	SL,SH,LL,LH/SH,LH
	30007	2007 Jun 25	17683200/3456	SL,SH,LL,LH/SH,LH
	40060	2007 Aug 30	22265088/5344	SL,SH,LL,LH/SH,LH
	40060	2008 Feb 25	22265600/5856	SL,SH,LL,LH/SH,LH
	40060	2008 Jul 02	22270976/1232	SL,SH,LL,LH/SH,LH
	50011	2008 Jul 02	25192960/3216	SL,SH,LL,LH/SH,LH

Continued on Next Page...

Table 2.1 – Continued

Target	PID[a]	Date (UT)	AOR[b]	Modules[c]
	50011	2008 Sep 02	25198080/8336	SL,SH,LL,LH/SH,LH
	50011	2009 Feb 22	25201408/1664	SL,SH,LL,LH/SH,LH
DZ Cru	40060	2007 Sep 06	22269952/70208	SL,SH,LL,LH/SH,LH
	30076	2008 Feb 25	17734912/40032	SL,SH,LL,LH/LH
	30076	2008 Sep 06	17735168/40288	SL,SH,LL,LH/LH
T CrB	40060	2007 Aug 30	22258944/9200	SL,SH,LL,LH/SH,LH
V1280 Sco	30007	2007 Apr 17	17680128/0384	SL,SH,LL,LH/SH,LH
	30007	2007 May 03	17681664/1920	SL,SH,LL,LH/SH,LH
	40060	2007 Sep 06	22270464/0720	SL,SH,LL,LH/SH,LH
	40060	2008 May 06	22271488/1744	SL,SH,LL,LH/SH,LH
	50011	2008 Sep 14	25190912/1168	SL,SH,LL,LH/SH,LH
	50011	2008 Oct 04	25196032/6288	SL,SH,LL,LH/SH,LH
V1186 Sco	02333	2004 Aug 27	10273536	SL,SH,LH
	02333	2004 Aug 29	10273792	SL,SH,LH
	02333	2004 Aug 31	10274048	SL,SH,LH
	02333	2005 Mar 21	10274304	SL,SH,LH
	02333	2005 Mar 21	20175328	SL,SH,LH
	20262	2006 Mar 22	14474240/6544	SL,SH,LL,LH/SH,LH
	20262	2006 Apr 25	14474496	SL,SH,LL,LH
	40060	2007 Oct 01	22264064/4320	SL,SH,LH/SH,LH
	30076	2007 Oct 15	17730560/5680	SL,SH,LH/SH,LH
	30076	2008 Apr 25	17730816/5936	SL,SH,LH/LH
	30076	2008 Oct 04	17731072/6192	SL,SH,LH/LH
V1187 Sco	02333	2004 Sep 28	10274816	SL,SH,LH
	02333	2005 Mar 21	10275584/5840	SL,SH,LH
	20262	2006 Apr 22	14475008/6800	SL,SH,LL,LH/SH,LH
	30076	2007 Sep 30	17730304/5424	SL,SH,LH/LH
	40060	2007 Oct 01	22264576/4832	SL,SH,LH/SH,LH
V2615 Oph	50011	2008 Oct 02	25193984/4240	SL,SH,LL,LH/SH,LH
	50011	2009 Apr 21	25199104/9360	SL,SH,LL,LH/SH,LH
V378 Ser	40060	2007 Oct 03	22266112/6368	SL,SH,LL,LH/SH,LH
	30076	2007 Oct 15	17734144/9264	SL,SH,LH/LH

Continued on Next Page...

Table 2.1 – Continued

Target	PID[a]	Date (UT)	AOR[b]	Modules[c]
	40060	2008 Apr 21	22266624/6880	SL,SH,LL,LH/SH,LH
	30076	2008 Apr 25	17734400/9520	SL,SH,LH/LH
	50011	2008 Oct 02	25191424/1680	SL,SH,LL,LH/SH,LH
	30076	2008 Oct 04	17734656/9776	SL,SH,LH/LH
	50011	2008 Oct 18	25196544/6800	SL,SH,LL,LH/SH,LH
RS Oph	00270	2006 Apr 16	17057024/7280	SL,SH,LL,LH/SH,LH
	00270	2006 Apr 26	17056768/7792	SL,SH,LL,LH/SH,LH
	00270	2006 Sep 10	17058560/7536	SL,SH,LL,LH/SH,LH
	00270	2006 Oct 17	17058304/8048	SL,SH,LL,LH/SH,LH
	30007	2007 Apr 19	17681152/1408	SL,SH,LL,LH/SH,LH
	30007	2007 Sep 30	17682688/2944	SL,SH,LL,LH/SH,LH
	40040	2007 Oct 03	22259456/60244	SL,SH,LL,LH/SH,LH
	40060	2008 Apr 26	22259968/60224	SL,SH,LL,LH/SH,LH
	50011	2008 Oct 02	25193472/3728	SL,SH,LL,LH/SH,LH
	50011	2009 Apr 29	25198592/8848	SL,SH,LL,LH/SH,LH
V745 Sco	40060	2007 Oct 01	22260992/1248	SL,SH,LL/SH
V5558 Sgr	50011	2008 Oct 02	25195520/5776	SL,SH,LL,LH/SH,LH
	50011	2009 Apr 29	25200640/0896	SL,SH,LL,LH/SH,LH
V5116 Sgr	50011	2008 Oct 04	25195008/5264	SL,SH,LL,LH/SH,LH
	50011	2009 Apr 29	25200128/0384	SL,SH,LL,LH/SH,LH
V3890 Sgr	40060	2007 Oct 11	22260480/0736	SL,SH,LL/SH
V1494 Aql	00122	2004 Apr 14	5022464	SL,SH,LH
	30076	2007 Jun 08	17732864/7984	SL,SH,LH/LH
	40040	2007 Oct 12	22268928/9184	SL,SH,LL,LH/SH,LH
NQ Vul	00124	2004 Apr 16	5040384	SL,SH,LH
V458 Vul	50011	2008 Jul 06	25194496/4752	SL,SH,LL,LH/SH,LH
	50011	2008 Nov 11	25199616/9872	SL,SH,LL,LH/SH,LH
V2361 Cyg	02333	2005 May 23	10278144	SL,SH,LH
	02333	2005 Jun 06	10278400	SL,SH,LH
	00124	2005 Oct 19	15865600/5344	SL,SH,LL,LH/SH,LH
	30076	2007 Jun 08	17733376/8496	SL,SH,LL,LH/LH
	30076	2007 Oct 03	17733632/8752	SL,SH,LL,LH/LH

Continued on Next Page...

Table 2.1 – Continued

Target	PID[a]	Date (UT)	AOR[b]	Modules[c]
	40060	2007 Oct 10	22263040/3296	SL,SH,LL,LH/SH,LH
	30076	2007 Dec 06	17733888/9008	SL,SH,LL,LH/LH
	40060	2008 Jun 04	22263552/3808	SL,SH,LL,LH/SH,LH
QU Vul	00124	2004 May 11	5044992	SL,SH,LH
V2467 Cyg	30007	2007 Jun 08	17686272/6528	SL,SH,LL,LH/SH,LH
	30007	2007 Jun 26	17686784/7040	SL,SH,LL,LH/SH,LH
	50011	2008 Jul 07	25192448/2704	SL,SH,LL,LH/SH,LH
	50011	2008 Nov 06	25197568/7824	SL,SH,LL,LH/SH,LH
V1974 Cyg	00124	2003 Dec 17	5043968	SL,SH,LH
	30076	2006 Oct 18	17732096/7216	SL,SH,LH/LH
	40060	2007 Aug 30	22267648/7904	SL,SH,LH/SH,LH
V2362 Cyg	30007	2006 Dec 13	17678592/8848	SL,SH,LL,LH/SH,LH
	30007	2006 Dec 24	17679104/9360	SL,SH,LL,LH/SH,LH
	30007	2007 Jun 22	17680640/0896	SL,SH,LL,LH/SH,LH
	40060	2007 Sep 06	22261504/1760	SL,SH,LL,LH/SH,LH
	40060	2007 Nov 02	22262016/2272	SL,SH,LL,LH/SH,LH
	40060	2008 Jul 08	22262528/2784	SL,SH,LL,LH/SH,LH
	50011	2008 Jul 09	25191936/2192	SL,SH,LL,LH/SH,LH
	50011	2008 Nov 11	25197056/7312	SL,SH,LL,LH/SH,LH
V1500 Cyg	00124	2003 Dec 17	5047040	SL,SH,LH
V1668 Cyg	00124	2003 Dec 15	5047552	SL,SH,LH
V705 Cas	00124	2004 Jul 17	5049088	SL,SH,LH
	30076	2007 Sep 01	17732352/7472	SL,SH,LH/LH
	40060	2007 Aug 30	22268160	SL,LL

[a]Program Identification Number – 00122 - PI R.D. Gehrz; 00124 - PI R.D. Gehrz; 00270 - PI A. Evans; 02333 - PI C.E. Woodward; 20262 - PI A. Evans; 30007 - PI C.E. Woodward; 30076 - PI A. Evans; 40060 - PI A. Evans; 50011 - PI C.E. Woodward

[b]Astronomical Observation Request – Target/Background

[c]Modules – Target/Background – SL = Short-Low; SH = Short-High; LL = Long-Low; LH = Long-High

2.3 Optical Observational Program

Optical observations were obtained at the Steward Observatory Bok 90" Telescope as part of a long running guaranteed time program consisting of $2-3$ night of grey-time each trimester. Observing time was obtained through the University of Minnesota's membership in the Research Corporation and its partnership with the University of Arizona, Steward Observatory, and the Large Binocular Telescope consortium.

The observations were made using the Boller & Chivens Spectrograph at f/9 Ritchey-Chretien focus in one of six different observing modes, labeled "Blue," "Red," "HR Blue," "HR Red," "Hα 1," and "Hα 2." The Blue set-up utilized the 400 line/mm 1$^{\rm st}$ order grating with the UV36 blocking filter to prevent order contamination. The spectral coverage was from $\sim$ 3600 to $\sim$ 6750 Å at a spectral resolution of roughly 2.8 Å\pixel. The Red set-up was identical but with the grating centered near 7600 Å providing coverage from $\sim$ 6000 to $\sim$ 9250 Å. For the Red set-up, the Y48 blocking filter was used. The HR Blue and HR Red set-ups both used the 1200 line\mm 1$^{\rm st}$ order high resolution grating. The HR Blue set-up was centered near 4440 Å, and the HR Red set-up was centered near 6060 Å. In both cases, the spectral coverage was 1185 Å at a resolution of 1.0 Å\pixel. The UV36 filter was used for both. The Hα 1 set-up used the 600 line\mm 1$^{\rm st}$ order grating at a central wavelength of 6570 Å and coverage of $\sim$ 2300 Å at a resolution of 1.9 Å\pixel. An alternative Hα 2 set-up used the 1200 line\mm 1$^{\rm st}$ order grating providing 1185 Å coverage at a resolution of 1.0 Å\pixel, again centered at Hα. Both Hα set-ups used the Y48 blocking filter.

Bias, dark, and flat fields were obtained each night. Flat fielding was performed using continuum arc lamps and, in some cases, dome flats. Preference was given to continuum lamps due to the greater consistency in the illumination of the CCD. Red observations at wavelengths beyond $\sim$ 7700 Å were subject to fringing effects arising at the CCD that were unable to be corrected by flat fielding. The effect of this fringing on the data depended upon the target position on the sky

and the target intensity. Wavelength calibration was performed using He-Ar-Ne calibration lamps at each target position. Spectroscopic standard stars were observed throughout each night over a range of airmasses. The standard stars selected varied based upon seasonal variation in visibilities, and included Wolf 1346, BD+28 4211, HD 192281, HD 188350, Feige 34, Feige 66, and Feige 67. Data reduction was performed in IRAF following standard optical data reduction procedures.

A log of the optical observations is provided in Table 2.2 below.

Table 2.2: Bok 90" Target Details

Target	Date (UT)	Coverage	Grating	Notes
V723 Cas	2006 Apr 27	Blue	400	
	2006 Apr 28	Blue	400	
	2006 Sep 29	Blue	400	
	2007 Oct 19	Blue	400	Full night
	2007 Oct 20	Blue	400	Full night
	2008 Sep 22	Blue	400	
	2008 Sep 22	Hα 1	600	Full night
	2008 Sep 23	Hα 1	600	Full night
	2008 Sep 24	Hα 1	600	Full night
	2010 Jul 04	Blue/Red	400	
V466 And	2008 Sep 22	Blue	400	
	2008 Sep 23	Red	400	
	2008 Sep 24	Red	400	
	2008 Nov 28	Blue	400	Weak detection
	2009 Jul 12	Blue	400	Null detection
CSS 081007:030559				
+054715	2008 Nov 28	Blue	400	
	2009 Jul 12	Blue	400	Weak detection
CSS 100217:102913				
+404220	2010 Apr 24	Blue	400	
V1311 Sco	2010 Apr 26	Blue/Red	400	

Continued on Next Page...

Table 2.2 – Continued

Target	Date (UT)	Coverage	Grating	Notes
V1281 Sco	2008 Jun 27	Blue	400	
	2009 May 07	Blue	400	Null detection
V1280 Sco	2008 Jun 25	Blue	400	
	2008 Jun 27	Blue	400	
	2009 May 07	Blue	400	
	2009 May 08	Red	400	
	2009 Jun 22	Blue	500	MMT Blue Channel
	2009 Jul 13	Blue	400	
	2010 Apr 24	Blue	400	
	2010 Apr 26	Red	400	
	2010 Jul 04	Blue	400	
	2010 Jul 05	Red	400	
	2010 Jul 06	Hα 2	1200	
V1310 Sco	2010 Apr 24	Blue	400	
	2010 Apr 25	Red	400	
V1186 Sco	2008 Jun 27	Blue	400	
	2009 May 09	Blue/Red	400	Weak detection
V2674 Oph	2010 Apr 24	Blue	400	
	2010 Apr 26	Red	400	
	2010 Jul 04	Blue	400	
	2010 Jul 05	Red	400	
V1187 Sco	2008 Jun 27	Blue	400	Weak detection
V2487 Oph	2008 Jun 27	Blue	400	
	2009 May 07	Blue	400	Null detection
V2575 Oph	2007 Apr 26	Blue	400	
	2007 May 09	Blue	400	
V2671 Oph	2008 Jun 27	Blue	400	
	2009 May 07	Blue	400	
V2673 Oph	2010 Apr 24	Blue	400	
	2010 Apr 26	Red	400	
	2010 Jul 04	Blue	400	
	2010 Jul 05	Red	400	

Continued on Next Page...

Table 2.2 – Continued

Target	Date (UT)	Coverage	Grating	Notes
	2010 Jul 06	HR Blue	1200	
V2670 Oph	2008 Jun 24	Blue	400	
	2008 Sep 23	Blue	400	
	2008 Sep 24	Red	400	
	2009 May 07	Blue	400	
	2009 May 08	Red	400	
	2009 Jul 11	Blue	400	
V5581 Sgr	2009 May 07	Blue	400	
	2009 May 08	Red	400	
	2009 Jul 11	Blue	400	
V5582 Sgr	2009 Jul 11	Blue	400	
	2009 Jul 14	Red	400	
	2010 Apr 24	Blue	400	
	2010 Jul 04	Blue	400	
	2010 Jul 05	Red	400	
	2010 Jul 06	Hα	1200	
V378 Ser	2009 Jun 24	Blue	400	Null detection
RS Oph	2006 Sep 28	Blue	400	
	2006 Sep 30	Blue	400	
	2007 Apr 25	Blue	400	
	2007 May 09	Blue	400	
	2007 May 10	Blue	400	
	2008 Jun 25	Blue	400	
	2008 Sep 25	Hα 1	600/1200	
	2009 May 07	Blue	400	
	2009 May 08	Red	400	
	2009 Jul 13	Blue	400	
	2009 Jul 14	Red	400	
	2010 Apr 25	Blue	400	
	2010 Jul 05	Red	400	
V5586 Sgr	2010 Apr 25	Blue/Red	400	
	2010 Jul 03	Blue	400	

Continued on Next Page...

Table 2.2 – Continued

Target	Date (UT)	Coverage	Grating	Notes
V1309 Sco	2008 Sep 23	Blue	400	
	2008 Sep 24	Red	400	
	2009 May 07	Blue	400	Null detection
V5579 Sgr	2008 Apr 28	Blue/Red	400	
	2009 May 07	Blue	400	Weak detection
	2009 May 08	Red	400	Weak detection
V5583 Sgr	2010 Apr 24	Blue	400	
	2010 Jul 04	Blue	400	
	2010 Jul 05	Red	400	
	2010 Jul 06	HR Blue	1200	
V5585 Sgr	2010 Apr 25	Blue	400	
	2010 Apr 26	Red	400	
	2010 Jul 04	Blue	400	
	2010 Jul 05	Red	400	
	2010 Jul 06	HR Blue	1200	
V5558 Sgr	2008 Apr 27	Blue	400	
	2008 Jun 26	Blue	400	
	2008 Jun 28	Red	400	
	2008 Sep 23	Blue	400	
	2008 Sep 24	Red	400	
	2009 May 07	Blue	400	
	2009 May 08	Red	400	
	2009 Jul 11	Blue	400	
	2009 Jul 14	Red	400	
	2010 Jul 03	Blue	400	
	2010 Jul 05	Red	400	
	2010 Jul 06	HR Red	1200	
V5116 Sgr	2008 Apr 27	Blue	400	
V5580 Sgr	2009 May 07	Blue	400	
	2009 May 08	Red	400	
V3890 Sgr	2007 May 09	Blue	400	
V5584 Sgr	2010 Apr 24	Blue	400	

Continued on Next Page...

Table 2.2 – Continued

Target	Date (UT)	Coverage	Grating	Notes
	2010 Jul 05	Red	400	
V496 Sct	2010 Apr 24	Blue	400	
	2010 Apr 26	Red	400	
	2010 Jul 05	Red	400	
V358 Lyr	2009 May 08	Blue	400	Null detection
V4743 Sgr	2006 Sep 29	Blue	400	
V1721 Aql	2008 Sep 25	Blue/Red	400	
	2009 May 07	Blue	400	Null detection
V1722 Aql	2010 Apr 25	Blue	400	
	2010 Jul 04	Blue	400	
	2010 Jul 05	Red	400	
BF Cyg	2006 Sep 27	Blue	400	
	2006 Sep 29	Blue	400	
	2006 Sep 30	Blue	400	
V2491 Cyg	2008 Apr 27	Blue	400	
	2008 Apr 28	Red	400	
	2008 Jun 24	Blue	400	
	2008 Jun 27	Blue/Red	400	
	2008 Sep 22	Blue	400	
	2008 Sep 23	Red	400	
	2008 Sep 24	Red	400	
	2009 May 07	Blue	400	Weak detection
	2009 May 08	Red	400	Weak detection
	2009 Jul 12	Blue	400	Weak detection
V459 Vul	2008 Apr 27	Blue	400	
	2008 Apr 28	Red	400	
	2008 Jun 24	Blue	400	
	2008 Jun 28	Red	400	
	2008 Sep 22	Blue	400	
	2008 Sep 23	Red	400	
	2008 Sep 24	Red	400	
	2009 May 07	Blue	400	

Continued on Next Page...

Table 2.2 – Continued

Target	Date (UT)	Coverage	Grating	Notes
	2009 May 09	Red	400	
	2009 Jul 12	Blue	400	
	2009 Jul 13	Red	400	
	2010 Apr 25	Blue	400	
	2010 Jul 05	Red	400	
CI Cyg	2008 Sep 22	Blue	400	
	2008 Sep 23	Red	400	
	2008 Sep 24	Red	400	
V458 Vul	2007 Oct 19	Blue	400	
	2008 Apr 27	Blue	400	
	2008 Apr 28	Red	400	
	2008 Jun 24	Blue	400	Null detection
V2468 Cyg	2008 Apr 27	Blue	400	
	2008 Apr 28	Red	400	
	2008 Jun 24	Blue	400	
	2008 Jun 27	Red	400	
	2008 Sep 22	Blue	400	
	2008 Sep 23	Red	400	
	2008 Sep 24	Red	400	
	2009 May 07	Blue	400	
	2009 May 08	Red	400	
	2009 Jul 12	Blue	400	
	2010 Apr 25	Blue	400	
	2010 Apr 26	Red	400	
	2010 Jul 03	Blue	400	
	2010 Jul 04	Red	400	
	2010 Jul 06	HR Blue/HR Red	1200	
V2361 Cyg	2006 Sep 27	Blue	400	
	2006 Sep 28	Blue	400	
	2006 Sep 29	Blue	400	
	2007 Apr 26	Blue	400	
	2007 May 09	Blue	400	

Continued on Next Page...

Table 2.2 – Continued

Target	Date (UT)	Coverage	Grating	Notes
	2007 Oct 20	Blue	400	
V2467 Cyg	2007 Apr 25	Blue	400	
	2007 May 09	Blue	400	
	2007 Oct 19	Blue	400	
	2008 Apr 27	Blue	400	
	2008 Apr 28	Red	400	
	2008 Jun 24	Blue	400	
	2008 Jun 27	Red	400	
	2008 Sep 22	Blue	400	
	2008 Sep 23	Red	400	
	2008 Sep 24	Red	400	
	2009 May 07	Blue	400	
	2009 May 08	Red	400	
	2009 Jul 12	Blue	400	
	2010 Apr 25	Blue	400	
	2010 Jul 03	Blue	400	
	2010 Jul 04	Red	400	
	2010 Jul 06	HR Blue/HR Red	1200	
V1974 Cyg	2006 Sep 28	Blue	400	
	2006 Sep 30	Blue	400	
	2007 Oct 20	Blue	400	
	2008 Sep 22	Blue	400	
	2008 Sep 23	Red	400	
	2008 Sep 24	Red	400	
V2362 Cyg	2006 Sep 30	Blue	400	
	2007 Apr 25	Blue	400	
	2007 Apr 26	Blue	400	
	2007 Apr 27	Blue	400	
	2007 May 10	Blue	400	
	2007 Oct 19	Blue	400	
	2008 Jun 26	Blue	400	
	2008 Jun 28	Red	400	

Continued on Next Page...

Table 2.2 – Continued

Target	Date (UT)	Coverage	Grating	Notes
	2008 Sep 22	Blue	400	
	2008 Sep 23	Red	400	
	2008 Sep 24	Red	400	

Table 2.3: Optical Target Details

Target	Equatorial Coordinates RA	DEC	Extinction E(B-V)[a]	t_0[b] (UT)	$m_{V,max}$	t_2 (Days)	t_3 (Days)	Dust?[c]	Notes & References[d]
V723 Cas[e]	01:05:05.37	+54:00:40.5	0.6	1995 Dec. 16	7.1	?	~ 170	No	1,2,3
V466 And	02:00:25.40	+44:10:18.7	0.088	2008 Sept. 1.6	12.7	n/a	n/a	n/a	D,4,5
CSS 081007[e]	03:05:59	+05:47:15	0.146	2008 Sep 07	15.3	?	?	?	6,7
GK Per	03:31:11.82	+43:54:16.8	0.354	1901 Feb 22	0.2	7	13	No	D[f],8
V574 Pup	07:41:53.76	-27:06:36.9	0.5[12]	2004 Nov 22.7	6.9	13	58	No	9,10,11,12
V382 Vel	10:44:48.37	-52:25:30.6	< 0.1[14]	1999 May 23	2.3	4.5-6	9-12.5	No	13,14,15,16
V1065 Cen	11:43:10.33	-58:04:04.3	0.5[19]	2007 Jan 21.0	7.6	11	26	Yes	17,18,**19**
DZ Cru	12:23:16.20	-60:22:34.0	1.1[21]	2003 Aug 20	9.2	15	?	Yes,UIRs	20,21,**22**
T CrB	15:59:30.16	+25:55:12.6	0.11[24]	1946 Feb 9.4	~ 3	~ 6	~ 8	No	R,23,24
V1311 Sco	16:55:13.16	-38:03:46.9	1.314	2010 Apr 26.3	8.6	?	?	?	25
V1281 Sco	16:56:59.35	-35:21:50.2	0.894	2007 Feb 22.7	9.1	?	?	?	26,27
V1280 Sco[e]	16:57:40.91	-32:20:36.4	0.7[28]	2007 Feb 16.7	3.8	21.3	34.3	Yes,UIRs	27,28,29,30,**31**
V1310 Sco	17:06:07.53	-37:14:27.4	2.297	2010 Feb 20.9	~ 13	?	?	?	32
V1186 Sco[e]	17:12:51.28	-30:56:37.6	0.45[35]	2004 Jul 8.8	9.6	20	45-70	No	33,34,**35**
V2576 Oph	17:15:33.00	-29:09:39.9	0.25[37]	2006 Apr 9.5	9.3	~ 18	~ 32	?	36,37
V2674 Oph	17:26:32.19	-28:49:36.3	0.7[39]	2010 Feb 21.2	9.3	18	31	?	38,39
V1187 Sco[e]	17:29:18.81	-31:46:01.5	1.56[40]	2004 Aug 3.6	7.4	< 8.7	< 15	No	40,41
V2487 Oph	17:31:59.8	-19:13:56	0.38[43]	1998 Jun 15.6	10.0	6.3	8.3-9.5	No	R?,42,43,44,45
V2575 Oph	17:33:13.06	-24:21:07.1	1.42-1.5[47,48]	2006 Feb 12.3	11.1	30	63	No	46,47,48
V2671 Oph	17:33:29.67	-27:01:16.4	2.0[50]	2008 Jun 2.2	12.8	?	?	CO	49,50,**51**
V2673 Oph	17:39:40.9	-21:39:50.5	0.7[54]	2010 Jan 18.3	8.4	10	23.5	?	52,53,54
V2670 Oph	17:39:50.93	-23:50:00.9	1.3[56]	2008 May 26.3	10.3	?	42 ± 2	No	55,56,**57**,58,59
V2615 Oph	17:42:44.00	-23:40:35.1	0.44[62]	2007 Mar 28.1	8.5	26.5	48.5	CO,Yes	60,61,62
V5581 Sgr	17:44:08.48	-26:05:47.37	2.040	2009 Apr 21.7	~ 12	?	?	?	63
V5582 Sgr	17:45:05.42	-20:03:22.0	0.775	2009 Feb 23.9	> 11.5	?	?	?	64,65
V378 Ser	17:49:24.57	-12:59:59.2	0.74[47]	2005 Mar 21.4	11.8	44	90	?	66,67,68
RS Oph[e]	17:50:13.20	-06:42:28.48	0.747	2006 Feb 12.8	4.5	4.6-7.9	~ 9	Yes[g]	R,68,8,69,**70**,**71**,30

Continued on Next Page...

Table 2.3 – Continued

Target	Equatorial Coordinates RA	DEC	Extinction E(B-V)[a]	t_0[b] (UT)	$m_{V,max}$	t_2 (Days)	t_3 (Days)	Dust?[c]	Notes & References[d]
V5586 Sgr	17:53:02.99	-28:12:19.4	4.785	2010 Apr 24.7	14.7	?	?	?	72,73,**74**
V745 Sco	17:55:22.27	-33:14:58.5	1.1[77]	1989 Jul 30	~ 9.7	5	9	No	R,75,76,77
V1309 Sco	17:57:32.93	-30:43:10.1	0.55[80]	2008 Sep 5.5	7.9	21	25	No	78,79,80
V5579 Sgr	18:05:58.88	-27:13:56.0	1.2[83]	2008 Apr 23.4	6.6	7	13	Yes	81,82,83
V5583 Sgr	18:07:07.67	-33:46:33.9	0.33[85]	2009 Aug 7.6	7.4	4.5	10	?	84,85
V5585 Sgr	18:07:26.79	-29:00:42.8	1.847	2010 Jan 22.9	9.0	?	?	?	86
V5558 Sgr[e]	18:10:18.4	-18:46:51	0.8[90]	2007 Jul 10.0	6.5	12[h]	> 130	No	87,88,89,90
V5116 Sgr[e]	18:17:50.77	-30:26:31.2	0.24[12]	2005 Jul 04	< 8	20	33	No	91,92,93,8,12
V5580 Sgr	18:22:01.39	-28:02:39.8	0.363	2008 Nov 29.0	< 8	?	?	?	94
V3890 Sgr	18:30:43.32	-24:01:08.6	0.558	1990 Apr 27.7	8.5	~ 7	17	No	R,95,96
V5584 Sgr	18:31:32.79	-16:19:07.5	0.969	2009 Oct 29.7	9.2	?	?	Yes	97,98,99
V496 Sct	18:43:45.65	-07:36:41.5	1.469	2009 Nov 19.2	7.1	?	?	CO,Yes	100,101,102,99
V358 Lyr	18:59:32.99	+42:24:12.0	0.103	2008 Nov 23.1	15.9	?	?	?	D?,103,104
V4743 Sgr	19:01:09.38	-22:00:05.8	0.174	2002 Sep 18.3	5.0	9	16	Yes[g]	105,106,107
V1721 Aql	19:06:28.58	+07:06:44.3	3.7[90]	2008 Sep 22.6	< 14	?	?	?	108,**109**,**110**
V1722 Aql	19:14:09.73	+15:16:34.7	1.88	2009 Dec 17.7	10.3	?	?	?	111
V1494 Aql	19:23:05.28	+4:57:21.6	0.6[114]	1999 Dec 3.4	4.0	6.6	16	No	112,113,114
BF Cyg	19:23:53.51	+29:40:29.22	0.285	2006 Oct 12	9.6	n/a	n/a	n/a	S,115,116
NQ Vul	19:29:14.68	+20:27:59.7	0.6-0.9[118]	1976 Nov 2.5	~ 6	~ 1	58	CO,Yes	117,118,119
V2491 Cyg	19:43:01.96	+32:19:13.8	0.43[122]	2008 Apr 11.4	7.5	4.6	?	No	R?,120,121,122,**123**
V459 Vul	19:48:08.81	+21:15:29.9	1.0[126]	2007 Dec 27.8	7.6	19	~ 30	Yes	124,125,126
CI Cyg	19:50:11.83	35:41:03.00	0.45[129]	2008 Sep 18	9.5	n/a	n/a	n/a	S,127,128,129
V458 Vul[e]	19:54:24.3	+20:52:47	0.6[131]	2007 Aug 10.4	7.7	7	15[h]	No	130,131,132
V2468 Cyg[e]	19:58:33.4	+29:52:04	0.8[135,137]	2008 Mar 12.1	8.1	~ 10	18	No	133,134,135,136,**137**
V2361 Cyg[e]	20:09:19.05	+39:48:52.9	1.2[139]	2005 Feb 11.8	9.3	6	8	Yes,UIRs	138,139,8
QU Vul	20:26:46.03	+27:50:42.3	0.17[142]	1992 Feb 22.5	4.4	25	33	Yes	140,141,142,143
V2467 Cyg[e]	20:28:12.52	+41:48:36.5	1.5[144]	2007 Mar 15.8	7.4	~ 10	~ 20[h]	No	144,145,146
V1974 Cyg[e]	20:30:31.66	+52:37:50.8	0.3[149]	1992 Feb 20.8	4.3	16	42	No	147,148,149,150

Continued on Next Page...

Table 2.3 – Continued

Target	Equatorial Coordinates RA	DEC	Extinction E(B-V)[a]	t_0[b] (UT)	$m_{V,max}$	t_2 (Days)	t_3 (Days)	Dust?[c]	Notes & References[d]
V2362 Cyg[e]	21:11:32.35	+44:48:03.66	0.58[152]	2006 Apr 2.8	7.5	10.5	24	Yes,UIRs	151,152
V1500 Cyg	21:11:36.61	+48:09:01.9	0.5[155]	1975 Aug 30.9	1.9	2.4	4.0	No	153,154,155
V1668 Cyg	21:42:35.31	+44:01:55.0	0.38[158]	1978 Sep 12	6.0	12	24	Yes	156,157,158,159
V705 Cas	23:41:47.25	+57:30:59.7	0.5[162]	1993 Dec 11	6.5	65	?	CO,Yes,UIRs	160,161,162,163,164

[a]The reddening is a rough estimate derived from the Schlegel et al. (1998) exctinction maps unless indicated otherwise.

[b]The t_0 date is reported at $m_{V,max}$ when different than the discovery date.

[c]The presence or absence of dust is indicated. If CO was present in emission, or if UIR features were observed, they too are indicated here.

[d]Targets that are dwarf (D), recurrent (R), or symbiotic novae (S) are noted. Numbers refer to references as given below. Bolded references indicate publications utilizing data obtained as part of this program.

[e]These data are currently under analysis and will be published elsewhere.

[f]After the initial CN outburst, GK Per began undergoing relatively frequent dwarf nova outbursts, the most recent of which began on 2010 Mar 5 (Evans et al. 2010a).

[g]The dust observed was likely pre-existing dust illuminated in the outburst.

[h]The light curve underwent several strong flares or oscillations making determination of the true t_2 and t_3 times difficult.

Table 2.4: References for Table 2.3

No.	Reference	No.	Reference	No.	Reference[a]
1	Hirosawa et al. (1995)	2	Chochol & Pribulla (1997)	3	Gonzalez-Riestra et al. (1996)
4	Yamaoka et al. (2008a)	5	Challis et al. (2008)	6	Pejcha et al. (2008)
7	Prieto et al. (2008)	8	Hachisu & Kato (2007)	9	Nakano et al. (2004)
10	Sostero et al. (2004)	11	Siviero et al. (2005)	12	Ness et al. (2007a)
13	Lee et al. (1999)	14	Della Valle et al. (2002)	15	Della Valle et al. (1999)
16	Liller & Jones (2000)	17	Liller et al. (2007a)	18	Liller et al. (2007b)
19	**Helton et al. (2010b)**	20	Tabur et al. (2003)	21	Rushton et al. (2008)
22	**Evans et al. (2010b)**	23	Pettit (1946)	24	Hachisu & Kato (2001)
25	Nishiyama et al. (2010c)	26	Yamaoka et al. (2007)	27	Henden & Munari (2007)
28	Russell et al. (2007a)	29	Munari et al. (2007a)	30	Hounsell et al. (2010a)
31	**Ness et al. (2009)**	32	Nishiyama et al. (2010a)	33	Pojmanski et al. (2004)
34	Waagen et al. (2004)	**35**	**Schwarz et al. (2007b)**	36	Williams et al. (2006)
37	Lynch et al. (2006b)	38	Nakano et al. (2010b)	39	Munari et al. (2010)
40	Yamaoka (2004)	41	Lynch et al. (2006a)	42	Nakano et al. (1998)
43	Lynch et al. (2000)	44	Liller & Jones (1999)	45	Kato (2002)
46	Pojmanski et al. (2006)	47	Russell et al. (2006)	48	Rudy et al. (2006a)
49	Nakano et al. (2008e)	50	Rudy et al. (2008c)	**51**	**Helton et al. (2008b)**
52	Nakano et al. (2010a)	53	Vollmann (2010)	54	Munari & Dallaporta (2010)
55	Nishiyama et al. (2008)	56	Russell et al. (2008c)	**57**	**Helton et al. (2008c)**
58	Sitko et al. (2008)	59	Poggiani (2009)	60	Nakano et al. (2007b)
61	Das et al. (2007c)	62	Munari et al. (2008b)	63	Kinugasa et al. (2009a)
64	Sun & Gao (2009)	65	Kinugasa et al. (2009b)	66	Pojmanski et al. (2005)
67	Russell et al. (2005b)	68	Narumi et al. (2006)	69	Hric et al. (2008)
70	**Evans et al. (2007a)**	**71**	**Evans et al. (2007b)**	72	Nishiyama et al. (2010b)
73	Kiyota (2010)	**74**	**Helton et al. (2010a)**	75	Liller (1989)
76	Sekiguchi et al. (1990)	77	Harrison et al. (1993)	78	Nakano et al. (2008f)
79	Rudy et al. (2008d)	80	Mason et al. (2010)	81	Nakano et al. (2008d)
82	Samus et al. (2008)	83	Russell et al. (2008b)	84	Nishiyama et al. (2009a)
85	Hachisu et al. (2009)	86	Kiyota et al. (2010)	87	Nakano et al. (2007c)

Continued on Next Page. . .

Table 2.4 – Continued

No.	Reference	No.	Reference	No.	Reference[a]
88	Munari et al. (2007c)	89	Munari et al. (2007d)	90	Rudy et al. (2007)
91	Liller (2005)	92	Gilmore & Kilmartin (2005)	93	Russell et al. (2005c)
94	Liller (2008)	95	Kilmartin et al. (1990)	96	Gonzalez-Riestra (1992)
97	Kabashima et al. (2009)	98	Munari et al. (2009a)	99	Russell et al. (2010)
100	Nakano et al. (2009)	101	Munari et al. (2009b)	102	Rudy et al. (2009)
103	Henden et al. (2008)	104	Shears et al. (2009)	105	Haseda et al. (2002)
106	Morgan et al. (2003)	107	Nielbock & Schmidtobreick (2003)	108	Yamaoka et al. (2008b)
109	**Helton et al. (2008d)**	**110**	**Hounsell et al. (2010b)**	111	Nishiyama et al. (2009b)
112	Pereira et al. (1999)	113	Kiss & Thomson (2000)	114	Iijima & Esenoğlu (2003)
115	Munari et al. (2006)	116	Munari et al. (2008a)	117	Milbourn et al. (1976)
118	Klare & Wolf (1978)	119	Mattei (1978)	120	Nakano et al. (2008c)
121	Tomov et al. (2008)	122	Rudy et al. (2008b)	**123**	**Helton et al. (2008a)**
124	Nakano et al. (2008b)	125	Munari et al. (2007d)	126	Russell et al. (2008a)
127	Munari et al. (2008d)	128	Munari et al. (2008e)	129	Kenyon et al. (1991)
130	Nakano et al. (2007d)	131	Lynch et al. (2007)	132	Poggiani (2008)
133	Nakano et al. (2008a)	134	Munari et al. (2008c)	135	Rudy et al. (2008a)
136	Sitko & Lynch (2009)	**137**	**Schwarz et al. (2009)**	138	Nakano et al. (2005)
139	Russell et al. (2005a)	140	Collins et al. (1984)	141	Gehrz et al. (1986)
142	Saizar et al. (1992)	143	Rafanelli et al. (1995)	144	Nakano et al. (2007a)
145	Mazuk et al. (2007)	146	Russell et al. (2007b)	147	Collins (1992)
148	Schmeer (1992)	149	Shore et al. (1992)	150	Hachisu & Kato (2006)
151	Nakano et al. (2006)	152	Lynch et al. (2008b)	153	Honda et al. (1975)
154	Young et al. (1976)	155	Ferland (1977)	156	Morrison et al. (1978)
157	Mallama & Skillman (1979)	158	Kolotilov (1980)	159	Gehrz et al. (1980)
160	Nakano et al. (1993)	161	Skiff et al. (1993)	162	Scott et al. (1994a)
163	Hauschildt et al. (1994)	164	Evans et al. (1997)		

[a]References in **bold** indicate publications originating in our classical nova observing program.

Chapter 3

V1065 Centauri (Nova Cen 2007)

A modified version of this chapter appears in The Astronomical Journal with the following bibliographic reference: Helton, L. A., Woodward, C. E., Walter, F. M., Vanlandingham, K., Schwarz, G. J., Evans, A., Ness, J.-U., Geballe, T. R., Gehrz, R. D., Greenhouse, M., Krautter, J., Liller, W., Lynch, D. K., Rudy, R. J., Shore, S. N., Starrfield, S., & Truran, J. 2010 AJ, 140, 1347. Reproduced with the permission of the American Astronomical Society.

3.1 Introduction

Classical novae (CNe) are important contributors to the cycle of chemical enrichment and evolution in galaxies. They violently eject substantial quantities of material that is elementally enriched through explosive nucleosynthesis and through dredge-up from the surface layers of the mass-accreting white dwarf (WD) progenitor. The characteristics of the thermonuclear runaway (TNR) and the subsequent evolution of the nova outburst depend strongly on the mass and composition of the underlying WD. Eruptions on low mass carbon-oxygen (CO) WDs typically have low expansion velocities, slow light curve evolution, and often, prodigious dust production. In contrast, CNe arising on high mass ($\gtrsim 1.25$ $M_{\odot}$) oxygen-neon (ONe) WDs are generally characterized by high expansion velocities, fast

light curve evolution, and little, if any, dust production (Bode & Evans 2008). Novae arising from the latter progenitor frequently are identified by detection of strong [Ne II2] λ12.81 μm emission. Overall, outbursts on CO WDs are predicted to eject more mass under less energetic conditions than novae on ONe WDs (Schwarz et al. 2007a; Townsely & Bildsten 2004). CN energetics may be determined by the speed class, quantified by the parameter t_2, which is the time for the V-band light curve to decline by 2 magnitudes. Faster CNe have higher bolometric (and visual) luminosities at maximum and higher ejection velocities.

More than 10^{-4} $M_\odot$ of material, enriched in CNONeMg and other intermediate mass elements, can be ejected from the WD at velocities $\gtrsim 10^3$ km s^{-1} as a result of the TNR. As the ejecta disperse, an emission line spectrum is produced and the pseudophotosphere shrinks, revealing a hotter source of emission from stable nuclear burning on the WD surface. CN spectra are remarkable for the temporal development of the ionization states and line profiles present, examination of which is critical for understanding the dynamics of ejection. Low-energy permitted lines of CNO and Fe II give way to He II, as well as highly ionization lines, e.g., [Fe VII] 6087 Å, and in some cases to infrared (IR) "coronal" lines (Lynch et al. 2008b, 2006a; Woodward et al. 1997, 1992). The latter lines are sources of abundance information since a wide range of isoelectronic sequences (e.g., Greenhouse et al. 1990) and adjacent ionization states of metals are observable. Often, as the ejecta cool and evolve, molecules (e.g., Rudy et al. 2003) and dust form. CNe are often dust-formers and, while amorphous carbon is a major grain component, silicates, PAH-like molecules, and SiC can also be present, occasionally in the same nova (Gehrz 1998a).

Many CNe in outburst have exhibited super-soft source (SSS) X-ray spectra (e.g., Ness et al. 2007b). The most likely origin of SSSs is from steady nuclear burning on the surface of a WD (Kahabka & van den Heuvel 1997). One possible fuel source driving this on-going fusion in CNe is from remnant H-rich material left over on the WD surface after the initial mass ejection event. The duration of the SSS, in this case, is expected to be rather short. An alternative fuel source is from

continued deposition of material onto the WD surface due to the re-establishment of accretion. This latter mechanism would be able to support a much longer duration SSS stage in post-eruption CN systems. The duration of the SSS phase for Galactic CNe is typically short, only few years, yet a few CNe have been observed to have SSS spectra of much longer duration. V723 Cas, for example, has been a SSS for more than 13 years (Ness et al. 2008b).

Here we discuss synoptic spectrophotometric ground-based and *Spitzer* observations of V1065 Centauri (Nova Cen 2007). The broad temporal and wavelength coverage of our observations affords an opportunity to study the dynamical evolution of this CN, to determine absolute abundances (i.e., metals relative to H), and to infer the physical properties of dust formed in the cooling dense ejecta. The observations of V1065 Cen are discussed in §3.2. Following are discussions of the light curve evolution (§3.3.1), the spectral evolution (§3.3.2), and the reddening and distance estimates (§3.3.3). Photoionization modeling and abundance determinations are presented (§3.4) followed by a discussion of the derived dust properties of V1065 Cen in §3.5. We summarize our conclusions in §3.6.

3.2 Observations

V1065 Centauri (Nova Cen 2007) was a relatively bright classical nova outburst first reported by Liller et al. (2007a) at $m_V \simeq 8.2$. A subsequent search of patrol plates revealed a pre-discovery image of the system at $m_V = 7.6 \pm 0.2$ on January 21.04 UT (JD 2454121.5) (Liller et al. 2007b). The nova was detected by the "Pi of the Sky" detector (Małek et al. 2010) on Jan 20.32 UT (JD 2454120.8) at an unfiltered magnitude of 6.9. We shall adopt this latter date as day 0 (t_0). Coordinated observations of V1065 Cen commenced shortly after the discovery report and spectrophotometric data were obtained on a variety of facilities including the Small And Moderate Aperture Research System (SMARTS) 1.5-m, the Gemini-South 8-m, the NASA *Spitzer Space Telescope*, and the NASA *Swift* X-ray/UV

telescope.[1] Our data span more than 900 days, beginning 9 days after the initial eruption.

3.2.1 Optical Photometry

The BVRI and unfiltered light curves of V1065 Cen obtained from the AAVSO[2] database and from the "Pi of the Sky" project[3] for a period of $\sim$ 230 days post-outburst are shown in Fig. 3.1. The vertical tick marks at the top of the panel indicate the dates of our SMARTS, *Spitzer* and Gemini observations. Three more epochs of *Spitzer* data were obtained beyond the terminus of Fig. 3.1 at days 529, 590, and 763. Also indicated on the figure are three temporal epochs characterized by changes in the observed spectra (§3.3) that delineate different stages in the evolution of V1065 Cen.

The V1065 Cen light curves show a fairly smooth decline after maximum light. They are devoid of secondary maxima and oscillations seen in the light curves of CNe such as V1186 Sco (Schwarz et al. 2007a) and V723 Cas (Evans et al. 2003). The most noticeable feature in the early light curve evolution is the dip in the B- and V-bands of $\sim$ 1 magnitude near day 40 and the subsequent recovery, a behavior associated with a dust condensation event in the ejecta (Gehrz 2008b).

The well-sampled light curves following the decline of V1065 Cen from maximum light enable a determination of the nova's speed-class. The optical *BVRI* photometry was fitted with a broken-power law relationship, with each arm $\propto t^{-\alpha}$, using a non-linear least squares fitting algorithm (the Marquardt method; Bevington & Robinson 1992), which excluded photometry in all bands near the dust formation event (day 40). Figure 3.2 shows the resultant power-law fits. The derived early light decline rates (prior to day 90) were $\alpha = 0.99 \pm 0.01$, 1.10 ± 0.01, 1.04 ± 0.01, and 1.28 ± 0.01 for B-, V-, R-, and I-band, respectively. At later dates

[1] All spectroscopic data presented in the figures in this paper are provided online at: http://www.astro.sunysb.edu/fwalter/SMARTS/NovaAtlas/v1065cen/data/index.html

[2] http://www.aavso.org

[3] http://grb.fuw.edu.pl/

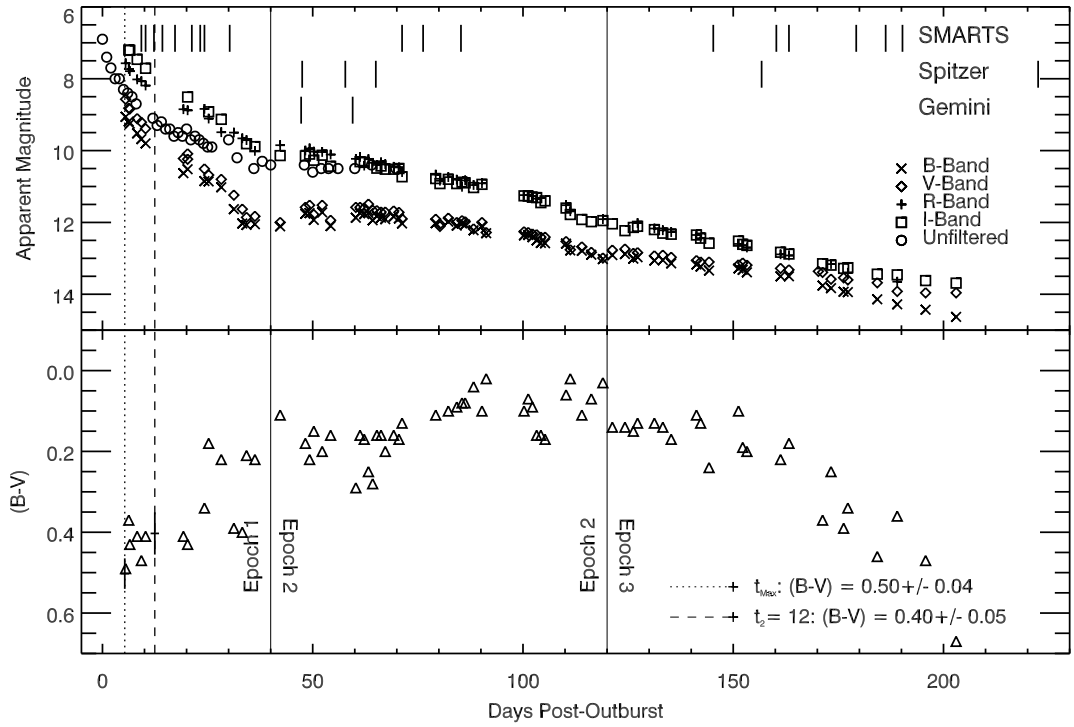

Figure 3.1: Light curve of V1065 Cen. *(Top:)* The *BVRI*-band photometry is taken from the AAVSO database while the unfiltered photometry is taken from the "Pi of the Sky" project data. Vertical tick marks delineate dates of the SMARTS, *Spitzer*, and Gemini observations (§3.2). *(Bottom:)* The (B-V) color of V1065 Cen is derived from the AAVSO photometry.

($\gtrsim$ day 90) $\alpha = 2.33 \pm 0.01$, 1.90 ± 0.01, 3.12 ± 0.01, and 2.96 ± 0.01. The time for the V-band light curve to decline 2 magnitudes, t_2, and 3 magnitudes, t_3, are ~ 11 days and ~ 26 days, respectively. The decay time calculated from the unfiltered "Pi of the Sky" data was in excellent agreement, $t_2 \sim 11$. These values are commensurate with the "fast" speed class of CNe (Gaposchkin 1957; Duerbeck 2008), similar to V382 Vel (Shore et al. 2003). Novae in this speed class are typically believed to arise on massive WDs (Gehrz et al. 1998b).

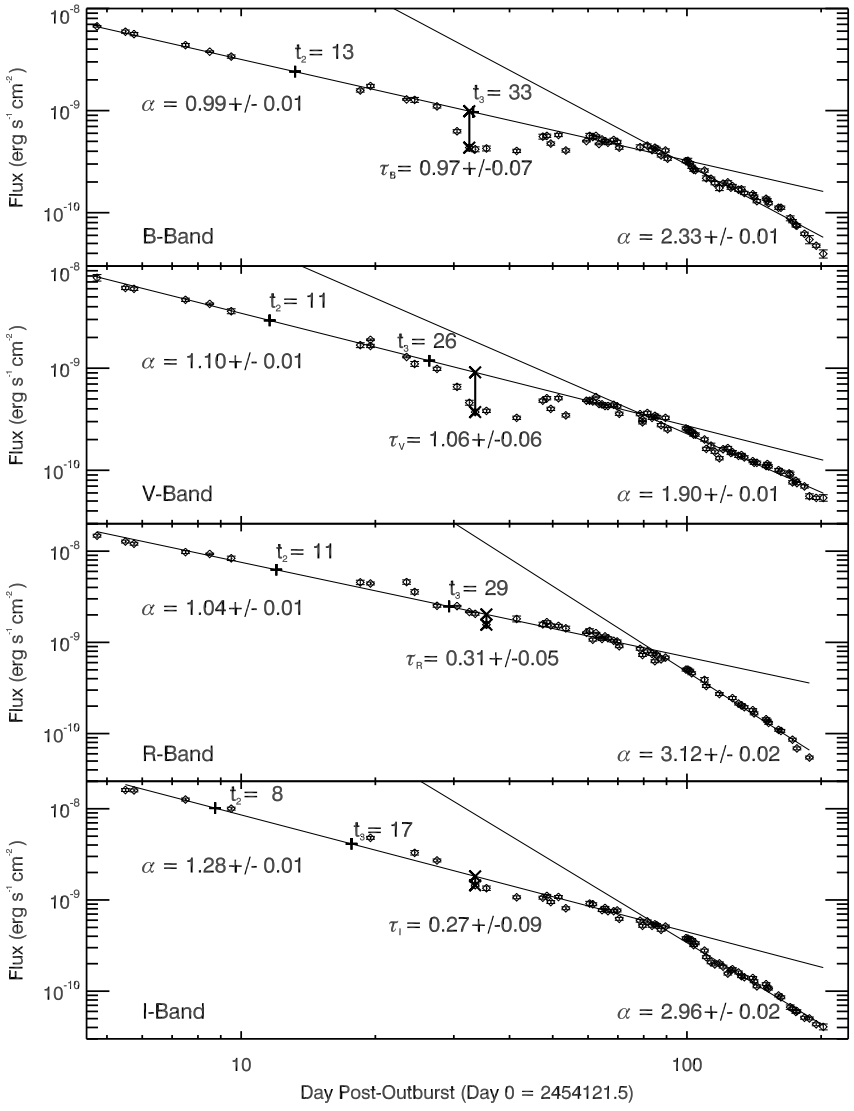

Figure 3.2: The power-law behavior of the V1065 Cen $BVRI$ light curves. The fluxes are derived from photometry in the AAVSO database and the solid lines indicate the $t^{-\alpha}$ power-law fit where the best-fit value of α is indicated. The time to decline 2 magnitudes, t_2, and 3 magnitudes, t_3, from maximum light are labeled (*cross*), while the optical depth, τ_λ, of the dust extinction event maximum in each photometric band is also indicated.

3.2.2 Optical Spectroscopy

V1065 Cen was observed using the R-C Spectrograph on the 1.5-m telescope operated by the SMARTS (Small and Moderate Aperture Research Telescope System) Consortium at the Cerro Tololo Inter-American Observatory (CTIO) as part of the Stony Brook Nova program (Table 3.1). The data were obtained using four different instrumental setups. The low resolution blue (B) setup used a 600 lines mm^{-1} grating with a resolution of 4.1 Å pix^{-1} ($\lambda/\Delta\lambda = R \sim 1200$) and spectral coverage of 3650 - 5400 Å. The high resolution blue (B2) setup achieved a 1.6 Å pix^{-1} resolution ($R \sim 2600$) over two band-passes, 3870 to 4540 Å and 4050 to 4700 Å, with an 831 lines mm^{-1} grating at second order. The red portion of the spectrum was observed at low resolution (3.1 Å pix^{-1}; $R \sim 2000$) with the grating positioned at first order with coverage of 5650 - 6950 Å. The long wavelength red (R2) setup covered the range 6000 to 9000 Å at a resolution of 6.5 Å pix^{-1} ($R \sim 1200$). The low resolution data were observed with a 1.1″ slit while the high resolution observations utilized a 0.83″ slit width.

The data were reduced in IDL using standard optical spectral data reduction procedures, as described on the Stony Brook SMARTS Nova Atlas web page.[4] For each set of observations, three images were obtained and median combined to remove cosmic rays. Wavelength calibration was performed using Th-Ar or Ne calibration lamps. Only a single spectrophotometric standard was observed each night, typically LTT 4364 or Feige 110. Thus slit losses, changes in seeing, and sky transparency permit only approximate flux calibration. Differences in air-mass between the target and the standard may have resulted in small wavelength-dependent offsets, but we expect this to have only a minimal impact on the continuum shape. To determine the flux in the emission lines, a non-linear least squares Gaussian fitting routine was used that fit the line center, line amplitude, line width, continuum amplitude, and the slope of the continuum. Selected SMARTS optical spectra are presented in Fig. 3.3. A summary of identified lines and the

[4] http://www.astro.sunysb.edu/fwalter/SMARTS/NovaAtlas/atlas_spec.html

measured line fluxes (in units of 10^{-12} erg s^{-1} cm^{-2}), uncorrected for reddening, are collated in Table 3.2.

Table 3.1: Ground Based Spectroscopic Observing Log

Observation Date (UT)	JD (+2450000)	Band[a]	Exposure Time (s)	Age (days)[b]
SMARTS - Epoch 1				
2007 Jan 29.29	4129.79	R	180	8.97
2007 Jan 29.34	4129.84	B2	600	9.02
2007 Jan 30.24	4130.74	B	300	9.92
2007 Jan 31.24	4131.74	R	180	10.92
2007 Jan 31.29	4131.79	B2	600	10.97
2007 Feb 01.27	4132.77	B	360	11.95
2007 Feb 02.25	4133.75	R	150	12.93
2007 Feb 02.33	4133.83	B2	600	13.01
2007 Feb 04.28	4135.78	R	150	14.96
2007 Feb 04.35	4135.85	B2	600	15.03
2007 Feb 05.21	4136.71	B	450	15.89
2007 Feb 06.21	4137.71	B2[c]	150	16.89
2007 Feb 06.30	4137.80	R	150	16.98
2007 Feb 07.21	4138.71	B	540	17.89
2007 Feb 09.20	4140.70	B	720	19.88
2007 Feb 10.13	4141.63	B2[c]	900	20.81
2007 Feb 10.23	4141.73	R	150	20.91
2007 Feb 10.25	4141.75	B2	1200	20.93
2007 Feb 11.29	4142.79	R2	300	21.97
2007 Feb 12.20	4143.70	B	600	22.88
2007 Feb 13.10	4144.60	B2[c]	1200	23.78

Continued on Next Page...

Table 3.1 – Continued

Observation Date (UT)	JD (+2450000)	Band[a]	Exposure Time (s)	Age (days)[b]
2007 Feb 13.21	4144.71	R	180	23.89
2007 Feb 13.36	4144.86	B2	1200	24.04
2007 Feb 14.17	4145.67	B	600	24.85
2007 Feb 18.14	4149.64	B	600	28.82
2007 Feb 22.17	4153.67	B2	1200	32.85
Epoch 2				
2007 Mar 31.16	4190.66	B	1200	69.84
2007 Apr 01.29	4191.79	R	540	70.97
2007 Apr 02.12	4192.62	R	540	71.80
2007 Apr 06.14	4196.64	B	1200	75.82
2007 Apr 07.11	4197.61	R	720	76.79
2007 Apr 09.10	4199.60	R2	300	78.78
2007 Apr 12.12	4202.62	B	1200	81.80
2007 Apr 19.18	4209.68	R	540	88.86
Epoch 3				
2007 Jun 09.99	4261.49	R2[d]	900	140.67
2007 Jun 22.01	4273.51	B	1800	152.69
2007 Jun 28.00	4279.50	B	1200	158.68
2007 Jun 28.97	4280.47	B2	1200	159.65
2007 Jun 29.97	4281.47	R	540	160.65
2007 Jun 30.95	4282.45	B2	1200	161.63
2007 Jul 02.08	4283.58	B	1200	162.76
2007 Jul 03.96	4285.46	B2	1200	164.64
2007 Jul 17.96	4299.46	R2	900	178.64
2007 Jul 18.99	4300.49	B	1200	179.67

Continued on Next Page...

Table 3.1 – Continued

Observation Date (UT)	JD (+2450000)	Band[a]	Exposure Time (s)	Age (days)[b]
2007 Jul 25.07	4306.57	B	900	185.75
2007 Jul 25.96	4307.46	B2	1800	186.64
2007 Jul 28.96	4310.46	B	1200	189.64
2007 Jul 30.96	4312.46	B2	1800	191.64
2009 Jun 07.21	4338.71	R	1200	717.89
2009 Jun 08.24	4834.74	B	1800	718.92
Gemini-South - Epoch 2				
2007 Mar 08.14	4167.63	SC/XD[e]	80	46.81
2007 Mar 20.16	4179.65	SC/XD	80	58.83

[a]Spectral ranges are 0.365-0.540 μm for B band, 0.405-0.470 μm for B2 band, 0.565-0.695 μm for R band, and 0.622-0.886 μm for R2 band, unless specified otherwise.

[b]From 2007 Jan 20.32 (JD 2454120.82)

[c]Spectral range is 0.387-0.454 μm

[d]Spectral range is 0.544-0.808 μm

[e]Spectral range is 0.88-2.50 μm

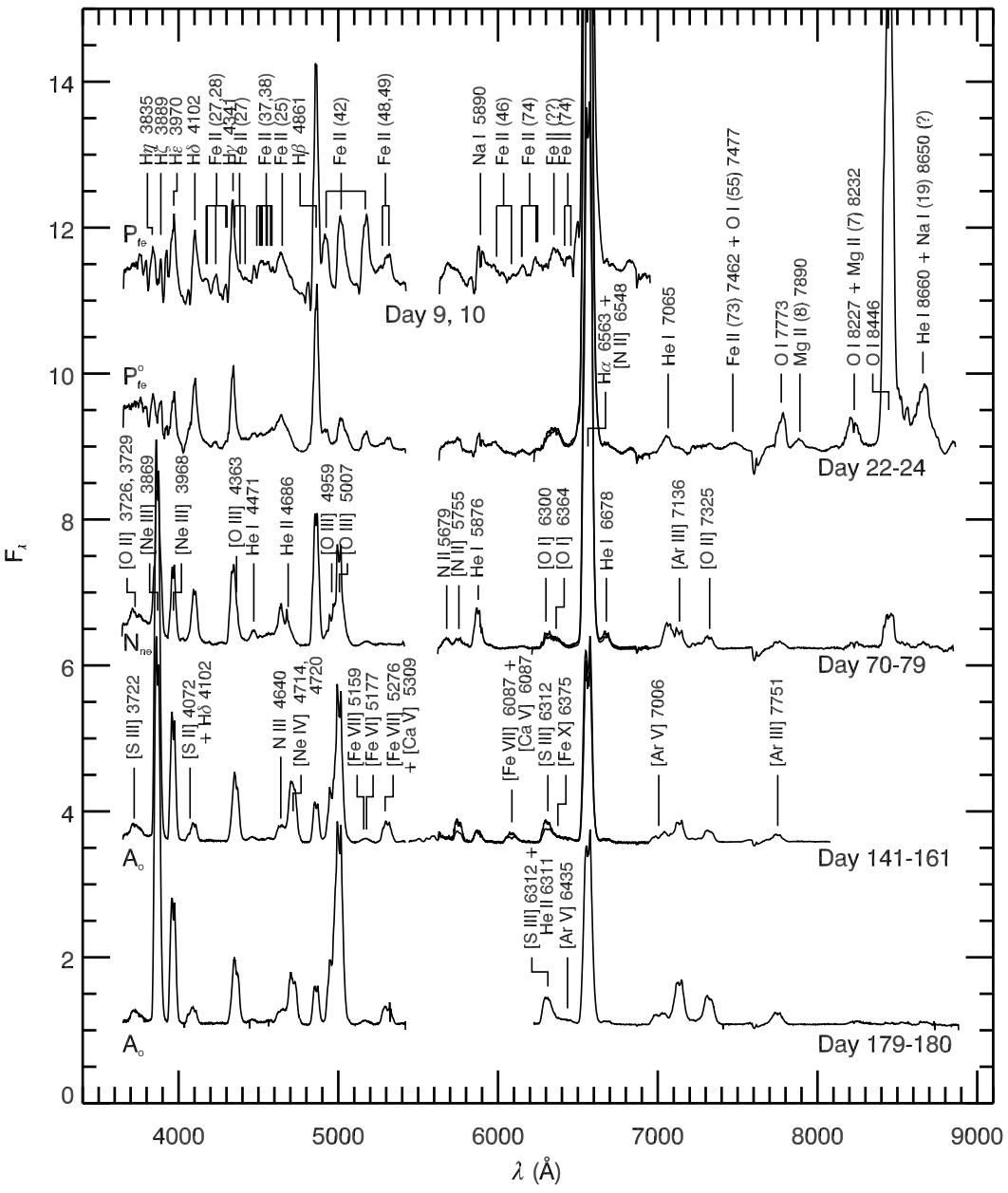

Figure 3.3: Evolution of the optical spectrum on V1065 Cen. The spectra have been arbitrarily scaled and prominent features labeled. The associated spectral evolutionary phase (P^o_{fe},N_{ne},A_o) for each epoch is listed to the left of the spectra.

Table 3.2: Emission Lines Observed in SMARTS Optical Spectra[a]

	Epoch 1		Epoch 2	Epoch 3	
	29 Jan 2007[b]	11 Feb 2007	31 Mar 2007	10 Jun 2007	18 Jul 2007
Identification	(Days 9, 10)	(Days 22-24)	(Days 70, 71, 79)	(Days 141, 159, 161)	(Days 179, 190)
[O II] λ3738+					
[Fe VII] λ3738	. . .	. . .	. . .	2.75 ± 0.02	1.49 ± 0.01
H(10) λ3798	1.46 ± 0.06	1.25 ± 0.06	. . .	. . .	. . .
Hη λ3835	9.68 ± 0.16	7.57 ± 0.08	. . .	. . .	. . .
[Ne III] λ3869	. . .	. . .	16.3 ± 0.07	20.8 ± 0.01	7.70 ± 0.00
Hζ λ3889	8.19 ± 0.09	6.19 ± 0.07	. . .	. . .	. . .
[Ne III] λ3967+					
Hϵ λ3970	. . .	. . .	6.15 ± 0.07	6.80 ± 0.01	2.68 ± 0.00
Hϵ λ3970	14.0 ± 0.10	12.7 ± 0.08	. . .	. . .	. . .
Hδ λ4102	4.73 ± 0.08	17.1 ± 0.08	5.74 ± 0.08	1.44 ± 0.01	0.75 ± 0.01
Fe II (27) λ4173+					
Fe II (28) λ4179	17.9 ± 0.15	. . .	. . .	. . .	. . .
Fe II (27) λ4233	17.7 ± 0.14	0.16 ± 0.03	. . .	. . .	. . .
Hγ λ4341+					
Fe II (27) λ4352	12.4 ± 0.10	18.7 ± 0.07	9.90 ± 0.08	. . .	. . .
[O III] λ4363	. . .	. . .	. . .	4.37 ± 0.01	1.22 ± 0.00
He I λ4471	. . .	. . .	0.61 ± 0.07	0.83 ± 0.02	1.40 ± 0.02
Fe II (37) $\lambda(4491 + 4489)$	6.42 ± 0.09	4.70 ± 0.22	. . .	. . .	. . .
Fe II (37) $\lambda(4515 + 4520)$ +					
Fe II (38) $\lambda(4523 + 4508)$	20.2 ± 0.31	2.60 ± 0.26	. . .	. . .	. . .
Fe II (37) λ4555+					
Fe II (38) λ4549	18.7 ± 0.29	. . .	0.57 ± 0.29	. . .	. . .
Fe II (26) λ4584+					
Fe II (37) λ4583 +					
Fe II (38) $\lambda(4576 + 4584)$	3.65 ± 0.10	4.16 ± 0.23	. . .	. . .	. . .
N III λ4640	. . .	. . .	2.91 ± 0.10	1.26 ± 0.01	0.33 ± 0.00

Continued on Next Page. . .

Table 3.2 – Continued

	Epoch 1		Epoch 2	Epoch 3	
Identification	29 Jan 2007[b] (Days 9, 10)	11 Feb 2007 (Days 22-24)	31 Mar 2007 (Days 70, 71, 79)	10 Jun 2007 (Days 141, 159, 161)	18 Jul 2007 (Days 179, 190)
Fe II (25) λ4649	68.1 ± 0.42	17.0 ± 0.19	. . .	. . .	. . .
[Ne IV] $\lambda(4714 + 4720)$	. . .	. . .	. . .	4.84 ± 0.01	1.22 ± 0.01
Hβ λ4861	29.2 ± 0.14	36.3 ± 0.08	15.3 ± 0.07	2.37 ± 0.01	0.85 ± 0.00
Fe II (42) λ4924	27.5 ± 0.12	5.76 ± 0.09	. . .	. . .	. . .
[O III] λ4959	. . .	. . .	2.96 ± 0.11	2.13 ± 0.01	0.83 ± 0.00
[O III] λ5007	. . .	. . .	13.1 ± 0.12	10.7 ± 0.01	5.82 ± 0.01
Fe II (42) λ5014	67.5 ± 0.23	11.1 ± 0.09	. . .	. . .	. . .
[Fe VII]λ5159+					
[Fe VI]λ5176	. . .	. . .	. . .	0.23 ± 0.01	0.14 ± 0.00
Fe II (42) λ5174	45.4 ± 0.17	4.39 ± 0.08	0.33 ± 0.07	. . .	. . .
Fe II (49) λ5276	14.7 ± 0.37	1.38 ± 0.09	. . .	. . .	. . .
[Ca V] λ5309+					
[Fe VII] λ5276	. . .	. . .	. . .	1.63 ± 0.01	0.48 ± 0.00
Fe II (49) λ5317	13.3 ± 0.22	2.90 ± 0.05	. . .	. . .	$\times$[c]
N II λ5679	27.4 ± 0.02	4.16 ± 0.01	1.58 ± 0.01	. . .	$\times$
[N II] λ5755 + [Fe VII] λ5738	. . .	. . .	. . .	1.60 ± 0.07	$\times$
[N II] λ5755	14.0 ± 0.02	3.48 ± 0.01	2.14 ± 0.2	. . .	$\times$
He I λ5876	. . .	. . .	5.62 ± 0.01	0.82 ± 0.05	$\times$
Na I λ5890	42.7 ± 0.02	6.46 ± 0.02	. . .	. . .	$\times$
Fe II (46) λ6084	10.6 ± 0.02	. . .	. . .	. . .	$\times$
[Ca V] λ6087+					
[Fe VII] λ6087	. . .	. . .	. . .	0.92 ± 0.05	$\times$
Fe II (74) $\lambda(6148 + 6149)$	13.1 ± 0.02	2.08 ± 0.01	0.36 ± 0.01	. . .	$\times$
Fe II (74) $\lambda(6248 + 6238)$	10.8 ± 0.01	1.54 ± 0.01	. . .	. . .	$\times$
Fe II (??) λ6315	26.1 ± 0.03	25.0 ± 0.02	. . .	. . .	$\times$
[O I] λ6300+					
[S III]λ6312	. . .	. . .	1.42 ± 0.02	1.79 ± 0.06	$\times$

Continued on Next Page. . .

Table 3.2 – Continued

	Epoch 1		Epoch 2	Epoch 3	
	29 Jan 2007[b]	11 Feb 2007	31 Mar 2007	10 Jun 2007	18 Jul 2007
Identification	(Days 9, 10)	(Days 22-24)	(Days 70, 71, 79)	(Days 141, 159, 161)	(Days 179, 190)
[O I] λ6364	. . .	. . .	2.66 ± 0.02	1.03 ± 0.09	×
Hα λ6563+					
[N II] λ6548	908 ± 0.02	442 ± 0.01	106 ± 0.01	14.7 ± 0.04	×
He I λ6678	1.09 ± 0.02	2.11 ± 0.01	2.54 ± 0.01	0.36 ± 0.05	×
[Ar V] λ7007	×	15.4 ± 0.1	. . .	0.25 ± 0.00	0.24 ± 0.01
He I λ7067	×	. . .	4.14 ± 0.03	0.86 ± 0.00	0.51 ± 0.02
[Ar III] λ7136	×	. . .	2.54 ± 0.03	1.91 ± 0.01	2.18 ± 0.01
[Ar IV] λ7236	×	. . .	. . .	0.31 ± 0.00	0.17 ± 0.01
He I λ7281	×	10.7 ± 0.1	2.10 ± 0.04	. . .	. . .
[O II] λ7325+					
[Ca II] λ7324	×	. . .	. . .	1.09 ± 0.00	1.36 ± 0.01
Fe II (73) λ7462	×	10.9 ± 0.1	. . .	. . .	. . .
He II λ7593	×	. . .	. . .	0.05 ± 0.00	0.004 ± 0.001
[Ar III] λ7751	×	. . .	. . .	0.81 ± 0.00	0.67 ± 0.01
[Ar III] λ7751+ O I λ7773	×	. . .	1.19 ± 0.02	. . .	. . .
O I λ7773	×	27.1 ± 0.1	. . .	. . .	. . .
Mg II (8)λ7890	×	9.02 ± 0.10	. . .	×	. . .
O I λ8227	×	34.2 ± 0.1	. . .	×	. . .
O I λ8227+ He II λ8239	×	. . .	1.06 ± 0.03	×	0.30 ± 0.01
O I λ8446	×	453.6 ± 0.3	6.13 ± 0.04	×	0.13 ± 0.01
He I λ8653+ He I λ8665	×	86.7 ± 0.2	0.91 ± 0.03	×	0.14 ± 0.01

[a]Flux values are in units of 10^{-12} erg s^{-1} cm^{-2}.

[b]For observations spanning multiple days, this marks the first observation in the series.

[c]For entries with an x the data does not extend to that wavelength.

3.2.3 Near-IR Spectroscopy

Near-IR spectra of V1065 Cen were obtained at Gemini-South with the Gemini Near Infra-Red Spectrograph (GNIRS; Elias et al. 2006) on 2007 March 08.22 UT (JD 2454167.72; day 47) and 2007 March 20.2 UT (JD 2454179.69; day 59) as part of a queue nova target of opportunity program GS-2007A-Q-25. The first GNIRS observations were obtained soon after the V-band light curve resumed its smooth decline after recovery from the initial dust extinction event (§3.5). Spectra were obtained in Cross-Dispersed mode (XD) using a $0\farcs45\times6\farcs1$ slit (~ 3 pixels in width) and the 31.7 line mm^{-1} grating, providing spectral coverage from $0.9-2.5$ μm with a resolution of $R = 1700$. Due to target brightness, multiple exposure strategies were attempted to prevent saturation of emission lines. Unsaturated exposure sequences included 20 coadded 1.0 second exposures (20×1.0), 80×1.0, and 40×2.0. For the final analysis, all unsaturated data were combined. Acquisition images obtained with the H_2 filter ($\lambda_o = 2.122$ μm) were saturated preventing their use as reliable flux points.

The data were reduced using the Gemini IRAF[5] package v1.9.1 (2006 December 20) following the methodology described on the Gemini Data Documentation page.[6] Wavelength calibration was established using arc-lamp spectra. The telluric calibration star, HIP 59084, exhibited strong hydrogen absorption lines in its spectrum, requiring interpolation of the continuum across the stronger absorption features. Regions of the spectra near Pa ϵ (0.955 μm), Br 13 (1.611 μm), and Br 15 (1.57 μm) were blended with telluric features preventing rectification. The standard HIP 53285 was used for flux calibration.

Prominent emission lines in the GNIRS spectra were fitted in a manner similar to that described for the optical spectra (§3.2.2). The GNIRS spectra are shown in Figure 3.4 while line identification and the measured line fluxes (in units of 10^{-12} erg s^{-1} cm^{-2}), uncorrected for reddening, are summarized in Table 3.3.

[5] IRAF is distributed by the National Optical Astronomy Observatories, which are operated by the Association of Universities for Research in Astronomy, Inc., under cooperative agreement with the National Science Foundation.

[6] http://www.gemini.edu/sciops/data/dataIndex.html

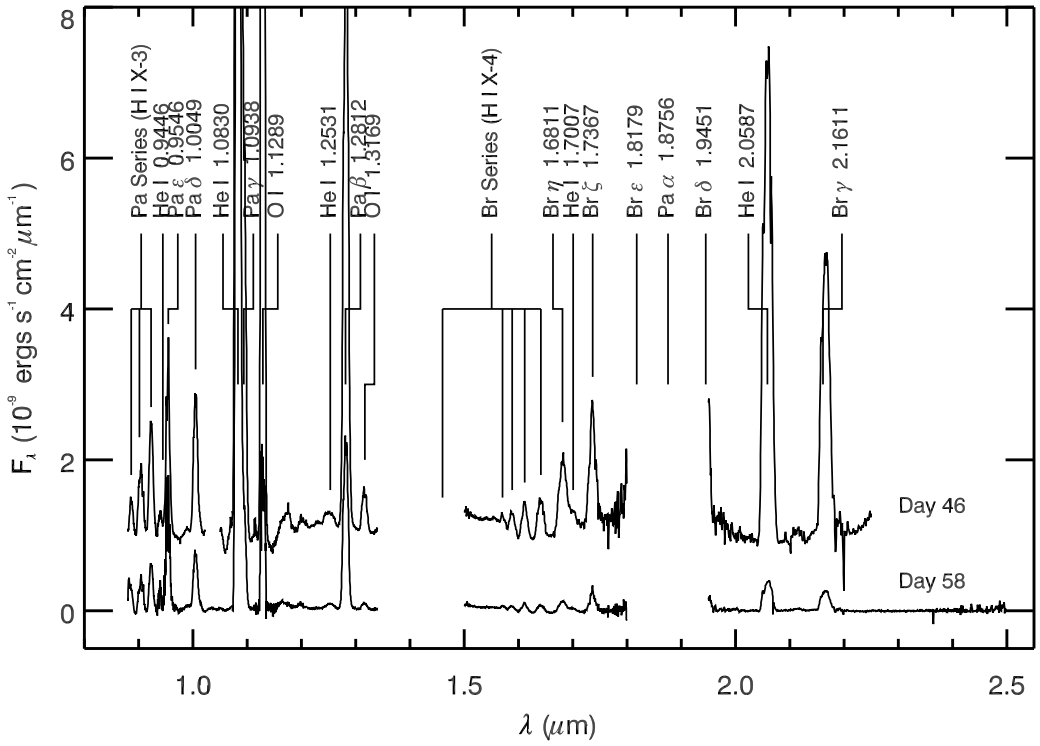

Figure 3.4: Evolution of the near-infrared spectrum of V1065 Cen. The spectra have been arbitrarily scaled and prominent features labeled. The breaks in the spectral energy distribution are due to roll-off of the eschelle orders and telluric contamination.

Table 3.3: Emission Lines Observed in GNIRS Near-IR Spectra

Identification	08 Mar 2007[a]	20 Mar 2007
Pa(11) λ0.8863	7.53 ± 1.52	3.84 ± 0.24
Paη λ0.9015 + [S III] λ0.9069[b]	12.2 ± 0.6	8.23 ± 0.10
Paζ λ0.9229[b]	13.0 ± 0.3	6.81 ± 0.06
He I? λ0.9466[b]	3.33 ± 0.3	1.68 ± 0.05

Continued on Next Page...

Table 3.3 – Continued

Identification	08 Mar 2007[a]	20 Mar 2007
Paϵ λ0.9546 + [S III] λ0.9532	18.6 ± 1.8	12.7 ± 0.06
Paδ λ1.0049	16.8 ± 0.2	7.29 ± 0.06
He I λ1.0830	417.3 ± 0.5	179 ± 0.03
Paγ λ1.0938	44.8 ± 0.5	9.31 ± 0.03
O I λ1.1289	104.6 ± 0.4	17.2 ± 0.02
C I? $\lambda 1.1600 - 1.1800$	13.7 ± 0.8	-
N I?, C I? $\lambda 1.2074; 1.2088$	11.2 ± 1.3	-
He I λ1.2531	2.90 ± 0.31	1.56 ± 0.03
Paβ λ1.2818	87.9 ± 0.2	24.1 ± 0.02
O I λ1.3169	6.87 ± 0.26	3.08 ± 0.04
Br(15) λ1.5705 (?)	-	0.40 ± 0.02
Br(14) λ1.5884	-	0.54 ± 0.02
Br(13) λ1.6114	2.16 ± 0.32	1.09 ± 0.02
Br(12) λ1.6412	6.44 ± 0.32[c]	1.37 ± 0.02
Brη λ1.6811	-	2.59 ± 0.03
He I λ1.7007	15.4 ± 0.5	0.87 ± 0.02
Brζ λ1.7367	-	3.27 ± 0.02
C I? λ1.7662	17.5 ± 0.4	-
He I λ2.0587	111.1 ± 5.4	6.28 ± 0.04
Brγ λ2.1661	68.1 ± 5.7	4.49 ± 0.04

[a]Flux values are in units of 10^{-12} erg s^{-1} cm^{-2}.
[b]Weighted average of eschelle orders 7 & 8
[c]Weighted average of eschelle orders 4 & 5

3.2.4 Spitzer Spectroscopy

V1065 Cen was observed on six dates with the NASA *Spitzer Space Telescope* (*Spitzer;* Gehrz et al. 2007; Werner et al. 2004) using the Infrared Spectrograph (IRS; Houck et al. 2004) as part of our long term *Spitzer* CNe study conducted over multiple Spitzer cycles. A summary of the *Spitzer* observations conducted under various Program Identification Numbers (PIDs) is provided in Table 3.4. Spectra were obtained using all modules of the IRS. The resolving power of the low-resolution modules, i.e., the short wavelength ($5.2 - 14.5$ μm) low resolution module (SL) and the long wavelength ($14.0 - 38.5$ μm) low resolution module (LL), is $R = \lambda/\Delta\lambda \sim 60 - 128$. $R \sim 600$ for the high resolution modules, the short wavelength ($9.9 - 19.5$ μm) high resolution module (SH) and long wavelength ($18.7 - 37.2$ μm) high resolution module (LH). Emission lines observed in V1065 Cen with the latter modules are resolved. All observations utilized Blue ($13.3 - 18.7$ μm) IRS peak-up "on source" to ensure proper placement of the target in the narrow IRS slits.

IRS Basic Calibrated Data (BCD) products from the first three visits (Table 3.4) were calibrated and processed with the *Spitzer* Science Center (SSC) IRS pipeline v16.1.0 for the short-low (SL) module and v15.3.0 for all other modules. BCDs generated from all IRS modules for the last two target visits were processed entirely with pipeline version v16.1.0. Details of the calibration and raw data processing are specified in the IRS Pipeline Description Document.[7] Bad pixels in individual BCDs were identified using bad pixel masks provided by the SSC and corrected using a linear interpolation. Multiple data collection events were obtained at two different positions on the slit using *Spitzer's* nod functionality for the low resolution modules, which enabled differencing of the two dimensional SL and LL BCDs to remove the background flux contribution. For SH and LH BCDs, adjacent follow-on observations of "blank-fields" were averaged together to create two dimensional sky images that were then subtracted from each on-source

[7] v1.0; http://ssc.spitzer.caltech.edu/irs/dh/

BCD. Spectra were then extracted from the background corrected BCDs using Spice (v1.4.1) with the default point source extraction widths. The extracted spectra were then combined using a weighted linear mean into single output data files with the standard deviations of the flux at each wavelength bin providing an estimate for the uncertainty in the observed flux. Since no appreciable fringing was detected in the IRS data, the spectra were not defringed. Emission line fluxes were measured as described in §3.2.2.

The *Spitzer* IRS data are shown in Figures 3.5–3.7. Table 3.5 summarizes the line identifications and the measured line fluxes, uncorrected for reddening.

3.2.5 X-ray and Ultraviolet Observations

More than two years after outburst (t_0), V1065 Cen was observed three times with *Swift*, on 2009 February 5.7, February 14.1, and July 11.0 UT, corresponding to days 746.7, 755.3, and 902.4 after outburst. Data acquisition, reduction, and analysis followed the methods presented by Ness et al. (2007a). The exposure times were 2.15, 2.40, and 4.95 ks, yielding only marginal detections with $(1.5 \pm 1.2) \times 10^{-3}$, $(1.2 \pm 1.1) \times 10^{-3}$, and $(0.8 \pm 0.6) \times 10^{-3}$ counts per second, respectively. Errors quoted are 1-σ errors calculated using likelihood statistics (Ness et al. 2007a). Not enough events were recorded to characterize the X-ray spectrum. The X-ray observations clearly indicate low activity likely from the accretion disk or X-ray line emission. With no significant soft X-rays detected, the data strongly imply that nuclear burning on the WD surface ended well before the observations were taken. This suggests that if V1065 Cen underwent a SSS stage, it was less than 2 years in duration.

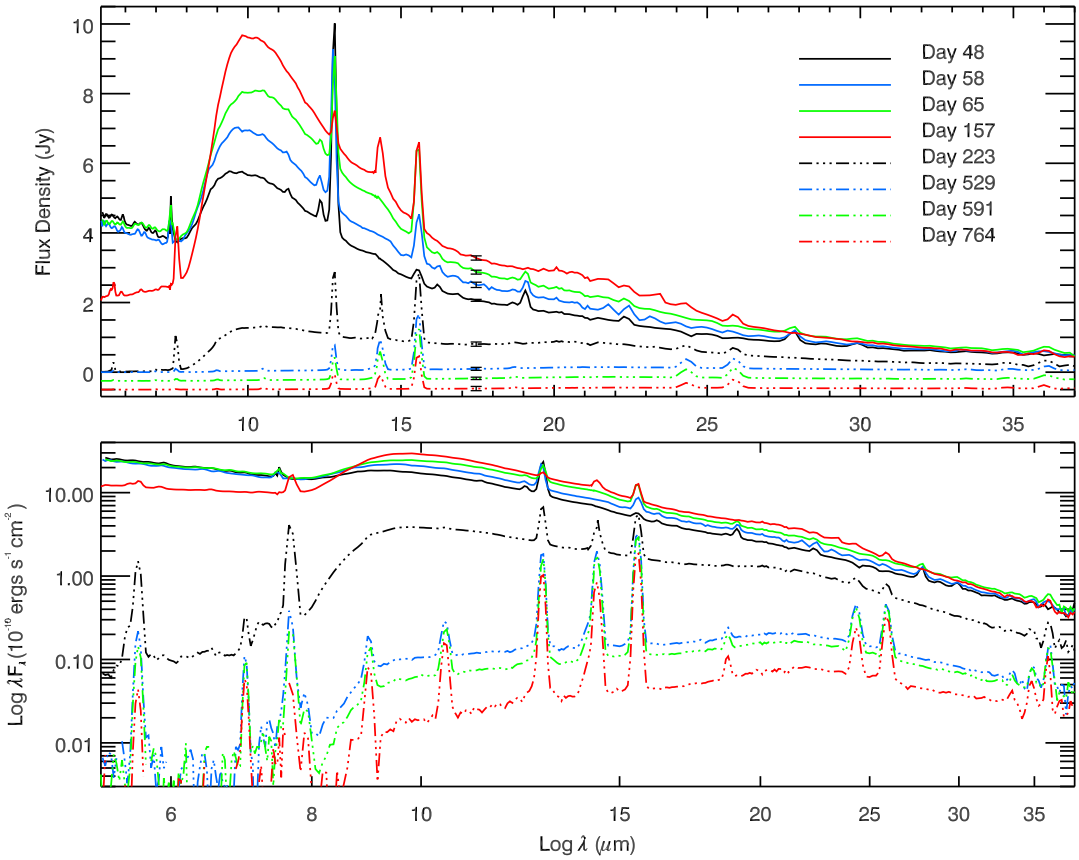

Figure 3.5: Evolution of the *Spitzer* low-resolution IRS spectra. *(Top:) Spitzer* spectra in Fν vs. linear λ highlighting the strong 10 μm silicate dust feature that appeared. The final three observations only, including the day 529 (02 July 2008), day 590 (02 September 2008), and day 763 (22 February 2009) data, have been multiplied by a factor of 10 and offset for clarity. The error bars presented at 17.5 μm show representative 3σ errors for each epoch. *(Bottom:)* Same spectra in λF$_\lambda$ vs. log λ. No scaling has been applied to the data in this plot.

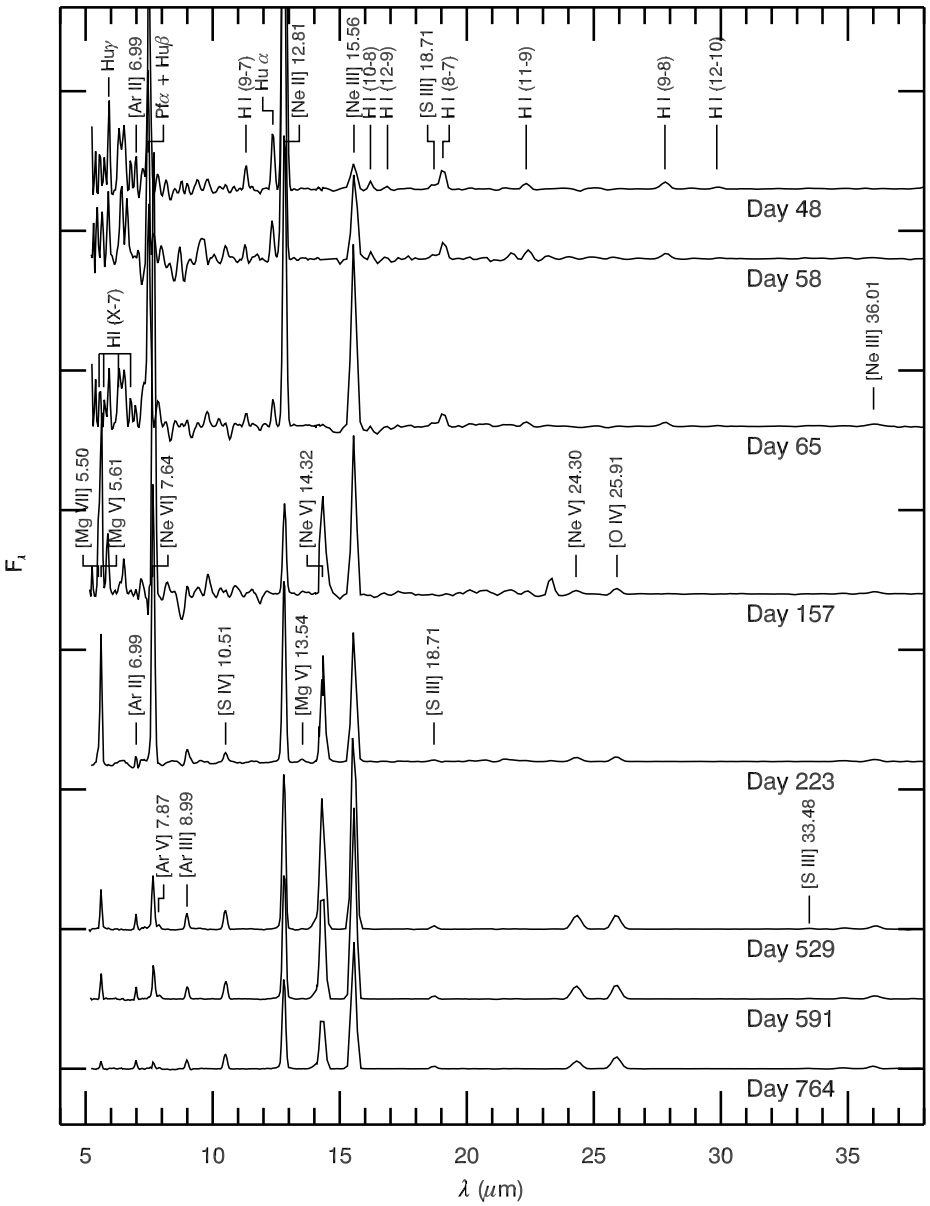

Figure 3.6: Evolution of the *Spitzer* low-resolution IRS spectra. The observed spectral energy distributions have been fit with a cubic spline function to remove the underlying dust continuum emission to highlight the emission lines. Continuum over-subtraction occurred in some regions of the spectral energy distribution, particularly near 7 μm for the day 157 (26 June 2007) data and near 8.2 μm for days 48 and 65 (08 and 26 March 2007).

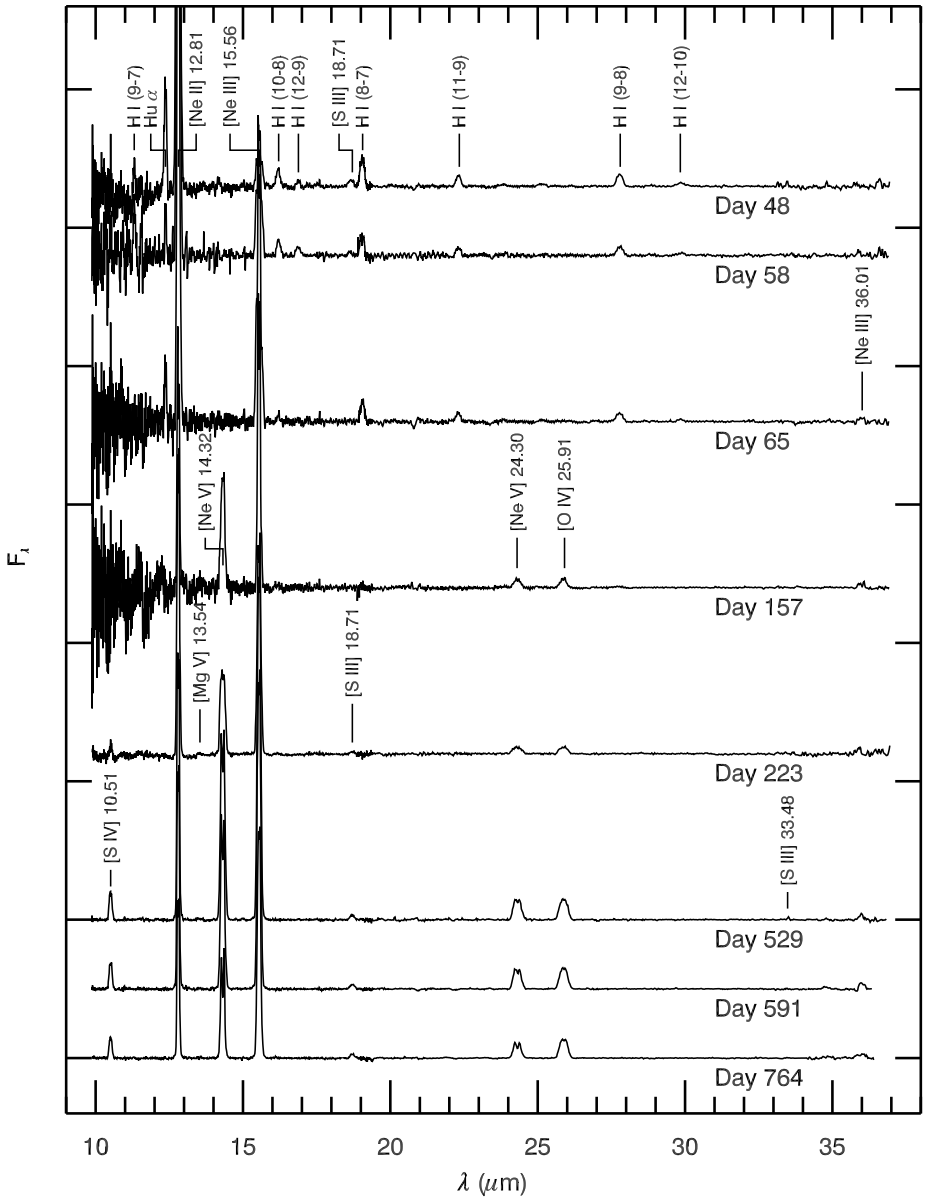

Figure 3.7: Evolution of the *Spitzer* high-resolution IRS spectra. The observed spectral energy distributions have been fit with a cubic spline function to remove the underlying dust continuum emission to highlight the emission lines.

Table 3.4: *Spitzer* Spectroscopic Observation Log

Observation Date (UT)	JD (+2450000)	PID	Source/Background AOR	Time on Source (sec) SL	SH	LL	LH	Age[a] (Days)
			Epoch 2					
2007 Mar 08.78	4168.28	30007	17677568/824	140	300	140	140	47.46
2007 Mar 18.99	4178.49	30007	17678080/336	140	300	140	140	57.67
2007 Mar 26.22	4185.72	30007	17679616/872	140	300	140	140	64.90
			Epoch 3					
2007 Jun 25.95	4277.45	30007	17683200/456	140	300	300	600	156.63
2007 Aug 30.84	4343.34	40060	22265088/344	140	300	140	140	222.52
2008 Jul 02.70	4650.20	50011	25192960/3216	140	300	300	600	529.38
2008 Sep 02.14	4711.64	50011	25198080/8336	140	300	300	600	590.82
2009 Feb 22.04	4884.54	50011	25201408/1664	140	300	1200[b]	600	763.72

[a]From 2007 Jan 20.32 (JD 2454120.82)

[b]Order 1 was exposed for 1200 s while Order 2 was exposed for only 720 s

Table 3.5: Emission Lines Observed in *Spitzer* Mid-IR Spectra[a]

		Epoch 2			Epoch 3				
Identification	λ (μm)	08 Mar 2007[b]	18 Mar 2007	26 Mar 2007	25 Jun 2007	30 Aug 2007	02 Jul 2008	02 Sep 2008	22 Feb 2009
[Mg VII]	5.50	. . .	. . .	. . .	22.2 ± 6.2	. . .	. . .	. . .	. . .
[Mg V]	5.61	. . .	. . .	. . .	37.8 ± 0.4	25.0 ± 6.2	3.11 ± 0.23	2.10 ± 0.20	0.58 ± 0.21
H I (15-7)	5.71	15.5 ± 5.6	. . .	. . .	. . .	. . .	. . .	. . .	. . .
Huγ (9-6)	5.91	20.3 ± 5.5	. . .	. . .	. . .	. . .	. . .	. . .	. . .
[Mg VIII]?	5.95	. . .	. . .	. . .	11.2 ± 1.8	. . .	. . .	. . .	. . .
H I (13-7)	6.29	13.6 ± 3.5	. . .	. . .	. . .	. . .	. . .	. . .	. . .
[Si VII]?	6.51	26.3 ± 5.9	. . .	19.3 ± 6.7	5.91 ± 0.49	. . .	. . .	. . .	. . .
H I (12-7)	6.77	8.47 ± 2.66	. . .	15.6 ± 6.1	. . .	. . .	. . .	. . .	. . .
H I (20-8)	6.95	. . .	. . .	11.1 ± 6.6	. . .	. . .	. . .	. . .	. . .
[Ar II]	6.98	7.34 ± 2.09	. . .	. . .	. . .	1.47 ± 0.41	1.07 ± 0.20	0.95 ± 0.15	0.67 ± 0.21
Pfα (6-5) + Huβ (8-6)	7.46	64.3 ± 16.0	41.2 ± 17.8	42.4 ± 14.0	. . .	. . .	. . .	. . .	. . .
[Ne VI]	7.64	. . .	. . .	. . .	124.4 ± 0.9	70.6 ± 1.8	5.97 ± 0.48	3.79 ± 0.28	0.87 ± 0.29
[Ar V]	7.90	. . .	. . .	. . .	. . .	. . .	0.75 ± 0.28	0.35 ± 0.20	. . .
[Ar III]	8.99	. . .	. . .	. . .	. . .	. . .	1.91 ± 0.18	1.60 ± 0.13	1.11 ± 0.15
[S IV]	10.51	. . .	. . .	. . .	. . .	2.21 ± 0.25	3.07 ± 0.01	3.02 ± 0.1	2.21 ± 0.07
H I (9-7)	11.31	7.75 ± 1.20	5.29 ± 2.54	5.01 ± 4.57	. . .	. . .	. . .	. . .	. . .
Huα (7-6)	12.37	18.2 ± 0.31	14.7 ± 2.0	10.3 ± 2.2	. . .	. . .	. . .	. . .	. . .
[Ne II]	12.81	199.9 ± 0.80	150.9 ± 3.1	117.7 ± 0.5	30.0 ± 2.1	60.9 ± 0.3	24.3 ± 0.1	21.7 ± 0.1	14.5 ± 0.10
[Mg V]	13.54	. . .	. . .	. . .	. . .	0.34 ± 0.23	. . .	. . .	. . .
[Ne V]	14.32	. . .	. . .	. . .	32.6 ± 0.4[c]	30.6 ± 0.4	28.5 ± 0.2	26.6 ± 0.11	14.2 ± 0.13
[Ne III]	15.56	12.0 ± 0.85	46.2 ± 0.6	74.7 ± 2.7	54.7 ± 0.4	57.3 ± 0.6	45.7 ± 0.4	40.1 ± 0.13	29.5 ± 0.21
H I (10-8)	16.21	3.73 ± 0.98	4.44 ± 1.05	3.89 ± 2.18[c]	. . .	. . .	. . .	. . .	. . .
H I (12-9)	16.88	3.07 ± 1.28	4.26 ± 0.52	5.30 ± 3.54	. . .	. . .	. . .	. . .	. . .
[S III]?	18.71	2.48 ± 0.37	15.3 ± 0.22	1.26 ± 0.35	. . .	0.71 ± 0.21	0.90 ± 0.07	1.08 ± 0.07	1.15 ± 0.07
H I (8-7)	19.06	9.20 ± 0.55	6.52 ± 0.41	5.42 ± 0.53	. . .	. . .	. . .	. . .	. . .
H I (11-9)	22.34	3.66 ± 0.26	2.94 ± 0.32	2.78 ± 0.27	. . .	. . .	. . .	. . .	. . .

Continued on Next Page. . .

Table 3.5 – Continued

Identification	λ (μm)	Epoch 2			Epoch 3				
		08 Mar 2007 [b]	18 Mar 2007	26 Mar 2007	25 Jun 2007	30 Aug 2007	02 Jul 2008	02 Sep 2008	22 Feb 2009
[Ne V]	24.30	. . .	. . .	. . .	3.35 ± 0.26	3.82 ± 0.23	6.30 ± 0.09	6.02 ± 0.09	4.14 ± 0.06
[O IV]	25.91	. . .	. . .	. . .	4.38 ± 0.14	3.53 ± 0.16	6.04 ± 0.06	6.20 ± 0.06	5.72 ± 0.05
H I (9-8)	27.80	5.22 ± 0.17	3.53 ± 0.20	3.31 ± 0.18	. . .	. . .	. . .	. . .	. . .
H I (12-10)	29.84	1.73 ± 0.20	0.96 ± 0.21	0.71 ± 0.12	. . .	. . .	. . .	. . .	. . .
[Si II]	34.81	. . .	. . .	. . .	. . .	0.72 ± 0.54	0.34 ± 0.16	0.46 ± 0.12	0.81 ± 0.12
[Ne III]	36.01	. . .	12.8 ± 0.70[d]	2.06 ± 0.75[d]	1.54 ± 0.35	1.79 ± 0.66[d]	1.47 ± 0.27	1.32 ± 0.34	. . .

[a]Flux values in units of 10^{-13} ergs s^{-1} cm^{-2}.

[b]Fluxes for lines observed in more than a single module are the weighted average of the flux in each module, unless noted otherwise.

[c]Detected in SH module only.

[d]Detected in LL module only.

Swift UV filter magnitudes were obtained simultaneously with the X-ray observations. In the uvw2 filter (1928 Å), the magnitude evolved from 17.98 ± 0.07 to 18.23 ± 0.07 between day 746.7 and 755.3. In the uvm2 band-pass (2246 Å), the magnitudes were 18.31 ± 0.10, 18.14 ± 0.09, and 18.76 ± 0.13, and in the uvw1 filter (2600 Å), the magnitudes were 17.52 ± 0.05, 17.77 ± 0.07, and 18.10 ± 0.04 observed on days 746.7, 755.3, and 902.4, respectively.

3.3 Discussion

3.3.1 Light Curve Evolution

Ennis et al. (1977) used a fixed mass, optically thin, expanding spherical shell model to fit the light curve of the fast nova V1500 Cyg (Nova Cygni 1975), assuming emission from a free-free continuum. They described the light curve decline by the relationship

$$\mathrm{F}_\lambda \propto t^{-2} \left(1 + \frac{2\mathrm{c_s}t}{\mathrm{H}}\right)^{-1}, \tag{3.1}$$

where H is the initial shell thickness, $\mathrm{c_s}$ is the sound speed in the plasma, and t is the number of days since outburst. This model predicts that the flux will decline as t^{-2} at early times with a transition to a t^{-3} power-law decline at later epochs.

The trend in the early light curves (Fig. 3.2) of V1065 Cen deviates strongly from that predicted by Ennis et al. (1977). Instead, we find that the early light curve decline is $\propto t^{-1}$. One possible cause of the observed divergence from the theoretical light curve behavior is the presence of strong emission lines. Early in the evolution, the spectra are dominated by Fe II. As the system evolves, emission by [O III] $\lambda\lambda$4959, 5007 Å begins to dominate the spectra near 5000 Å (Fig. 3.3). In order to determine the contribution to the light curve by the continuum alone, we combined those blue and red SMARTS spectra that were observed nearly simultaneously, providing 10 data points covering the first 160 days after outburst. We interpolated across the emission lines and the gap between the two spectral

regions to isolate the continuum contribution to the visual photometric band-pass. We fitted the rectified photometry and found a decay rate $\propto t^{-1.4}$. Though there were large uncertainties in fitting the continuum and, hence, in determining the decay rate of the continuum alone, the derived rate of decline still suggests that emission line intensities have a significant impact on the decay rate of the light curve, but are not entirely sufficient to explain the light curve behavior. This supports the conclusion that the system is not well characterized by a simple, homogeneous, expanding shell model.

A break in the decay rate is evident near day 90 (Fig. 3.2). Power-law fits to the decline rates after the break at B- and V-bands are $\propto t^{-2}$, while for the redder passbands, the decay rate is $\propto t^{-3}$. This behavior is more consistent with the expanding optically thin shell model of Ennis et al.

3.3.2 Spectral Evolution

A typical CN at maximum light has an optical spectrum resembling that of an F-type supergiant with strong neutral lines of O I, C I, Fe II, and Mg I coexisting alongside the H I recombination spectrum. In some cases, Na I emission is also observed at this stage. This "principal" spectrum lasts until the light curve has declined by $\simeq 3.5$ mag. As the pseudophotospere recedes and the ejecta densities decline, the optical spectrum transitions into the "diffuse-enhanced" spectrum, during which strong Fe II and O I lines persist. Both early stages of development are characterized by P-Cygni profiles that often exhibit complex, multi-component absorption features (Williams 1994). The declining optical depth of the expanding ejecta, eventually leads to the appearance of the "nebular" spectrum during which forbidden transitions dominate. Optical spectra at this later stage include forbidden lines of [N I], [N II], and [O I-III]. Some CNe go on to exhibit "coronal" emission (Greenhouse et al. 1990) from highly ionized species of Ne, Mg, and Fe. A more complete discussion of the spectral development of CNe is provided by

Hack et al. (1993), Williams et al. (1991), and Williams (1992). We obtained optical and nearly contemporaneous IR observations of V1065 Cen throughout much of this development.

Epoch 1 (E1) - Principal & Diffuse-Enhanced Spectra

The initial principal spectrum (Fig. 3.3) was dominated by hydrogen Balmer series emission including Hα and going beyond Hη. Higher order transitions rapidly blended into the Balmer continuum at short wavelengths. Near day 9, Hα had a full-width half-maximum (FWHM) expansion velocity of nearly 3000 km s^{-1} while Hβ and Hγ were nearer to 1200 km s^{-1} due to suppression of the line wings from P-Cygni absorption. Within days, all these strong H-recombination lines were observed to have FWHM velocities of 2000 - 2500 km s^{-1}, with no indication of deceleration for the next 130 days, at which point the lines became blended with other emission lines from metals. The consistency of the expansion velocity inferred from the FWHM measurements as the line flux declined suggests that the primary source of emission was a distinct, thin shell with a weak velocity gradient rather than a thick shell with a high velocity gradient (Shore et al. 1993).

Fe II multiplet emission was also prominent during the early epochs. Of these, only the Fe II (42) lines were distinct and strong enough to obtain unambiguous line fits. These lines had FWHM velocity widths between 2700 and 3900 km s^{-1} (HWZI $\sim 4650 - 6750$ km s^{-1}). The high expansion velocity of the iron lines resulted in a blending of the numerous other multiplet lines (e.g., 27, 28, 37, 38), explaining the complicated structure of the continuum and the many broad, complex features such as those observed near 4350 - 4800 Å. We classify V1065 Cen as an "Fe II"-type nova due to the predominance of strong iron emission at early epochs and suggest that it is a member of the "broad" subclass since the HWZI line widths exceeded 2500 km s^{-1} (Williams et al. 1994). No other non-Balmer emission lines were of comparable brightness at this epoch, which implies a spectral evolutionary stage of P_{fe} using the CTIO classification system (Williams et al. 1991, 1994).

Na I D was observed in emission with a single very strong P-Cygni absorption component. Interstellar sodium absorption lines were in evidence near the rest wavelength (§3.3.3). Observations from day 9 and 10 exhibited a broad complex near 5700 Å possibly due in part to N II λ5679 Å. As this feature evolved, its individual components became more distinct, eventually resolving into N II λ5679 Å and [N II] λ5755 Å(see §3.3.2).

Initial observations showed a complex around 6330 Å that we tentatively attribute to Fe II. As the ejecta thins, this complex broadened and strengthened relative to the continuum. In other "Fe II"-type novae, this region frequently gives rise to emission from [O I] $\lambda\lambda$6300, 6364 Å (^{1}D$_2$ $-^3$ P$_2$ and ^{1}D$_2$ $-^3$ P$_1$, respectively; Williams 1994). The attribution to [O I] at this epoch is not straight forward, however. Based upon the transition probabilities alone, one expects a roughly 3:1 line ratio. The high expansion velocities observed in the ejecta would blend the doublet together, but the resulting structure should be asymmetrical. Instead, the observed structure at day 22 is quite smooth and symmetric. At this stage, a correct identification is elusive.

Observations obtained on day 22 extended to nearly 9000 Å. These spectra revealed additional permitted emission from He I λ7065 Å, λ8660 Å, O I λ7773, λ8227, λ8446 Å, and possible multiplet emission from Mg II at λ7890 and λ8232 Å. Of particular interest in these data are the O I lines. O I λ8446 was the strongest non-Balmer line in the spectrum followed by O I λ7773 (see §3.3.2). Due to the presence of O I λ8446 at a strength greater than Hβ, we classify this stage of development as P$^o_{fe}$.

Both the Balmer lines and the isolated Fe II (42) lines in the principal spectrum had asymmetrical profiles due to strong P-Cyg absorption with multiple complex components (Fig. 3.8). Initially there were two dominant P-Cyg absorption components. The higher velocity component was $\sim$ -4250 km s^{-1} for each Balmer line. The lower velocity component was $\sim$ -2500 km s^{-1} for Hα but nearer to $\sim$ -2250 km s^{-1} for the other Balmer transitions. Absorption by the high velocity component rapidly disappeared while the signature of the low velocity component

remained for at least the first 30 days after outburst, disappearing completely near day 60. Around Day 10 a third weak P-Cygni absorption component was clearly evident in the high resolution spectra at velocities of $\sim$ -1650 km s^{-1}. The strength of this third component remained fairly constant as the absorption depth from other components diminished. The absorption minima near the Fe II (42) lines had velocities between -900 and -1450 km s^{-1} and, thus, was likely due to the material producing the low velocity P-Cygni absorption observed in the Balmer lines.

P-Cygni absorption profiles in CNe are often interpreted as arising in a shell of material ejected at high velocities during the initial TNR. Understanding the clumpiness and the morphology of these ejecta is useful to constrain photoionization model assumptions. In V1065 Cen, there were three distinct absorption components with behavior similar to the evolution observed in other CN systems (e.g., V603 Aql, McLaughlin 1960). Observations of V1974 Cyg revealed two distinct absorption components that Shore et al. (1993) attributed to a high velocity polar outflow along with a low velocity equatorial wind. Woodward et al. (1997), in their analysis of early observations of V1974 Cyg, argued that initially there was a P-Cygni absorption component that was much slower than the full-width zero intensity (FWZI) of prominent hydrogen emission lines. These latter P-Cygni components were accelerated by $\sim$ 700 km s^{-1} as the nova evolved and were interpreted to be evidence of high density optically thick clumps ejected by an early slow wind. Following the arguments of Shore et al. (1993) and Woodward et al. (1997), the high velocity P-Cygni absorption component (-4250 km s^{-1}) in V1065 Cen could be attributed to polar plumes of ejecta and the low velocity components to an equatorial wind.

Alternatively, in a study of resolved nova shells, Slavin et al. (1995) found that those CNe classified as "fast" novae typically had spherical shells of emission embedded with knots of higher density material, while CNe having the polar blob/equatorial ring morphology were in the "slow" class. Slavin et al. (1995) posited that this difference in morphology was due to the duration of time that

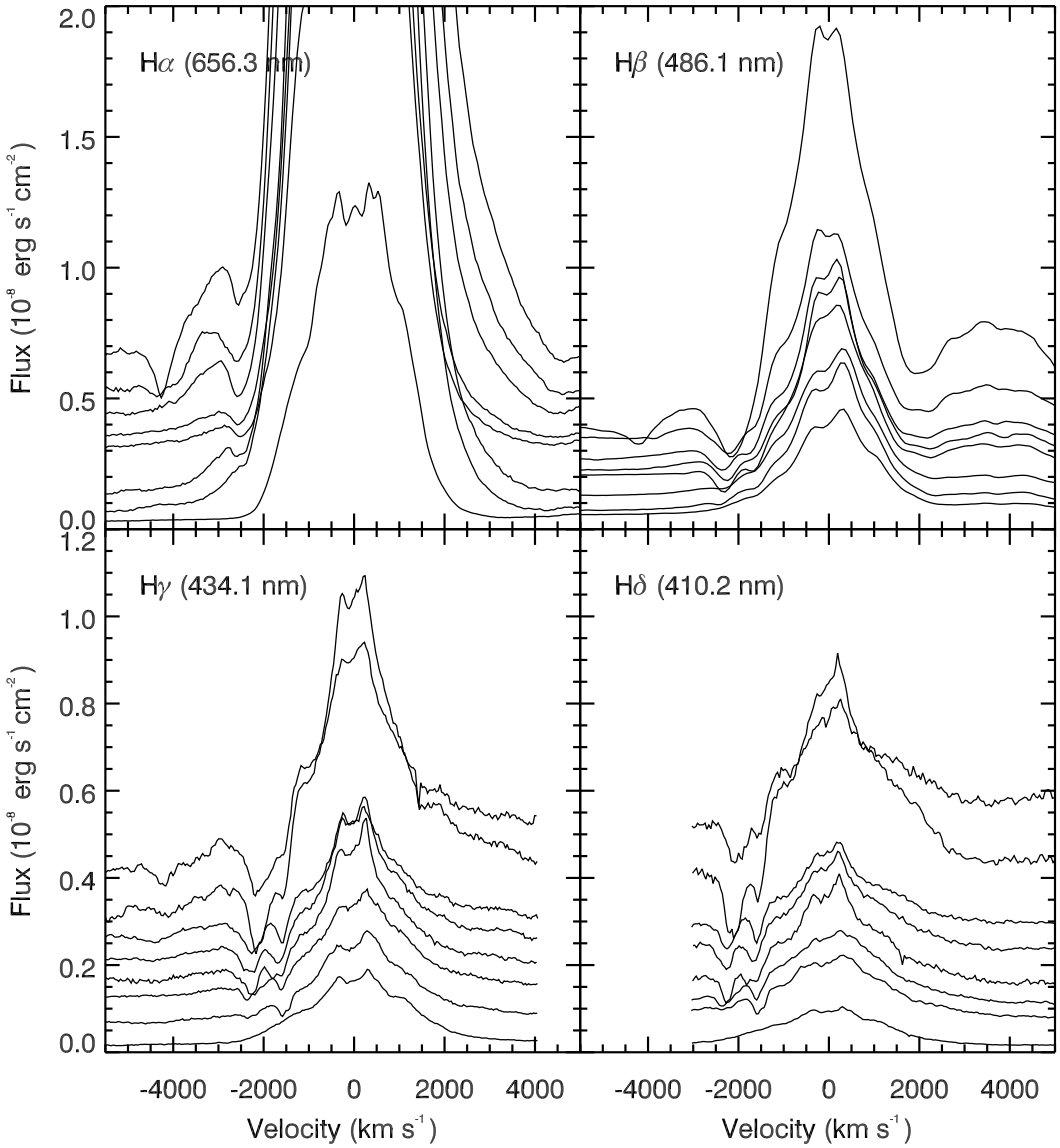

Figure 3.8: Evolution of the P-Cygni profiles associated with Balmer emission lines in V1065 Cen. The spectra, offset slightly in each panel for clarity, span from day 8.97 (*top-most curve*), Epoch 1, through day 71.80 (*bottom-most curve*), Epoch 2. The Hα and Hβ spectra were obtained at low dispersions, while the Hγ and Hδ spectra are derived from high-dispersion observations (§3.2.2).

the ejecta were subject to sculpting in the common envelope phase. If such arguments are applicable to V1065 Cen, then the ejecta of this nova are likely to have a spherically symmetric morphology. For our subsequent analysis, we assume a spherically symmetric shell of ejecta. It is apparent, however, that spatially resolved imaging of V1065 Cen is needed to establish the true distribution of the ejecta.

Epoch 2 (E2) - Early Nebular Spectrum

Observations resumed on Day 70 (2007 March 31), after a break of nearly 40 days, during which substantial changes in the ejecta took place. These observations indicated that permitted emission from iron had nearly disappeared, giving way to the first unambiguous appearance of nebular emission from oxygen and neon. The strongest non-Balmer emission line was [Ne III] λ3869 Å, which indicated that the nova had transitioned from the permitted to the nebular stage of spectral development with spectral phase N_{ne} (Williams et al. 1991, 1994). Nebular oxygen emission at $\lambda\lambda$4959,5007 Å was also strong along with doubly ionized argon at λ7136 Å. Emission lines of He I appeared at λ4471 and λ5876 Å.

By the second epoch, the profile of the emission complex at 6330 Å had become more asymmetric. It exhibited a flat-topped blue peak with a broad red shoulder. Though the relative intensities of the two components were still not 3:1, the change in morphology could indicate that the feature was due to [O I] emission superimposed on emission from Fe II. Alternatively, the blue peak may have been due to the appearance of [S III] λ6312 Å blended with the emission complex observed in E1.

Careful examination of the He I λ5876 Å line profile reveals a shoulder corresponding to Na I λ5890 Å. The presence of Na I at this epoch is interesting. With an ionization potential of only 5.1 eV, one would expect that sodium would be nearly all ionized at this stage. The persistence of this feature can be explained if there were regions in the ejecta with densities high enough to shield the sodium from the underlying hard radiation. By this stage of development,

dust had formed in the ejecta. Indeed, the *Spitzer* spectra reveal an exceptionally strong IR dust signature at this epoch. Dust condensation is thought to progress in relatively dense regions of the ejecta (Evans & Rawlings 2008), which can then persist for years afterward (Evans et al. 2010b). Shielding by this dust could readily explain the persistence of neutral sodium in the ejecta at this epoch, emission from which may be due to recombination. This is consistent with the declining signature of O I λ7773 Å at this epoch, which arises primarily from recombination (Rudy et al. 1989, 1991, and references therein).

Figure 3.4 presents the Gemini-South GNIRS observations of V1065 Cen obtained during the second epoch. The data exhibit hydrogen recombination line emission with prominent features of O I λ1.1287 μm and λ1.3165 μm, and He I λ1.0830 μm and λ2.0587 μm. These lines of oxygen and helium were at strengths only rarely observed in CNe. Nevertheless, the characteristics of these lines were quite similar to those observed in the spectra of V1974 Cyg, the prototypical ONe novae (Woodward et al. 1995). Between the first and second GNIRS observation, a span of twelve days, the fluxes in these emission lines declined sharply relative to the continuum. In the case of He I at 2.0587 μm, the flux dropped by more than an order of magnitude. This implies that conditions within the ejecta were evolving rapidly during this epoch.

The observed emission from Paη λ0.9015 μm and Paϵ λ0.9546 μm both show emission in excess of that expected for the standard recombination decrement. Based upon the emergence of [S III] in the mid-IR at this epoch (below), and the additional sulfur lines observed during E3 (§3.3.2), we attribute this excess to emission from [S III] λ0.9069 μm and λ0.9532 μm. A full accounting of the observed emission lines in the GNIRS data is presented in Table 3.3.

Figures 3.5 through 3.7 present a sequence of six *Spitzer* IRS low and high resolution spectra obtained starting in the early nebular stage of development and proceeding through nearly 800 days after outburst. To better illustrate the evolution of the emission lines, we have used the IRAF *continuum* algorithm with a *spline3* function to fit and remove the continuum emission from the data. The

resultant spectra are plotted in Figures 3.6 and 3.7. The low-res continuum fits are generally very good with the exception of the regions at the ends of the short and long wavelength spectral ranges and at the sharp increase at the blue edge of the 10 μm dust feature near 8 μm. In the 2007 June 25 SH data, there is a pronounced saw-tooth pattern arising from poor order rectification in the original BCD data. Provided the emission lines of interest are near the center of the order in these data, fitting the lines with the local continuum yields accurate line fluxes. Table 3.5 lists the details of the fits to the emission lines showing the evolution of the integrated line flux by epoch.

The *Spitzer* spectra acquired during the early nebular stage were dominated by a suite of hydrogen recombination lines, the strongest being the blend of Pfund α (Pfα) and Humphreys β (Huβ) at 7.46 μm. This feature, though prominent, was dwarfed by the [Ne II] λ12.81 μm emission, the strong presence of which is often used as a diagnostic for identification of an ONe nova (see §3.3.2). Also present in these early spectra was [Ne III] λ15.56 μm. The short wavelength spectra exhibited a surprising amount of structure with many apparent features between 5.2 and 8 μm. The central wavelengths of these features were unstable from one observation to the next making line identification difficult. An emission line at λ6.99 μm, which we tentatively identify as [Ar II], became increasingly apparent as the ejecta evolved. What may be [S III] λ18.71 μm was present, though weak, and remained throughout the evolution of the ejecta. The presence of [S III] in the IR spectra supports the hypothesis that the optical emission complex at 6330 Å was due, at least in part, to [S III] λ6312 Å.

Epoch 3 (E3) - Mature Nebular Spectrum

As the ejecta of a classical nova continue to expand, their density declines exposing more of the ejecta to the underlying radiation field of the WD. In V1065 Cen, this was exhibited by the appearance of highly ionized species of neon, magnesium and iron. The optical spectra were still dominated by [Ne III] and [O III], but they also revealed [Ne IV] $\lambda\lambda$4714,4720 Å. The IR spectra during the mature nebular

stage were still dominated by emission from [Ne II] λ12.81 μm and [Ne III] λ15.56 and λ36.01 μm, but they also exhibited prominent emission from [Ne V] λ14.32 and λ24.30 μm along with [Ne VI] λ7.64 μm. There was also strong emission from [Mg VII] λ5.50 μm and [Mg V] λ5.61 μm and weak [Mg V] emission at λ13.54 μm.

At these late stages, many CNe also exhibit emission signatures from [Fe VI] λ5177 Å and [Fe VII] at λ5159, λ5276, and λ6087 Å. In some cases, [Ca V] is observed at λ5309 Å and blended with [Fe VII] at λ6087 Å (Williams et al. 1991, 1994). These features were clearly evident during epoch 3 (E3). Due to the broad line widths, however, they were subject to blending. Interestingly, there appeared to be little, if any, emission from [Fe VII] λ5721 Å. Based upon the transition strength alone, one would expect this transition to dominate the optical [Fe VII] emission. Hence, the features at 5305 Å and 6087 Å could be primarily due to [Ca V] with only a weak contribution from [Fe VII].

During this epoch, the emission complex at 6330 Å became narrower, more distinct, and peaked around 6310 Å. As the nebular stage progressed, the relative strength of the line near 6310 Å continued to strengthen relative to the red component of the complex, eventually growing well beyond the 3:1 intensity ratio expected for the [O I] doublet. This behavior further supports the claim that [S III] λ6312 Å was the dominant contributor to this feature. This conclusion was bolstered by the continued signature of [S III] λ18.71 μm and the conspicuous appearance of [S IV] λ10.51 μm in the IR.

As the H recombination spectrum faded, the presence of a shoulder on the blue-ward side of Hδ became apparent. Based upon the signature of various other species of sulfur in the optical and IR, the most probable identification for this line is [S II] λ4072 Å. Interestingly, the presence of [S II] at 4072 Å without the shock induced emission features at $\lambda\lambda$6716, 6730 Å leads us to conclude that shocks did not play a significant role at this late stage of evolution. This confirms that photoionization effects dominated at this epoch.

As the 6310 Å feature grew in intensity, the red component of the 6330 Å complex weakened and broadened becoming more plateau-like in appearance. It

is possible that [Fe X] λ6375 was present during this late stage, but if so, it was exceedingly weak and cannot be identified with confidence. A more likely contributor to the red plateau was from [Ar V] λ6435, the companion of which was clearly present at 7006 Å. Barring reddening effects, we would expect the transition at 7006 Å to have an intensity roughly 2.4 times that at 6435 Å, consistent with what was observed.

Argon emission was observed throughout E3 in both the optical and the IR in a range of ionization states reminiscent of that observed for neon. The strongest features were [Ar II] λ6.99 μm, [Ar III] λ7136 Å and λ8.99 μm, and [Ar V] λ7006 Å. But during the late stages, additional transitions of [Ar V] became visible including emission at λ7.87 μm as well as the previously mentioned emission at λ6435 Å.

Ejecta Structure

The velocity widths of the hydrogen recombination lines measured from the FWHM Gaussian line fits suggested that the lines originated in a single emitting region with an expansion velocity of 2200 - 2500 km s^{-1}. The widths of the lower ionization states of neon and oxygen were comparable to this and were nearly constant throughout the evolution of the ejecta. The higher ionization states (e.g., Ne IV, Ne V, O IV) had consistently higher velocity widths at $\sim$3500 km s^{-1} suggesting that the source of this emission was from a different and kinematically distinct region of the ejecta.

Figure 3.9 presents the evolution of the Hα profile with time. During E1, the profile exhibited shoulders near the peak indicating that the line was not entirely optically thin at this stage. As the ejecta expanded and the optical depth declined, the line edges became more smooth and the peak broadened. By E2, the line profile had developed somewhat flat-topped or saddle-shaped peak and the width had become fixed. Very little change was observed in the line shape after this epoch. The overall behavior of this line is consistent with a finite thickness shell that underwent nearly constant expansion.

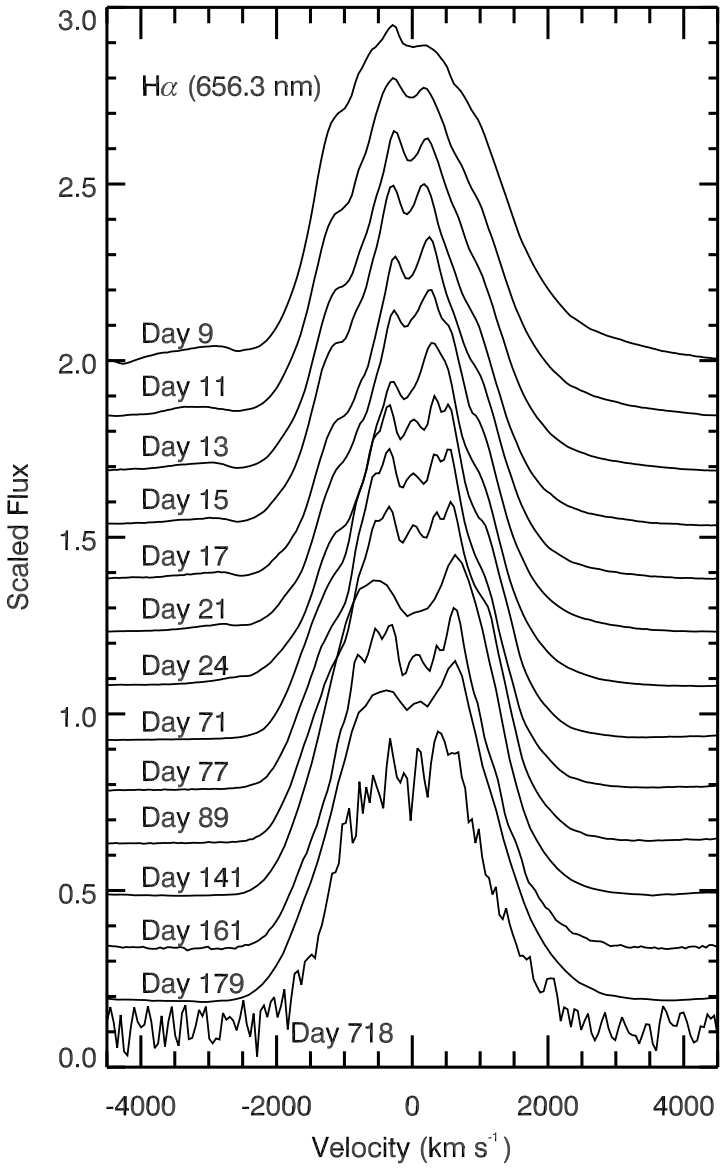

Figure 3.9: Evolution of the Hα line profiles throughout the evolution of the ejecta, day 9 to day 719. The profiles have been scaled to their peak value and offset for clarity.

Throughout our observations, the emission line structures were quite similar. The emission peaks had a weak saddle-shape and were temporally stable. The emission line structure observed in the hydrogen recombination lines was echoed by the low ionization emission lines such as [O III], [Ne II], and [Ne III] in both the optical and the IR. In Figure 3.10, we plot some of these emission lines to show the uniformity of the structure from one species and ionization state to another. The data have been scaled to the Hβ line flux and offset for clarity. The similarity of the line shapes suggested that the elemental abundance distribution was nearly uniform throughout the shell of ejecta. Models generated by Lynch et al. (2006a) for an annular ejecta distribution produced saddle-shaped line profiles slightly more pronounced than that observed in V1065 Cen. This suggests that the ejecta of V1065 Cen was nearly spherical with an additional weak annular component.

Though there did not appear to be significant differences in the elemental abundances throughout the ejecta, there did appear to be density inhomogeneities. The first *Spitzer* spectra on day 47 (E2) revealed that dust was still present in the ejecta in spite of the light curve having returned to its pre-dust formation decline. As the ejecta became more optically thin, the 9.7 μm silicate feature continued to strengthen while the emission lines came to be dominated by highly ionized species such as [Ne V], [Ne VI], [Mg V], and [Mg VII]. Dust formation requires cool, dense regions in the ejecta while the formation of the highly ionized atomic species requires low density regions subjected to a hard radiation field. Further, the spectrum of V1065 Cen during E3 exhibited emission lines from atomic transitions arising from a wide range of ionization states. Ionization potentials ranged from 29.6 eV in the case of N II to 224.95 eV for Mg VII. This order of magnitude span in ionization potential supports the conclusion that by E3, there existed substantial density inhomogeneities within the ejecta. The observed low density regions were wholly subjected to energetic photons from the WD pseudo-photosphere, which gave rise to emission from highly ionized atomic species, while the shielded interior of high density regions gave rise to emission from states with low ionization potential. The important role of fragmentation

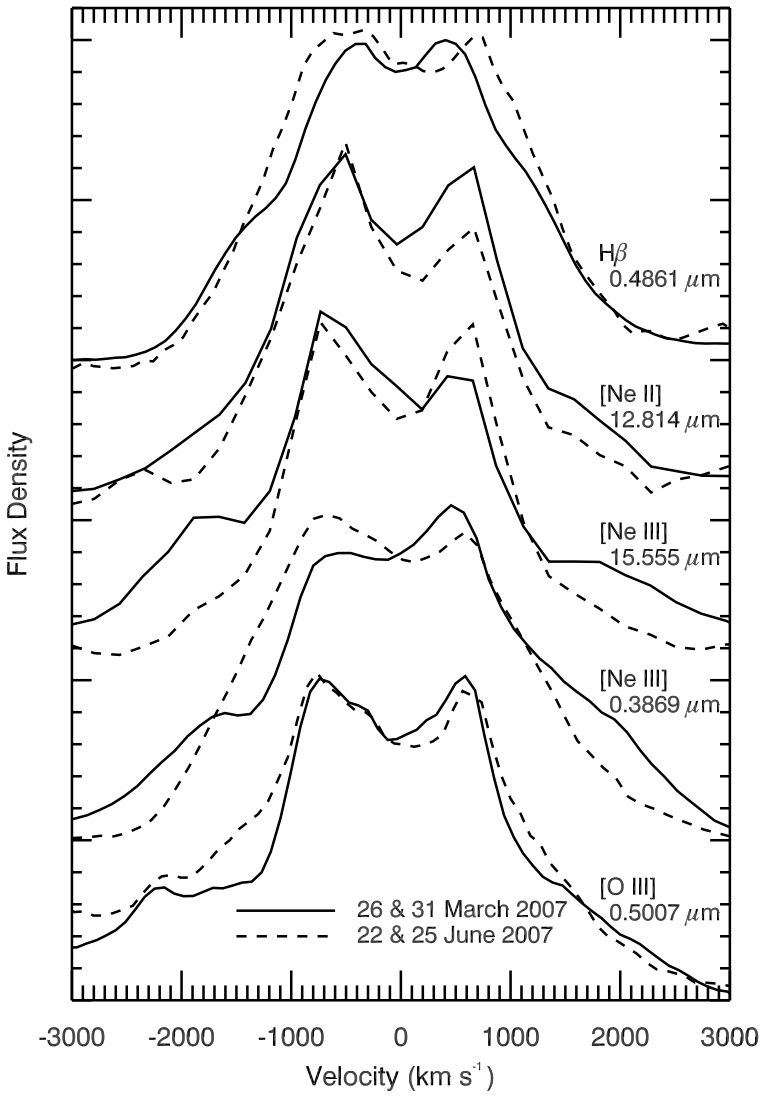

Figure 3.10: Line profiles of prominent emission lines in V1065 Cen. The profiles are arbitrarily normalized and offset for clarity. Line profiles from contemporaneous optical and mid-infrared observations on days 64 (26 March 2007) and 70 (31 March 2007) are depicted with *solid* lines, while those for days 152 (22 June 2007) and 157 (26 June 2007) are presented with *dashed* lines.

in the ejecta becomes apparent when modeling the observed emission (see §3.4 below).

Permitted O I Emission

The strength of O I 8446 Å ($3s\ ^3S^0 - 3p\ ^3P$) during the first epoch (E1) (§3.3.2) was remarkable. Its flux ratio relative to Hα, uncorrected for reddening, was $F_{8446}/F_{6563} = 1.0$. By the second epoch (E2), the flux ratio had declined by nearly a factor of 20 to $F_{8446}/F_{6563} = 0.06$. Emission from O I 7773 Å ($3s\ ^5S^0 - 3p\ ^5P$) was significantly weaker, exhibiting a relative flux of $F_{7773}/F_{6563} = 0.06$ in E1 and 0.01 in E2. As mentioned above (§3.3.2), the 7773 Å transition of oxygen arises primarily from recombination and is unable to be efficiently excited by other mechanisms. For recombination alone, however, the flux of O I λ7773 should be slightly greater than λ8446 (Rudy et al. 1989). During E1 (day 22), $F_{8446}/F_{7773} = 16.7$, while at E2 (day 79), $F_{8446}/F_{7773} = 5.2$. This leads us to conclude that excitation of the 8446 Å feature was due to a mechanism other than recombination.

O I 8446 Å can also be produced through continuum fluorescence. If this were the primary excitation mechanism, then the intensity of O I 8446 Å should be significantly greater than O I 1.1287 μm. Unfortunately, the GNIRS data with coverage of the 1.1287 μm feature was obtained 18 days before the SMARTS observations of λ8446 Å. Since the flux in the 8446 Å transition was clearly declining rapidly between E1 and E2, we cannot make a direct comparison between the two features. We can, however, compare the strength of the 1.1287 μm feature to the O I 1.3164 μm feature ($3p\ ^3P - 4s\ ^3S^0$), which was obtained simultaneously. Assuming excitation through continuum fluorescence alone, the 1.3164 μm flux should be slightly greater than 1.1287 μm (Rudy et al. 1989). We find that on day 47, $F_{1.1287}/F_{1.3164} = 15.2$, and on day 59, $F_{1.1287}/F_{1.3164} = 5.6$. It is unlikely, then, that continuum fluorescence played a critical role during E2.

A remaining source for excitation of O I 8446 Å is through the Bowen mechanism of Lyman-β (Lyβ) fluorescence. This process occurs due to the proximity of Lyβ λ1025.72 Å to O I λ1025.77 Å ($2p^4\ ^3P_2 - 3d\ ^3D^0$) (Bowen 1947). Population of

the $3d\ ^3\mathrm{D}^0$ state results in a cascade sequence that includes transitions at 1.1287 μm ($3p\ ^3\mathrm{P} - 3d\ ^3\mathrm{D}^0$), 8446 Å ($3s\ ^3\mathrm{S}^0 - 3p\ ^3\mathrm{P}$), and 1304 Å ($2p\ ^3\mathrm{P} - 3s\ ^3\mathrm{S}^0$). Assuming no collisional de-excitation, the photon fluxes of 1.1287 μm and 8446 Å should be equivalent. Though our observations of these two transitions do not occur simultaneously, their exceptional line strengths support the conclusion that they arise due to Lyβ fluorescence.

For Lyβ fluorescence to be active, the optical depth of Hα must be high. Equation (1) of Rudy et al. (1989) provides an estimate for the escape probability of Hα assuming a solar abundance of oxygen. The escape probability can then be used to estimate the optical depth of Hα, $\tau_{\mathrm{H}\alpha}$. It is clear from our analysis below (e.g., 3.4.2) that oxygen is significantly overabundant with respect to solar. Thus, the escape probability derived by this method must be scaled by the oxygen abundance relative to solar. Taking into account the high oxygen abundance, we estimate $\tau_{\mathrm{H}\alpha} \gtrsim 150$ in E1 and $\gtrsim 50$ in E2. The decline of $\tau_{\mathrm{H}\alpha}$ is exhibited in the evolution of the P-Cyg components presented in Figure 3.8.

3.3.3 Reddening and Distance

The derivation of the distance dependent physical parameters of V1065 Cen is heavily dependent upon the assumed reddening toward the system. An estimate of the reddening can be obtained using various techniques. One is to use the equivalent widths of optical interstellar Na I D lines detected toward the CN shortly after outburst. The Na I D absorption profiles from the first six observations of V1065 Cen have equivalent widths of 0.68 ± 0.06 Å. Using the relationship derived by Munari & Zwitter (1997) for single component Na I D1 absorption, we estimate a reddening of $\mathrm{E(B\text{-}V)} = 1.05^{+0.55}_{-0.4}$. Assuming $\mathrm{R_V} = \mathrm{A_V/E(B\text{-}V)} = 3.07$, this yields a line of sight extinction of $\mathrm{A_V} = 3.22^{+1.69}_{-1.23}$ mag. In many CNe, however, the Na I D absorption profiles are saturated, compromising distance determination. Since our data do not have the spectral resolution necessary to identify with certainty whether these features are saturated, we suggest that this estimate be

used with extreme caution for V1065 Cen.

Alternatively, (B-V) colors can be used to estimate the extinction. Research into the light curve behavior of CNe by van den Bergh & Younger (1987) revealed that the average (B-V) colors for CNe at maximum light and at t_2 are 0.23 ± 0.06 mag and -0.02 ± 0.04 mag, respectively. The bottom panel of Fig. 3.1 shows that the (B-V) color of V1065 Cen near maximum light is (B-V) = 0.52 ± 0.04 mag and that (B-V) = 0.41 ± 0.05 mag at $t_2 = 11$ days. These values yield extinctions of $A_V^{max} = 0.93 \pm 0.22$ mag (E(B-V) = 0.30 ± 0.07) at maximum light and $A_V = 1.38 \pm 0.19$ mag (E(B-V) = 0.45 ± 0.06) at t_2. V1065 Cen was not observed photometrically on the rise to maximum light. Thus, A_V^{max} may be underestimated.

The Balmer decrement can be used independently to deduce the reddening. Table 3.6 summarizes the flux of Hα relative to Hβ for the first 160 days after outburst. Other recombination line fluxes (e.g., Hγ) were not included in the estimates of the decrement as they are blended with other lines (e.g., [O III] λ4363 Å) due to their high velocity widths. Initially, the $F_{H\alpha}/F_{H\beta}$ ratios were $\gtrsim 10$, declining as the nova evolved. The measured line fluxes of Hα and Hβ at early epochs have uncertainties much larger than the formal uncertainties presented in Table 3.6 because of errors associated both with fitting of the associated P-Cygni absorption complexes and due to structure in the underlying continuum arising from Fe II multiplet emission. As the ejecta evolved, the continuum structure became less pronounced and the fitting uncertainties diminished. The variability in the Hα to Hβ ratio seen during the first $\sim$ 100 days was likely real, however, and not due to measurement uncertainties alone.

As late as day 58, there was strong emission from O I λ1.1289 μm (Tab. 3.3, Fig. 3.4), while O I λ8446 Å persisted in the optical through day 79. As discussed above, (§3.3.2), these features arise due to Lyβ fluorescence. Active Lyβ fluorescence requires that Hα be optically thick. We estimate that $\tau_{H\alpha}$ was

Table 3.6: Balmer Decrement

Obs. Date (mm/dd/yyyy)		Day			
B-band	R-band	Number	$F_{H\alpha}/F_{H\beta}$	$I_{H\alpha}/I_{H\beta}{}^{a}$	E(B-V)
01/30/2007	01/29/2007	9/10	7.83 ± 0.03	2.62	1.11
02/01/2007	01/31/2007	11/12	13.24 ± 0.17	2.62	1.64
02/05/2007	02/04/2007	15/16	5.89 ± 0.02	2.62	0.82
02/07/2007	02/06/2007	17/18	6.06 ± 0.02	2.62	0.85
02/09/2007	02/10/2007	20/21	12.75 ± 0.13	2.62	1.60
02/12/2007	02/13/2007	23/24	10.73 ± 0.02	2.62	1.43
02/14/2007	02/13/2007	24/25	11.35 ± 0.11	2.62	1.48
03/31/2007	04/01/2007	70/71	6.93 ± 0.03	2.70	0.95
04/06/2007	04/07/2007	76/77	5.02 ± 0.03	2.70	0.63
04/12/2007	04/19/2007	82/89	7.01 ± 0.03	2.70	0.97
06/28/2007	06/30/2007	159/161	6.22 ± 0.03	2.85	0.79

[a]Expected recombination values derived from Hummer & Storey (1987) using appropriate values for T_e and n_e.

high at least until the third epoch of observations. A high optical depth in Hα violates the Case B approximation, which assumes that all non-Lyman photons are radiated away without scattering. This means that the Balmer decrement during these stages will not yield a reliable reddening estimate.

In principle, the ejecta should become increasingly transparent to Hα photons as they expand. Hence, the observed Hα to Hβ ratio should continue to decline, asymptotically approaching the intrinsic recombination ratio extinguished by reddening. Table 3.6 indicates, however, that at late times, there was still relatively high variability in the Hα to Hβ ratio implying that conditions within the ejecta still did not emulate the Case B approximation.

Taking this into consideration, we used the minimum observed Hα to Hβ ratio to calculate an upper limit to the reddening towards V1065 Cen. The reddening from the Balmer decrement was calculated according to

$$\mathrm{E}(B-V) = a \times log\left(\frac{R_0}{R}\right) \tag{3.2}$$

(Lee et al. 2003) where R is the observed flux ratio $\mathrm{F_{H\alpha}/F_{H\beta}}$, R_0 is the intrinsic intensity ratio $\mathrm{I_{H\alpha}/I_{H\beta}}$ for the Case B approximation (Hummer & Storey 1987), and $a = (0.4[\mathrm{A_1}(\lambda) - \mathrm{A_1(H_\beta)}]^{-1}$. $\mathrm{A_1}(\lambda)$ is the extinction at wavelength λ for a reddening E(B-V) = 1.0, calculated using the reddening law of Cardelli et al. (1989) with a ratio of total to selective extinction $\mathrm{R_V = A_V/E}(B-V) = 3.07$. Assuming $R_0 = 2.72$ for T= 2×10^4 K and $\mathrm{n_e} = 10^6$ cm^{-3} (Hummer & Storey 1987) yields a reddening of E(B-V) = 0.61 ± 0.02. The error on the reddening estimate reflects the range of reddening values for reasonable variation in $\mathrm{T_e}$ and $\mathrm{n_e}$. Use of alternative reddening laws such as Fitzpatrick (1999) results in differences in the derived E(B-V) values of only $\sim 3\%$.

Galactic extinction maps (e.g., Schlegel et al. 1998) provide the *total* integrated extinction along the line of sight. Hence, they can provide a useful upper limit to the extinction towards V1065 Cen. Assuming that $R_\mathrm{V} = 3.07$ in the interstellar medium, then the total extinction towards V1065 Cen normalized to the CTIO V band-pass is $\mathrm{A_V} = 2.2$ corresponding to a reddening of E(B-V) = 0.7. Since V1065 Cen has a Galactic latitude of $b = +03.613°$ and there is substantial contamination from unresolved Galactic sources in the Schlegel et al. (1998) maps near the Galactic plane ($|b| < 5°$), these extinction estimates should be taken with caution.

Table 3.7 summarizes the various reddening and extinction estimates with their associated errors. The mean is $\mathrm{E}(B-V) = 0.5 \pm 0.1$ ($\mathrm{A_V} = 1.5 \pm 0.3$), which we will adopt throughout our subsequent discussion. This is comparable to the upper limit on the reddening derived from the Schlegel et al. (1998) extinction maps.

We estimate the distance to V1065 Cen using the maximum magnitude-rate of decline relationship (MMRD; Della Valle & Livio 1995). For $\mathrm{t_2}$ = 11 days,

the MMRD yields an absolute magnitude of $M_V = -8.6 \pm 0.5$, where the error is estimated from the 3σ variation in the MMRD fit to the data reported by Della Valle & Livio (1995). Adopting $m_{V,max} = 7.6 \pm 0.2$ and correcting with the mean extinction, $A_V = 1.5 \pm 0.3$ (Table 3.7), results in a distance modulus of m_V - $M_V = 14.7 \pm 0.6$. This implies a distance of d = $8.7^{+2.8}_{-2.1}$ kpc to V1065 Cen. Recent work by Del Pozzo (2005) examining CNe in the Large Magellanic Cloud has indicated that there is a much higher uncertainty in the relationship between $m_{V,max}$ and M_V for ONe novae than for CO novae. Hence, the MMRD relation may not be valid for ONe novae and the derived distance for V1065 Cen may not be well constrained.

Table 3.7: Reddening and Extinction

Method		E(B-V)	A_V[a]
Equivalent Width	Munari & Zwitter (1997)	1.05 ± 0.5	3.22 ± 1.54
Color	t_{max}	0.29 ± 0.07	0.89 ± 0.21
	t_2	0.43 ± 0.06	1.32 ± 0.19
Balmer Decrement		0.79 ± 0.01	2.43 ± 0.03
Extinction Map	Schlegel et al. (1998)	≤ 0.71	≤ 2.18
Mean[b]		0.5 ± 0.1	1.5 ± 0.3

[a]Calculated assuming $R_V = A_V/E(B-V) = 3.07$
[b]Calculated without the equivalent width and extinction map estimates.

3.4 Photoionization Modeling

Photoionization models provide estimates of ejecta abundance and density as well as source luminosity and temperature. Modeling of multiple epochs also enables assessment of whether abundance patterns change as the ejecta evolve and the radiation field varies. The Cloudy photoionization code, C07.02.02 (Ferland et al.

1998) was used to model the line emission observed on 2007 March 20 - April 01 (Epoch 2; day 58-70) and 2007 June 26-30 (Epoch 3; day 157-160). Cloudy generates predictions of output spectra from non-LTE, illuminated gas clouds by solving the equations of thermal and statistical equilibrium for a given set of input parameters. We assumed a spherically symmetric, expanding shell morphology. The inner and outer shell radii were calculated using the minimum and maximum expansion velocities as determined from the average FWHM of the emission lines (2400 km s^{-1}) and the maximum P-Cygni absorption velocity (4250 km s^{-1}), respectively. The ejecta density was assumed to follow a power law, $\rho \propto r^{-\alpha}$ with $\alpha = 3.0$ for a shell undergoing ballistic expansion, and the covering factor was set to unity. The abundances of all elements were held fixed at their solar values except for He, N, O, Ne, Mg, Ar, S, and Fe. The difference between the number of observed emission lines (n) and the number of free parameters (n_p) gives the number of degrees of freedom (DoF), $\nu = n - n_p$. The model free parameters included the source temperature, source luminosity, electron density (n_e), and the aforementioned elemental abundances, yielding a total of 11 free parameters. Tables 3.8 - 3.11 display the best fit models and parameters for E3 and E2 along with the degrees of freedom and the calculated reduced χ^2, where $\chi^2_{red} = \chi^2/\nu$ for the free model parameters n_p.

The χ^2 goodness of fit of a given model to the observed spectral energy distribution was determined from

$$\chi^2 = \sum_{i=1}^{n} \frac{(M_i - O_i)^2}{\sigma_i^2} \tag{3.3}$$

where n is the number of emission lines used in the model, M_i is the modeled ratio of line flux to hydrogen line flux, O_i is the measured flux ratio, and σ_i is the error in the observed flux ratio. To minimize errors associated with flux calibration between dates and wavelength regime, we calculate the modeled and observed flux ratios relative to prominent hydrogen lines within a given wavelength regime when available, i.e., relative to Hβ in the optical, Paschen β in the near-IR, and

Humphreys α in the mid-IR. Unless stated otherwise, the error estimates ranged from 10-30%, depending upon the strength of the line relative to continuum, the possibility of line blending with unidentified emission or atmospheric absorption features, and the formal calculated error in the measured line flux.

The measured line fluxes were dereddened using $E(B-V) = 0.5$ and compared to the output of each Cloudy model to calculate a reduced χ^2 for the fit. The model electron density was constrained by the ratio of [O III] λ4363 to [O III] λ4959 + λ5007, while limits on the source luminosity and temperature where determined from the ratio of [Ne III] λ15.56 μm to [Ne II] λ12.81 μm. The parameters from the resulting best fit model were then applied to the near-IR observations.

Table 3.8: Best Fit Cloudy Models - Epoch 3

			One Component		Two Component	
Line ID	λ (μm)	Observed[a]	Modeled	χ^2	Modeled	χ^2
Optical - (Days 153,159,161)						
[Ne III]	0.3869	12.13	11.99	0.00	12.09	0.00
[Ne III]	0.3968	3.83	3.61	0.05	3.64	0.04
H I	0.4340	0.36	0.52	3.01	0.51	2.69
[O III]	0.4363	1.82	1.96	0.11	2.09	0.36
He II	0.4686	0.20	0.12	1.03	0.17	0.15
[Ne IV]	0.4720,0.4725	1.95	1.66	0.55	1.95	0.00
H I	0.4861	1.00	1.00	0.00	1.00	0.00
[O III]	0.4959	1.29	1.13	0.24	1.11	0.30
[O III]	0.5007	3.86	3.40	0.23	3.33	0.30
[Fe VII]+ [Fe VI]	0.5159,0.5177	0.09	0.08	0.10	0.09	0.01
[N II]	0.5755	0.52	0.39	0.67	0.49	0.04
He I	0.5876	0.26	0.29	0.36	0.26	0.00

Continued on Next Page...

Table 3.8 – Continued

			One Component		Two Component	
Line ID	λ (μm)	Observed[a]	Modeled	χ^2	Modeled	χ^2
[S III]	0.6312	0.51	0.57	0.14	0.55	0.07
H I	0.6563	4.01	3.58	0.29	3.42	0.55
He I	0.6678	0.10	0.07	0.58	0.07	1.04
[Ar V]	0.7007	0.06	0.07	0.12	0.08	0.60
He I	0.7065	0.21	0.23	0.04	0.21	0.01
[Ar III]	0.7135	0.47	0.51	0.03	0.41	0.11
[Ar III]	0.7751	0.18	0.12	0.66	0.10	1.29
		Mid-IR - (Day 157)				
[Mg VII]	5.5030	0.28	0.01	10.27	0.20	1.05
[Mg V]	5.6100	0.48	0.08	7.58	0.59	0.57
[Ne VI]	7.6520	1.57	0.07	10.09	1.22	0.54
[Ne II]	12.8100	0.29	0.39	1.48	0.44	3.46
[Ne V]	14.3200	0.41	0.03	9.68	0.40	0.00
[Ne III]	15.5550	0.68	0.18	6.13	0.19	5.88
[Ne V]	24.3100	0.04	0.00	9.58	0.05	0.22
[O IV]	25.9100	0.05	0.01	9.15	0.05	0.12
[Ne III]	36.0100	0.02	0.01	5.20	0.01	4.95
TOTAL χ^2				75.96		24.35

[a]All lines are normalized to Hβ

Table 3.9: Best Fit Cloudy Model Parameters - Epoch 3

Parameter	One Component	Two Component
log T_{BB} (K)	5.80 ± 0.03	5.78 ± 0.04
log Luminosity (erg s^{-1})	38.27 ± 0.10	38.15 ± 0.02
log $n_{H,diff}$ (cm^{-3})	7.80 ± 0.03	6.73 ± 0.01
log $n_{H,clump}$ (cm^{-3})	. . .	7.79 ± 0.05
α^a	-3.0	-3.0
log R_{in} (cm)^b	15.44	15.44
log R_{out} (cm)^c	15.76	15.76
Filling Factor	0.10	0.10
Power^a	0.0	0.0
Covering Factor (Diffuse)	1.00^a	0.49 ± 0.04
Covering Factor (Clump)	. . .	0.51 ± 0.04
He^d	-0.81 ± 0.07 (4)	-0.82 ± 0.05 (4)
N	-1.90 ± 0.10 (1)	-1.82 ± 0.06 (1)
O	-1.50 ± 0.11 (4)	-1.42 ± 0.03 (4)
Ne	-1.53 ± 0.03 (9)	-1.46 ± 0.04 (9)
Mg	-2.74 ± 0.22 (2)	-2.75 ± 0.11 (2)
S	-2.97 ± 0.08 (1)	-2.93 ± 0.18 (1)
Ar	-3.86 ± 0.10 (3)	-3.90 ± 0.13 (3)
Fe	-3.40 ± 0.16 (1)	-3.68 ± 0.13 (1)
Ejected Gas Mass	1.0×10^{-3}	1.7×10^{-4}
Number of Lines	27	27
Degrees of Freedom	16	14
Total χ^2	75.96	24.35
Reduced χ^2	4.75	1.74

[a]This was not a free parameter in the model.

[b]Calculated assuming a minimum expansion velocity of 2400 km s^{-1} over 157 days and was not a free parameter in the model.

[c]Calculated assuming a maximum expansion velocity of 4250 km s^{-1} over 157 days and was not a free parameter in the model.

[d]The log abundance by number relative to hydrogen. All elements not listed in the table above were set to their solar values. The number of lines used in determining each abundance estimate is given in parentheses.

3.4.1 Epoch 3

E3 exhibited a much greater variety of emission line species and hence provided a more robust set of constraints than E2. Consequently, we modeled this epoch first. The data used to construct the model spanned days 141-161. For simplicity, we assumed that changes occurring in the spectrum during this period were minimal. This is undoubtedly not the case. During this interval, we expect both the conditions in the ejecta and the source illumination to have undergone considerable changes. Examination of the data ranging from $\sim 6600 - 7000$ Å in Figure 3.3 reveals that during this interval the line fluxes of some species were nearly constant while others varied considerably. In particular, the fluxes of [N II] λ5755 Å and [S III] λ6312 Å declined by 20-30%. Therefore, we assume a relatively high error of 40% on optical emission line fluxes of [N II] λ5755 Å and of lines at wavelengths longer than 7000 Å.

The dereddened fluxes for the Balmer lines Hγ, Hδ, and Hϵ, were much greater than predicted by the Balmer decrement. For Hγ, we attribute this discrepancy to blending with the [O III] λ4363 line (Fig 3.3), while the Hϵ line is contaminated by [Ne III] λ3988. The source of additional emission in the Hδ line is unclear, but may be due to [S II] λ4074 or [Fe V] λ4072. We removed the flux predicted by the dereddened Balmer decrement and attributed the remaining flux to the blended forbidden lines. Due to the high uncertainties, we did not include these hydrogen lines in our models.

Our initial attempts to model the E3 data with only a single density regime failed to achieve a suitable fit to the data. The best fit for a single component model yielded a total χ^2 of 75.96 with a χ^2_{red} of 4.75. The emission lines for the best fit model are presented in Table 3.8 and the best fit Cloudy parameters are summarized in Table 3.9. The derived abundances in Table 3.9 are given as the log abundance by number relative to hydrogen with the number of lines used in the model calculation given in parentheses. The more lines used in the model, the greater the certainty in the modeled abundance. We stress, however, that all solutions are non-unique. The total number of lines and free parameters used in calculating the reduced χ^2 from the best fit model χ^2 are provided.

A single component model was clearly unable to reproduce the range of ionization states observed in the ejecta. For example, emission lines from [Ne II] to [Ne IV] were fit quite well, yet the more highly ionized species of [Ne V] and [Ne VI] were underestimated by orders of magnitude. The case of magnesium is more complicated. Though these lines were underestimated by a substantial amount, a simple increase in the magnesium abundance improved the fits to the Mg emission lines while degrading the global fit. Hence, the magnesium abundance was constrained by the global model as well as by the emission lines.

As discussed above, there is strong support for the conclusion that by E3, the ejecta had differentiated into regions of higher and lower density. Following the assumption that the ejecta did not have a homogeneous density distribution during E3, we attempted to model the observed emission with a two component model following the method of Vanlandingham et al. (2005). In this model, we assumed that the ejecta were composed of two different density regimes but that the abundances were uniform throughout. Both density components had an associated covering factor, the sum of which was unity. This effectively increased the number of parameters by two ($n_p = 13$), one additional density component and the ratio of high to low density covering factors. Hence, there were 14 degrees of freedom. We conducted the modeling in a manner similar to that for a single component, but combined the predicted fluxes of the low and high density

components when comparing to the observed flux ratios.

The resulting best fit model had a total χ^2 of 24.4 with a χ^2_{red} of 1.7. The two component model greatly improved the overall fit to the more highly ionized species.

3.4.2 Epoch 2

We then applied the abundance solution derived for E3 to the day 58-70 data in E2. The spectral coverage of the data used in this epoch's analysis was more broad, including optical, near-IR, and mid-IR data, but exhibited fewer elemental species and a more limited range of ionization states. During this interval, the emission lines were changing rapidly. To minimize the effect of these changes between the times when each band-pass was observed, each wavelength regime, optical, near-IR, and mid-IR, was modeled independently and the subsequent χ^2 values were combined. The optical emission lines were modeled relative to Hβ, the near-IR lines to Paβ, and the mid-IR lines to Huα. After an initial solution was obtained using the derived abundances from E3, we then adjusted the abundances of elements that had associated emission lines while keeping the other abundances fixed at the E3 values. Again, this was done in a self-consistent manner within individual band-passes. We derived an upper limit to the sulfur abundance by assuming that excess of emission in Paη and Paϵ was due to [S III].

The resulting best fit model had a total χ^2 of 24.2 with a χ^2_{red} of 1.4. The derived blackbody temperature and luminosity for the illuminating source and the shell hydrogen densities were consistent with expectations for an expanding shell morphology. The E2 modeled abundance enhancements were not found to be as extreme as in E3, but we note that this earlier epoch had fewer metal lines with which to constrain the abundances.

Though the χ^2_{red} is quite good, the Cloudy model still has some significant problems. It was unable to adequately reproduce the observed emission in the complex at 6330 Å or the near-IR O I emission lines at 1.1284 μm and 1.3169

μm. There were additional problems in the near-IR modeling the He I emission at 2.0587 μm. One of the strongest lines in the near-IR spectrum, this feature was underestimated in our model by nearly two orders of magnitude.

Our initial models were unable to generate any significant flux from [O I] $\lambda\lambda$6300, 6364 Å. These transitions may, however, be excited by gas warmed by hot dust in the photo-dissociation region (PDR). To explore this possibility, we included continuum dust emission with a composition and grain size distribution predicted by our Dusty model (§3.5). The effects of depletion of the gas phase elements into the dust grains was considered in estimating the abundances. The inclusion of dust to the photoionization model resulted in little additional [O I] flux and had only a marginal ($\leq 10\%$) affect on the calculated model abundances. The weak impact of metal depletion on to the dust grains is not surprising if the dust to gas ratio was very low in the ejecta of V1065 Cen (§3.5).

As mentioned above (§3.3.2), the E3 IR spectra clearly reveal the presence of sulfur in the ejecta, which suggests that the 6330 Å emission complex could also be due to [S III] λ6312 Å. The predicted model flux from sulfur is given in Table 3.10 and likely accounts for much of the observed emission in this complex.

Table 3.10: Best Fit Cloudy Models - Epoch 2

Line ID	λ (μm)	Observed	Modeled	χ^2
Optical[a] - (Days 70,71,79)				
[Ne III]	0.3869	1.63	1.47	0.24
[Ne III]	0.3968	0.40	0.44	0.10
H I	0.4340	0.48	0.58	0.48
[O III]	0.4363	0.34	0.30	0.12
H I	0.4861	1.00	1.00	0.00
[O III]	0.4959	0.25	0.26	0.03
[O III]	0.5007	0.74	0.77	0.03

Continued on Next Page...

Table 3.10 – Continued

Line ID	λ (μm)	Observed	Modeled	χ^2
[N II]	0.5755	0.10	0.10	0.01
He I	0.5876	0.25	0.27	0.10
[S III]	0.6312	0.10	0.14	2.22
H I	0.6563	3.89	5.27	3.13
He I	0.6678	0.09	0.07	0.64
Near-IR[b] - (Day 59)				
H I	0.9015	0.12	0.14	0.19
[S III]	0.9069	0.33	0.21	1.58
[S III]	0.9532	0.43	0.51	0.37
H I	0.9546	0.29	0.23	0.46
H I	1.0050	0.36	0.34	0.23
He I	1.0830	8.16	9.64	0.81
H I	1.0940	0.61	0.55	0.12
He I	1.2530	0.07	0.04	1.74
H I	1.2820	1.00	1.00	0.00
H I	1.6810	0.10	0.05	2.91
H I	2.1660	0.15	0.15	0.03
Mid-IR[c] - (Day 65)				
H I	11.3100	0.56	0.32	4.52
H I	12.3700	1.00	1.00	0.00
[Ne II]	12.8100	13.04	13.01	0.00
[Ne III]	15.5550	8.69	7.52	0.81
H I	19.0600	0.60	0.42	0.93
H I	27.8000	0.36	0.20	2.32
[Ne III]	36.0100	0.23	0.29	0.84
TOTAL χ^2				22.75

[a]Normalized to Hβ
[b]Normalized to Paβ
[c]Normalized to Huα

Table 3.11: Best Fit Cloudy Model Parameters - Epoch 2

Parameter	Value
log T_{BB} (K)	4.77 ± 0.02
log Luminosity (erg s^{-1})	38.05 ± 0.09
log $n_{H,diff}$ (cm^{-3})	6.97 ± 0.24
log $n_{H,clump}$ (cm^{-3})	8.24 ± 0.04
α[a]	-3.0
log R_{in} (cm)[b]	15.16
log R_{out} (cm)[c]	15.40
Filling Factor	0.10
Power[a]	0.0
Covering Factor (Diffuse)	0.57 ± 0.05
Covering Factor (Clump)	0.43 ± 0.05
He[d]	-0.94 ± 0.07 (4)
N	-2.36 ± 0.07 (1)
O	-1.72 ± 0.16 (3)
Ne	-1.72 ± 0.08 (5)
Mg[e]	-2.75 ± 0.11 (. . .)
S	-3.60 ± 0.12 (2)
Ar[e]	-3.90 ± 0.13 (. . .)
Fe[e]	-3.68 ± 0.13 (. . .)
Ejected Gas Mass	1.4×10^{-4}
Number of Lines	27

Continued on Next Page...

Table 3.11 – Continued

Parameter	Value
Degrees of Freedom	16
Total χ^2	22.75
Reduced χ^2	1.42

[a]This was not a free parameter in the model.

[b]Calculated assuming a minimum expansion velocity of 2400 km s^{-1} over 70 days and was not a free parameter in the model.

[c]Calculated assuming a maximum expansion velocity of 4250 km s^{-1} over 70 days and was not a free parameter in the model.

[d]The log abundance by number relative to hydrogen. All elements not listed in the table above were set to their solar values. The number of lines used in determining each abundance estimate is given in parentheses.

[e]This was set to the abundance value derived for E3.

During this epoch, the best fit models predicted high optical depths in Hα and Lyβ, $\tau_{\mathrm{H}\alpha} = 25$ and $\tau_{\mathrm{Ly}\beta} = 7.0 \times 10^7$. The Cloudy prediction for $\tau_{\mathrm{H}\alpha}$ is consistent with our estimate based upon the observed intensity ratio of O I λ8446 Å to Hα at this epoch. In spite of this, our models underestimated the flux in the O I emission lines at 8446 Å, 1.1284 μm, and 1.3169 μm significantly. In part, we attribute these difficulties to the complexity in reproducing the excitation mechanisms governing the O I emission, including Lyβ fluorescence, and to a lesser extent, recombination and continuum fluorescence (§3.3.2). Further, even the two component models likely fail to adequately reproduce the complicated density structure characterizing the ejecta. The conditions in the regions in which these lines originate are likely not accurately reproduced. A detailed solution for the neutral oxygen emission, correctly encapsulating the above affects into photoionization models is beyond

the scope of this paper, and thus, we excluded these line fluxes from consideration in estimating the goodness of fit for all photoionization analysis.

The flux in He I λ2.06 μm ($2p^1$ $P_1^0 - 2s^1$ S_0) was severely underestimated in the Cloudy model. The excitation mechanisms for this transition are complex. The transition arises from the $2p^1$ P_1^0 level, which can decay either to the $2s^1$ S_0 level at 2.06 μm or to the $1s^2$ ^{1}S level at 584 Å. The branching ratio for these transitions is $\sim 10^{-3}$:1, but under Case B conditions, the λ584 Å transition is optically thick, potentially enhancing emission at 2.06 μm through resonant scattering. The rate of fluorescence is dependent upon T_e, n_e, the He abundance and ionization fraction, and the presence of dust (Shields 1993; DePoy & Shields 1994; Luhman, Engelbracht, & Luhman 1998). We conclude that extreme flux of He I λ2.06 μm line is probably due to the high optical depth in the 584 Å transition. Hence the He I λ2.06 μm emission line was excluded from consideration during the χ^2 minimization to determine the best-fit model parameters.

We calculated the average abundances by taking the linear mean of the abundances derived for E3 and E2. The average abundances by number relative to hydrogen are shown in Table 3.13. Overall, our best-fit models suggest a moderate overabundance of helium and iron in the ejecta, with abundances by number, relative to solar of He/H $= 1.6 \pm 0.3$ and Fe/H $= 6.6 \pm 2.3$. The abundances of O, Mg, S, and Ar were all significantly enhanced with O/H $= 58 \pm 18$, Mg/H $= 45 \pm 13$, S/H $= 54 \pm 31$, and Ar/H $= 50 \pm 18$. Neon and nitrogen were both found to be heavily enhanced relative to solar. The nitrogen abundance was N/H $= 144 \pm 34$ and the neon abundance was even greater, Ne/H $= 316 \pm 58$. All relative abundances are based upon the solar abundance values reported by Asplund et al. (2009).

Models of the TNR predict very little enhancement of iron in the ejecta. Consequently, the observed overabundance of iron suggests that hydrogen in the ejecta is significantly depleted. One explanation for the high abundances is that a substantial mass of material was dredged up from the underlying WD (Truran & Livio 1986). On the other hand, the high sulfur abundance may imply "breakout" from

the CNO cycle. Recent models of TNR on slowly accreting massive WDs were able to produce conditions capable of breakout from the hot CNO cycle resulting in enhancements of the sulfur abundance (Glasner & Truran 2009). The predicted sulfur enhancement was moderate, however, and still would not account for the observed overabundance. Further, the errors on the sulfur abundance determined by the Cloudy models are quite high, so related conclusions must be taken with extreme caution. The most probable explanation for the observed overabundances is due to dredge-up from the ONe WD.

The high neon enhancement clearly indicates that V1065 Cen is an ONe nova and situates it at the upper extreme of the class. The high neon abundance invites comparison to other ONe CNe such as V838 Her, which had a neon abundance of $\sim$ 180 times solar (José & Shore 2008). Besides the similarities in the neon enhancement, both of these objects were also overabundant in helium and sulfur. For V838 Her, He and S were 1.4 and 27.9 times solar, respectively.

3.4.3 Ejecta Mass Estimates

The mass of hydrogen in the ejecta can be estimated using the techniques described by Vanlandingham et al. (2005). Adopting their approach, the ejecta were divided into 1000 nested shells using the inner and outer radii calculated above (Tables 3.11 and 3.9). The density within each shell was computed from model best-fit density distribution where n_H is the density at the inner radius. Likewise, we applied the filling factor to each shell - in this case at a constant value of 0.1 throughout. We then determined the total shell mass and multiplied by the covering factor to estimate a final ejected mass. The best fit model for E2 predicts a shell mass of 1.4×10^{-4} M$_{\odot}$. For E3, the sum of the contribution from the diffuse and clump components yields an ejected mass of 1.7×10^{-4} M$_{\odot}$. The average ejecta mass derived for V1065 Cen, 1.6×10^{-4} M$_{\odot}$, is comparable to that estimated in other ONe CNe, such as V1187 Sco ($\sim 10^{-4}$ M$_{\odot}$; Lynch et al. 2006a) and V1974 Cyg ($\sim 2 \times 10^{-4}$ M$_{\odot}$; Vanlandingham et al. 2005).

3.5 Dust

In CNe, dust formation occurs if the local density and temperature in the ejecta are commensurate with the physical conditions required for grain condensation (Gehrz 2008b). The resultant obscuration of the central source at the time of the condensation event is characterized by a marked inflection in the decline of the broadband optical light curves, especially at blue wavelengths, and recovery as the dust formation subsides in the expanding ejecta. The depth of the transition in the light curve enables estimation of the optical depth, $\tau_{\rm V}$, of the dust at maximum extinction. The B- and V-band light curves of V1065 Cen (Fig. 3.2) both exhibit a shallow dip and recovery that we interpret as a dust condensation event. The optical depth of the extinction event in the V-band is $\tau_{\rm V} = 1.06 \pm 0.06$, while $\tau_{\rm B} = 0.97 \pm 0.07$, $\tau_{\rm R} = 0.31 \pm 0.05$, and $\tau_{\rm I} = 0.27 \pm 0.09$, for the B, R, and I bands, respectively.

The optical extinction appears to be relatively flat in the B and V-bands, i.e., at wavelengths below about 5800 Å. The break in the absorption efficiency between the V and R bands allows us to make a rough estimate of the dust grain radius. If we assume that the dust grains are of uniform size, then the extinction curve will be relatively flat or "grey" when,

$$\frac{2\pi a}{\lambda} > 1, \tag{3.4}$$

where a is the grain radius. Equation 3.4 yields an approximate grain size of $a \gtrsim 0.09$ μm. This is necessarily an oversimplification since in reality the dust will have a much more complicated grain size distribution. Nevertheless, we consider this to be a reasonable first order estimate.

The dust mass in the ejecta can be deduced from

$$\mathrm{M_d} = \frac{16\pi}{3} \frac{\mathrm{R}^2 \tau_{\rm V} a \rho_{\rm gr}}{\mathrm{Q_{abs}}}. \tag{3.5}$$

(Gehrz et al. 1995), where $\mathrm{R} = \mathrm{v}_0 t$, the grain density $\rho_{\rm gr} = 3$ g cm^{-3} with absorption coefficients $\mathrm{Q_{abs}} \sim 0.5$ at $\lambda = 0.55$ μm (i.e., for grain sizes near $a = 0.3$ μm;

Draine & Lee 1984). Assuming that the dust originated within a region of the ejecta expanding with the average velocity $v_0 \sim 3325$ km s^{-1}) thirty-three days after outburst, we find a dust mass of, $M_d \sim 1.5 \times 10^{-8}$ $M_\odot$.

The first IR observations of V1065 Cen were obtained about 20 days after onset of dust formation, just as the light curve was resuming its normal, post-extinction event decline. The initial *Spitzer* observations revealed a broad feature near 10 μm superimposed on a strong dust continuum. The Gemini coverage extended only to 2.5 μm while the *Spitzer* coverage began at 5.2 μm leaving a gap in the IR spectral coverage. In spite of the gap in coverage, it is apparent that at this epoch the underlying continuum mimicked a black body that likely peaked around 3-4 μm. We identify the broad emission feature near 10 μm as the Si—O stretching mode vibration of silicates, which typically occurs at 9.7 μm. This solid-state feature has an associated 18 μm feature caused by O—Si—O bending mode oscillations (Kwok 2007). In CNe these features are believed to arise from small (radii $\lesssim 1.0$ μm) silicate grains being illuminated by the outburst, and are best observed under optically thin conditions. There was no evidence for unidentified infrared features (UIRs) as was observed in other dust producing novae such as V705 Cas (Evans et al. 2005), DZ Cru (Evans et al. 2010b), V2361 Cyg, or V2362 Cyg (Lynch et al. 2008b; Helton et al. 2010b).

The IR spectral energy distribution (SED) of V1065 Cen evolved rapidly through the first few months post-outburst (Fig. 3.5). Between day 47 and day 157, the underlying continuum declined sharply while the peak 9.7 μm flux density nearly doubled. Over the next 66 days, however, the 9.7 μm flux declined by a factor of ~ 7. By day 529, the peak emission had transitioned to longer wavelengths, between 20-23 μm. From this point on, the overall shape of the SED remained steady while the total emission gradually declined. Though the shape of the SED is not well characterized by a blackbody curve, the general behavior is consistent with the gradual cooling of the dust grains. The lingering presence of highly ionized elemental species of magnesium and neon at late times ($t \geq$ day 529) implies that the radiation field was still quite hard. Consequently, we expect

there to be ongoing grain processing at this epoch. The evidence for this, however, is not readily apparent. More detailed analysis is required to properly characterize the development of the dust at late times and to understand the active grain processing mechanisms involved.

3.5.1 Dusty Modeling

To better understand the composition and evolution of the dust present in the ejecta of V1065 Cen, we modeled the *Spitzer* and Gemini observations from days 57-58 using the DUSTY radiative transport code (Ivezić et al. 1999). This program propagates incident radiation through a dust cloud accounting for the composition specific absorption and emission efficiencies to calculate the temperature distribution in the cloud and the emergent SED. We assumed a spherical ejection distribution with a power law density distribution $\eta \propto y^{-3}$, where η is the dimensionless profile function and y is the scaled radius of the shell ($y = R/R_{\rm in}$ with $R_{\rm in}$ equal to the inner shell radius). We estimated y to be 1.8 based upon the minimum and maximum expansion velocities, 2400 and 4250 km s$-$1, respectively. The grain size distribution (power law index, minimum, and maximum grain sizes), the dust temperature at the inner boundary, and the relative abundances of different grain types, including two types of silicates, warm silicates from Ossenkopf et al. (1992) and silicates from Draine & Lee (1984), and amorphous carbon from Hanner (1988), were free parameters in our DUSTY models.

We assessed the quality of the fit through visual comparison to observations. The continuum flux levels of the Gemini data were only poorly constrained. There were significant difficulties in flux calibration of these data due in part to the source brightness, but also to poor rectification and matching of the spectral orders. Also, during E2, the continuum flux due to dust emission was changing rapidly. Between days 58 and 65, the flux density at 7 μm grew by 10% while the shape of the continuum between 5.2 and 7 μm flattened noticeably. To deal with these uncertainties, we allowed a bias level offset to be applied independently to

each spectral order of the Gemini data while matching the overall slope of the near-IR SED. Since the flux calibration of the *Spitzer* data was robust, they were used to fix the modeled mid-IR continuum flux. In order to adequately fit the near-IR data, it was also necessary to include a weak free-free component with of the form $\lambda F_\lambda \propto \lambda^{-0.8} exp(-hc/\lambda kT)$. Our model for the dust in V1065 Cen is presented in Figure 3.11 with model parameters and output presented in Table 3.12.

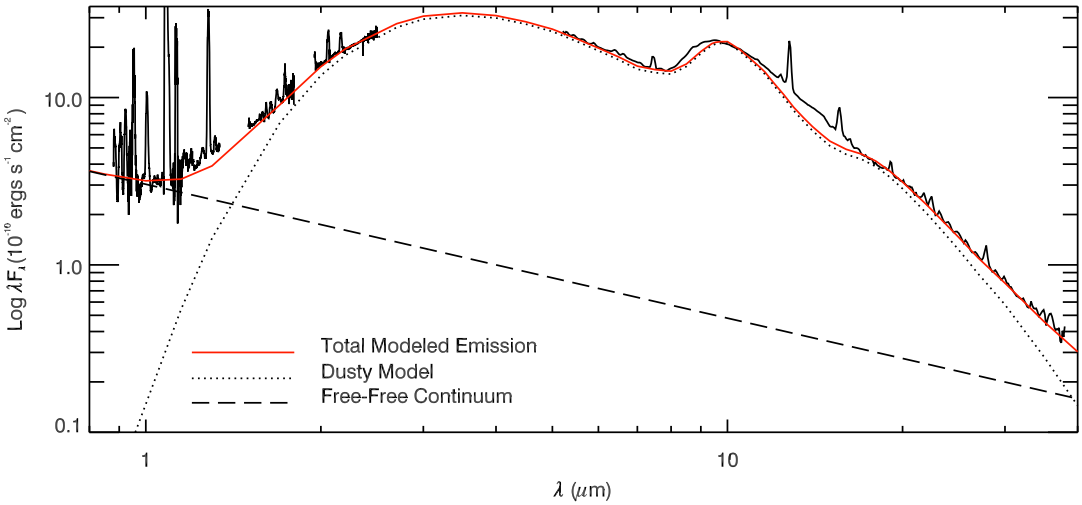

Figure 3.11: Plotted above are the combined Gemini and *Spitzer* data from days 58 and 57. Overlaid on the plot is the Dusty model fit with the addition of a weak underlying free-free component. See text for discussion.

Table 3.12: Best Fit DUSTY Model Parameters - Epoch 2

Parameter	Value
log T_{BB} (K)[a]	5.30
T_{dust} at R_{in} (K)	1050

Continued on Next Page...

Table 3.12 – Continued

Parameter	Value
y	1.8[b]
α	3.0
$\tau_{9.7}$	0.20
Silicate Fraction	0.95
Amorphous Carbon Fraction	0.05
a_{min} (μm)	0.005
a_{max} (μm)	5.000
q	3.0
F_{bol} at R_{in} (W m^{-2})	5.25×10^4
R_{in}[c] (cm)	2.41×10^{14}
$R_{in}/R_\star$[d]	4.16×10^4
θ[e] ($''$)	1.80
T_{dust} at R_{out} (K)	644

[a]This is the blackbody temperature of the illuminating source.

[b]Calculated assuming minimum and maximum expansion velocities of 2400 and 4250 km s^{-1}, respectively, over 58 days. This was not a free parameter in the model.

[c]For a luminosity of 1×10^4 $L_\odot$.

[d]$R_\star$ is the radius of the central source. This ratio is calculated assuming an external radiation temperature of T_e=10000 K.

[e]Angular size when $F_{bol} = 1 \times 10^{-6}$ W m^2.

The model for the observed SED suggests that the grains in the ejecta of V1065 Cen were comprised primarily of silicates (95% by number) with a small fraction (5% by number) of amorphous carbon (AC). The 9.7 μm feature had a broad shape that we were unable to fit using any of a wide range of model parameters but with

only a single silicate grain type. In order to better match both the width of the feature and the emission peak, we included a roughly 15/4 mix of silicates with optical properties described by Draine & Lee (1984) and warm silicates described by Ossenkopf et al. (1992). Models that included no carbonaceous grains failed to match the slope of the near-IR emission and underestimated the *Spitzer* 5.2 to 8 μm continuum. The substitution of graphitic carbon in place of AC resulted in a worse fit overall to both the near-IR data and the *Spitzer* blue continuum data. We consider the fraction and composition of the carbon grain component is poorly constrained.

Our DUSTY SEDs fitted the silicate emission features poorly. Unlike silicate emission observed in many sources of astronomical silicates, in V1065 Cen, the 9.7 μm and 18 μm features are exceptionally broad and not well differentiated. Our models suggest that the relative strengths and overall shape of the two silicate peaks is a complex function of the grain size distribution and the optical depth. Increasing the maximum grain size made the features less distinct from one another, improving the fit to the inter-feature region, but at the expense of the overall strength of the silicate emission. Likewise, decreasing the optical depth resulted in an increase in strength of the emission features, but with a corresponding sharpening of the profiles.

The difficulty in fitting the shape of the silicate emission features is due in part to the optical properties used by the Dusty model. The optical properties of both the Ossenkopf warm silicate and the Draine and Lee silicate models are for environments that are intended to be representative only. The former were intended to fit warm dust in an oxygen deficient environment (Ossenkopf et al. 1992) and the latter were a compromise between matching the observed characteristics of silicates in the "Trapezium" cluster and the absorption components arising from dark clouds (Draine & Lee 1984). None of these environments are good proxies for the ejecta of a CN. This is particularly apparent in the case of V1065 Cen. As we have discussed, the nebula from which the dust condensed was very hot and, perhaps more importantly, heavily enriched in oxygen. One would

expect these extreme conditions to play an influential role in the composition and observational characteristics of the grains produced in this environment.

In addition, the width of the silicate emission profiles also may be influenced by the inclusion into the dust grains of high charge density cations, such as Mg^{2+} or Fe^{2+} (Nuth & Hecht 1990), both of which are present and enhanced in the ejecta of V1065 Cen (see §3.4), or emission from aluminium oxide (AlO, or Al_2O), which has been detected in the atmospheres of some evolved stars. It is also possible that the broad shape may be due to a high grain porosity. Increasing grain porosity has been shown to result in broadening of the 9.7 μm feature with a correlated blue-ward shift in the central wavelength of emission (Voshchinnikov & Henning 2008). Both of these characteristics are observed in the silicate features in V1065 Cen.

The presence of multiple species of dust in the ejecta of V1065 Cen, both silicates and AC, is not unusual for dust producing CNe. This chemical dichotomy can be explained if the CO nucleation sites did not saturate leaving both C and O free to form different grain types. Likewise, an inhomogeneous abundance distribution in the ejecta would allow local variations in dust production possibly coinciding with locations of higher density condensations (Evans & Rawlings 2008). We discount this latter possibility based upon the apparent uniformity in the abundance distribution throughout the ejecta.

Our models assumed dust grains with a Mathis, Rumpl, and Nordsieck (MRN; Mathis et al. 1977) power law size distribution of the form $n(a) \propto a^{-q}$ with sharp boundaries, $a_{\rm min} \leq a \leq a_{\rm max}$. We found that a power law index, q= 3.0 most accurately fitted the data. This is slightly flatter than the standard power law index for the ISM of q = 3.5 and steeper than that found for the dusty nova V705 Cas (q = 2.3; Evans et al. 2005). The MRN size distribution for the ISM has $a_{\rm min} = 0.005$ μm and $a_{\rm max} \geq 0.250$ μm. The lower and upper limits to the grain size distribution for V1065 Cen were found to be $a_{\rm min} = 0.005$ μm and $a_{\rm max} \geq 5.000$ μm with an average grain size by number of $a_{\rm avg} = 0.006$ μm. The modeled minimum grain size is within a factor of two of the grain size estimated for

a uniform size population from the dust extinction event above. Though the mass is dominated by grains that are large compared to the ISM, the lower limit to the grain size is comparable to the ISM and is not atypical of the dust grains found in CNe (cf., V705 Cas; Evans et al. 2005). The maximum grain size, however, is much larger even than that determined for other dusty novae. As mentioned above, the 9.7 and 18 μm silicate features in V1065 Can are much less distinct than is typical, and it is this characteristic along with the underlying blackbody-like continuum that dictates the maximum grain size in the model. Due to the difficulty in fitting this region, we consider $a_{\rm max}$ to be poorly constrained.

The V-band optical depth determined by our Dusty modeling is $\tau_{\rm V} \sim 0.5$. Though this is less than the peak optical depth of the extinction event, it is slightly higher than the observed optical depth at the time of the IR observations. This discrepancy can easily be resolved if the dust in the ejecta formed with a non-uniform, clumpy distribution. Taking this into account, the modeled extinction is consistent with the observed light curve properties.

The DUSTY model predicts an inner radius of $\rm R_{in} = 2.41 \times 10^{14}$ cm for a luminosity of $\rm L = 1 \times 10^4\ L_{\odot}$. This inner radius scales as $\rm R_{in} \propto L^{1/2}$. Based upon the assumption that the nova is still radiating at or near the Eddington luminosity for a 1.3 $\rm M_{\odot}$ WD, this yields a predicted inner shell radius of 5.4×10^{14} cm. This is consistent with the radius calculated assuming a velocity of 2400 km $\rm s^{-1}$ over 58 days, $\rm R = 6.0 \times 10^{14}$ cm.

The mass in the dust was computed assuming an r^{-3} power law density distribution according to

$$\rm M_d = 8\pi R_{in}^2 (1 - Y^{-2})^{-1} ln Y \frac{\tau_{9.7}}{\kappa_{9.7}}, \tag{3.6}$$

(Sarkar & Sahai 2006) where $\rm R_{in}$ is the inner radius of the dust shell, Y is the relative shell thickness, $\rm R_{out}/R_{in}$, and $\tau_{9.7}$ is the model optical depth at 9.7 μm, which we find to be ~ 0.01. $\kappa_{9.7}$ is the dust mass absorption coefficient at 9.7 μm. We choose $\kappa_{9.7} = 1.87 \times 10^3$ by linearly interpolating across the values tabulated

by Ossenkopf[8] for uncoagulated astronomical silicates. These values yield a dust mass of $M_d = 3.7 \times 10^{-7}$ $M_\odot$.

The assumptions in the DUSTY model of spherical symmetry and homogeneity in the ejecta clearly contradict the conclusions drawn from the line profiles and photoionization modeling, which indicate that the ejecta are spherically asymmetric and clumpy. Thus, the dust mass predicted by the model is likely an upper limit to the true mass of dust produced in the ejecta of V1065 Cen. On the other hand, the dust mass estimated from the optical depth of the extinction event is probably a lower limit. The majority of the optical extinction by dust condensation is due to absorption of continuum photons within the line of sight. Clumpiness in the ejecta may result in the underestimation of the dust mass contributing to the extinction event (cf., V842 Cen, Gehrz 1990). A dust mass between these extremes, $1.5 \times 10^{-8} M_\odot \leq M_d \leq 3.7 \times 10^{-7} M_\odot$, is still high for a standard ONe nova. QU Vul, for example, only formed around $1 \times 10^{-8} M_\odot$ of dust (Gehrz 2008b), while V1187 Sco and V1974 Cyg produced very little dust at all (Lynch et al. 2006a; Vanlandingham et al. 2005, respectively).

3.6 Conclusions

We have assessed the properties of V1065 Centauri through examination of the light curve, Cloudy photoionization modeling of the observed emission lines, and DUSTY modeling of the solid-state emission features. We find the following:

1. The reddening towards the system is $E(B-V) = 0.5 \pm 0.1$ based upon the B-V color at maximum and at t_2, and the Balmer decrement.

2. The distance calculated by the MMRD relation using the mean extinction $A_V = 1.5 \pm 0.3$ was $d = 8.7^{+2.8}_{-2.1}$ kpc.

3. The spectra reveal that this was a "Fe II broad"-type nova with a spectral evolutionary sequence of $P^o_{fe} N_{ne} A_o$ according to the CTIO classification

[8] http://hera.ph1.uni-koeln.de/∼ossk/Jena/tables.html

system.

4. Our *Swift* observations did not detect a SSS phase in V1065 Cen. This implies that if this target underwent a period of SSS emission, it turned off in less than 2 years.

5. The abundances of He, N, O, Ne, Mg, S, Ar, and Fe by number, relative to solar were found to be He/H = 1.6 ± 0.3, N/H = 144 ± 34, O/H = 58 ± 18, Ne/H = 316 ± 58, Mg/H = 45 ± 13, S/H = 54 ± 31, Ar/H = 50 ± 18, and Fe/H = 6.6 ± 2.3. These abundance enhancements are consistent with V1065 Cen being a nova eruption arising on the surface of an ONe WD.

6. Our Cloudy models predict an ejected gas mass of $M_{\rm g} = (1.6 \pm 0.2) \times 10^{-4}$ $M_{\odot}$, comparable to the ejected masses observed in other ONe novae.

7. DUSTY models suggest that the dust is composed primarily of silicates ($\sim 95\%$) with a possible weak contribution from amorphous carbon ($\sim$5%).

8. The dust grains were found to have a modified MRN power law grain size distribution. The power law slope of the distribution was $q = 3.0$ with a minimum grain size, $a_{min} \sim 0.005$ μm, and a maximum grain size, $a_{max} \gtrsim 5.0$ μm. This value of a_{max} is only poorly constrained.

9. Dust mass calculations from estimates of the optical depth of the dust, τ_V yield $M_{\rm d} \sim 1.5 \times 10^{-8}$ $M_{\odot}$, while calculations based upon DUSTY models suggest $M_{\rm d} \sim 3.7 \times 10^{-7}$ $M_{\odot}$. We take these values to represent the lower and upper limits to the true dust mass.

10. Based upon the light curve decline, the observed emission lines, the calculated abundances, and the presence of silicate dust, we classify V1065 Cen as an ONe-type classical nova.

A summary of the properties of V1065 Cen is provided in Table 3.13.

Table 3.13: V1065 Centauri Properties

Property	Value
Discovery	2007 Jan. 23.35 = JD 2454123.85
t_0	2007 Jan. 20.32 = JD 2454120.82
Equatorial Coords.	11:43:10.33 -58:04:04.3
Galactic Long. & Lat.	$l = 293.9841$ $b = +03.6130$
Peak Magnitude	$m_V = 7.6 \pm 0.2$ on 2007 Jan. 21.04
t_2	$t_{2,V} \sim 11$ days
t_3	$t_{3,V} \sim 26$ days
Speed Class	Fast
Reddening & Extinction	$E(B-V) = 0.5 \pm 0.1$; $\mathrm{A_v} = 1.5 \pm 0.3$
Distance	$\mathrm{d} = 8.7^{+2.8}_{-2.1}$ kpc
WD Type	ONe
Ejection Velocity	$\mathrm{v}_{min} = 2400$ km s^{-1}
	$\mathrm{v}_{max} = 4250$ km s^{-1}
He	-0.89 ± 0.11 $(1.6 \pm 0.3)^a$
N	-2.00 ± 0.11 (144 ± 34)
O	-1.54 ± 0.17 (58 ± 18)
Ne	-1.57 ± 0.09 (316 ± 58)
Mg	-2.75 ± 0.11 (45 ± 13)
S	-3.14 ± 0.37 (54 ± 31)
Ar	-3.90 ± 0.13 (50 ± 18)
Fe	-3.68 ± 0.13 (6.6 ± 2.3)
Gas Mass	$\mathrm{M}_g = (1.6 \pm 0.2) \times 10^{-4} M_\odot$
Dust Mass	$\mathrm{M}_d = (0.2 - 3.7) \times 10^{-7} M_\odot$
Spectral Seq.	$\mathrm{P}^o_{fe}\mathrm{N}_{ne}\mathrm{A}_o$
Dust	Silicates (+ Amorphous Carbon)

[a]The first number is the mean log abundance by number relative to hydrogen. The number in parentheses is the abundance relative to hydrogen by number, relative to solar based upon the solar values reported by Asplund et al. (2009) of: He, -1.07; N, -4.17; O, -3.31; Ne, -4.07; Mg, -4.40; S, -4.88; Ar, -5.60; and Fe, -4.50.

Chapter 4

Old Novae

4.1 Introduction

The ejecta of classical novae (CNe) exhibit a varied emission spectrum in the near and mid-infrared (IR). Two fundamentally different types of novae, CO and ONe, are distinguished by their IR spectra due to the differing elements dredged up from the WD and synthesized during the TNR (Gehrz 2008b). The former appear to involve low mass CO WDs, while the latter involve more massive ONe WDs and have shells whose gas phase is highly enriched in light metals. Our *Spitzer* Space Telescope (Werner et al. 2004; Gehrz et al. 2007) observations reveal that the spectra of the mature CNe V1974 Cyg, V382 Vel, and V1494 Aql are dominated by O and Ne forbidden emission lines during their late nebular stages. For a given observed spectral region, the existence of a single forbidden emission line for some ionization species of O and Ne can be used to estimate a lower limit to the total abundance of these species (Gehrz et al. 2008a, hereafter G08). The determination is a lower limit because there may exist additional emission lines for the same and other ionization species of the same element that fall outside the bandpass of the observed spectral region.

Late-epoch observations of CNe are particularly valuable for revealing the presence of elements that may not have been detectable at optical wavelengths

during the early development of the nova. Ideally, calculations of abundances of metals are made by comparing the flux of each metal's emission lines to hydrogen recombination emission lines present at the same epoch. Our metallic abundance calculations made from late-epoch spectra are limited by the absence of hydrogen recombination emission lines. In cases where early post-eruption measurements constrain the total mass of the hydrogen expelled by the nova, the number density of free electrons at later epochs is known and the abundances of metals relative to hydrogen may be calculated in the straight-forward manner described in §4.3. This method was employed in analyzing late-epoch IR spectra of the old nova QU Vulpeculae (Nova Vul 1984 No. 2), where neon was found nearly twenty years after the eruption to be $\gtrsim 168$ times overabundant by number with respect to hydrogen as compared to the solar value (G08).

In this paper, we report on observations of nine CNe in their late nebular stages (> 4 years post-outburst). In §4.2, we detail the optical and *Spitzer* observations followed by a description of the properties of the prominent emission lines observed in these spectra (§4.3.1). Then, in §4.3, we provide an overview of abundance determination in the low density regime. In the following sections, §4.5-4.7, we calculate the abundances of three of our targets based upon their IR spectra. Finally, we present our conclusions in §4.8.

4.2 Observations and Reduction

4.2.1 *Spitzer* Mid-Infrared Spectroscopy

We observed nine old CNe (QU Vul, GK Per, V1500 Cyg, NQ Vul, V1668 Cyg, V705 Cas, V1974 Cyg, V382 Vel, and V1494 Aql) using the IRS instrument (Houck et al. 2004) on board the *Spitzer* Space Telescope (*Spitzer*; Werner et al. 2004; Gehrz et al. 2007) as part of our *Spitzer* CN monitoring program (program identification numbers (PIDs) 122, 124 (P.I. RDG), 30076, and 40060 (P.I. AE)). A summary of the *Spitzer* observations is provided in Table 4.1. The observations

were conducted using the short wavelength (5 – 15 μm) low resolution module (SL), the short wavelength (10 - 19 μm) high resolution module (SH), and the long wavelength (19 – 37 μm) high resolution module (SH). The resolving power for SL is $R = \lambda/\Delta\lambda \sim 60 - 120$ and R $\sim$ 600 for SH and LH. Emission lines observed with the latter modules are marginally resolved. Observations in PIDs 122 and 124 utilized visual Pointing Control Reference Sensor (PCRS, Mainzer et al. 1998) peak-up on nearby isolated stars to ensure proper placement of the target in the narrow IRS slits, while PIDs 30076 and 40060 used on-source peak-up. The time on source varied by module and program and is provided in Table 4.1.

IRS Basic Calibrated Data (BCD) products were calibrated and processed with the *Spitzer* Science Center (SSC) IRS pipelines version v15.3.0, v16.1.0, and v17.2.0 depending upon the module and epoch of observation (see Table 4.1). Details of the calibration and raw data processing are specified in the IRS Pipeline Description Document, v1.0.[1] Bad pixels were interpolated over in individual BCDs using bad pixel masks provided by the SSC. For all PIDs, multiple data collection events were obtained at two different positions on the slit using *Spitzer's* nod functionality. For PIDs 122 and 124, sky subtraction was only possible for the SL observations as no dedicated sky observations were performed for the SH and the LH mode observations. Multiple data collection events were obtained at two different nod positions along the slit for the low resolution modules. The median combined two-dimensional SL and LL spectra were then differenced to remove the background flux contribution. PIDs 30076 and 40060 specified separate offset observations of "blank" sky from which background images were derived by median combining the two-dimensional spectral images. These were then subtracted from the on-source BCDs. Spectra were then extracted from the two-dimensional images with the *Spitzer* IRS Custom Extraction Software (SPICE;[2] version 1.4.1) using the default point source extraction widths. The extracted spectra were combined using a weighted linear mean into a single output data file. Due to the low

[1] http://ssc.spitzer.caltech.edu/irs/dh/PDD.pdf
[2] http://ssc.spitzer.caltech.edu/dataanalysistools/tools/spice/

continuum signal, it was not necessary to defringe the data. Errors were estimated from the standard deviation of the flux at each wavelength bin. Fitting of the spectral lines was performed using a non-linear least squares Gaussian routine (the Marquardt method; Bevington & Robinson 1992) that fit the line center, line amplitude, line width, continuum amplitude and the slope of the continuum. All of the lines were resolved in the high resolution modules. Those lines exhibiting castellated or saddle-shaped structure were fit with multiple Gaussians in order to accurately assess the line widths and fluxes.

4.2.2 Optical Spectroscopy

We observed V1974 Cyg using the Boller & Chivens Spectrograph[3] at the Steward Observatory 90" (2.29-m) Bok telescope at Kitt Peak, Arizona as part of our ongoing CN optical monitoring campaign. Details of the observations are provided in Table 4.2. The data were obtained with a 1.5″ slit using a 400 line/mm, first order grating. The blue setup had spectral coverage from 3550 – 6850 Å at a spectral resolution of $\sim$ 3 Å pixel^{-1} ($\lambda/\Delta\lambda = R \sim 1900$). The red setup had coverage from 5975 – 9375 Å with a similar spectral resolution ($R \sim 2600$). Blue observations were taken with the UV36 blocking filter, except where otherwise noted, and the red observations with the Y48 filter.

The data were reduced in IRAF[4] using standard optical spectral data reduction procedures. For each set of observations, five or more images were obtained and median combined to allow the removal of cosmic rays. Wavelength calibration was performed using a He-Ar calibration lamp and flat-fielding was done with a continuum lamp. In the case of the red setup, fringing occurred beyond 7000 Å.

[3] http://james.as.arizona.edu/ psmith/90inch/90finst.html

[4] IRAF is distributed by the National Optical Astronomy Observatories, operated by the Association of Universities for Research in Astronomy, Inc., under cooperative agreement with the National Science Foundation.

Table 4.1: *Spitzer* Observations

Target	PID	Modules	AOR	Pipeline	Observation Date (UT)	JD (+2450000)	Δt^a (Days)	On-Source Time[b] (sec)
V1974 Cyg	124	SL, SH, LH	5043968	15.3.0	2003 Dec 17.4	2990.9	4318	24/84/84
	30076	SL, SH, LH	17732096/7216[c d]	15.3.0/17.2.0	2006 Oct 18.4	4026.9	5354	72/72/168
	40060	SL, SH, LH	22267648/7904	16.1.0/17.2.0	2007 Aug 30.2	4342.7	5669	140/300/600
V382 Vel	122	SL, SH, LH	5021696	15.3.0	2004 May 13.6	3139.1	1820	60/72/72
	30076	SL, SH, LH	17733120/8240[d]	16.1.0/15.3.0/17.2.0	2007 Mar 26.2	4185.7	2867	600/72/72
	40060	All	22269440/9696	17.2.0	2008 Feb 25.4	4521.9	3203	140/300/140/600
V1494 Aql	122	SL, SH, LH	5022464	15.3.0	2004 Apr 14.3	3109.8	1594	60/72/72
	30076	SL, SH, LH	17732864/7984[d]	16.1.0/17.2.0	2007 Jun 08.2	4259.7	2744	48[e]/96/224
	40060	All	22268928/9184	16.1.0/17.2.0	2007 Oct 12.3	4385.8	2870	140/60/140/140
NQ Vul	124	SL, SH, LH	5040384	15.3.0	2004 Apr 16.6	3112.1	10039	60/72/72
GK Per	124	SL, SH, LH	5028608	15.3.0	2004 Mar 01.4	3065.9	37626	56/120/240
V1500 Cyg	124	SL, SH, LH	5047040	15.3.0	2003 Dec 16.8	2990.3	10335	60/72/72
V1668 Cyg	124	SL, SH, LH	5047552	15.3.0	2003 Dec 15.5	2989.0	9227	60/72/72

[a]Days from t_0, the values of which are as follows: V1974 Cyg – 1992 Feb. 20.8 (JD 2,448,673.3); V382 Vel – 1999 May 23.4 (JD 2,451,321.9); V1494 Aql – 1999 Dec. 3.4 (JD 2,451,515.9); NQ Vul – 1976 Nov. 2.5 (JD 2,443,085.0); GK Per – 1901 Feb. 22 (JD 2,415,438); V1500 Cyg – 1975 Aug. 30.9 (JD 2,442,655.4); V1668 Cyg – 1978 Sep. 12 (JD 2,443,763.5).

[b]On-source integration times are given in SL/SH/LL/LH order.

[c]The second number is the last four digits of the background AOR.

[d]For these observations a background exposure was acquired for the LH module only.

[e]For this observation, the on-source integration time in the SL module was 48 seconds in the 5.2-8.7 μm range and 72 sec in the 7.4-14.5 μm range.

Table 4.2: Bok 90" Observations

Target	Grating	Filter	Int. Time (sec)	Obs. Date (UT)	JD (+2450000)	Δt (Days)
V1974 Cyg	Blue	. . .	5100	2006 Sep 28.3	4006.8	5334
	Blue	UV36	2700	2006 Sep 30.2	4008.7	5335
	Blue	UV36	2700	2007 Oct 20.1	4394.6	5720
	Blue	UV36	300	2008 Sep 22.3	4731.8	6059
	Red	Y48	300	2008 Sep 23.3	4732.8	6060
	Red	Y48	1500	2008 Sep 24.3	4733.8	6061

These fringes can be problematic when one is trying to interpret flat-fielded images of bright targets, but in the case of V1974 Cyg, the fringes were weaker than the relatively high noise level and did not have an appreciable effect. Observations of BD +28 4211 at similar airmass were applied to the target data for flux calibration. Line fluxes were measured using the same method as for the *Spitzer* spectra.

4.3 Determination of Abundances

There are two general methods for determining the abundances within the ejecta of novae – nebular analysis and photoionization modeling. The choice of analysis depends upon the properties of the expanding material within the line emitting region.

Mid-IR forbidden emission lines in novae are produced through spontaneous emission from excited states that were populated through collisions within the ejecta. For very low density gas, the spontaneous emission of a photon from an excited atom will occur before collisional de-excitation. In this low density limit, we assume that every collisional excitation results in subsequent photon emission such that the rate of emission is directly related to the rate of collisions within the gas. In this regime, standard nebular analysis techniques such as those described by Osterbrock & Ferland (2006) are valid and allow a straight-forward

determination of the abundances within the line emitting region provided that the electron densities and temperatures are known.

The density at which significant portions of the excited ions no longer have time to emit a photon before they suffer de-excitation through particle collisions is called the critical density, n_{crit}. Collisional damping of the lines invalidates the assumptions used in basic nebular analysis since the rate of emission is no longer directly related to the rate of collisional excitation. If the densities are above n_{crit} in the line emitting region, then it is necessary to utilize the full level balancing equations. In this high density regime, it is necessary to use photoionization codes, e.g., Cloudy (Ferland et al. 1998).

Photoionization analysis cannot be used to reliably estimate the abundances in the ejecta at late times in CNe. This method assumes an illuminating source that provides a steady flux of incident photons leading to radiative excitation. As discussed below, the central source has "turned off" in each of the CNe in our sample, which means that the luminosity of the central system is low, of order a few $L_{\odot}$, and does not have a significant UV photon flux capable of photoionization and radiative excitation. Hence, photoionization models may yield results that accurately reproduce the observed emission, but they would not necessarily be physically meaningful.

The targets observed in the present study have all undergone many years of expansion. Based upon our estimates for the shell geometries, masses of ejected hydrogen, and electron temperatures, we assess whether or not the ejecta densities had declined below the critical densities for the observed transitions. In cases where this is true, we use standard nebular analysis techniques following the methodology of G08. A more complete discussion can be found in Osterbrock & Ferland (2006).

It is typically assumed that the electron density, n_e, for a fully ionized medium is roughly equal to the hydrogen density of the gas, n_H. In a strict sense, this is the lower limit to the electron density as there is also a contribution to the electron population by ionized metals. In the case of ejecta with a high metal

abundance (e.g., > 100 times solar), this contribution to the electron population may, indeed, be high, possibly within an order of magnitude of the value for n_e that we assume here. Increasing n_e due to the contribution from ionized metals results in a decrease of the calculated abundances. For our analysis, we neglect this contribution to n_e since the dominant factor in determining the electron density arises from our assumptions for the ejecta mass and distribution (as described below).

The critical density is determined from the ratio of the Einstein A spontaneous emission, coefficient, A_{ij} (s^{-1}), to the de-excitation rate coefficient, q_{ji} (cm^3 s^{-1}), which is determined according to:

$$q_{ji} = \frac{8.63 \times 10^{-6}}{\omega_j T_e^{1/2}} \Upsilon_{ij}, \tag{4.1}$$

where j indicates the upper excitation state, i the lower excitation state, ω_j is the statistical weight of the upper state, T_e is the electron temperature, and Υ_{ij} is the thermally averaged effective collision strength. The statistical weight is determined according to $\omega_j = (2J+1)$, where J is the quantum angular momentum term for the upper excitation level.

The choice of effective collision strength is determined by the assumed electron temperature of the ejecta. In a study of the shell of DQ Her nearly 50 years post-outburst, Ferland et al. (1984) found that the effective temperature of the shell was quite low, of order 500 K. They showed that cooling by IR fine structure lines of oxygen be could very efficient provided that the densities in the ejecta were lower than the critical densities of the prominent IR transitions. Enhanced abundances of elemental species that have strong IR forbidden lines, such as oxygen and neon, allowed the ejecta to cool to temperatures of order 1000 K or less. These authors note, however, that abundance enhancements of elements without prominent IR fine structure lines (e.g., He and C) actually raise the equilibrium nebular temperatures since they increase the opacity in the ejecta without a corresponding increase in cooling efficiency.

A direct estimate of the temperature in the ejecta can be obtained using the

ratio of [O III] λ4363 Å to [O III] $\lambda\lambda$4959, 5007 Å (Osterbrock & Ferland 2006). This ratio can be used to estimate the temperature in the ejecta since the upper level of the 4363 Å transition ($^1S_0$) has an excitation energy of 5.4 eV, significantly higher than the excitation energy of the 4959, 5007 Å doublet ($^1D_2$) at 2.5 eV. At low temperatures, however, the 4363 Å transition cannot be effectively excited, making temperature diagnostics in the low density regime using the [O III] line ratio difficult.

The effective collision strengths were determined at the electron temperatures of 1000 K and 5000 K, considered to be reasonable limits to T_e based upon our assumptions above and the temperature estimates discussed in detail below (§4.5-4.7). The Υ_{ij} and A_{ij} adopted values and the sources from which they were obtained are given in Table 4.3.

The collisional excitation rate is determined by:

$$q_{ij} = \frac{8.63 \times 10^{-6}}{\omega_i T_e^{1/2}} \Upsilon_{ij} exp\left(-\frac{h\nu_{ij}}{kT_e}\right), \tag{4.2}$$

where ω_i is the statistical weight of the lower excitation state, ν_{ij} is the transition frequency, h is the Planck constant, and k is the Boltzmann constant.

If n_e is lower than n_{crit} such that collisional de-excitation is negligible, then the population of the upper excitation state can be determined from the observed line intensities. If all transitions from the upper state are observed, then the population can be determined quite accurately. The population of the upper level is:

$$N_j = \frac{L_l}{A_{ij} h\nu_{ij}}. \tag{4.3}$$

The population of the lower excitation state can be derived by similar means:

$$N_i = \frac{L_l}{q_{ij} h\nu_{ij}} \frac{\left[1 + \left(\frac{n_e}{n_{crit}}\right)\right]}{n_e}. \tag{4.4}$$

Table 4.3: Line Parameters

Ion	λ	Term	A_{ij}	Υ_{ij}		n_{crit} (cm^{-3})		References[ab]
	(μm)	($j \rightarrow i$)	(s^{-1})	(1000 K)	(5000 K)	(1000 K)	(5000 K)	
[O IV]	25.91	$^2P^0_{3/2} \rightarrow ^2 P^0_{1/2}$	5.19×10^{-4}	1.641	2.0214	4.63×10^3	8.40×10^3	[1]; NIST
[Ne II]	12.81	$^2P^0_{1/2} \rightarrow ^2 P^0_{3/2}$	8.59×10^{-3}	0.272	0.277	4.61×10^5	1.01×10^6	[2]; NIST
[Ne III]	15.56	$^3P_1 \rightarrow ^3 P_2$	5.84×10^{-3}	0.596	0.739	1.84×10^5	3.31×10^5	[3]; NIST
	36.01	$^3P_0 \rightarrow ^3 P_1$	1.10×10^{-3}	0.193	0.226	2.09×10^4	3.99×10^4	[3]; NIST
[Ne V]	14.32	$^3P_2 \rightarrow ^3 P_1$	4.59×10^{-3}	9.551	7.653	8.80×10^3	2.31×10^4	[4]; ALL
	24.32	$^3P_1 \rightarrow ^3 P_0$	1.25×10^{-3}	1.830	1.688	7.51×10^3	1.76×10^4	[4]; ALL
[Ne VI]	7.64	$^2P^0_{3/2} \rightarrow ^2 P^0_{1/2}$	2.01×10^{-2}	2.400	1.880	1.23×10^5	3.50×10^5	[5]; ALL
[Mg V]	5.61	$^3P_1 \rightarrow ^3 P_2$	8.09×10^{-2}	0.556	0.808	1.60×10^6	2.46×10^6	[6]; ALL
[Mg VII]	5.50	$^3P_2 \rightarrow ^3 P_1$	1.27×10^{-1}	0.704	0.768	3.31×10^6	6.77×10^6	[4]; ALL
[S IV]	10.51	$^2P^0_{3/2} \rightarrow ^2 P^0_{1/2}$	7.74×10^{-3}	5.50	7.905	2.06×10^4	3.21×10^4	[7]; ALL
[Ar III]	8.99	$^3P_2 \rightarrow ^3 P_1$	3.09×10^{-2}	3.88[c]	3.84[c]	1.46×10^5	3.30×10^5	[8]; ALL

[a]The first reference is for Υ_{ij} and the second is for A_{ij}. The NIST database is located at http://physics.nist.gov/PhysRefData/ASD/lines_form.html. The Atomic Line List version 2.05b12 (ALL) is located at http://www.pa.uky.edu/∼peter/newpage/.

[b]REFERENCES: [1] - Blum & Pradhan (1992); [2] - Saraph & Tully (1994); [3] - McLaughlin & Bell (2000); [4] - Lennon & Burke (1994); [5] - Zhang et al. (1994); [6] - Hudson et al. (2009); [7] - Tayal (2000); [8] - Munoz Burgos et al. (2009)

[c]These values were obtained by linear interpolation of the data reported by Munoz Burgos et al. (2009).

The total number of atoms in the ionization state in question is simply the sum of the populations of the two excitation states, $N_i + N_j$. If some of the transitions arising from the upper excitation state are not observed, then the derived population will be a lower limit only.

We derive the abundances of metallic species in the ejecta by number relative to hydrogen. Comparison of the sum of the numbers of all population levels of an given species to the total number of hydrogen atoms yields the ion abundance of that species by number in the ejecta. We then compare these ionic abundances to the total solar abundances as presented by Asplund et al. (2009). The logarithmic solar abundances are: He = -1.07; O = -3.31; Ne = -4.06; Mg = -4.40; S = -4.88; Ar = -5.60; and Fe = -4.50. The abundances we determine for the novae in our sample are necessarily lower limits since we calculate the abundances by number only from the ions observed within the limited bandpass of our IRS/Bok spectra.

As noted in G08, one of the limitations of this undertaking is that the present observations no longer contain any signatures of hydrogen recombination emission. This means that we have no way to derive a direct comparison between the observed emission lines and the emitting population that they imply to the amount of hydrogen within the ejecta. Thus, we are forced to rely on determining the ejected hydrogen mass using information obtained at earlier epochs. This source of uncertainty dominates our estimates of the elemental abundances with respect to hydrogen. The accuracy of this method of determining abundances presumes that the amount of hydrogen in the ejected shell remained roughly constant since the early stages of the development of the ejecta following outburst.

4.3.1 Emission Lines

Each of the targets in our sample exhibited [O IV] emission at 25.91 μm. Indeed, this transition has been observed in every *Spitzer* CN target to date (e.g., V1186 Sco, V1187 Sco, V1065 Cen; Schwarz et al. 2007b; Lynch et al. 2006a; Helton et al. 2010b, respectively). This line arises due to the transition from

the $^2P^0_{3/2}$ level to the $^2P^0_{1/2}$ ground state. Though the production of the O^{3+} ion responsible for this line is produced through photoionization, the excitation from the ground state to the upper $^2P^0_{3/2}$ level is due primarily to collisional interactions (see Gehrz 1990, and references therein). The excitation energy of this transition is only 0.048 eV allowing it to be easily excited through collisions. This is the only measurable transition of [O IV] in the optical to IR regime.

Optical observations of both V1974 Cyg and V1494 Aql revealed emission from [O III] $\lambda\lambda$4959, 5007 Å. This doublet, also common in CNe, is due to transitions from the $^1D_2$ level to the ground state levels $^3P_1$ and $^3P_2$ for the 4959 and 5007 Å transitions, respectively. Since they arise from the same upper level, the ratio of these two lines is fixed by their transition probabilities at 5007Å:4959Å = 3. Another prominent [O III] line occurs at 4363 Å due to a transition from the $^1S_0$ to the $^1D_2$ level. Since the 4363 transition has a higher spontaneous emission coefficient than the 4959, 5007 Å doublet lines ($A_{ji} = 1.71 \times 10^0$ s^{-1} for 4363 Å compared to $A_{ji} = 6.21 \times 10^{-3}$ and $A_{ji} = 1.81 \times 10^{-2}$ s^{-1} for 4959 and 5007 Å, respectively), it is more likely to radiatively de-excite for a given density than the other lines. Consequently, the ratio 4363Å:(4959 + 5007)Å can be used as a diagnostic of temperature and density. The primary complication is that the 4363 Å line has a higher excitation energy than the 4959, 5007 doublet (5.35 eV versus 2.51 eV) and consequently is less likely to be collisionally excited in low density, cool gas.

Numerous species of neon appear in our spectra, including [Ne II] λ12.81 μm, [Ne III] λ15.56 μm, [Ne V] λ 14.32, λ24.30 μm, and [Ne VI] λ7.61 μm. In other novae, these transitions have all been observed simultaneously arising in regions of the ejecta having different densities and temperatures. Once the central source turns off, the radiative recombination timescale will depend upon the abundance of the element in the ejecta, the initial ionization fraction, and the densities in the ejecta. The excitation energies for these transitions are all quite low, and they all arise from ground state excitation, making them relatively easy to excite collisionally.

4.4 Null Detections

As part of our old nova initiative, we observed the venerable novae GK Per, V1500 Cyg, NQ Vul, and V1668 Cyg. These observations detected no emission lines at signals above the noise level and only negligible continuum. Hence, they will be excluded from further discussion.

4.5 V1974 Cyg (Nova Cygni 1992)

V1974 Cyg (Nova Cygni 1992) was discovered before maximum light by Collins (1992) on 1992 February 19.1UT at a magnitude of $m_V = 6.8$. The nova reached maximum on 1992 February 20.8UT (JD 2448673.3), which we take to be t_0, at m_V=4.3 (Schmeer 1992). The exceptionally bright outburst of V1974 Cyg allowed an unprecedented degree of coverage. Initially, the light curve showed slight variations that complicated the determination of the t_2 times, the time it took the V-band light curve to decay by two magnitudes. The most reliable estimates ranged from $16 \leq t_2 \leq 18$ days with high end estimates nearer to 24 days. A summary of estimates is provided by Chochol et al. (1997) with additional estimates by Austin et al. (1996) and Quirrenbach et al. (1993). These estimates situate the nova in the "moderately fast" class of CNe (Gaposchkin 1957). Some fundamental properties of V1974 Cyg are summarized in Table 4.4 along with properties of the other targets to be presented in this chapter.

The detection of Fe II, with accompanying permitted emission from species such as Ca II, Mg II, N II, Na I, and O I (Baruffolo et al. 1992; Chochol et al. 1993), identified this an "Fe II"-type nova. Both the principal and diffuse-enhanced components of the P-Cygni profiles were observed in Hβ from very early in the outburst with velocities of -910 and -1670 km s^{-1}, respectively (Garnavich 1992). Later analysis of these absorption components revealed that they accelerated with terminal velocities, $v_\infty = 1975 \pm 5$ km s^{-1} for the principal system and 2899 ± 8 km s^{-1} for the diffuse-enhanced system (Cassatella et al. 2004).

Table 4.4: Fundamental Properties

Target	RA (J2000.0)	Dec (J2000.0)	t_{max}	$m_{V,max}$	t_2	t_3	Speed Class	Type
V382 Vel	$10^h44^m48^s.37$	-52°25'30".6	1999 May 22.4UT	2.6	4-6	9-10	Fast	Fe IIb; ONe
V1494 Aql	$19^h23^m05^s.28$	+04°57'21".6	1999 Dec. 03.4UT	4.0	6.6	16	Fast	Fe II; CO?
V1974 Cyg	$20^h30^m31^s.66$	+52°37'51".3	1992 Feb. 20.8UT	4.2	19	47	Fast	Fe II; ONe

Gehrz et al. (1992a) detected emission from [Ne II] λ 12.81 μm just over a week post-outburst and subsequent observations of neon emission in the optical prompted Austin et al. (1996) to classify V1974 Cyg as an ONe nova. [Ne II] and other mid-IR lines exhibited FWHM velocities of $\sim$ 3000 km s^{-1} (Gehrz et al. 1992b), comparable to that of the diffuse-enhanced system.

V1974 Cyg transitioned into the coronal stage of nebular development within $\sim$ 150 days of outburst with the emergence of [Ne V] $\lambda\lambda$ 3346, 3426 Å (Barger et al. 1993) followed by the detection of numerous coronal lines in the IR, including [Al VI] λ 3.661 μm, [Al VIII] λ 3.720 μm, [S IX] λ 1.250 μm, [Mg VIII] λ 3.028 μm, and [Ca IX] λ 3.088 μm (Woodward et al. 1995). There was no evidence for significant dust production in the ejecta.

Our data were obtained 11.8, 14.7, and 15.5 years after outburst. The *Spitzer* spectra showed emission only from [Ne II] λ12.81 μm, [Ne III] λ15.56 μm, and [O IV] λ25.91 μm. The profiles of these lines are presented in Figure 4.1. The signal to noise (S/N) for all of the observations of [Ne II] and the last two epochs of [Ne III] is very low, making accurate determination of flux values and characterization of the profiles difficult. On the other hand, the first observation of [Ne III] and all three observations of [O IV] have very good S/N. The resolution of the *Spitzer* SH and LH modules is $R \approx 600$, yielding a resolution element of $\sim$ 500 km s^{-1}. This means that the observed emission lines having FWHM velocity widths $>$ 2100 km s^{-1} are resolved and the structure seen in the profiles of these lines is real. There are distinct differences between the rounded shape of the neon emission profiles and the flat-topped profiles of the oxygen lines. These differences imply that these lines may originate in regions of the ejecta having different physical and dynamical structure. Further, the long term stability in the shape of the [O IV] line indicates that the ejecta were no longer subjected to shaping effects at late times.

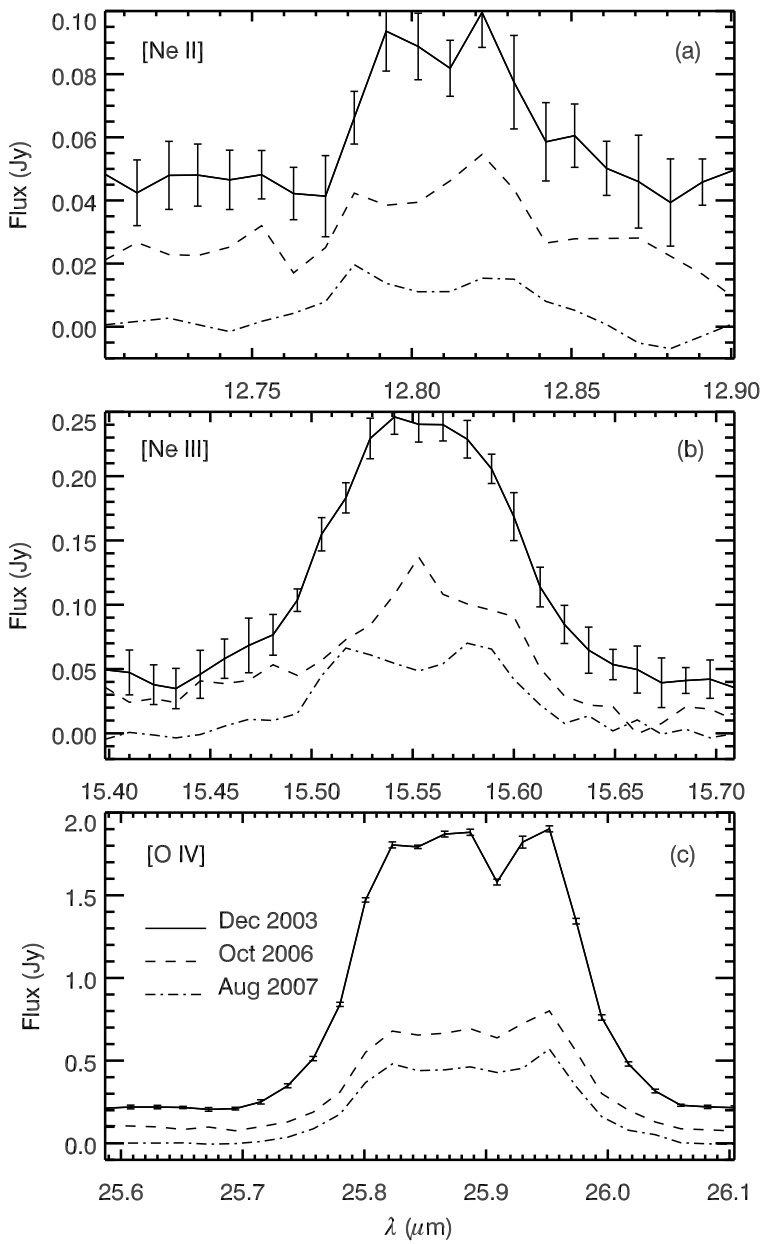

Figure 4.1: V1974 Cyg: Emission lines observed at three different epochs. Representative errors are shown on the first epoch data and are comparable for the next two epochs. *Panel (a)*: [Ne II] λ12.81 μm *Panel (b)*: [Ne III] λ15.56 μm *Panel (c)*: [O IV] λ25.91 μm

4.5.1 V1974 Cyg - Adopted Values

The distance to V1974 Cyg has been estimated using several methods. A thorough discussion of selected estimates is presented by Chochol et al. (1997) who calculate a weighted mean distance of 1.77 ± 0.11 kpc. This mean value, however, relied heavily on various forms of the maximum magnitude-rate of decline relation (MMRD), which may be unreliable for ONe novae (Del Pozzo 2005). There are, however, other distance estimates that were not included in their mean distance calculation and that utilized the more reliable expansion parallax method of distance estimation. Among these is an estimate by Shore et al. (1994) based upon the interferometric measurement of Quirrenbach et al. (1993) but using a flux-weighted expansion velocity of ∼2000 km s^{-1}, which they claim is a better representation of the ejecta giving rise to the Hα emission. This velocity leads to an estimated distance of 2.3-4.6 kpc. The expansion parallax based upon the data of Quirrenbach et al. (1993) was also recalculated by Cassatella et al. (2004) using the ejecta radius calculated from their fit to the velocity law of the principal absorption system yielding a distance of 2.9 ± 0.2 kpc. Finally, Krautter et al. (2002) made an independent calculation of the expansion parallax from HST images assuming v_{exp} = 2900 km s^{-1} and found a distance of d = 3.72 kpc. In Table 4.5 we present the distance estimates using the expansion parallax methods and calculate a new weighted mean distance of 3.0 ± 0.2 kpc, which we use for subsequent analysis.

A few authors have estimated the mass of ejecta generated in the outburst of V1974 Cyg. Shore et al. (1993) used early spectroscopic observations of He II λ1640 Å to determine the helium enhancement dependent ejecta mass. They calculated that $M_{ej} = (1-4)\times10^{-4}Y^{-1/2}$ $M_\odot$, where $Y^{-1/2}$ is the enhancement factor for the He abundance. Using this relationship and the results for the He abundance from their CLOUDY models of optical and UV data, Vanlandingham et al. (2005) estimated an ejecta mass of $M_{ej} = 1.9 \times 10^{-4}$ $M_\odot$. These authors also calculated the mass of ejecta directly from their CLOUDY models for three different dates and obtained a weighted mean $M_{ej} = (2.2 \pm 0.1) \times 10^{-4}$ $M_\odot$. We adopt

2×10^{-4} $M_{\odot}$ for our analysis.

Table 4.5: Distance Estimates for V1974 Cyg

Reference	Distance (kpc)	Method
Cassatella et al. (2004)	2.9 ± 0.2	Expansion Parallax
		Quirrenbach et al. (1993)
Krautter et al. (2002)	3.72 ± 0.55^{a}	Expansion Parallax
Shore et al. (1994)	2.3-4.6	Expansion Parallax
Weighted Mean	3.0 ± 0.2	

[a]The error used in the weighted mean calculation is based upon the spread in adopted values of v_{exp}.

Based upon the behavior of the P-Cyg absorption components, we take the values of the minimum and maximum expansion velocities to be $v_{min} = 2000$ and $v_{max} = 3000$ km s^{-1}. Observations of the emission lines observed throughout the first $\sim$ 500 days of the evolution in the near-IR indicated that the emission line widths remained nearly constant at 2500 - 3000 km s^{-1} (Woodward et al. 1995). The mid-IR neon lines observed with *Spitzer* and presented here exhibited a similar width. Hence, we take v_{max} to be robust.

Early after outburst (day 23.5), Woodward et al. (1995) estimated the electron temperature to be $T_e \sim 5000$ K. After 180 days of expansion, they estimated that ejecta temperature had declined to $\sim$ 1000 K. Krautter et al. (2002) observed V1974 Cyg 2184 days after eruption (JD 2450855) with the *Hubble Space Telescope* using the Near-Infrared Camera and Multi-Image Spectrometer (NICMOS). They obtained narrow-band imaging of the hydrogen recombination lines Paschen-α and Brackett-γ as well as associated continuum. Using their results, we estimate a line ratio of [H I (7-4) / H I (4 - 3)] = $(4.90 \pm 0.57) \times 10^{-2}$. Comparison of this ratio to that predicted for Case B recombination by Hummer & Storey (1987)

confirms that the electron temperature is less than 1000 K and that the electron density is less than 1000 cm^{-3}. Based upon the hydrogen recombination line ratio from day 2814 and the earlier temperature estimates by Woodward et al., we chose temperature estimates of 1000 and 5000 K with which to calculate the abundances in the ejecta. A summary of the parameters used in our analysis for all three targets presented in this chapter is provided in Table 4.6.

Table 4.6: Adopted Parameters

Parameter	V1974 Cyg	V382 Vel	V1494 Aql
D (kpc)	2.1	2.3	1.6
M_{ej} $(M_\odot)^a$	2×10^{-4}	4×10^{-4}	2.5×10^{-5}
v_0 (km s^{-1})^b	3000	3000	2900
v_0 (km s^{-1})^c	2000-3000	2000-3000	980-2900
T_e (K)	1000-5000	1000-5000	1000-5000
n_e (cm^{-3})	60-150	1100-4000	400-1750

[a]See text for discussion of the M_{ej} values used.

[b]This is the value used to calculate the volume of a spherical shell assuming $\Delta r/r \sim 0.1$.

[c]These are the values used to calculate the shell volume for other geometries as described in the text.

4.5.2 V1974 Cyg - Abundance Calculations

The results of our analysis are presented in Table 4.7.We calculated the electron density assuming two different geometries, a spherical shell of material expanding at 3000 km s^{-1} with a shell depth of $\Delta r = 0.1r$, and a spherical shell with $v_{min} = 2000$ km s^{-1} and $v_{max} = 3000$ km s^{-1}. Assuming an electron temperature, T_e, of 1000 K, we found a minimum neon ionic abundance by number of 45 times

solar. Assuming a temperature of 5000 K resulted in a relative abundance only marginally lower at 39 times solar. The oxygen abundance was found to be more than 10 times solar. Relative to O^{3+}, (Ne^{2+} + Ne^{3+}) was found to be more than 3.9 times solar. The shell geometries used in each calculation dominated the abundance estimates. In the low density model ($n_e = 60$ cm^{-3}), the derived abundances were higher than the high density model ($n_e = 150$ cm^{-3}) by a factor of ~ 2.5. The abundance estimation is much more sensitive to the assumed n_e than T_e.

These abundance estimates correspond well to the abundances derived from earlier observations by other authors. Vanlandingham et al. (2005) modeled an extensive set of data using the CLOUDY photoionization code and found that V1974 Cyg was overabundant in oxygen relative to solar by a factor of 12.8 ± 7 and neon by 41.5 ± 17. Gehrz et al. (1994) used observations of [Ne VI] λ7.62 μm and [Si VI] λ 1.959 μm to estimate the abundance of neon to silicon by number relative to solar. Under the assumption that the neon to silicon abundance is roughly equivalent to the neon to hydrogen abundance, they found the neon abundance relative to hydrogen to be $\sim$ 10 times solar. Salama et al. (1996) used IR observations of [Ne III] and [O IV] to determine the ratio of Ne/O, which they found to be $\sim$ 4 times solar. Paresce et al. (1995) used narrow band HST images and objective prism spectroscopy to estimate the abundances in a single knot of ejecta in the shell of V1974 Cyg. Their CLOUDY analysis suggested that neon was 20-30 times overabundant relative to solar in the knot, helium was a factor of 2 higher, and oxygen, their least constrained estimate, was 2-4 times solar. Shore et al. (1997) also estimated the abundances in a single knot based upon high resolution spectroscopy and found [He/H]=0.3, [O/H]=6.9, [Ne/H]=15.6, and [Fe/H]=1.0. The abundance estimates derived here for neon and oxygen using the late-time *Spitzer* spectra are consistent with those derived much earlier in the outburst.

Table 4.7: Abundances by Number Relative to Solar - V1974 Cyg

Species	Wavelength (μm)	Module	Line Flux (erg cm^{-2} s^{-1})	n_e (cm^{-3}): T_e (K):	Derived Abundances[a] 60 1000	60 5000	150 1000	150 5000
[Ne II]	12.81	SH	4.60×10^{-14}		-2.72	-2.76	-3.13	-3.18
[Ne III]	15.56	SH	2.80×10^{-13}		-2.10	-2.16	-2.51	-2.58
Total Neon					-2.00 (117)	-2.07 (101)	-2.41 (44.9)	-2.48 (39.0)
[O IV]	25.91	LH	1.49×10^{-12}		-1.91 (24.8)	-1.85 (28.7)	-2.31 (10.0)	-2.25 (11.5)

[a]The number given is the log abundance by number relative to hydrogen. The number in parentheses is the abundance by number relative to hydrogen, relative to solar assuming the solar values of Asplund et al. (2009).

4.6 V382 Vel (Nova Velorum 1999)

V382 Vel (Nova Velorum 1999) was discovered by P. Williams, and independently by Gilmore on 1999 May 22.4UT (JD 2451320.9) at a magnitude of $m_V = 3.1$ (Lee et al. 1999) and reached a maximum a day later on May 23, which we take to be t_0, near $m_V \sim 2.3$ (Della Valle et al. 2002). The light curve decay was very rapid and smooth with decay times of $t_2 = (4.5 - 6)$ and $t_3 = (9 - 12.5)$ (Della Valle et al. 1999; Liller & Jones 2000) suggesting that V382 Vel was a "very fast" nova (Della Valle et al. 2002; Gaposchkin 1957). A summary of the photometric characteristics is provided by Della Valle et al. (2002). System properties are provided in Table 4.4.

Della Valle et al. (2002) reported on the optical spectroscopic evolution of V382 Vel. Initial observations revealed a complex spectrum with prominent permitted Fe II emission and hydrogen Balmer lines. Though additional emission from Na I, Al II, Mg II, and Ca II were present, the strongest lines were from O I λ7773 Å and O I λ8446 Å. The emission lines displayed strong P-Cyg absorption components a terminal velocities of 2300 and 3700 km s^{-1}, characterizing the "principal" and "diffuse enhanced" absorption systems respectively (Della Valle et al. 2002). The emission lines were broad (HWZI $\gtrsim$3500 km s^{-1}) and relatively flat-topped, suggesting that they originated in a discrete shell. The broad line widths of the iron lines indicated that this was an "Fe IIb" (broad) type CN (Steiner et al. 1999; Della Valle et al. 1999).

Within a month, the system transitioned into the nebular stage with the appearance of [O III] $\lambda\lambda$4959, 5007 Å, He I λ4471, 6678, and 7065 Å, He II λ5876 Å, and [N II] λ5755 Å (Della Valle et al. 2002). During the early nebular stage, the UV emission was still within the "iron curtain" stage and consequently optically thick. As this stage faded, P-Cyg absorption components remained in evidence on the resonance lines with absorption maxima near 5000 km s^{-1}. This behavior is consistent with the behavior of other ONe novae such as V1974 Cyg (Shore et al. 2003). Further support for the classification of V382 Vel as an ONe nova was the

detection of prominent [Ne II] λ12.81 μm emission at 43.6 days after maximum (Woodward et al. 1999). At this stage of development, there was still emission evident from H I (9-7) and (7-6) with a FWHM velocity of 3300 km s^{-1} for H I (7-6). The relative line fluxes were found to be H I (9-7)/H I (7-6) = 0.5 and [Ne II]/H I (7-6) = 3.4.

Late in the nebular stage, the overall state of ionization in the ejecta increased. The optical spectra exhibited emission from [Ne IV] λ4721 Å, additional lines of He II at 5412 and 7593 Å, and strong emission from [Fe VI] λ 5677 Å and [Fe VII] λ5158, 5276, and 6087 Å. More importantly, the ejecta also showed emission from [Fe X] λ6375 Å (Della Valle et al. 2002), which is commonly seen in novae that are in the super-soft source stage (SSS) of X-ray development (Ness et al. 2007b). Indeed, Beppo-SAX observations of V382 Vel taken during this same period found that it had transitioned from an early stage of hard X-ray emission into a relatively strong SSS (Orio et al. 1999a,b). There was no evidence for dust production.

The *Spitzer* data were obtained 8.6, 11.5, and 12.4 years after outburst (Table 4.1) and are presented in Figures 4.2 and 4.3. The first epoch spectra were dominated by [Ne II] λ12.81 μm, [Ne III] λ15.56 μm, and [O IV] λ25.91 μm. Emission lines of [Ne V] were present at 14.32 μm and 24.30 μm, but at a much lower level than the other neon species. No [Ne VI] λ7.61 μm emission was detected. There was also evidence for weak features of [S IV] λ10.51 μm and [Ar III] λ8.99 μm. Subsequent observations detected only emission from [Ne II], [Ne III], and [O IV].

Emission from [Ne II] λ12.81 μm was relatively strong with a castellated shape that persisted throughout our observations. The [Ne III] λ15.56 μm emission was exceptionally strong. The castellated structure in this feature was less well defined, but was similar to the [Ne II] line in that it was dominated by a blue-ward peak. The [Ne V] lines at 14.32 and 24.30 μm were strong only during the first epoch of observations after which they were no longer detected. Their line profiles were rounded, distinctly different than the [Ne II] and [Ne III] lines. The [O IV] λ25.91 μm line was the strongest in the spectra. The profile shape was rounded like the [Ne V] lines. The [S IV] λ10.51 μm line was barely detected. Due to the

low signal-to-noise in this line, its line profile is not well defined.

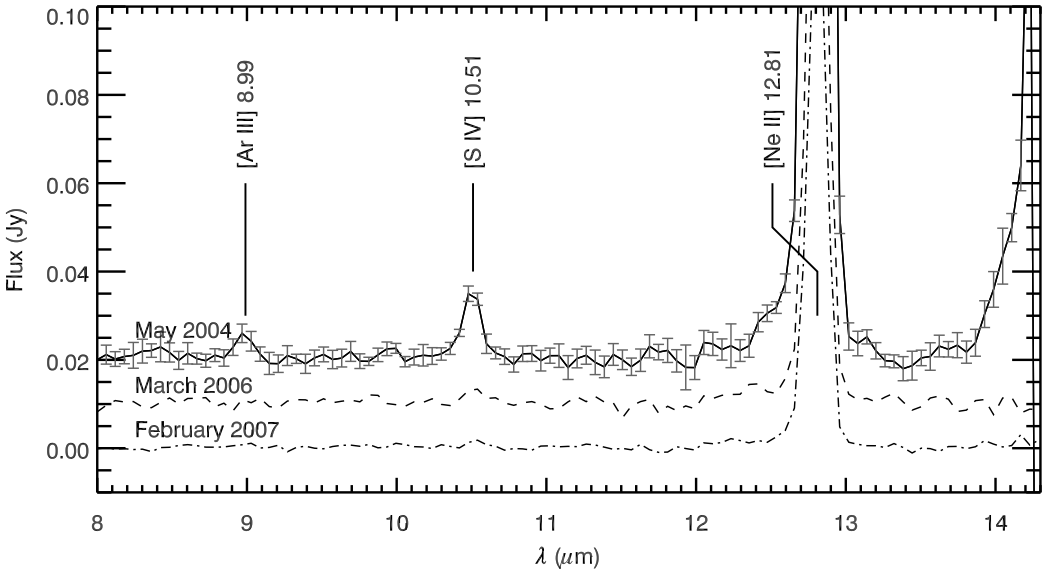

Figure 4.2: V382 Vel: *Spitzer* SL spectra of V382 Vel obtained on 2004 May 14, 2007 March 26, and 2008 February 25. Prominent emission lines are labeled. The strong feature beyond 14 μm in the 2004 May spectrum is due to [Ne V] λ14.32. The shape of this feature in this spectrum is not well characterized due to its proximity to the end of the spectral range of the SL module.

The spectral profiles of the emission lines fell into two distinct classes. The [Ne II] and [Ne III] lines both showed castellated profiles with a stronger blue-ward peak. Emission in the [Ne V] and [O IV] lines all showed a smooth, rounded profile, more akin to that expected for a spherical distribution of material. The profile shapes were stable throughout the late time observations. The difference in the line shapes of the low ionization lines in comparison to the high ionization lines may imply that they arise in physically distinct regions of the ejecta. Indeed, the [Ne III] profile exhibits characteristics intermediate between those of [Ne II] and [Ne V] transitions, possibility indicating ionization gradients in the ejecta. Based upon the profile shapes, we hypothesize that the [O IV] emission is arising from the same region in the ejecta as the [Ne V] emission.

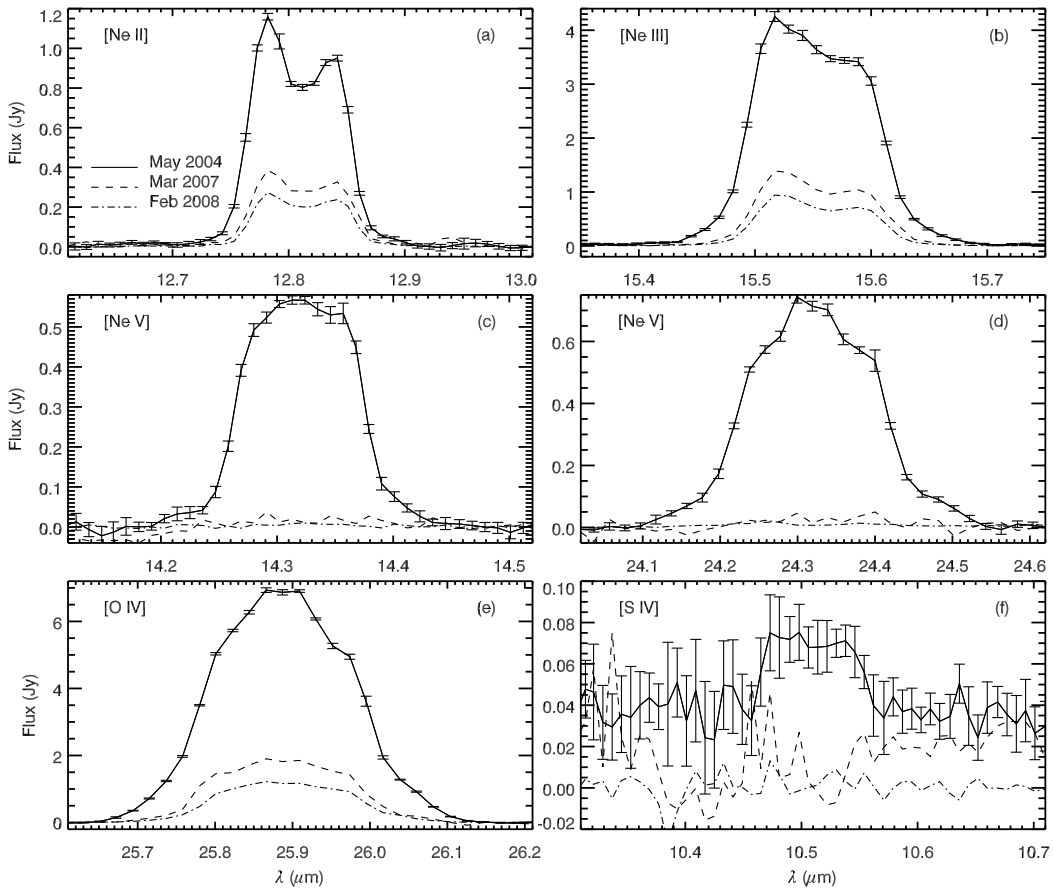

Figure 4.3: V382 Vel: Emission lines observed at three different epochs in the *Spitzer* high resolution modules. Representative errors are shown on the first epoch data and are comparable for the next two epochs. *Panel (a)*: [Ne II] λ12.81 μm *Panel (b)*: [Ne III] λ15.56 μm *Panels (c-d)*: [Ne V] lines at 14.32 and 24.30 μm *Panel (e)*: [O IV] λ25.91 μm *Panel (f)*: [S IV] λ10.51 μm

4.6.1 V382 Vel - Adopted Values

The distance to V382 Vel has been fairly well constrained. Della Valle et al. (2002) estimated a distance of D∼1.7 kpc using the maximum MMRD relationship derived by Della Valle & Livio (1995) and a decay time of t_2=4.5 days. As discussed above, this mechanism of distance estimation should be used with caution in the case of ONe-type novae (§4.5.1). Alternatively, Shore et al. (2003) found a lower limit to the distance of 2 kpc based on ^{12}CO absorption and an upper limit of 3 kpc via comparison to novae of very similar spectroscopic behavior, V1974 Cyg and Nova LMC 2000. Other estimates included comparison of He II line flux to that derived by CLOUDY models, a luminosity estimate from UV continuum measurements, and an estimate based upon the quiescent magnitude of the system. Their derived distances converged near 2-2.5 kpc, hence, for the following analysis, we assume a distance of 2.3 kpc.

The mass of hydrogen in the ejecta has been estimated using a variety of methods. Shore et al. (2003) estimated an ejected mass of $M_{ej} = (4 - 5) \times 10^{-4}$ $M_\odot$ based upon photoionization models of their UV spectra. In comparison, Della Valle et al. (2002) derived a mass of 6.5×10^{-6} $M_\odot$ using the luminosity of Hα assuming a distance of 1.7 kpc. Scaling this estimate to a distance of 2.3 kpc results in a mass of $\sim 10^{-5}$, $M_\odot$. Though there are undoubtedly significant uncertainties in both methods, the more thorough treatment by Shore et al. is likely more reliable. Consequently, we assume a mass of 4×10^{-4} $M_\odot$ for the ejecta.

In order to adequately constrain electron density in the shell, we must determine the appropriate expansion velocity of the emitting region. The presence of [Ne II] λ12.81 μm, [Ne III] λ15.56 μm and λ36.0 μm alongside [Ne V] λ14.3 μm and λ24.3 μm plus [Ne VI] λ7.6 μm suggests that the ejecta are divided into two distinct emitting regions, likely a diffuse, high velocity region and a dense, low velocity region. This velocity structure may be common in CNe (cf. V1065 Cen, Helton et al. 2010b; Vanlandingham et al. 2005). In the following analysis, we present two cases assuming a spherical shell defined by a minimum expansion

velocity of v_{min} = 1000 km s^{-1} and a maximum of v_{max} = 3000 km s^{-1} and a spherical shell defined by an expansion velocity of v_{avg} = 3000 km s^{-1} and a thickness of $\Delta r = 0.1r$.

The UV spectra revealed a wide array of emission lines, most of which had line structure consistent with a clumpy, flattened, ring-like shell of ejecta having a thickness to radius ratio of 0.5. There was also evidence for an asymmetric, high velocity diffuse component with a HWZI $\sim$ 2000 km s^{-1} (Shore et al. 2003).

4.6.2 V382 Vel - Abundance Calculations

In Table 4.8 we have present the calculated elemental abundances by number relative to solar for the observed neon, oxygen, argon and sulfur lines for four different combinations of electron density and temperature. The calculated abundance solutions depend more strongly on the electron number density than on the electron temperature. The derived abundance of neon, calculated by combining the implied abundances from each of the observed emission lines, ranges from 11 times solar at a temperature of 5000 K and an electron density of 4000 cm^{-3} (13 times solar at 1000 cm^{-3}) to 39 times solar at T = 1000 K and 4000 cm^{-3} (44 times solar at 1000 cm^{-3}). The oxygen abundance was at least 1.4-3.0 times solar depending upon the density assumed. These abundance estimates are lower limits as they include only a small fraction of the true emission from each element.

Shore et al. (2003) used the CLOUDY photoionization code to model the emission lines observed in UV spectra obtained 110 days post-outburst. Their results suggested that carbon and silicon were of roughly solar abundance, while nitrogen, oxygen, neon, magnesium and aluminum were all significantly overabundant. They derived oxygen, neon, and magnesium abundances by number relative to solar of 3.4 $\pm$ 0.3, 17 $\pm$ 3, and 2.6 $\pm$ 0.1 respectively. However, the Shore et al. abundance solutions were calculated under the assumption that the helium abundance was 1.0 relative to solar. Accordingly, if the helium abundance was in fact less than solar, the modeled metal abundances would be underestimated.

Table 4.8: Abundances by Number Relative to Solar - V382 Vel

Species	Wavelength (μm)	Module	Line Flux (erg cm^{-2} s^{-1})	n_e (cm^{-3}): T_e (K):	Derived Abundances[a] 1100 1000	1100 5000	4000 1000	4000 5000
[Ne II]	12.81	SL[b]	1.71×10^{-12}		-2.97	-3.02	-3.51	-3.56
		SH	1.66×10^{-12}		-2.98	-3.03	-3.53	-3.57
[Ne III]	15.56	SH	6.12×10^{-12}		-2.58	-2.64	-3.12	-3.18
[Ne V]	14.32	SH	9.70×10^{-13}		-4.50	-4.44	-4.90	-4.84
	24.30	LH	6.90×10^{-13}		-4.30	-4.16	-4.61	-4.50
Total Neon					-2.42 (43.4)	-2.48 (38.2)	-2.96 (12.6)	-3.01 (11.2)
[O IV]	25.91	LH	7.01×10^{-12}		-2.89 (2.6)	-2.84 (3.0)	-3.17 (1.4)	-3.13 (1.5)
[Ar III]	8.99	SL	3.89×10^{-13}		-6.06 (0.35)	-6.26 (0.22)	-6.59 (0.10)	-6.79 (0.07)
[S IV]	10.51	SL	6.88×10^{-14}		-5.61	-5.89	-6.09	-6.39
		SH	7.52×10^{-14}		-5.58 (0.20)	-5.85 (0.11)	-6.04 (0.07)	-6.35 (0.03)

[a]The number given is the log abundance by number relative to hydrogen. The number in parentheses is the abundance by number relative to hydrogen, relative to solar assuming the solar values of Asplund et al. (2009).

[b]When both high and low resolution data are available, we preferentially select the high res data for the estimation of the total abundances.

An illuminating comparison can be made between the spectroscopic behavior of V382 Vel and V1065 Cen. The light curve decay of V1065 Cen was similar with $t_2 = 11$ days and $t_3 = 26$ days, as was its optical spectral development, which exhibited most of the same emission lines and very similar line structure to that observed in V382 Vel. IR spectra of V1065 Cen were obtained at nearly the same stage in evolution, and they too exhibited strong [Ne II] λ12.81 μm emission. The ratios of [Ne II]/H I (7-6) on days 47.5, 57.7, and 64.9 were 11.0, 10.3, and 11.5, respectively, a factor of 3 higher than that observed in V382 Vel (Helton et al. 2010b).

4.7 V1494 Aql (Nova Aquila 1999 NO. 2)

V1494 Aql was discovered by A. Pereira on 1999 December 1.785 UT at a pre-maximum visual magnitude of $m_V \sim 6.0$ (Pereira et al. 1999). Kiss & Thomson (2000) analyzed subsequent photometric observations and reported that the nova reached maximum at $m_V = 4.0$ magnitudes roughly one day later on December 3.4 UT (t_0; JD 2451515.9). They found that the light curve declined rapidly with $t_2 = 6.6 \pm 0.5$ days and $t_3 = 16.0 \pm 0.5$ days, which situates the nova in the "very fast" speed class of Gaposchkin (1957). The light curve was initially smooth, but during the transition stage, it exhibited strong oscillations of ~ 1.2 magnitudes in V-band with a period of approximately 16.5 ± 0.1 days (Iijima & Esenoğlu 2003). There was no evidence for dust production in the ejecta. System properties are provided in Table 4.4.

Optical spectroscopy during the early stages of development revealed a strong hydrogen recombination spectrum along with emission from O I λ7773 Å and Fe II, the latter resulting in the classification of V1494 Aql as an "Fe II"-type nova. Strong P-Cygni absorption components were observed on the Balmer series at -1850 km s^{-1} (Fujii 1999) and weaker absorption systems on the O I and Fe II lines at velocities of -1020 km s^{-1} (Moro et al. 1999). Iijima & Esenoğlu (2003) calculated a mean expansion velocity from the absorption components of

-2510 km s^{-1}. Within a few days of maximum, the P-Cyg absorption components disappeared, leaving behind bullet shaped emission lines characteristic of an optically thin wind (Anupama et al. 2001; Kamath et al. 2005). These emission lines rapidly developed a double peaked, saddle-shaped structure that was attributed to an equatorial-ring/polar-cap morphology of the ejecta (Kiss & Thomson 2000; Anupama et al. 2001) based upon the synthetic models of Gill & O'Brien (1999). Spectropolarimetric observations very early in the evolution supported the conclusion that the ejecta were asymmetric and that the asymmetry was likely established during the pre-maximum rise (Iijima & Esenoğlu 2003). The fine scale structure in the saddle-shaped profiles of [O III], [N II], and Hβ was nearly identical, indicating that these lines formed from the same location in the ejecta and that they likely characterize the emitting region as a whole quite well.

The system evolved to the coronal stage by about 150 days after outburst with the appearance of [Fe X] at a level greater than [Fe VII] in the optical (Kamath et al. 2005). Interestingly, at the onset of the coronal stage, bullet-shaped line profiles were observed in N II and N III in striking contrast to the saddle-shaped profiles, which persisted in the nebular lines (Iijima & Esenoğlu 2003). As the coronal spectrum matured, emission lines from He II and the highly ionized species of iron, such as [Fe X], and [Fe XI] appeared also with smooth, bullet-shaped profiles. This suggests that there may have been an additional spherically symmetric component in the ejecta. The optical spectra during this stage were dominated by [O III] and numerous forbidden iron lines. Though there was a weak signature of emission from sulfur, at no point in the evolution of V1494 Aql was there clear evidence for emission by neon.

The underlying radiation at this stage in development was extremely energetic. Mazuk et al. (2000) reported emission from [S IX] λ1.2523 μm on day 226, which has an ionization potential of 329 eV, while Rudy et al. (2001) observed [S XI] λ1.9196 μm (447 eV) on day 580. X-ray observations indicated that during this period the underlying source exhibited characteristics similar to super-soft sources (Drake et al. 2003; Rohrbach et al. 2009).

We obtained three epochs of mid-IR observations as part of our *Spitzer* CN monitoring campaign. These data were obtained roughly 4.4, 7.5, and 7.9 years after maximum. The spectra are shown in Figures 4.4 and 4.5. The *Spitzer* spectra are dominated by emission lines of [O IV] at 25.91 μm, [Ne V] λ14.32, λ24.30 μm, and [S IV] λ10.51 μm. There is also weak emission from [Ne VI] λ7.61 μm, [Mg V] λ5.61 μm, and possibly [Mg VII] λ5.50 μm.

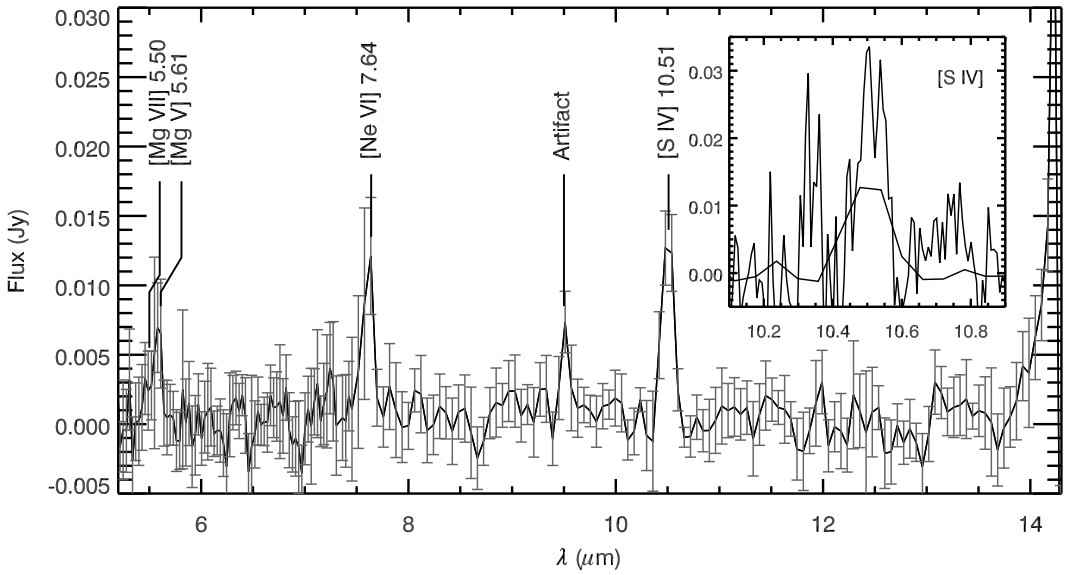

Figure 4.4: V1494 Aql: *Spitzer* SL spectra of V1494 Aql obtained on 2004 April 14. Prominent emission lines are labeled. *Inset*: Comparison of the region around [S IV] λ10.51 μm in the SL module to the SH module. Since the SH data were not background corrected, they were offset to match the continuum level of the SL data.

The presence of strong neon in emission at these late times is particularly interesting since neon was not observed in the optical at any time during the early development. A clue to origin of the neon lines is obtained by examination of the line profiles. The oxygen line at 25.91 μm has the same saddle-shaped structure present in most of the optical and near-IR emission lines reported during the first few hundreds of days post-outburst. The neon lines, on the other hand, have a

smooth bullet-shaped profile, similar to the profiles of the He II and highly ionized iron lines observed during the coronal stage. Fast novae exhibiting characteristics similar to those seen in V1494 Aql are often found to have arisen on ONe WDs. If the abundance of neon in the ejecta is low, then early in the evolution, the optical emission lines may have been obscured by other lines. As the ejecta were exposed to the SSS emission, the neon may have been very rapidly ionized to higher levels preventing lines of [Ne III] and [Ne IV] from being observed in the optical. When the SSS turned off, the ejecta may have been at low enough density that the lines were "frozen-in", slowing recombination and the subsequent production of emission lines from lower ionization states.

4.7.1 V1494 Aql - Adopted Values

Kiss & Thomson (2000) estimated the maximum brightness of V1494 Aql to be $M_V = -8.8 \pm 0.2$ using various MMRD relations based upon the t_2 and t_3 times calculated from the light curve. The resulting unreddened distance modulus yielded a distance to the system of 3.6 ± 0.3 kpc. Subsequent observations by Iijima & Esenoğlu (2003) exhibited Na I D interstellar absorption lines, which they used to estimate a reddening of $E(B-V) = 0.6 \pm 0.1$ ($A_V = 1.8 \pm 0.3$). Correcting for extinction, they derived a distance of 1.6 ± 0.2 kpc. Hachisu et al. (2004) used a model for an accretion disk with two-armed spiral shocks, to model the observed transit events in the optical light curve. Based upon their models, they estimated a distance to the system of 1.0 - 1.4 kpc. Their estimate, however, was sensitive to their assumed WD luminosity, which was very poorly constrained. We take the 1.6 kpc estimate to be more robust.

Iijima & Esenoğlu (2003) compared the nebular lines to the auroral lines of both oxygen and nitrogen to estimate the electron temperature (T_e) and density (n_e in the ejecta at 5 dates in the nebular stage). The analysis covered nearly 150 days. They found that throughout the period, the electron temperature stayed nearly constant at $T_e = 10,700 \pm 600$ K. The electron density, on the other hand,

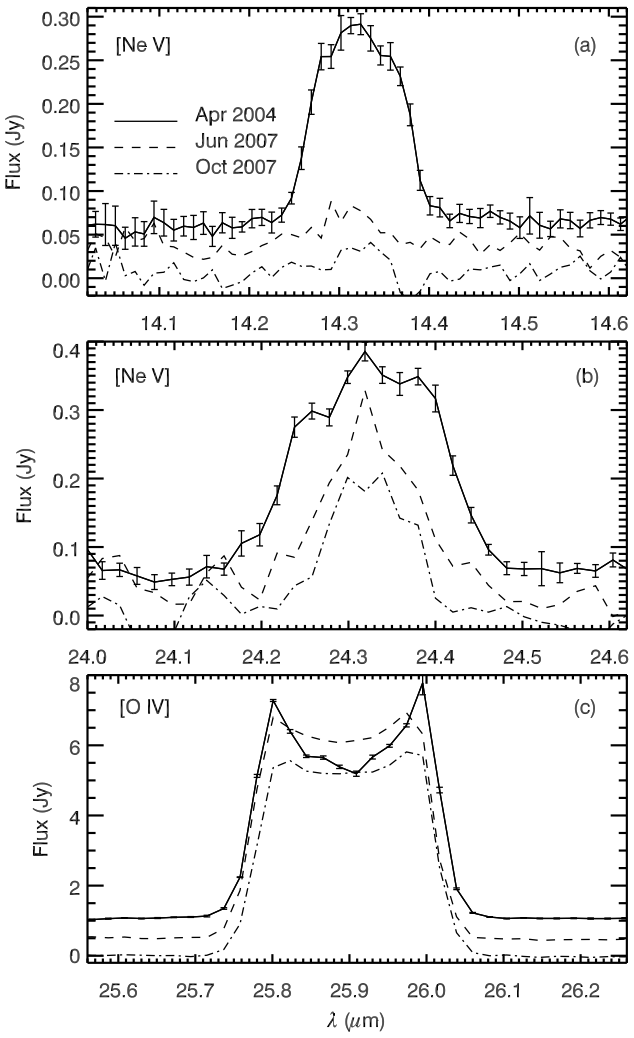

Figure 4.5: Plotted above are line profiles for the dominant emission lines in V1494 Aql from three epochs of observations. Representative errors are plotted on the profiles for 14 April 2004. Arbitrary bias levels have been applied to the April 2004 and June 2007 data for clarity. *Panel (a)*: [Ne V] λ14.32 μm *Panel (b)*: [Ne V] λ24.32 μm- The June 2007 and October 2007 spectra have been scaled by a factor of 3.0. *Panel (c)*: [O IV] λ25.91 μm- The June 2007 and October 2007 spectra have been scaled by a factor of 3.0.

was found to decay as $N_e \propto t^{-0.8}$, going from 9.4×10^6 at day 164 to 5.2×10^6 at day 289. The authors note that for spherically symmetric expansion the relation would be $N_e \propto t^{-3}$. This further supports the conclusion that the ejecta were highly asymmetrical. Using their estimates for the electron density (8×10^6 cm^{-3}, electron temperature 10,700 K), their measured intensity of Hβ, and a distance of 1.6 kpc, and factoring in the calculated helium abundance, Iijima & Esenoğlu (2003) derive a hydrogen mass of $(4.7 \pm 1.0) \times 10^{-5}$ M$_\odot$ and a total ejecta mass of $(6.2 \pm 1.4) \times 10^{-5}$ M$_\odot$.

Eyres et al. (2005) used the ratio of [O III] $\lambda\lambda$4959,5007 to [O III] λ4363 Å to determine the ejecta density, assuming $T_e = 10,700$ K. They found $N_e = (1.2 \pm 0.4) \times 10^6$ cm^{-3}. Imaging of V1494 Aql at 6 cm by Eyres et al. (2005) on day 136 revealed that the ejecta were clearly asymmetrical. The authors suggest that the twin lobed structure observed was consistent with the hypothesis that the ejecta distribution was ring-like at an inclination of $\sim 36°$, though it is not conclusive. Instead of a ring or sphere, they estimate the mass of hydrogen assuming that the ejecta had an ellipsoidal distribution characterized by their measured major and minor axes. They take the mean of these two axes to characterize the third axis of the ellipsoid. Assuming a distance of 1.6 kpc, the authors calculate a hydrogen mass of $m_H \sim 1.8 \times 10^{-5}$ M$_\odot$.

Another estimate for the mass of hydrogen in the ejecta was obtained by Kamath et al. (2005). They used the Hβ luminosity to calculate the electron number density at day 510 to be $N_e = (1.1 \pm 0.1) \times 10^5$ cm^{-3} for $T_e = 1.5 \times 10^4$. They assumed a spherical shell expanding at 2500 km s^{-1} with a filling factor of 0.01. The adopted filling factor is consistent with that estimated by Iijima & Esenoğlu (2003) who obtained a value of 0.016 at day 189. These parameters yielded $m_H = 6 \times 10^{-6}$ M$_\odot$. We use the mean of these mass estimates, 2.5×10^{-5} M$_\odot$, for our abundance analysis.

The measured ejecta velocities varied as the system evolved. As noted above, observations during the principal component stage measured absorption troughs ranging from -1020 to -1850 km s^{-1}. The FWHM expansion velocities at this

stage were quite low, e.g., of order 1200 km s^{-1} for Hα (Fujii 1999), but fitting the lines at the early stages of the outburst was complicated by the P-Cygni absorption components. More accurate FWHM velocity estimates were obtained during the later stages of development. During the nebular stage, 226 days after maximum, Mazuk et al. (2000) measured the FWHM of the near-IR coronal lines to be $\sim$ 2800 km s^{-1}. Rudy et al. (2001) found that 354 days later the expansion velocities had increased to 2900 km s^{-1}. The 6 cm images of the semi-resolved shell led to the only expansion velocity estimate independent of the emission line characteristics. Based on the distance of 1.6 kpc, Eyres et al. (2005) estimated the expansion velocities to be 980 and 2500 km s^{-1} for the minor and major axes, respectively. We base our subsequent analysis on two different models The first is a spherical shell with an outer radius calculated assuming v_{exp} = 2900 km s^{-1} and depth 10% of the radius, $\Delta r = 0.1 r_{out}$. This geometry results in n_e = 400 cm^{-3}. The second follows the calculation by Eyres et al. (2005) for an ellipse with r_1 calculated for v_{exp} = 980 km s^{-1}, r_2 assuming v_{exp} = 2900 km s^{-1}, and r_3 calculated from the mean of r_1 and r_2. This model yields n_e = 1750 cm^{-3}.

4.7.2 V1494 Aql - Abundance Calculations

The results of our abundance analyses are presented in Table 4.9. The ejecta appear to be mildly enhanced in neon with minimum ionic abundance of 3 times solar. The abundances of oxygen are likewise enhanced, but to a greater extent, $>$ 12 times solar. These enhancements are not high enough to suggest that the outburst of V1494 Aql arose on an ONe WD (Livio & Truran 1994), but instead suggest a CO WD origin. We estimate the minimum sulfur abundance to be 0.4 times solar by number, with respect to hydrogen.

Relatively few authors have calculated abundances in the ejecta of V1494 Aql. Iijima & Esenoğlu (2003) estimated an abundance of helium based upon the the observed intensities of He I λ5876 Å and He II λ4686 Å relative to Hβ. They found a helium abundance by number of N(He)/N(H)= 0.13 ± 0.01. In a similar

manner, Kamath et al. (2005) estimated a helium abundance of 0.24 based upon the ratio of He IIλ4686 Å under the assumption that all of the helium was ionized.

Kamath et al. (2005) also used the IRAF NEBULAR package to calculate the ionic abundances of oxygen and sulfur. If both the nebular lines and the hydrogen lines arose in the same region of the ejecta, then they estimate the lower limits of the abundances to be N(O)/N(H) = 1.61×10^{-5} and N(S)/N(H) = $(0.75 - 3.4) \times 10^{-7}$, corresponding to values of roughly 0.03 by number, relative to solar for both oxygen and sulfur. These values are lower than the minimum abundances estimated in the present analysis by orders of magnitude.

Finally, Rohrbach et al. (2009) modeled the X-ray spectra and estimated oxygen to be 17-35 times solar abundance and nitrogen to be overabundant relative to solar by a factor of $<$ 112-840. The authors noted that the spectral fits were non-unique and, though the derived abundances were likely over-estimated, the X-ray spectra should be considered highly overabundant in oxygen and nitrogen. The oxygen abundances estimated by Rohrbach et al. are consistent with the results derived here.

4.8 Conclusions

This chapter has summarized observations of seven CNe in their late nebular stages ($>$ 4 years post-outburst). In the case of three of these targets, we derived lower limits to abundances by number, relative to hydrogen based upon ejecta masses obtained during earlier stages of the outbursts.

We have placed lower limits on the abundances of oxygen and neon (10 and 39 times solar, relative to hydrogen, respectively) in the ejecta of V1974 Cygni and have found that the high abundances of these elements is consistent with earlier studies. Our derived abundances support the conclusion that the system contains an ONe WD. The emission lines of neon were weak relative to the [O IV] line at

Table 4.9: Abundances by Number Relative to Solar - V1494 Aql

Species	Wavelength (μm)	Module	Line Flux (erg cm^{-2} s^{-1})	n_e (cm^{-3}): T_e (K):	Derived Abundances[a] 1750 1000	1750 5000	400 1000	400 5000
[Ne V]	14.32	SH[b]	3.61×10^{-13}		-4.18	-4.13	-3.63	-3.54
	24.32	LH	2.98×10^{-13}		-3.88	-3.78	-3.39	-3.24
[Ne VI]	7.64	SL	4.62×10^{-14}		-4.65	-4.85	-4.01	-4.21
Total Neon					-3.65 (2.6)	-3.60 (3.0)	-3.13 (8.7)	-3.03 (10.9)
[O IV]	25.91	LH	5.23×10^{-12}		-2.23 (12.1)	-2.22 (12.3)	-1.77 (34.6)	-1.72 (38.5)
[S IV]	10.51	SL	5.56×10^{-14}		-4.97	-5.25	-4.37	-4.65
		SH	5.73×10^{-14}		-4.96 (0.84)	-5.24 (0.44)	-4.36 (3.3)	-4.64 (1.7)

[a]The number given is the log abundance by number relative to hydrogen. The number in parentheses is the abundance by number relative to hydrogen, relative to solar assuming the solar values of Asplund et al. (2009).

[b]When both high and low resolution data are available, we preferentially select the high res data for the estimation of the total abundances.

25.91 μm. The profiles suggest, however, that the oxygen and neon emission may arise in different regions of the ejecta. Further, the stability of the oxygen line implies that the line is optically thin and its profile reflects the distribution of the emitting region rather than being determined by optical depth effects.

The late time spectra of V382 Vel revealed emission lines from oxygen, neon, argon and sulfur allowing us to estimate lower limits to the abundances of each of these elements. In particular, we found that the neon abundance is at least 11 times solar, with respect to hydrogen, oxygen is at least 1.4 times solar, and argon and sulfur are at least 0.07 and 0.03 times solar, respectively. The neon and oxygen abundances are consistent with previous studies. These are the first abundance estimates for argon or sulfur in the ejecta of V382 Vel, but unfortunately, they provide only very weak constraints. The derived low relative abundances of these species are likely biased due to the ionization state of the ejecta and do not reflect an extreme depletion of these elements. Examination of the emission line structure during this late optically thin stage demonstrated that the various emitting species have different sources in the ejecta and may indicate the presence of ionization gradients.

Our *Spitzer* data on V1494 Aql provided the first observations of neon in this object. Based upon these data, we derived a minimum abundance of neon relative to hydrogen, relative to solar of about 3. This abundance estimate is not high enough to distinguish between a CO or an ONe progenitor WD in V1494 Aql. However, the oxygen abundance estimate, with a lower limit of 12 times solar, in combination with the moderate neon abundance, makes a convincing argument for a CO WD. The lack of neon detection at other wavelengths combined with the neon abundance estimated here implies that optical observations of CNe may not reveal the presence of elements of even moderate overabundances. The late time observation of neon in the ejecta of V1494 Aql reveals the importance both of high sensitivity observations in the IR regime and the value of late time observations.

Chapter 5

Atypical Dust Species in the Ejecta of Classical Novae

A portion of this chapter is a modified version of a chapter published in the proceedings of the conference entitled PAHs and the Universe (31 May - 4 June, 2010) with the following bibliographic reference: Helton, L. A., Evans, A., Woodward, C. E., & Gehrz, R. D. in ***PAHs and the Universe****, EAS Publications Series, eds. C. Joblin & A.G.G.M. Tielens, 2011. Additionally, Sections 5.3 and 5.4 are summaries of work presented on two targets from our campaign, DZ Crucis and V2362 Cygni, which were published with the following bibliographic references (for DZ Cru and V2362 Cyg respectively): Evans, A., Gehrz, R.D., Woodward, C.E., Helton, L.A., et al. 2010, MNRAS, 406, L85 and Lynch, D.K., Woodward, C.E., Gehrz, R.D., Helton, L.A., et al. 2008, AJ, 136, 1815.*

5.1 Introduction

Many astronomical sources display broad emission features in the $3-4$, $6-12$, and $15-20$ μm IR emission bands. These so-called unidentified infrared features (UIR; see also Geballe 1997; Tokunaga 1997) often exhibit broad ($\Delta\lambda \sim 0.1-0.2$ μm) emission peaks at 3.3, 3.4, 6.2, '7.7', 8.6, and 11.3 μm (Russell et al. 1977).

The precise position and relative strengths of these features show a high degree of variability based upon the environment in which they are observed (Peeters et al. 2002; van Diedenhoven et al. 2004). This is especially true of the '7.7' μm feature, which has a peak wavelength that can range from 7.6 - 8.1 μm. Taking advantage of the high sensitivity and resolution of the *Spitzer Space Telescope*, recent observations have revealed the presence of additional features at 5.25, 5.7, 10.6, 12.0, 12.7, 13.5, 14.1, 16.4, and 17.4, among others (Boersma et al. 2010).

The pervasiveness of the 3.3 μm feature amongst sources of UIR emission has led to the conclusion that the UIR carrier is some sort of organic molecule. This feature is generally attributed to C–H stretching mode vibrations in hydrocarbons molecules. Numerous hypotheses have been made for the nature of the molecular carrier of the UIR features, including polycyclic aromatic hydrocarbons (PAH; Duley & Williams 1981; Allamandola et al. 1985, 1989), hydrogenated amorphous carbons (HAC; Duley & Williams 1983; Duley & Jones 1990), and small carbonaceous molecules (SCMs; Bernstein & Lynch 2009), among others. Although there is growing support for the hypothesis that the UIR features are due to linear combinations of emission from an array of PAH molecules of various sizes and molecular conformations, there is still no general consensus.

Until recently, only a handful of CNe have exhibited UIR emission features, including V842 Cen (Nova Centauri 1986; Hyland & McGregor 1989; Gehrz 1990; Smith et al. 1994), QV Vul (Nova Vulpeculae 1987; Gehrz 1990; Gehrz et al. 1992c), and V705 Cas (Nova Cassiopeiae 1993; Gehrz et al. 1995; Lynch et al. 1997; Evans et al. 1997; Mason et al. 1998). Examination of the appearance and evolution of the UIR features in these novae provide insight into the molecular carriers and the UIR carrier formation mechanisms. Here we give a brief overview of the behavior of the UIR features in dusty novae, present new *Spitzer* results for the novae DZ Cru, V2362 Cyg, and V2361 Cyg, and discuss possible identifications for the UIR carrier in these systems.

5.2 Unidentified Infrared Features in Classical Novae

An optically thick dust shell ($\tau_V > 6$ magnitudes) formed in the ejecta of V842 Centauri 55 days after eruption. Hyland & McGregor (1989) report that during the first $\sim$ 200 days after condensation, the dust exhibited a smooth blackbody curve arising from amorphous carbon (AC) without any signature of UIR emission. Silicate emission at 10 μm was present by day 146 (Smith et al. 1994). Within days of the initial dust condensation event, the dust temperature was 650 K. By 240 days after condensation, when the dust was optically thin, the dust temperature had increased to 800 K. At this point, the dust shell began an "isothermal" stage of development in which the dust temperature remained relatively steady throughout the following $\sim$ 100 days (Smith et al. 1994). During this period, UIR emission features were observed at $\sim$ 3.25 and $\sim$ 3.5 μm by Hyland & McGregor (1989) and at 8.6, 11.3, and 12.7 μm by Gehrz (1990) and Smith et al. (1994). After their appearance, the UIR features persisted for many months, with the 11.3 μm feature lasting at least until 671 days after outburst (Smith et al. 1994).

Hyland & McGregor noted that even if the UIR features had been present at the same flux level during the observations of the initial condensation event, they would not have been detectable. During their previous UIR-free set of observations ($\sim$ 200 days post-dust formation), however, the features should have been detected. Interestingly, during the 4 month period of observations by Hyland & McGregor in which the near-IR UIR features were detected, the integrated flux in the 3.25 and 3.5 μm features declined by only a factor of $\sim$ 2.5 while the continuum dropped by a factor of $\sim$ 6. Based upon null detections during the optically thick and early, post-condensation optically thin phase, Hyland & McGregor suggested that the molecular carriers for the 3.28 and 3.5 μm features were produced by processing of dust, and further, that their persistence indicated an increasing number of molecules being subjected to a declining UV continuum. As noted by

Smith et al. (1994), the situation may not be so straightforward. The late appearance of the UIR features, around day 275, could imply that the UIR carriers were formed late in the dust condensation sequence as suggested by Hyland & McGregor, either by late time molecular growth or by production through AC grain destruction. Alternatively, the carriers may have been present earlier but they only were exposed to a radiation field conducive to grain excitation later in the development of the system.

The appearance and evolution of the dust in QV Vul followed much the same sequence as that in V842 Cen. Following a rapid and deep dust condensation event with $\tau_V \sim 5.6$ magnitudes, the dust signature was dominated by blackbody emission from AC, after which solid state features arising in silicates were observed just before the appearance of UIR emission features at ~ 3.3, ~ 3.4, and possibly at 11.4 μm (Gehrz et al. 1992c). After the initial decline in dust temperature from $\sim$ 780 K to $\sim$ 600 K, the dust entered an isothermal stage of development that lasted for many hundreds of days. Scott et al. (1994b) reported the possible detection of "extended red emission," i.e. broad features in the 0.5 to 0.75 μm range, 2084 days after outburst that they attributed to hydrocarbon emission.

Finally, the observed UIR evolutionary characteristics in the ejecta of V705 Cas were similar to those in both V842 Cen and QV Vul. The optical extinction event was rapid and very deep ($\tau_V \sim 6$ magnitudes). Initially, the dust emission appeared as a blackbody at a temperature of 1175 K due to AC grains (Mason et al. 1998). The dust temperature declined to $\sim$ 700 K, followed by a prolonged isothermal stage lasting more than 200 days. Observations of V705 Cas beginning 157 days after outburst revealed UIR features at 8.2, 8.7, and 11.4 μm superimposed on a 10 μm silicate emission feature (Evans et al. 1997). Subsequent analysis of the 8 μm complex by Evans et al. (2005) indicated that the profile shape and peak wavelength did not match those of standard UIR features and that the peak wavelength drifted bluewards as the system evolved. Simultaneously, the ratio of the 11.4 to 8 μm features increased. The $3 - 4$ μm region in the spectrum of V705 Cas showed emission features at 3.28 and 3.4 μm. The

observed 3.28 to 3.4 μm ratio was similar to that seen in post-AGB stars, but an order of magnitude higher than in stars with a high UV photon flux.

5.3 DZ Cru

DZ Crucis (Nova Cru 2003) was discovered by Tabur et al. (2003) on 2003 August 20.5 UT (JD 2452871.9) at an V-band magnitude of 10.2 while it was still rising towards maximum light. Palomar Sky Survey plates failed to detect the progenitor to this object, suggesting that the outburst amplitude was $\Delta V > 10$ (Tabur et al. 2003; Rushton et al. 2008), average for a moderately fast CN outburst (Warner 2008). The B - V color at maximum was exceptionally high, $+1.25 \pm 0.05$ (Rushton et al. 2008). For a CN at maximum light, the B - V color is expected to be $+0.23 \pm 0.05$ (van den Bergh & Younger 1987). Early spectroscopic observations by Della Valle et al. (2003) revealed neither emission lines from permitted Fe II nor helium and nitrogen, characteristic features observed in Fe II- and He/N-type classical novae respectively. Instead, their spectra revealed a reddened continuum with weak lines from Hα and Hβ, both of which exhibited low level P-Cyg absorption components at a velocity of only ~ 500 km s^{-1}. This "peculiar" behavior led Della Valle et al. to suggest that the system was not a CN, but a post-asymptotic-giant-branch star undergoing a flare, thus inviting comparison between DZ Cru and eruptive variables like V838 Monocerotis. Very few observations of DZ Cru were obtained after the initial detection.

Rushton et al. (2008) reported on near-IR (0.95-2.52 μm) spectroscopic observations of DZ Cru taken $1.5-1.9$ years after outburst. They found an emission line spectrum dominated by H I recombination lines superimposed on a strong dusty continuum. The spectra also revealed emission from [N I] λ1.0401 + He I λ1.0833 μm, He I λ2.0587 μm, and O I λ1.3168 μm. Interestingly, only the He I lines still exhibited significant P-Cyg absorption at this late stage in the spectral development. Throughout their observations, Rushton et al. found a mean expansion velocity based upon the hydrogen lines of ~ 500 km s^{-1}, in agreement with that

reported immediately after maximum. In contrast, the He I P-Cyg absorption troughs reached maximum near 1500 km s^{-1}. By fitting the dust continuum, assuming AC grains, the authors calculated a mean dust temperature of 690 ± 40 K during the first epoch and 620 ± 50 K around 120 days later.

Rushton et al. excluded DZ Cru as an eruptive variable based upon comparison to the prototype, V838 Mon. Eruptive variables tend to appear as a cool supergiant with molecular absorption features in their NIR spectra and very few emission lines with low expansion velocities ($\lesssim 500$ km s^{-1}). Likewise, the rapid increase to maximum light, the high amplitude of its outburst, and the strong emission lines observed in DZ Cru implied that it could not have been a "Born-Again Giant" star (BAG), like Sakurai's Object. These highly evolved objects are thought to be WDs that have undergone a Very Late Thermal Pulse (VLTP), which inflates the WDs back up to the size of a red giant. The expansion of the envelope causes a gradual rise to maximum that occurs over a year or more. Further, BAGs tend to be very hydrogen deficient in contrast to the hydrogen rich spectra evidenced by DZ Cru. Though the early spectra of DZ Cru were unusual for a nova, the light curve behavior and the late time spectra clearly indicate that it was a nova event.

5.3.1 *Spitzer* Observations of DZ Cru

DZ Cru was observed as part of our *Spitzer* Classical Novae Target-of-Opportunity and Monitoring campaign (PIDs 30076 and 40060; Evans et al. 2010b). Our first *Spitzer* Infrared Spectrograph (IRS) observations commenced 1477 days after eruption, with return visits on days 1650 and 1706 (AORs 22269952, 17734912, and 17735168). Data reduction followed the methods presented in §3.2.4. These observations revealed exceptionally strong emission from AC with superimposed unidentified infrared (UIR) emission features reminiscent of those observed in V705 Cas. The only emission lines present were [Ne III] λ15.56 μm and [O IV] λ25.91 μm. Our *Spitzer* observations of DZ Cru are presented in figure 5.1.

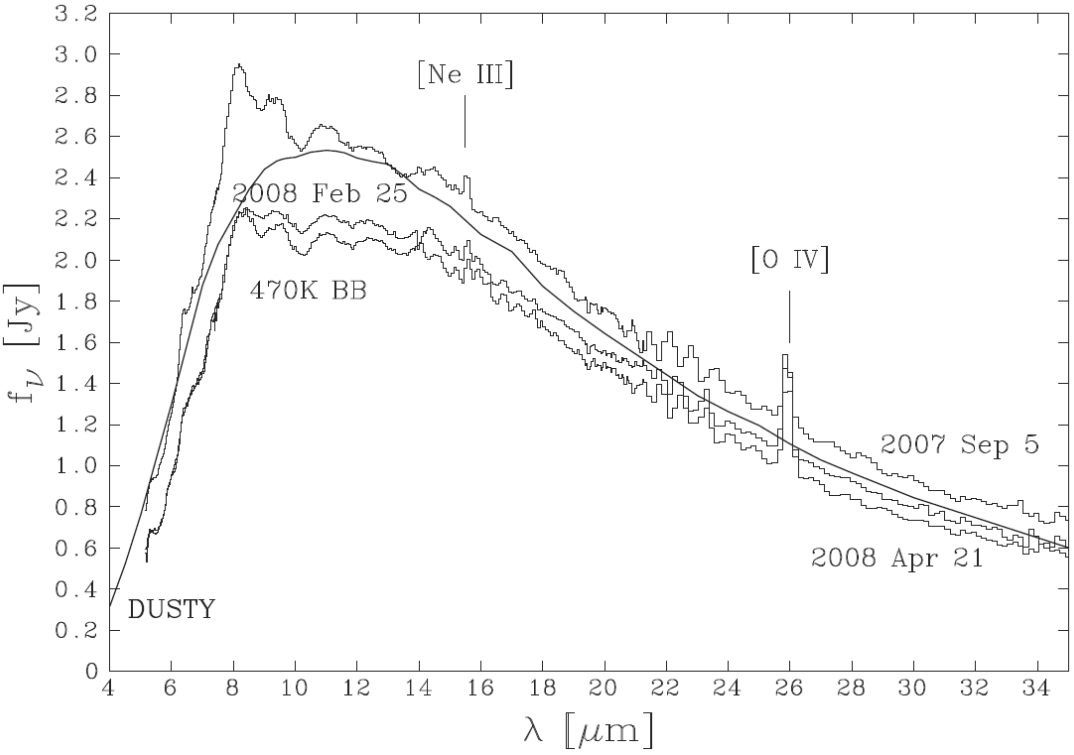

Figure 5.1: *Spitzer* IRS spectra of DZ Cru with a DUSTY model for AC at 470 K. From Evans et al. (2010b), and used with permission.

The expansion velocities in [Ne III] and [O IV] lines ranged from 800 to 1000 km s^{-1}, consistent with that reported by Rushton et al. (2008) based on the near-IR emission lines observed $\sim$ 150 days after outburst. If we assume that the O I lines observed early on arose from the same material that later produced the [O IV] emission in the mid-IR, then we also conclude that there was little, if any, deacceleration of the ejecta during the intervening period.

We refer to the structures observed in the 6-14 μm region of the *Spitzer* spectra as UIR features, though they did not exhibit the normal UIR spectral characteristics. Because of the complexity of these features, it is difficult to accurately remove the underlying continuum. We modeled the continuum using the DUSTY

radiative transport code (Ivezić et al. 1999) by matching the slope of the continuum beyond 14 μm while constraining the models to lie below the minima in the 6-14 μm emission complex. We assumed an illuminating blackbody source with a temperature of 10^5 K, an AC carrier for the dust emission with optical properties reported by Hanner (1988) and grain radius $a = 0.2$ μm. The ejecta shell followed a $\rho \propto r^{-2}$ density law with the optical depth, $\tau_V = 0.1$. The resulting model is overlaid in Figure 5.1.

Figure 5.2 shows the residual emission after subtraction of the DUSTY model. UIR emission features are labeled with tick marks at 6.5, 7.2, 8.1, 9.3, 11.0, and 12.4 μm. The FWHM of the UIR features in this object are of order $\sim 0.5 - 1.0$ μm, much too wide to be attributed to emission lines. At long wavelengths, the DUSTY fit lies along the continuum, but at a nearly constant offset. This plateau stretching from $\sim 14 - 34$ μm, is indicated with a horizontal bar in the figure. The apparent emission features from $20 - 24$ μm are artifacts due to fringing in the data.

Interestingly, there is evidence for evolution of the individual UIR features between the three epochs of observation. On day 1477, the 8.1 μm feature had a relatively sharp profile that was significantly stronger than its neighbor at 9.3 μm. Nearly 200 days later, the strength of this feature had declined until it was roughly equal to that at 9.3 μm. The rest of the UIR emission features appeared much as they had during the earlier observation. By the final epoch, however, the appearance of the 8.1 μm feature had returned to its previous aspect and was again the strongest feature in the spectrum.

5.4 V2362 Cyg

V2362 Cygni (Nova Cyg 2006) was discovered by H. Nishimura on 2006 April 2.81 near maximum light at an apparent magnitude of $m_V \sim 10.5$. Maximum was reached on April 5.00 at $m_V = 8.5$ (Nakano et al. 2006). This target was observed extensively as part of our multiwavelength classical novae monitoring campaigns.

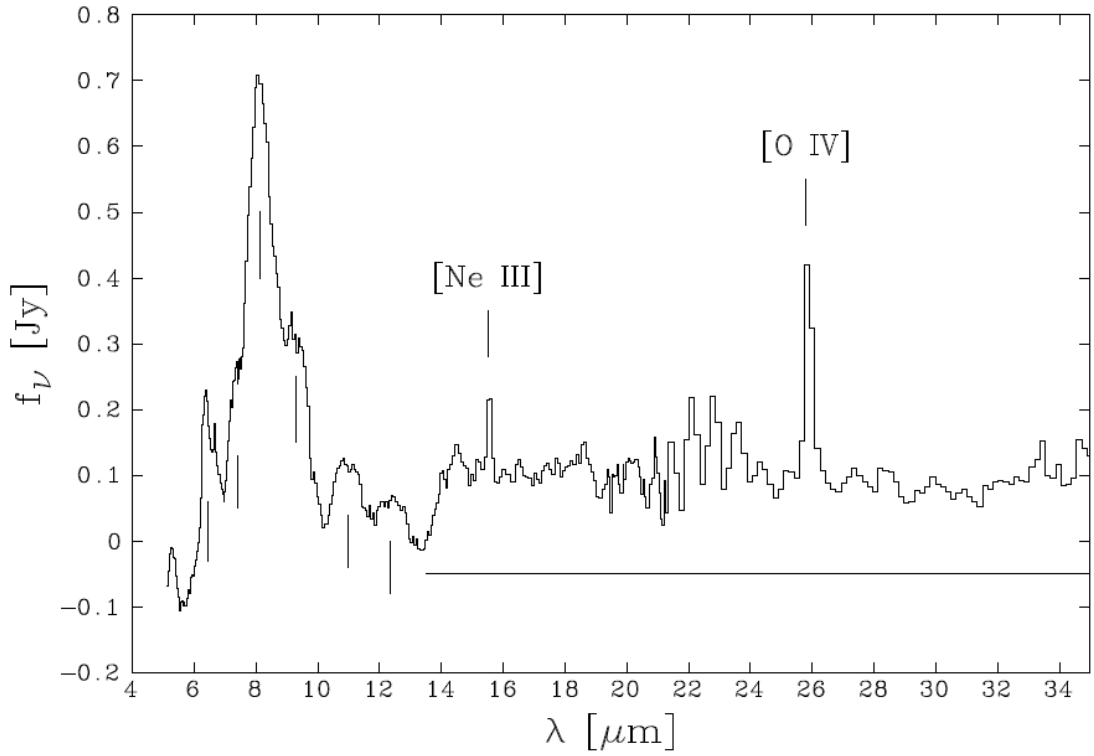

Figure 5.2: Residual UIR emission remaining after DUSTY model subtraction. From Evans et al. (2010b), and used with permission.

We obtained observational coverage in the X-ray and ultraviolet using the *Swift* telescope, in the optical with the Steward Bok 90" (2.29-m) and Lick Observatory 120" (3-m) telescopes, in the near-IR using the NASA Infrared Telescope Facility (IRTF)[1] and Lick telescopes, and in the mid-IR with the *Spitzer Space Telescope*. A comprehensive examination of these data, covering the first 500 days of spectral development, was presented by Lynch et al. (2008b).

V2362 Cyg was a peculiar nova in many respects. One of the most interesting characteristics was its optical light curve behavior (Figure 5.3). After a smooth initial decline with t_2 and t_3 times of 10.5 and 24 days respectively, the light

[1] The Infrared Telescope Facility is operated by the University of Hawaii under Cooperative Agreement no. NCC 5-538 with the National Aeronautics and Space Administration, Science Mission Directorate, Planetary Astronomy Program.

curve plateaued and experienced a secondary brightening event, which rivaled its initial outburst luminosity ($m_V \sim 9.8$). This light curve behavior is distinct from the oscillations observed in some CNe during the transition phase of their development (e.g., V2467 Cygni, Section 6.2.2) and has only been confirmed in two other CNe, V1493 Aql (Bonifacio et al. 2000; Venturini et al. 2004) and V2491 Cyg (Hachisu & Kato 2009).

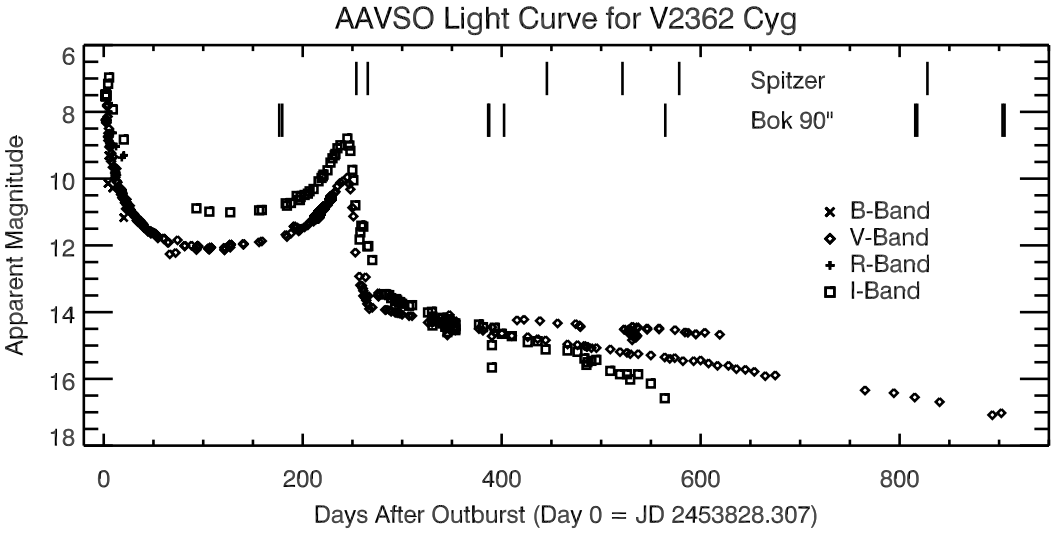

Figure 5.3: Light curve of V2362 Cyg. Tick marks indicate the epochs of *Spitzer* mid-IR and Bok 90" optical observations. Of particular interest is the prominent rebrightening event that peaks near day 240.

The spectral development during the initial decline was typical of a well behaved CN. The early stages were characterized by strong P-Cyg absorption components on the hydrogen and helium lines, which faded as the ejecta became optically thin. The spectra were dominated by H I and He I recombination lines with additional strong permitted lines of Fe II, C I, N I, and O I. As the system evolved to the nebular stage, the densities declined and the state of ionization increased, as demonstrated by the appearance of forbidden lines of [O II] and [O III].

During the plateau and rebrightening stages of the light curve, the ejecta

appeared to revert to an earlier stage of development. The emission signature returned to the pre-nebular state with the spectra being dominated by low ionization allowed transition lines once again. The hydrogen, helium, and oxygen lines developed P-Cyg profiles at blue-shifts greater than 2000 km s^{-1}. The emission lines during the second brightening event, however, were much more broad than during the initial decline. For example, the O I lines broadened from 1200 to 4250 km s^{-1}. The emission lines also developed a three-component, symmetric sub-structure suggesting a bipolar outflow.

Near the peak of the second outburst, our observations indicated that the nova underwent a rapid and extreme dust formation event. IRTF data obtained within days of the second maximum revealed a near perfect blackbody peaking at a temperature 1410 ± 15 K, and was some of the hottest astronomical dust ever observed in a CN outburst. These temperatures are near the theoretical extreme of condensation temperatures for carbon dust grains. *Spitzer* IRS spectra obtained immediately following dust condensation also confirmed blackbody emission from hot dust. At first, low ionization [Ne II], [Ne III], and [O IV] were observed in these spectra alongside hydrogen recombination lines. But within a few days, as the IR dust emission strengthened, the forbidden lines disappeared with the sole exception of [O IV], which remained strong throughout. During the same period, the flux in the optical and near-IR lines sharply declined, and the P-Cyg profiles quickly began to fade. Due to the nature of the light curve, it is difficult to accurately determine the depth of the optical extinction event. Nevertheless, the overall photometric and spectroscopic behavior during this period indicates that the optical depth was relatively high.

With the expansion of the ejecta and subsequent decline in the dust optical depth, the emission lines reappeared, but reached a much higher ionization level. Emission lines of [O III], [Ne II], and [Ne III] returned with profiles very similar to their earlier nebular incarnations. In the infrared, strong lines of highly ionized species were observed such as [Ne V], [Ne VI], [Mg V], and [Mg VII], indicating that the ejecta were exposed to a much more energetic radiation field. Indeed, *Swift*

observations from this period indicated that throughout the rebrightening event, optically thick dust condensation, and subsequent nebular phases, the X-ray flux continued to increase. During the return to the nebular stage, a strong, hard X-ray flux was observed that persisted for at least 300 days.

We consider a second mass ejection event to be the most likely explanation for the peculiar light curve and spectroscopic evolution of V2362 Cyg. The secondary eruption was characterized by a much higher ejection velocity than the initial outburst. Considering the relative expansion velocities of the material ejected in the initial and secondary eruptions, 1200 km s^{-1} and 3500 km s^{-1} respectively, it is possible that the onset of dust formation coincided with the collision of the two shells and that the observed hard X-ray flux was due to shocked gas. The interaction of the two shells may have resulted in shock-induced dust formation (Fleischer et al. 1992; Schirrmacher et al. 2003). The failure to observe SSS emission at later stages can be explained by preferential absorption of the soft X-ray flux by the dust. Even if this is true, however, we cannot determine whether the absorbed soft X-ray flux acted to destroy the intervening dust or not.

As the dust dispersed, it became optically thin. The IR SED changed dramatically and revealed strong, broad UIR features near $6 - 10$, 11.5, and 18 μm. The broad feature near 18 μm may have been due to the O–Si–O bending mode in silicates; however, the associated, stronger 9.7 μm Si–O stretch feature was apparently absent. It is tempting to relate the observed features to free-flying PAHs, but they do not correspond well with the standard emission bands of PAHs at 6.2, '7.7', 8.6, and 11.3 μm (Allamandola et al. 1989; Peeters et al. 2002).

5.4.1 New *Spitzer* Observations of V2362 Cyg

We continued following V2362 Cyg with *Spitzer* for two years beyond the final observations reported by Lynch et al. (2008b). Here we re-analyze the final epoch of data presented by Lynch et al. and present three subsequent epochs of *Spitzer* observations. An observational summary is provided in Table 5.1. In addition

to these mid-IR observations, we also obtained optical data during these late stages of evolution with the Steward Observatory Bok 90" telescope using the B&C Optical Spectrograph. Details of this instrument as well as observation and reduction notes are provided in Chapter 2.

Our first *Spitzer* observations of V2362 Cyg were obtained immediately following dust condensation coincident with the truncation of the optical rebrightening event. As mentioned by Lynch et al. (2008b), the mid-IR spectra obtained as the dust dispersed was optically thin and revealed a broad emission complex from $6 - 12$ μm. Subsequent *Spitzer* observations revealed that the emission complex underwent significant changes as the dust evolved.

Table 5.1: *Spitzer* Spectroscopic Observation Log of V2362 Cyg

Observation	JD		Source/Background	Time on Source (sec)				Age[a]
Date (UT)	(+2450000)	PID	AOR	SL	SH	LL	LH	(Days)
2007 Jun 22.21	4273.71	30007	17680640/0896	140	300	300	600	445.4
2007 Sep 06.28	4349.78	40600	22261504/1760	140	300	300	600	521.5
2007 Nov 02.29	4406.79	40600	22262016/2272	140	300	300	600	578.5
2008 Jul 08.67	4656.17	50011	25191936/2192	140	300	1200[b]	600	827.9

[a]From 2006 April 2.81 UT (JD 2453828.31)
[b]Order 1 was exposed for 1200 s while Order 2 was exposed for only 720 s

In order to better understand the evolution of the emission complexes observed by *Spitzer*, we isolated the features by fitting and subtracting a blackbody to the underlying continuum. The continuum was fit interactively to the regions of the spectra considered to be relatively free from other features, i.e., from $12 - 15$ μm and beyond 23 μm. The flux at the blue end of the spectrum declined sharply. We attempted to constrain the models by requiring that the blue extreme fall very close to the minimum of the observed emission in this region. The model was then subtracted from the observed SED. In Figures 5.4-5.7 we plot the *Spitzer* mid-IR SEDs for our final four epochs of observations. The dashed line indicates the fit to

the blackbody continuum and the dash-dotted line is the residual emission after continuum subtraction.

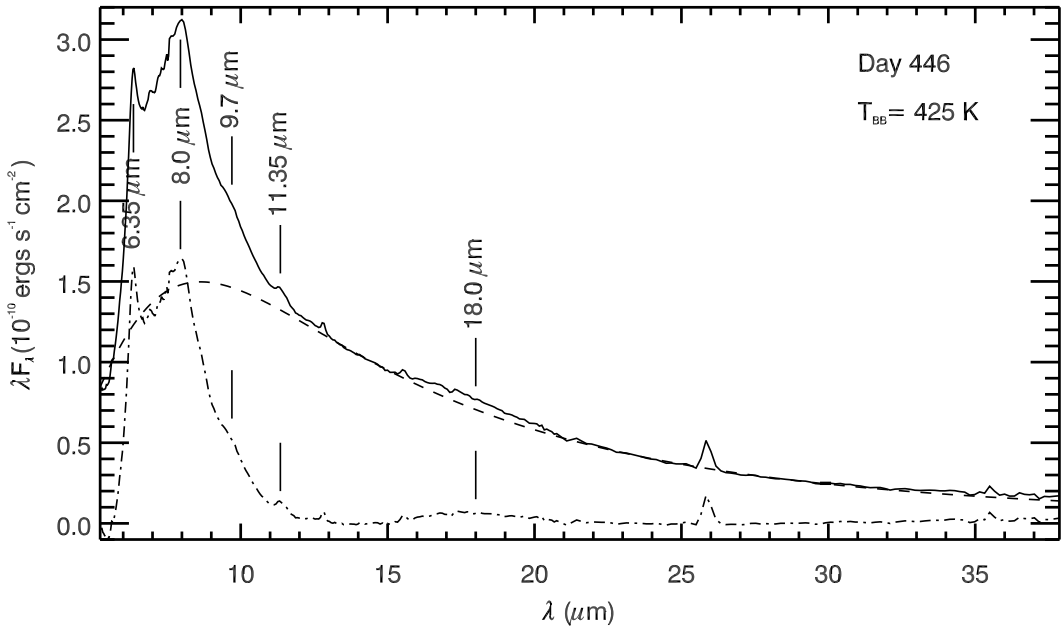

Figure 5.4: *Spitzer* SED of V2362 Cyg obtained on 2007 June 22 (Day 446). A representative 1-σ error bar, comparable to the line thickness of the data, is plotted near 30 μm. The dashed line indicates the blackbody fit to the continuum at a temperature of 425 K. The dash-dotted line indicates the residuals after blackbody subtraction. The approximate positions of significant emission features are labeled.

As discussed in Lynch et al. (2008b), the day 446 data exhibited strong, distinct emission peaks near 6.4, 8.0, and 11.35 μm (Figure 5.4). There appeared to be a broad shoulder on the red trailing edge of the 8.0 μm features near 9.7 μm as well as a weak, broad, and flat complex near 18.0 μm. Additionally, the plateau joining the 6.4 and 8.0 μm features had a complex structure, which may be indicative of multiple narrower components. Although the neon lines were very weak, emission lines of [Ne II] λ 12.81 μm, [Ne III] λ15.56 μm, and [O IV] λ25.91 μm were present. Additional emission lines may be present in these spectra, superimposed on the broad emission complex, but they cannot be confidently identified due to

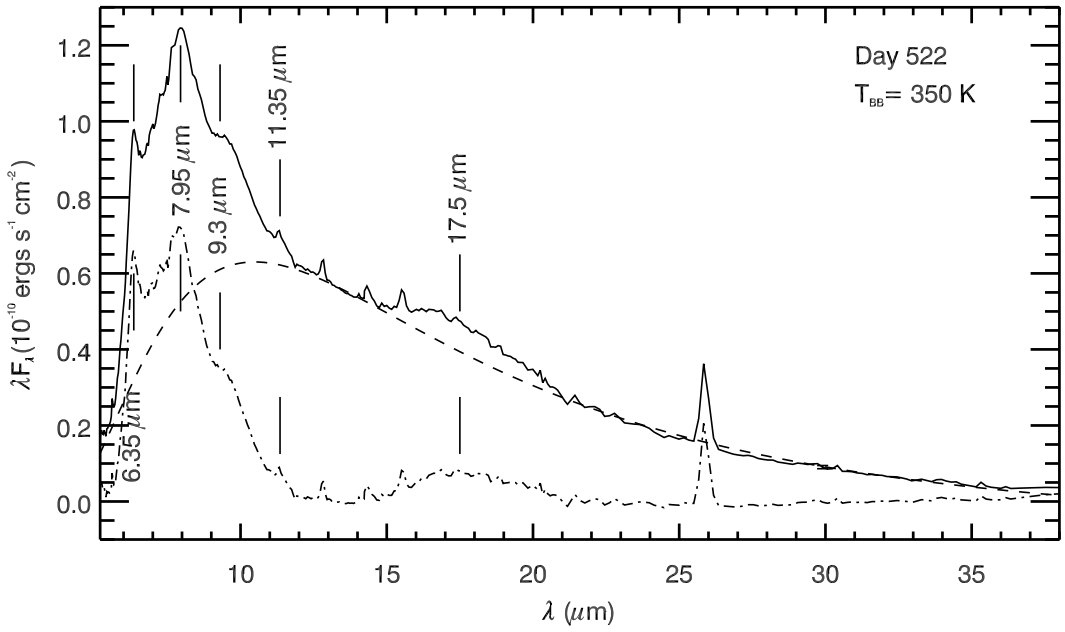

Figure 5.5: *Spitzer* SED of V2362 Cyg obtained on 2007 September 06 (Day 522). A representative 1-σ error bar, comparable to the line thickness of the data, is plotted near 30 μm. The dashed line indicates the blackbody fit to the continuum at a temperature of 350 K. Otherwise as Figure 5.4.

the complexity in the feature.

The second epoch of observations on day 522 revealed substantial changes in the SED (Figure 5.5). The peak wavelengths of the features varied slightly from those observed during the first epoch, though generally were within 0.1 μm of their original positions, comparable to the error in the fits. The strength of the 8 μm feature had declined relative to that of the 6.4 and 9.7 μm features resulting in an apparent broadening of the entire $6 - 12$ μm emission complex. The 11.4 μm feature was consistent with that observed on day 446. Likewise, the broad 18 μm feature strengthened relative to the continuum. The [Ne II], [Ne III], and [O IV] lines had also strengthened relative to the continuum. The appearance of emission from [Ne V] λ14.32 μm and [Mg V] λ5.61 μm indicates that the degree

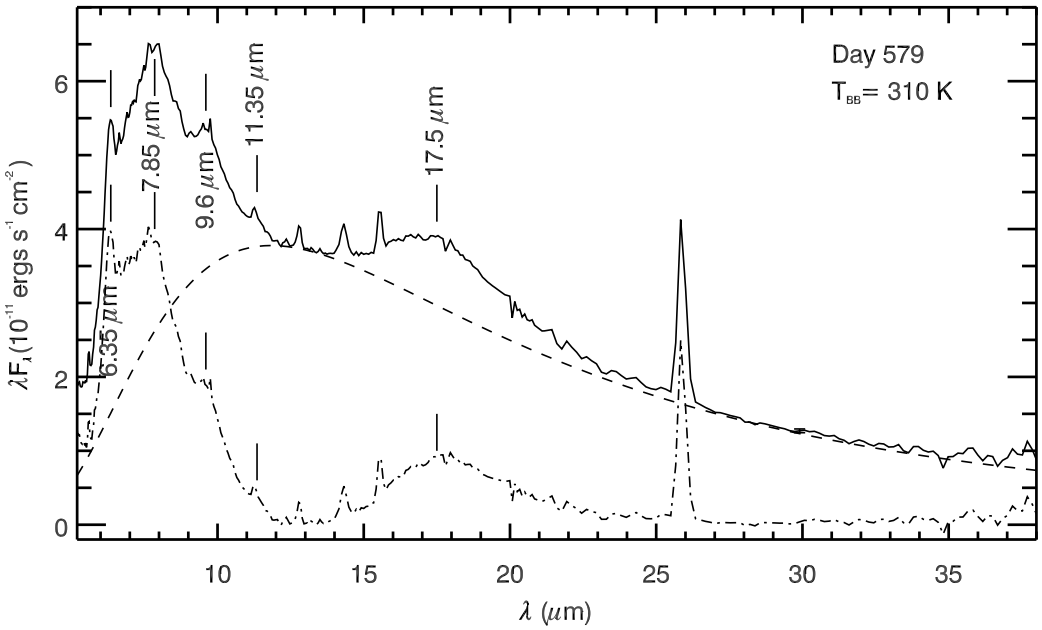

Figure 5.6: *Spitzer* SED of V2362 Cyg obtained on 2007 November 02 (Day 579). A representative 1-σ error bar, comparable to the line thickness of the data, is plotted near 30 μm. The dashed line indicates the blackbody fit to the continuum at a temperature of 310 K. Otherwise as Figure 5.4.

of ionization in the ejecta increased.

The trend of declining 8 μm emission relative to the 6.4 and 9.7 μm features continued into the third epoch of observations, day 579 (Figure 5.6). As the flux declined, the 9.7 feature became more distinct, taking on the appearance of an independent feature. Again, the shape of the 11.4 μm feature remained relatively unchanged. The characteristics of the emission lines were also similar to those observed on day 522.

Over the next 300 days, the SED changed substantially (Figure 5.7). By the final epoch, the continuum flux had decreased in a manner consistent with cooling of the ejecta. The 8 μm feature was no longer the strongest in the spectrum. It had declined in strength until comparable to that of the 9.7 μm feature. Similarly,

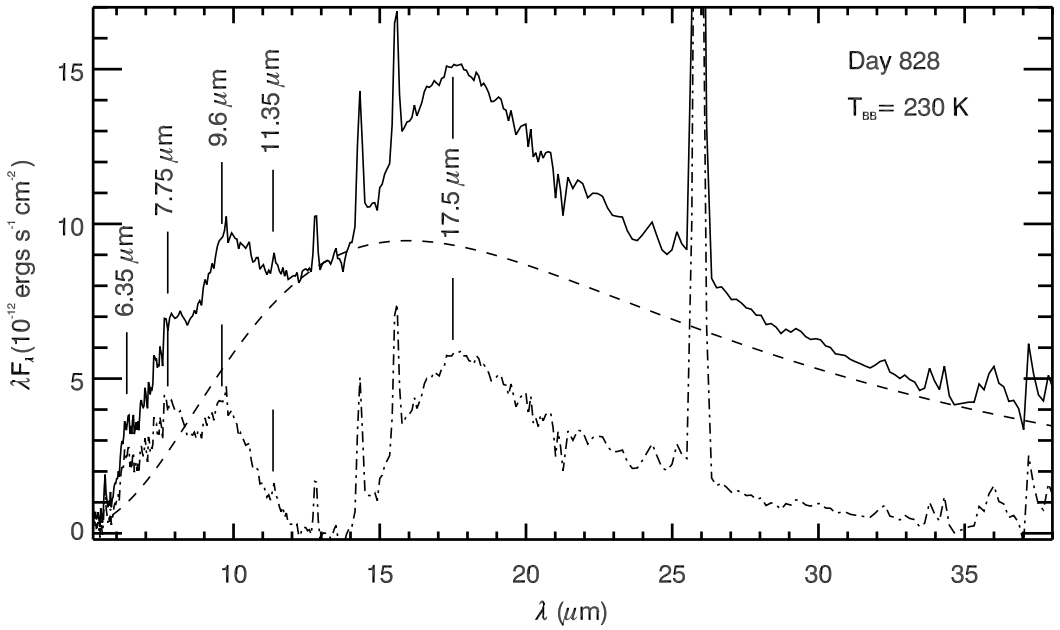

Figure 5.7: *Spitzer* SED of V2362 Cyg obtained on 2007 June 08 (Day 828). A representative 1-σ error bar is plotted near 30 μm. The dashed line indicates the blackbody fit to the continuum at a temperature of 230 K. Otherwise as Figure 5.4.

the 6.4 μm feature weakened considerably and was only just detectable above the noise. The 11.4 μm feature appeared to be narrower than previously observed, however, this was likely due to the wings of the emission being lost in the noise. At this epoch, the SED was dominated by the 17.5 μm feature, which developed a profile with a sharper blue edge and longer red tail than at previous epochs. The state of ionization in the ejecta appeared to be consistent with that observed in the previous epoch.

5.5 V2361 Cyg

V2361 Cygni (Nova Cyg 2005) was discovered by H. Nishimura at an unfiltered magnitude of ~ 9.7 on 2005 February 10.85 (Nakano et al. 2005), which we take to

be t_0. Spectra obtained one day after discovery indicated relatively broad Balmer emission, $\sim$ 3200 km s^{-1} FWHM at Hα (Naito et al. 2005). Spectra obtained on February 12.20 revealed complex P-Cyg absorption profiles with up to three components with blue-shifted velocities of -3200, -6500, and -7500 km s^{-1}. The spectra showed Fe II multiplet emission, O I, and N II (Ciroi et al. 2005). The brightness of V2361 Cyg declined very rapidly. By 2005 March 17.2, the nova was approaching $m_V \sim 19$ (Bode et al. 2005).

Examination of the light curve suggests that its rapid decay may have been due to the formation of dust (Figure 5.8). Near-IR observations obtained less than a month after outburst clearly revealed strong dust continuum fitted well by a blackbody of 970 ± 10 K (Russell et al. 2005a). Superimposed on this continuum was emission from He I λ1.083, and λ1.2818 μm, O I λ8446 Å, λ1.1287 μm, and λ1.3165 μm, along with weak H I emission. Based upon the O I lines, Russell et al. estimate an extinction of $A_V = 1.2$ magnitudes, though they suggest that a significant portion of this is local.

Additional spectroscopic observations were obtained by Gaggero et al. (2005) from days 78 to 80 with coverage from $0.4 - 1.0$ μm. These observations indicated that the system was entering the nebular stage. The spectra exhibited hydrogen Balmer and Paschen recombination lines, weakening O I lines at 7773 Å and 8446 Å, [O III] λ6363 and $\lambda\lambda$4959, 5007 Å, as well as features of He I, N I, and Mg II. All emission features were composed of multiple components at $\pm$700 km s^{-1} and -200 km s^{-1}. The lines were asymmetric with a strong red peak. Based on the spectral characteristics, Gaggero et al. suggested that V2361 Cyg was a CO-type nova.

Venturini et al. (2005) reported that the object had entered the coronal stage of development with the appearance of [Si VI] and [Ca VIII] by 2005 November 13.2 (day 275). At this epoch He I λ1.0830 μm still dominated the near-IR regions of the spectrum. The optical spectra were dominated by [O III] and [N II]. Weak He II lines were also present.

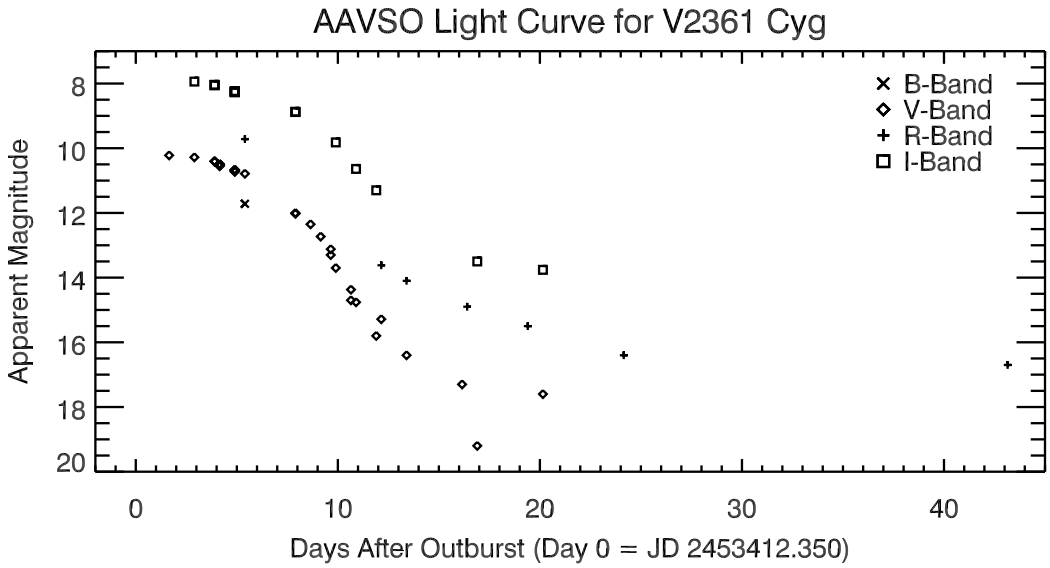

Figure 5.8: Light curve of V2361 Cyg. The first *Spitzer* mid-IR and Bok 90" optical observations occurred roughly 60 days after the last photometric detection by AAVSO observers. The rapid decline is due to dust condensation.

5.5.1 *Spitzer* Observations of V2361 Cyg

We obtained observations of V2361 Cyg with the *Spitzer Space Telescope* using the IRS instrument over a period of three years. Observational details are presented in Table 5.2. Data reduction followed the methodology presented in Chapter 3.

The SED of V2361 Cyg was similar to that of V2362 Cyg with three notable exceptions. First, the emission features at 9.5 and 18 μm in V2362 Cyg were absent in V2361 Cyg. Second, the shape of the $6 - 10$ μm emission complex was more flat and exhibited a greater amount of structure. Also, the 11.4 μm feature was much less distinct than seen in V2362 Cyg. Finally, there were additional features present near 5.4 and 12.3 μm that were not evident in the spectra of V2362 Cyg.

Table 5.2: *Spitzer* Spectroscopic Observation Log of V2361 Cyg

Observation Date (UT)	JD (+2450000)	PID	Source/Background AOR	Time on Source (sec) SL	SH	LL	LH	Age[a] (Days)
2005 May 24.45	3514.95	2333	10278144[b]	36	120	. . .	360	102.7
2005 Jun 07.56	3529.06	2333	10278400[b]	36	120	. . .	360	116.8
2007 Jun 06.59	4264.09	30076	17733374/8496	60	120	84	360	851.8
2007 Oct 08.42	4381.92	30076	17733632/8752	60	120	84	360	969.6
2007 Oct 12.45	4385.95	40060	22263040/3296	84	180	180	360	973.7
2007 Dec 07.63	4442.13	30076	17733888/9008	60	120	84	360	1029.8
2008 Jun 05.65	4623.15	40060	22263552/3808	84	180	180	360	1210.9

[a]From 2005 February 10.85 (JD 2453412.30)
[b]No independent background observations were obtained for this epoch.

Following the method discussed above for V2362 Cyg, we fitted a blackbody continuum to the SED and used the fit to isolate the residual emission. The results are shown in Figures 5.9-5.12. Prominent features are labeled with approximate positions in order to highlight the complex structure in the $6 - 12$ μm emission complex. Detailed fitting of these features is presented in Section 5.6.

The first *Spitzer* observations of V2361 Cyg were obtained only 102 days after outburst (Figure 5.9). These spectra exhibited a strong emission complex in the $6 - 10$ μm region reminiscent of that observed in V2362 Cyg. The similarity was even more apparent after the continuum blackbody removal. The strongest component is near 8.0 μm with a second prominent feature near 6.4 μm. The profile of this latter feature was narrower than that at 8.0 μm, though the broad plateau between the two likely contaminates the 8.0 μm emission profile. The red edge of the 8.0 μm feature was very smooth with no indication of an emission component near 9.7 μm. There were two broad and weak components in the $10 - 15$ μm region of the spectrum near 11.5 and 12.3 μm. The 11.5 μm feature may relate to the 11.4 μm feature in V2362 Cyg, but its weak, broad profile was much less distinct. The profile of the 12.3 μm structure was very similar to the 11.5 μm feature.

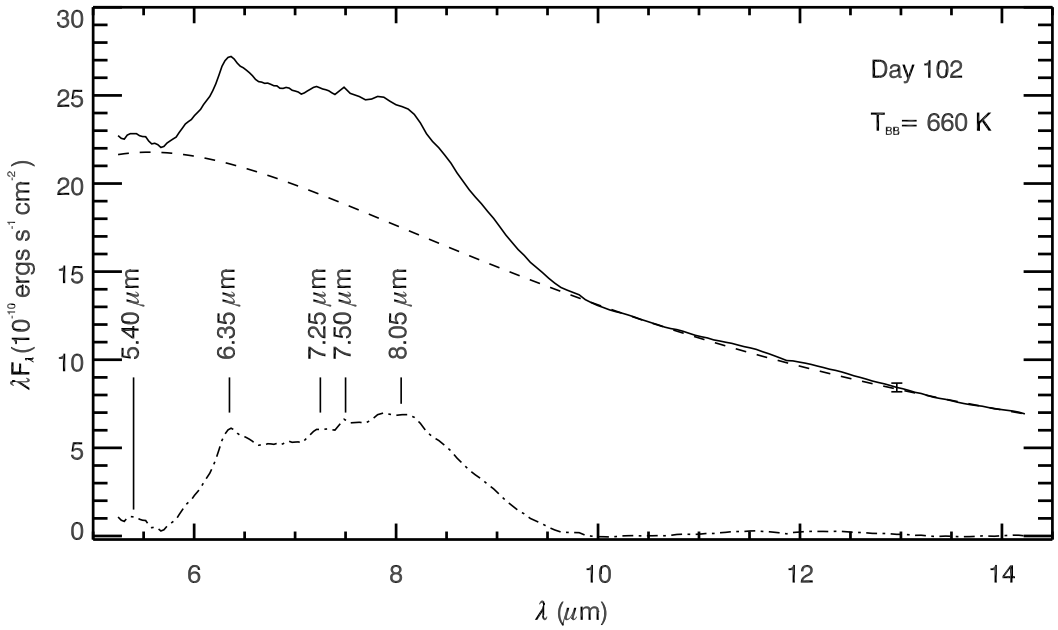

Figure 5.9: *Spitzer* SED of V2361 Cyg obtained on 2005 May 23 (Day 102). A representative 1-σ error bar is plotted near 13 μm. The dashed line indicates the blackbody fit to the continuum at a temperature of 660 K. The dash-dotted line indicates the residuals after blackbody subtraction. The approximate positions of significant emission features are labeled.

Remarkably, at this epoch, no emission lines can be seen in the $5 - 15$ μm region of the spectrum suggesting that the dust in the ejecta still had a high optical depth. The only emission line evident is [O IV] λ25.91 μm, observed with the LH module. This feature had a broad (FWHM $\sim$ 3200 km s^{-1}) profile that is consistent with the expanding shell models of Lynch et al. (2006a).

The next set of observations were obtained just 14 days later (Figure 5.10). The appearance and strength of the $6 - 10$ μm complex was much the same as on day 102, though the underlying continuum had declined by $\sim$ 25%. At this epoch, there was still a conspicuous lack of emission lines, again with the exception of [O IV] λ25.91 μm. The line width and intensity at this epoch was unchanged to within measurement errors.

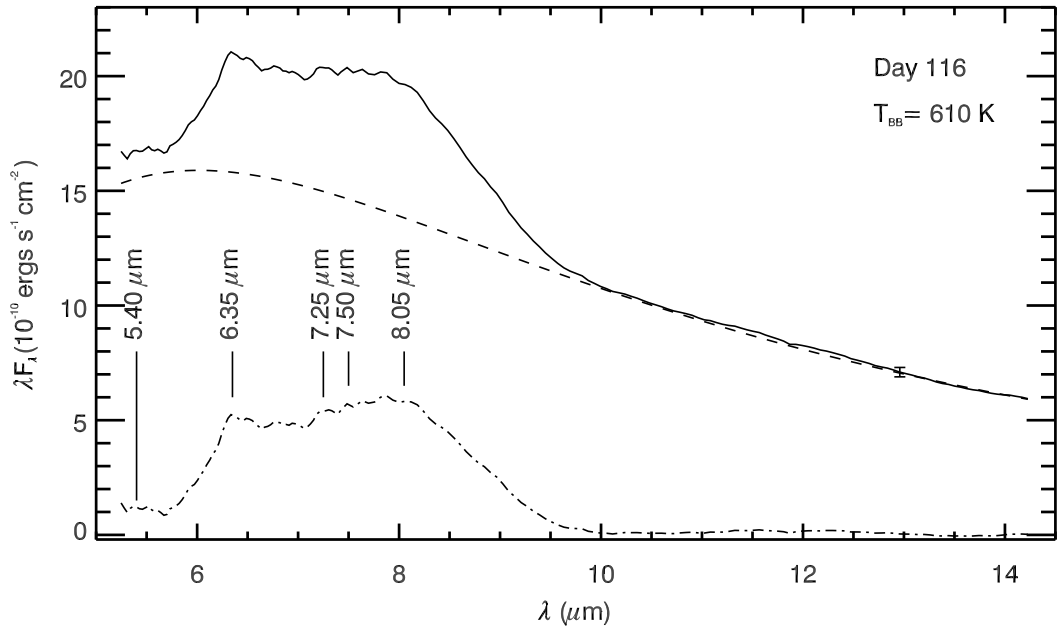

Figure 5.10: *Spitzer* SED of V2361 Cyg obtained on 2005 June 06 (Day 116). A representative 1-σ error bar is plotted near 13 μm. The dashed line indicates the blackbody fit to the continuum at a temperature of 610 K. Otherwise as Figure 5.9.

By the third epoch, day 251 after outburst (Figure 5.11), the 6-10 μm emission complex had taken on a much different appearance. Rather than being relatively broad and flat, the overall shape was much more sharp, peaking at 8 μm. The 6.4 μm emission component had declined significantly in strength with respect to the 8 μm feature and now appeared to be a shoulder on the broad triangular 8 μm component. The continuum fit at this epoch was exceptional, as evidenced by the flat residuals in the featureless regions of the SED from $15 - 38$ μm, and very closely resembled a blackbody of 380 K. This strongly supports our hypothesis that the continuum arose from regions of the ejecta that were optically thick, in spite of the expectation that the broad overlying emission complexes arose from optically thin dust.

This epoch marked the first appearance of emission lines other than the strong

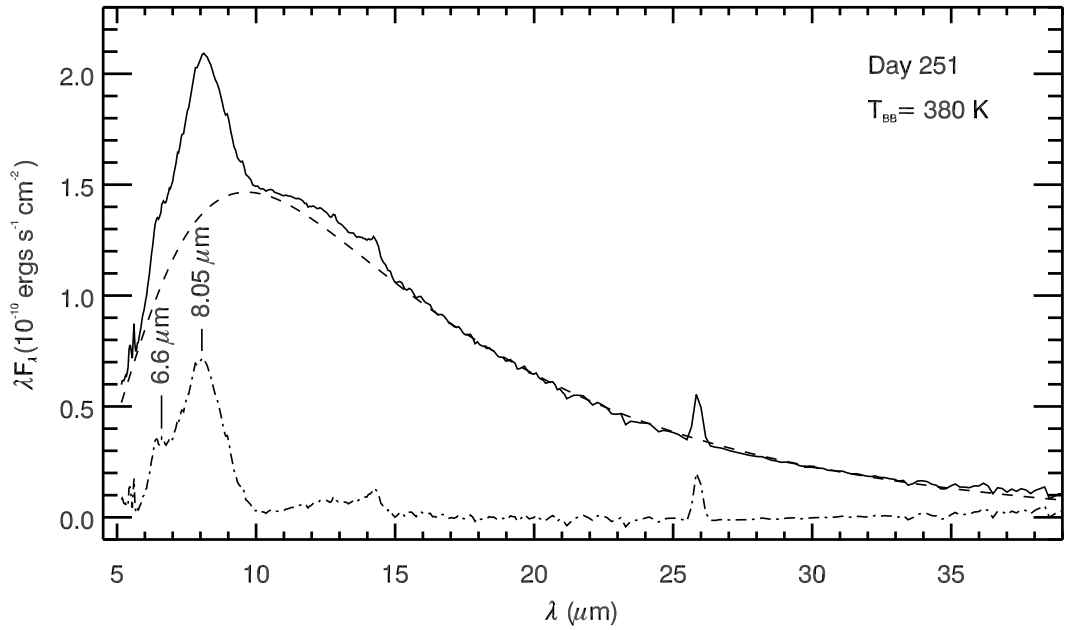

Figure 5.11: *Spitzer* SED of V2361 Cyg obtained on 2005 October 19 (Day 251). A representative 1-σ error bar, comparable to the line thickness of the data, is plotted near 30 μm. The dashed line indicates the blackbody fit to the continuum at a temperature of 380 K. Otherwise as Figure 5.9.

[O IV] line. [Ne II] λ12.81 μm and [Ne III] λ15.56 μm were present, though exceptionally weak and barely detectable above the noise. The strongest non-oxygen emission lines were from [Ne V] λ14.32 μm, [Ne VI] λ7.61 μm, [Mg VII] λ5.50 μm, and [Mg V] λ5.61 μm. [Ar III] λ8.99 μm and [S IV] λ10.51 μm were in evidence at levels comparable to [Ne II]. The conspicuous lack of [Ne V] λ24.30 μm suggests a nebular environment similar to that observed in V2362 Cyg on day 522. The [Ne III] λ15.56 μm and [Ne V] λ14.32 μm lines were of order 3100 km s^{-1} FWHM line width, while the [O IV] line was slightly narrower, FWHM $\sim$ 2750 km s^{-1}. The other emission lines were too weak to ascertain their widths. The dominance of the highly ionized species such as [Ne VI] λ7.61 μm and [Mg VII] λ5.50 μm indicates that at this point in the evolution the ejecta were being subjected to an

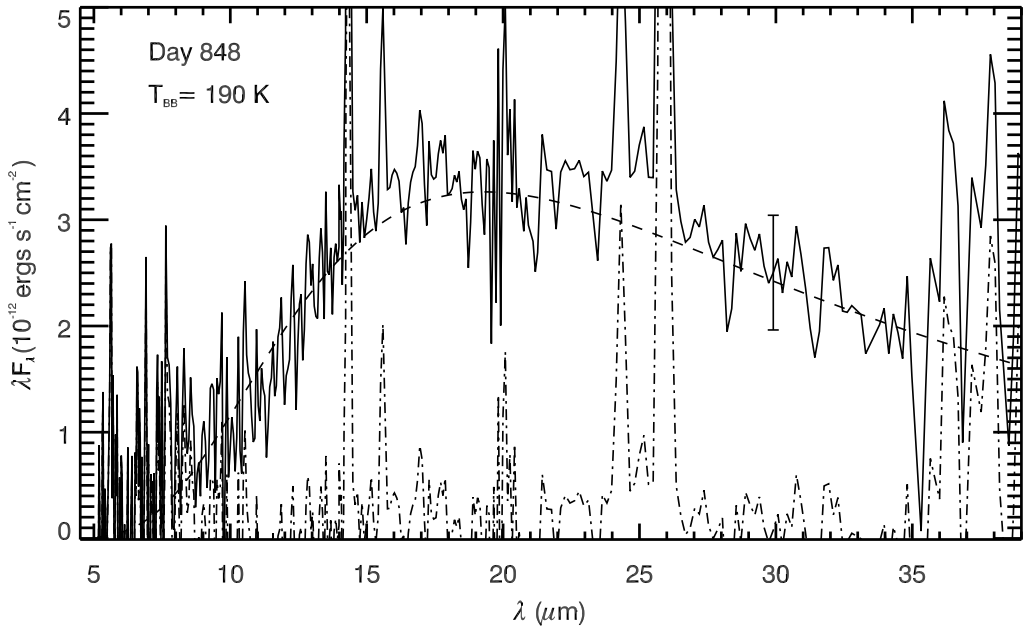

Figure 5.12: *Spitzer* SED of V2361 Cyg obtained on 2007 June 08 (Day 848). A representative 1-σ error bar is plotted near 30 μm. The dashed line indicates the blackbody fit to the continuum at a temperature of 190 K. None of the emission features in the $6 - 12$ μm region are still apparent in these spectra.

extremely intense radiation field. Production of Ne VI and Mg VII requires photon energies greater than 126.21 and 186.51 eV respectively.[2]

The next set of *Spitzer* observations were obtained nearly 600 days later (day 848, Figure 5.12). By this stage of evolution, the continuum intensity had declined by two orders of magnitude, though it was still well fit with a blackbody emission model, now at 190 K. The 6-10 μm emission complex was no longer in evidence. Due to the low flux, the only emission lines observable with any confidence at this late stage of evolution were [Ne III] λ15.56 μm, [Ne V] λ14.32 and λ24.30 μm and [O IV] λ25.91 μm, indicating that the general state of ionization of the ejecta remained unchanged. Again, the characteristics of the nebular lines were very

[2] http://www.ipac.caltech.edu/iso/lws/atomic.html

similar to that observed in V2362 Cyg. However, if V2361 Cyg exhibited the same contrast between the broad features relative to the emission lines as in V2362 Cyg, the broad features should have been detected at this epoch. Subsequent *Spitzer* observations over the following $\sim$ 400 days indicated that the dust was slowly cooling.

5.6 Carrier Identification for the $6 - 12$ μm Emission Complex

To identify the individual features present in the *Spitzer* spectra, we conducted multi-component Gaussian fitting to the emission residuals after blackbody subtraction. We fitted the profiles using a non-linear least squares Gaussian fitting routine as described in Chapter 3. The results are shown in Figure 5.13.

In V2362 Cyg, distinct emission peaks appeared at 6.4, 7.9, 9.5, 11.35, and 17.9 μm. Additional weak features may have been present at 6.9 and 12.5 μm. The peak wavelengths of the Gaussian components are slightly different than those identified in the discussion above since they are the formal fits to the data. As discussed in §5.4, the features near 9.5 and 18 μm may be associated with silicates. As the system evolved, the central wavelengths of the UIR features varied slightly and irregularly, while the flux ratios changed dramatically. The 6.9, 11.4, and 12.5 μm features declined rapidly and soon disappeared. The fluxes of the 6.4 and 7.9 μm features also declined relative to the 9.5 and 17.9 μm features and, at later times, the 17.9 μm feature began to dominate the spectrum.

In V2361 Cyg, UIR emission features were observed at 5.4, 6.4, 6.9, 7.1, 7.5, 8.1, 11.4, and 12.4 μm. As the ejecta evolved, the complex of features between 6.4 and 8.1 μm blended together to form a single plateau, while the 6.4 to 8.1 μm flux ratio diminished significantly. The 11.5 and 12.4 μm features joined to produce a broad structure around 13.1 μm.

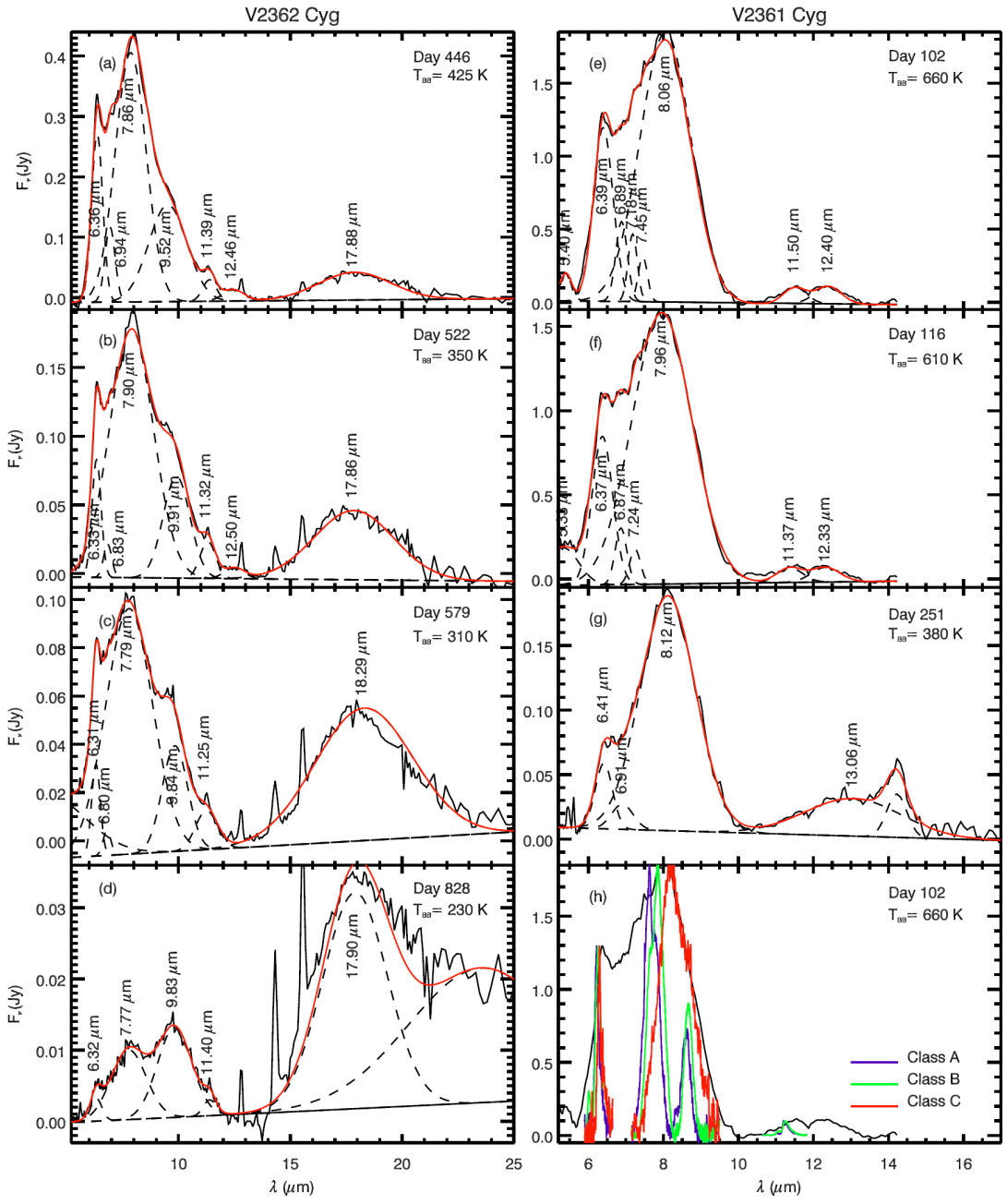

Figure 5.13: Residuals for V2362 Cyg, (a)-(d), and V2361 Cyg, (e)-(g). Dashed lines are individual Gaussian components of the composite fit shown in red. Panel (h) shows Class A, B, and C PAH profiles overlaid on the V2361 Cyg spectra from Day 102.

5.6.1 Silicates

The position of the $9.5 - 9.7$ and 18 μm features observed in V2362 Cyg are coincident with the Si–O stretching and O–Si–O bending modes, solid state features of astronomical silicates. In many CNe, the 9.7 μm feature is more broad (e.g., V705 Cas and V1065 Cen; Evans et al. 1997; Helton et al. 2010b, respectively) and shifted to a slightly longer wavelength than that observed here (e.g., V1370 Aql and V838 Her; Smith et al. 1995). Late time observations of CNe taking advantage of the excellent sensitivity of *Spitzer* have revealed never before seen changes in the silicate emission characteristics as the grains age in the nebular environment. Observations of V1065 Cen showed that as the system evolves, the intensity of the 9.7 μm feature declines substantially relative to that of the 18 μm feature. After day 500, the mid-IR SED was dominated by the 18 μm feature. The shape of this feature is similar to that observed by Rho et al. (2008) in the Cassiopeia A supernova remnant, which they identify as being due, in part, to magnesium protosilicates. Thus, we consider silicates to be likely candidates for the carrier of the $9.5 - 9.7$ and 18 μm emission features in V2362 Cyg.

None of the observed emission features correspond to those of crystalline silicates as seen in cometary spectra. Though the general shape is consistent, i.e., a broad complex plateau, the cometary crystalline features typically appear in the $9 - 12$ μm region (Harker et al. 2002).

5.6.2 Polycyclic Aromatic Hydrocarbons - PAHs

Though the coincidence of PAH emission features to the observed UIR bands is reassuring, there is no direct evidence supporting the identification of individual PAH molecules in an astronomical environment. As noted by Bernstein & Lynch (2009), the PAH hypothesis relies on a PAH population distribution of molecules, each having a unique emission spectrum, that can be linearly coadded to produce the observed UIR characteristics. These models typically require the inclusion

of a broad range of sizes C_xH_y, where x can range from a few to a few hundred, with a mix of ionization states, and varying degrees of nitrogenation and dehydrogenation.

The wavelengths of the features observed in our dusty novae targets do not correspond with the canonical PAH features observed at 6.2, '7.7', 8.6, and 11.3 μm. Peeters et al. (2002); van Diedenhoven et al. (2004) have examined a wide variety of astronomical sources exhibiting UIR features to empirically identify different classes of carrier. We have overlaid the 6-12 μm profiles of these features on the day 102 spectrum of V2361 Cyg in Figure 5.13, Panel (h). As can be seen from the figure, Classes A and B do not match the observed features well at 6.2, 8.0, or 11.2 μm, and hence, may be excluded as potential contributors. The Class C profile, however, does provide a relatively consistent match to the red edge of the 8 μm feature and may also fit the 6.2 μm feature.

The 6.2 and '7.7' μm features are attributed to C–C stretching mode vibrations while the features in the range of $11.3 - 13.3$ are attributed to C–H out-of-plane bending modes where the precise position of the feature is determined by the number of adjacent C–H bonds (Schutte et al. 1990). Based upon the environments in which the different classes were observed, Peeters et al. and van Diedenhoven et al. have described the carrier of the features within the context of the PAH hypothesis. They note that Class A profiles probably arise from nitrogenated PAHs (i.e., in which a nitrogen atom is substituted for a carbon) that are subjected to a relatively hard radiation field. For example, Class A sources in their sample included H II regions and planetary nebulae. Class B profiles are thought to arise on "pure" carbon PAHs and likely formed in a manner similar to terrestrial soot particles. These authors suggest that Class A profiles arise from molecules similar to those in Class B that have been processed by an energetic radiation field. In contrast, the Class C profile is only seen in sources with a relatively mild illuminating source ($T_{eff} \approx 5000 - 6000$ K), typically post-AGB stars (Peeters et al. 2002; Sloan et al. 2007).

Further, Boersma et al. (2010) have shown that additional features are often

present in the $15 - 20$ μm region. They find a significant positive correlation between the strength of the 6.2 μm feature and a feature at 16.4 μm. There is no evidence for a feature at 16.4 μm in any of our spectra. Based upon the strength of the 6.2 μm feature in the spectra of the sources presented here, however, the 16.4 μm feature may be within the noise, even if present.

The general trend observed in these PAH classifications (Peeters et al. 2002; van Diedenhoven et al. 2004) runs contrary to what might be expected for the environment of dusty novae. As demonstrated in Figure 5.13, Panel (h), the worst fit corresponds to Class *A* profiles, which bears a greater resemblance to the hard radiation to which CNe ejecta are submitted than to the soft radiation illuminating Class *C* sources. In fact, Sloan et al. (2007) and Keller et al. (2008) note that both the standard '7.7' and 11.3 μm features tend to shift bluewards for an increasingly energetic illuminating source. In dusty novae, the trend seems to be opposite; the dominant feature is nearer to $8.0 - 8.2$ μm and the 11.3 micron feature appears nearer to $11.4 - 11.5$ μm at a stage when the illuminating source has an effective temperature $T_{eff} \sim 10^5$ K (Evans et al. 2010b).

Thus, it seems that of the different classes of astronomical PAHs, Class *C* carriers are most likely to be present in the ejecta of dusty novae. As noted above, there are still difficulties with this identification in spite of the coincidence between the Class *C* profile and the shape of the 8 μm feature observed in these dusty novae. If the Class *C* carrier is a PAH molecule, what is the likelihood that it could survive being subjected to the hard radiation present in the environs surrounding CNe?

Evans & Rawlings (1994) have calculated that small PAHs (i.e., molecules with fewer than 24 C atoms) have a very short lifetime in the environment of a CN. Due to the high UV flux, a free-flying PAH molecule would absorb about one high energy photon every second. Full disruption of the molecule, however, would require multiple high energy photon interactions in order to break more than two C–C bonds before the molecular bonds have the chance to reconnect. Evans &

Rawlings estimate that the timescale for a PAH molecule to be completely disrupted due to multiphoton interactions is less than a day. Further, these same molecules would also be subjected to chemical erosion through collisional interactions in the ejecta. For reasonable densities, temperatures, and abundances in the ejecta, Evans & Rawlings estimate that these PAHs would be destroyed due to chemi-sputtering by H and O in a matter of hours. Consequently, it is very unlikely that there is a stable population of free-flying small PAHs contributing to the observed emission features.

Larger molecules, i.e. of order 30 C atoms or more, would be more stable against high energy photons. The energy absorbed by a UV photon by a large PAH, rather than leading to disruption, would be distributed amongst many vibrational modes. In this case, it is more likely that the high vibrational energy could lead to the ejection of the peripheral H atoms resulting in large dehydrogenated PAHs, also known as polycyclic aromatic compounds (PACs; Schutte et al. 1990). For large molecules such as these, the binding energy of the peripheral hydrogen atoms is greater than 13.6 eV and consequently either photons with a much greater energy or highly energetic multiphoton interactions are required for H atom ejection (Schutte et al. 1990). The energy required for C loss is even greater. A high abundances of PAC molecules are predicted to produce features primarily at the 3.43, 3.53, 6.2, and 7.7 μm. Though it is possible that a 7.7 μm feature is blended into the plateau between the 8 μm and 6.2 μm features, it cannot be securely identified.

5.6.3 Hydrogenated Amorphous Carbons - HACs

An alternative explanation to the PAH hypothesis to account for the UIR features was suggested by Duley & Williams (1981, 1983) who argued that the $3-4$ μm absorption features in diffuse clouds could be due to –CH_3 and –CH_2 functional groups bound to the surface of small AC grains or as pendant groups on aromatic structures. These groups should give rise to features at $3.4-3.5$ μm due to C–H

stretching mode oscillations in the pendant groups.

Present HAC models (e.g., Smith 1984; Duley 1987) consist of clusters of PAH and diamond-like molecular groups loosely bound together in a complex polymeric structure. Due to the complex structure of these molecular agglomerations, there will be a disproportionately large number of aliphatic bonds than in large PAHs with a similar number of C atoms. Absorption of energetic photons in this model may result in excitation and emission from the surface bound molecular groups or in excitation and desorption of the surface groups followed by emission (Duley 1987).

Support for this model was presented by Tamor et al. (1989) who confirmed the presence of molecular benzene groups bound on the surface of small AC particles in laboratory experiments. Meanwhile, Duley & Jones (1990) found that the formation of HACs is a natural byproduct of AC grain condensation based upon laboratory data and theoretical models.

The emission features associated with HACs have not been well characterized. Based upon the conditions in the environment of CNe during and after dust condensation, Evans & Rawlings (1994) have shown that the observations of V842 Cen and QV Vul are consistent with rehydrogenation of dehydrogenated HACs, leading to an increased abundance of surface C–H bonds and strength in the associated 3.4 μm C–H stretch feature. Destruction of HACs may be able to explain the "isothermal" stage of emission observed in dusty novae, such as V842 Cen and V705 Cas (Evans et al. 1997), in which the photometrically determined dust temperature fails to decline as would be expected for expanding ejecta, and instead remains nearly constant for many hundreds of days after becoming optically thin. This "isothermal" behavior is consistent with that expected if the grains were being destroyed with a resulting decrease in the average grain size (Evans & Rawlings 1994, and references therein). Rehydrogenation of HACs is also predicted to give rise to "extended red emission" in the 0.5 to 7.5 μm range as was detected in QV Vul (Scott et al. 1994b).

Additional support for the HAC hypothesis may be provided by the match

between the 8.0 μm feature and the Class C profile. Sloan et al. (2007) have attributed the Class C profiles to carriers with a high fraction of aliphatic bonds. As mentioned above, the environmental conditions in CNe are quite different than those in typical objects exhibiting Class C profile characteristics. Examination of the $3-4$ μm region of dusty novae like V705 Cas (Evans et al. 1997) clearly suggests a high fraction of aliphatic bonds. This model also predicts that desorption of the surface groups and subsequent photodissociation will preferentially lead to the formation of cyclopropenylidene (C_3H_2; Leach 1989; Duley & Jones 1990), the signature of which may be detectable at millimeter wavelengths.

5.6.4 Small Carbonaceous Molecules - SCMs

Another alternative to the PAH hypothesis for the carrier of the UIR features was proposed by Bernstein & Lynch (2009). This model hypothesizes that small carbonaceous molecules (SCMs) may account for the majority of observed UIR features as well as their underlying plateau components. Their primary candidates for the SCM hypothesis were the relatively simple molecules ethylene oxide (EO; c-C_2H_4O[3]) and cyclopropenylidene (CP; c-C_3H_2), both of which have strong transitions in the classical UIR bands at 3.3, 6.2, '7.7', 8.6, and 11.2 μm bands. SCMs are excited through absorption of UV photons in a manner similar to PAHs.

The SCM model has some distinct advantages in accounting for the standard astronomical UIR features. Rather than depending upon a diverse population of molecules, each with an exceptionally complex emission spectrum, the SCM hypothesis relies on a combination of emission from relatively few molecular species. Of the molecular species involved, at least one, CP, has been detected in other astronomical sources exhibiting UIR emission bands (Bernstein & Lynch 2009, and references therein).

[3] The lower case "c-" denotes the cyclic form of the molecule.

This model suffers some of the same hindrances as the PAH hypothesis. Neither laboratory nor theoretical spectra of both PAHs and SCMs correspond exactly with UIR features observed in astronomical sources. Hence, both models must rely on the assumption of various line shifting mechanisms (e.g., vibrational anharmonicity, Fermi resonance splitting, etc.; Barker et al. 1987) to align the emission features with those observed (Bernstein & Lynch 2009). Additionally, the small size of these molecules means that they would have a relatively short lifetime in the environment of a CN. Thus, if they are present, they would necessarily be a transient population.

The Bernstein & Lynch model provides another more probable source for the peculiar UIR emission features observed in the dusty novae presented. The UIR features in these novae may be due to emission from EO molecules bound to the surface of larger grains, likely amorphous carbon. In this model, the absorption of a UV photon results in excitation of the molecule to the extent that it desorbs from the surface of the dust grain and emits the UIR features. Upon being freed from its parent dust grain, the free flying SMC would be quickly destroyed by the energetic UV field. This model is very similar to that provided for emission from PAH components on small carbonaceous grains as described in §5.6.3 above.

5.7 The Model

The *Spitzer* IRS observations of DZ Cru, V2362 Cyg, and V2361 Cyg in combination with the previous studies of V705 Cas, V842 Cen, and QV Vul provide the basis for an elementary model for the production and processing of dust and complex hydrocarbon molecules in classical novae.

The dust formation process is still poorly understood. Many novae have exhibited the formation of CO and CN molecules, considered to be possible precursors for dust grain nucleation sites, prior to the dust condensation event (e.g., V842 Cen, V705 Cas; Hyland & McGregor 1989; Evans et al. 1996, respectively). On theoretical grounds, it is believed that these molecules arise in the carbon neutral

zone of the ejecta as energetic photons capable of ionizing carbon would also easily photodissociate these simple molecules (Rawlings 1988; Rawlings & Williams 1989). In order for CO to form efficiently, there must be H_2 present since it is a critical step in the most efficient chemical pathway to CO formation (Rawlings 1988). Rawlings (1988) also found that H_2 (and molecules like CO) cannot form in typical CNe ejecta unless there exist regions of significant overdensity.

In spite of the theoretical difficulties in the dust formation process, it is clear from observations that once initiated, dust production proceeds quite rapidly with dust grains condensing out of the gas phase and growing to sizes up to ~ 1 μm in a matter of days (Evans & Rawlings 2008, and references therein). The types of dust produced during the condensation event depends on the conditions and abundances in the ejecta. In typical novae, the dust formed is composed of AC, silicates, or some combination thereof. In the novae discussed here, the dominant dust species appears to be carbonaceous.

With the onset of dust condensation, the resultant shielding greatly enhances the rates at which the reactions can occur. Evans & Rawlings (1994) suggest that during the optically thick stage of dust formation, the rate of H capture is greater than the rate of UV photon absorption. Thus, the conditions are conducive to the growth of aliphatic bonds, e.g., HAC grains. Further, the ejecta of CNe are often highly overabundant in carbon, again favoring the growth of organic molecules and larger carbonaceous dust grains. Hence, the formation of HACs in the ejecta of dusty novae during the optically thick stages seems likely. This argument suggests that there may exist smaller PAH molecules and larger, more complex, HAC agglomerations.

Dust shielding and grain growth through aliphatic bonding provide a possible explanation for the correlation between the features seen in these dusty novae and Class *C* profiles. In this model the hydrocarbons form in an optically thick environment shielded from the hard excitation source. As the dust disperses, the carrier of the 8 μm emission feature is gradually exposed to the hard radiation field. If the profile shape is determined primarily by the molecular species present

and less by the excitation conditions, then the match to Class C profiles may indicate similar molecular carriers for that portion of the emission. This conclusion is supported to some extent by the association of Class C features with HACs discussed above (Sloan et al. 2007).

The 3.3 and 3.4 μm emission features are typically attributed to unsaturated C–H stretching mode oscillations in aromatic molecules and saturated C–H stretching vibrations in aliphatic bonds. Thus, the 3.28/3.4 μm ratio can be used as an indicator of the relative abundance of aromatic to aliphatic structures in the emitting material (Sloan et al. 1997). The behavior of these features in V705 Cas was similar to those observed in V842 Cen and QV Vul, suggesting a predominance of aliphatic bonds. This similarity supports the hypothesis that the peculiar emission features in these sources were due to HACs. Unfortunately, we have no near-IR observations of DZ Cru, V2362 Cyg, nor V2361 Cyg in the $3-4$ μm range during the post-dust condensation epochs.

If some of the emission features seen in V2361 Cyg, V2362 Cyg, and DZ Cru can be attributed to small PAHs instead of HACs, then there must be a reservoir of material from which the PAHs are being repopulated. A possible source for this material could be either HACs or the larger AC grains themselves. For example, if the UV photons are of high enough energy ($\geq$ 3.6 eV; Serra Díaz-Cano & Jones 2008), they could disrupt the aliphatic bonds in HACs, releasing molecular PAH components. Though rapidly destroyed, excitation of this transient population of free-flying PAHs could generate some of the observed UIR emission features. Destruction of these molecules could account for the observed changes in the emission profiles and relative intensities of the features as the system ages.

Alternatively, the absence of the UIR emission features at late times in the spectra of V2361 Cyg and the weakness of the UIR features in V2362 Cyg may be due to a lack of energetic UV photons capable of exciting the molecular carrier of these features rather than that the carrier is no longer present. Indeed, *Swift* was unable to detect significant X-ray emission from V2361 Cyg at 1070 days after outburst suggesting that by this date, and likely for some time prior, ongoing

nuclear fusion on the WD surface had turned off. *Swift* observations of V2362 Cyg exhibited significant X-ray flux that increased in intensity from days $195 - 381$, but that gradually declined over the following 100 days. By day 814, the source was only marginally detected in X-rays, indicating that the source had turned off.

At these late stages in the development, however, there should still be a significant UV flux from the hot ($\sim 10^5$ K) surface of the WD capable of exciting the UIR carrier. Further, models by Ferland et al. (1984) of the reestablished accretion disk of DQ Her decades after eruption, suggested a relatively high UV flux for a wide range of mass accretion rates. Assuming that the accretion disk behavior in V2362 Cyg and V2361 Cyg was similar to that in DQ Her, the UV flux should have been sufficient to excite whatever molecular carriers of the UIR features that were still present in the ejecta. Hence, that the lack of emission from the UIR features at late times most likely indicates that the molecular carriers had indeed been destroyed, supporting the hypothesis of grain destruction presented above.

5.8 Conclusions

Our observations of the dusty novae DZ Cru, V2362 Cyg, and V2361 Cyg, have revealed UIR emission features that were peculiar in many respects relative to the canonical UIR emission characteristics. Based upon these observations as well as previous studies of V842 Cen, QV Vul, and V705 Cas, we suggest that the carrier of these peculiar emission features could be hydrogenated AC compounds composed of agglomerations of PAH molecules of various sizes loosely bound by aliphatic bonds. Similarly, the carrier could be AC with surface bound SCM molecules. It may be possible to confirm the presence of HACs or AC with surface-bound SCMs by observations during dust condensation and subsequent tracking of the evolution in the $3-4$, $6-10$, and $15-20$ μm windows at high spectral resolution. Detection of the rotational transitions in SCM molecules such as CP and EO at radio wavelengths would provide strong additional support for these hypotheses.

Chapter 6

Conclusions and Future Work

6.1 Conclusions

The work presented in this thesis is an attempt to explore many fundamental questions about classical nova outbursts, the physics and chemistry involved in their eruptions, and the greater impact on their surroundings. This work is based upon our highly successful *Spitzer*, *Swift*, Gemini, and optical observational campaigns. I have presented the analysis of 7 CNe of different types throughout a broad range of evolutionary stages of development from a few days to many years after outburst. This research highlights the critical importance of multiwavelength observations obtained at a high temporal cadence necessary to generate a comprehensive picture of the evolution of the CN system and to examine many time sensitive physical processes. These processes range from the determination of abundances in the ejecta to the examination of dust condensation and identification of peculiar molecular species in the dusty nova environment.

My role in this effort has been to obtain time on various telescopes, to design observational strategies on both space and ground based telescopes with coverage from the optical through the infrared, and to analyze and publish the results. I have been involved in our optical observing program using the Bok 90" (2.29-m) telescope on Kitt Peak for the past four years and have been the lead on this

program for three years. I have played an active role in the observational planning of our highly successful *Spitzer* classical and recurrent nova monitoring and target of opportunity programs, and have been responsible for much of the data reduction and analysis. I have been the primary investigator on four successful programs to observe novae in the near- and mid-IR using instruments available on the Gemini Telescopes. I have reduced and analyzed much of these data using various analytical and computational modeling techniques, including the Cloudy photoionization code and the DUSTY radiative transport code.

This observational program has been highly successful. We have obtained high quality optical and IR data on nearly 50 different CNe, many of which are still being actively monitored. In addition to the CNe studies presented in this thesis, my involvement in this observational program has yielded numerous collaborative publications, including detailed optical, infrared, and X-ray analysis of the 2008 outburst of the recurrent nova RS Ophiuchi (Evans et al. 2007a,b; Ness et al. 2009), examination of the CO nova V1186 Scorpii (Schwarz et al. 2007b), and late stage evolutionary analysis of nova QU Vulpeculae (Gehrz et al. 2008a). This program has also resulted in the publication of 7 circulars, brief publications intended for rapid dissemination of discovery reports and critical evolutionary developments, including V5586 Sagittarii (Helton et al. 2010a), V2468 Cygni (Schwarz et al. 2009), V1280 Scorpii (Ness et al. 2009), V1721 Aquilae (Helton et al. 2008d), V2670 Ophiuchi (Helton et al. 2008c), V2671 Ophiuchi (Helton et al. 2008b), and V2491 Cygni (Helton et al. 2008a).

Below, I summarize the key discoveries and analytical results from the research on CNe presented in this thesis. This is followed by a brief discussion of the ongoing and future work involved in this observational program.

6.1.1 V1065 Cen

V1065 Cen was monitored extensively in the optical and mid-IR as part of this observational program. Based upon careful examination of these extensive data,

I have presented a detailed evolutionary sequence of this system and have estimated key fundamental properties, including the degree of extinction to which the spectra are subjected, E(B-V) = 0.5 ± 0.1, and the distance to the system, $d = 8.7^{+2.8}_{-2.1}$ kpc. X-ray observations at the later stages of the development revealed that thermonuclear fusion on the WD surface had halted within two years of the outburst.

Photoionization modeling indicated that the ejecta were heavily depleted of hydrogen and highly elementally enriched. The abundances, calculated by number relative to hydrogen, relative to solar were He/H = 1.6±0.3, N/H = 144±34, O/H = 58±18, Ne/H = 316±58, Mg/H = 45±13, S/H = 54±31, and Fe/H = 6.6±2.3. The high abundances of nitrogen and neon in particular confirm that V1065 Cen was an eruption on the surface of an ONe WD. The sulfur abundance was very high and though some TNR models suggest that breakout from the CNO cycle can result in elevated sulfur abundances, they do not predict an overabundance as high as that estimated in our Cloudy models. The most likely explanation is that the high sulfur content was due to dredge-up from the underlying WD. The results of the photoionization models were used to calculate the ejected mass. These calculations indicate a gas mass of $(1.6 \pm 0.2) \times 10^{-4}$ $M_{\odot}$, comparable to estimates for other ONe systems and an order of magnitude higher than expected from models of TNR on the surface of a WD.

Analysis using the DUSTY radiative transport code revealed that the dust in V1065 Cen was composed primarily of silicates ($\geq$ 95%) with a grain size distribution that was slightly flatter than that in the ISM with a power law slope of $q = 3.0$. The solid-state emission features arising from the silicate dust exhibited striking differences from those observed in other astronomical sources. These differences were likely due to the elevated oxygen content of the gas from which the dust condensed and a high grain porosity. The poor fit to the silicate emission indicates that additional work must be done to accurately determine the carrier of the silicate dust features in CNe. Based upon the DUSTY models and examination of the optical light curve, the dust mass was estimated to be of order $10^{-8} - 10^{-7}$

$M_{\odot}$, at the high end for dust production in ONe CNe.

6.1.2 Old Novae

Late time observations are useful in exploring the evolution of the CN ejecta. The presence of highly ionized species late in the development can be compared to the recombination timescales to determine whether the lines are "frozen-in" or are being ionized by emission from another source such as the reestablished accretion disk. Further, some atomic species are observable in the IR late in the evolution that could not be detected at earlier stages. This allows the determination of abundances of additional species important for understanding the ejecta and WD compositions.

Analysis of the *Spitzer* observations presented here yielded robust lower limits to the abundances of elemental species in the ejecta of V1974 Cyg, V382 Vel, and V1494 Aql. The abundance of neon by number, relative to hydrogen in V1974 Cyg was found to be at least 39 times the solar values (assuming the solar values provided by Asplund et al. 2009) and oxygen was found to be at least 10 times solar. The neon abundance in V382 Vel was found to be at least 11 times solar, while we estimated the oxygen abundance to be greater than 1.4 times solar. The abundance estimates for V1974 Cyg and V382 Vel were consistent with earlier reports and helped establish that these systems held an ONe WD progenitor. Additionally, we placed weak lower limits on the sulfur and argon abundances in the ejecta of V382 Vel, at 0.07 and 0.03 times solar respectively. These were the first abundance estimates for elements in this system. The observations of V1494 Aql revealed the first detection of neon in the ejecta of this object and allowed a lower limit to be set on the neon abundance of ~ 3 times solar. This abundance estimate, combined with that of oxygen abundance of > 12 times solar, implied that the progenitor in V1494 Aql was a CO WD.

The high resolution data were able to resolve the emission line profiles in each of these sources. These observations suggest that the different ionization species

arise from separate regions in the ejecta and that the sources of emission may have distinct morphological differences. The stability of the line profiles suggests that the ejecta distribution is stable at the late stages of the eruption and that the line profiles are no longer being shaped by optical depth effects.

6.1.3 Dusty Novae

Our *Spitzer* monitoring of the dusty CNe DZ Cru, V2362 Cyg, and V2361 Cyg has revealed an array of peculiar emission features that have been observed only rarely in dusty novae. The high sensitivity and spectral resolution of the observations presented here have enabled us to examine the emission profiles in detail providing us with new insights into the nature of the molecular carrier of the unidentified infrared features in dusty novae. These observations reveal extreme changes in the emission characteristics of the carrier as the dust evolves providing insight into the processes of molecular processing and destruction in CN ejecta.

To date, the UIR features observed in dusty novae are poorly understood. Attempts to associate them with free-flying polycyclic aromatic hydrocarbons and small carbonaceous molecules fail due to the poor match with observed emission profiles and the high rate of destruction by energetic photons expected in the environment of a CN. A more likely explanation is for emission from hydrogenated amorphous carbon agglomerations or similarly structured amorphous carbon with ethylene oxide (or other SCM) surface groups. The explanations involving processing of large molecular agglomerations and emission from molecular surface groups bound to larger particles are considered to be the most promising.

We have demonstrated that isolated observations of dusty novae will not prove adequate to understand dust formation and processing, and that observations with a high temporal cadence are desired. In order to better constrain the carriers of the UIR features observed in CNe, it is critical to obtain observations of the expanding ejecta throughout the dust condensation and subsequent optically thin stages. If the carrier molecules are being formed during the initial condensation

event, they may be observable during or immediately after condensation. Our observations highlight the need for data covering the $3 - 4$ μm region, which are required to determine the relative contributions of aromatic to aliphatic material. Further, a direct test of the HAC and SCM hypotheses for these sources can be made by attempting to observe the radio wavelength rotational bands of SCMs such as cyclopropenylidene and ethylene oxide. Though not conclusive, a positive detection in a dusty nova exhibiting the peculiar UIR emission bands would provide strong support for the processing of HACs or AC with surface bound SCMs.

6.2 Ongoing and Future Work

Many sources of interest from our database of *Spitzer*, *Swift*, Gemini, and optical programs remain to be examined. There is a wealth of data still unexplored that will provide additional insights into the CN phenomenon and the impact of CNe on a wider scale. Some of these data are the subject of active, ongoing examination and are briefly mentioned below. The research presented in this thesis has highlighted the need for observations with broad wavelength coverage and high temporal resolution. This research has also revealed specific observations needed to address remaining questions about CNe and provided direction for future observational studies.

6.2.1 V574 Puppis

V574 Puppis was discovered by by A. Tago and independently by Y. Sakurai on 2004 November 20.7-20.8 Nakano et al. (2004). Maximum occured on November 26.1 at $m_V \sim 8.0$ (Siviero et al. 2005). Preliminary spectra revealed P-Cyg profiles on Hα and Hβ at a blueshift of -860 km s^{-1} and Fe II in absorption (Ayani 2004). Near-IR observations obtained 5 days later by Ashok & Banerjee (2004) showed allowed transitions of O I, C I, and N I along with hydrogen recombination lines.

Initially, the nova light curve declined rapidly with $t_2 \sim 8$ days resulting in the classification of V574 Pup as a "fast" nova. The system subsequently experienced a plateau resulting in a much longer t_3 time of 58 days (Siviero et al. 2005).

Very few spectroscopic observations of V574 Pup were reported in the literature throughout the early nebular stages of development. Observations by Rudy et al. (2005), obtained more than a year after outburst, indicated that they system had evolved dramatically and was well within the coronal stage of nebular development. They reported the appearance of highly ionized species such as [Si VI], [Si VII], [Ca VIII], [S VIII], and [S IX]. They also noted that the unidentified nova lines at 0.8926, 1.1110, 1.5545, and 2.0996 microns were also present. *Swift* observations indicated that the system had been in a SSS state since July 2005 (Ness et al. 2007a).

Reddening estimates were derived for V574 Pup based upon both the intrinsic colors at maximum light and at t_2 expected for CNe and on the equivalent widths of the Na I D lines (Siviero et al. 2005). Both methods suggest a very low reddening, E(B-V) ≤ 0.05. With a negligible extinction and a t_2 time of 13 days, Siviero et al. (2005) estimate a distance of $\sim 15 - 20$ kpc depending on the MMRD relation used. The Galactic extinction maps of Schlegel et al. (1998) suggest a total extinction along the line of sight towards V574 Pup of E(B-V) = 0.716 magnitudes. Though the nova is at very low Galactic latitude ($\sim -2^{\circ}$) implying a high degree of uncertainty in the reddening estimate, the extreme distance implied by the MMRD relation would support a higher degree of extinction. This suggests either that the color of V574 Pup was atypical and was subjected to anomalously low Na I D absorption or that the distance was not accurately derived by the MMRD relation (Siviero et al. 2005). Using a better sampled light curve, Naik et al. (2010) determined t_2 and t_3 to be 10 ± 1 and 25 ± 2 days respectively. They also calculate a different reddening using the B-V color at t_2, E(B-V) = 0.63, more consistent with that expected for the target's position near the Galactic plane. Thus, Naik et al. estimate a distance to V574 Pup of 5.5 kpc based upon the MMRD relation of Della Valle & Livio (1995). For our analysis,

we assume a distance of 5.5 kpc.

V574 Puppis was observed with *Spitzer* on 10 dates from 120 to 1250 days after outburst (Rudy et al. 2006b). The initial spectrum was dominated by hydrogen recombination lines with additional strong emission from [Ne II] λ12.81 μm. There was already emission from [Mg V] λ5.61 μm and [Mg VII] λ5.50 μm at this epoch. By 350 days after outburst, the hydrogen emission had declined significantly. Emission from [Ne II] was now weak. Instead, the spectrum was dominated by [Ne VI] λ7.64 μm and the magnesium lines. Also present was emission from [Ar III] λ8.99 μm and [S IV] λ10.51 μm. The mid-IR emission spectrum was quite similar at 500 days after outburst, but at this stage, the continuum began to develop a broad emission feature near 10 μm that may be due to thermal emission by dust. If so, this is the first detection of dust in this object as no thermal emission from grains was observed at near-IR wavelengths (Rudy et al. 2006b; Naik et al. 2010). Throughout the remainder of the *Spitzer* observations, the emission lines observed near day 350 persisted with a gradual decline in strength relative to the continuum, but consistent strengths relative to one another. Likewise, the relative strength of the dust emission feature increased while the total flux declined.

We have begun preliminary photoionization modeling of the ejecta to determine the abundances using our *Spitzer* data along with optical and near-IR data obtained by other members of our group using the Visual and Near-Infrared Imaging Spectrograph (VNIRIS), a longslit spectrograph with coverage from 500 - 2200 nm, at the Lick 3-m telescope and the SpeX instrument (Rayner et al. 1998) at the Infrared Telescope Facility. Together, we had three epochs of observations with nearly contemporaneous observations from the optical through the infrared, near days 140, 360, and 785. We used a two component model following similar methods to those used in our analysis of V1065 Cen (Chapter 3 and estimated the abundances by combining the results of our analysis at all three epochs.

Our preliminary models suggest that helium and oxygen were only mildly overabundant by number relative to hydrogen, with respect to solar at 1.17 and 2.34 times solar respectively. Nitrogen was overabundant by a factor of roughly

20. All other elements were underabundant including neon (0.27 times solar), magnesium (0.22), silicon (0.60), calcium (0.30), and iron (0.81). Our models suggest an ejecta mass of $M_{\rm ej} = 1.5 \times 10^{-4}$ M$_\odot$. The model abundances suggest that the TNR processed the material via the standard CNO cycle with little production of heavier elements. Likewise, it appears that there was only minimal dredge-up from the underlying WD. We conclude that V574 Pup arose on a CO WD and that the abundances of the heavier metals likely reflect the composition of the secondary.

These results invite comparison to V1186 Sco, a nova that exhibited very similar behavior (Schwarz et al. 2007b). Interestingly, the photometric behavior of both of these systems bore a closer resemblance to expectations for a typical ONe type eruption, i.e. fast, smooth decline with little indication of dust formation. Similarly, [Ne II] emission at 12.81 μm was present in the mid-IR spectra of both systems at strengths beyond that of any other metal lines, in spite of low neon abundance. The behavior of V574 Pup supports the conclusion of Schwarz et al. (2007b) that true classification of CNe depends on the composition of the underlying WD. The composition is best determined from photoionization modeling, preferably using data with broad multiwavelength coverage obtained during different stages of development, and cannot be reliably inferred from observations of the light curve or phenomenological spectroscopic characteristics (e.g., observation of [Ne II] λ12.81 μm) alone.

6.2.2 V2467 Cygni

V2467 Cyg was discovered near maximum brightness by A. Tago at a magnitude of $m_V = 7.4$ on 2007 March 15.8 (Nakano et al. 2007a). Optical spectra obtained one day after discovery were just transitioning to the principal spectrum. They were characterized by absorption profiles in the Balmer lines and in Fe II, with a P-Cyg profile in Hα. The absorption trough was blueshifted by ~ -1200 km s^{-1} (Ayani 2007; Naito & Sakamoto 2007). Subsequent spectra obtained by

Munari et al. (2007b) on March 18.2 revealed Balmer recombination lines and strong Fe II multiplet emission leading to the classification of V2467 Cyg as an "Fe II"-type nova. These spectra exhibited two P-Cyg absorption components, at ~ -900 km s^{-1} and at ~ -1900 km s^{-1}.

Near-IR observations by Mazuk et al. (2007) indicated that within two months of outburst, the system had already transitioned to the coronal stage of development. Interestingly, the ejecta exhibited coronal line emission, such as [Si VI], [Si VII], [S VIII], and [S IX], at the same time as allowed transitions of neutral species including C I, N I, and O I. The coronal stage persisted through October 2007. The ionization of the ejecta had increased as indicated by emission from [Si X] and [S XI] (Russell et al. 2007b). The only neutral species that remained was O I. The FWHM expansion velocities at this epoch were ~ 2000 km s^{-1}, comparable to the maximum observed P-Cyg absorption components. Lynch et al. (2008a) noted that by 2008 June 15, the near-IR spectrum was dominated by [Mg VIII] $\lambda 3.03$ μm. Observations at this date and one hundred days later (September 23) with *Swift* revealed a strong underlying SSS (Ness et al. 2008c).

Munari et al. (2007b) made a preliminary estimate of the reddening towards the system of E(B-V) = 0.31 based upon the equivalent width of the interstellar Na I D2 line. Mazuk et al. (2007) were able to derive a more robust estimate of the reddening based upon the O I lines and found E(B-V) = 1.5. Later estimates using the same method found E(B-V) = 1.7, confirming this higher reddening value (Russell et al. 2007b). At no point was dust observed in the ejecta indicating that the extinction was entirely of interstellar origin.

The development of V2467 Cyg was quite interesting for a number of reasons. First, as the system entered into the transition stage of light curve development, it started to undergo oscillations of 0.5-1.1 magnitude with a period of ~ 20 days (Swierczynski et al. 2008). This behavior is observed only rarely (Gaposchkin 1957). Second, the system was found to exhibit two periods of short period variability on the order of 3.8 hours and 35 minutes with oscillation amplitudes of ~ 0.1 mag, which Swierczynski et al. (2009) have argued makes this system a

good intermediate polar candidate. Intermediate polars are characterized by very strong magnetic fields ($1 - 10 \times 10^6$ G) that truncate the accretion disk leading to the formation of accretion streams along the magnetic field lines (Patterson 1994). The prototype intermediate polar is the classical nova system DQ Her (Nova Her 1934). Finally, the spectroscopic evolution of the system progressed very rapidly, entering the coronal stage of development within only 60 days. Additionally, the coronal stage was characterized by extremely highly ionized species with ionization potentials as high as 447 eV (Russell et al. 2007b) as well as rarely observed species such as the unidentified nova lines at 1.11, 1.19, 1.55, and 2.10 μm (Mazuk et al. 2007; Rudy et al. 2002) and [P VII] at 1.37 μm.

V2467 Cygni was observed as part of our optical and *Spitzer* mid-IR CNe monitoring campaigns. Observation dates and basic details are provided in Chapter 2. The epochs of our observations are shown in Figure 6.1. The initial *Spitzer* observations were obtained during the transition stage of the light curve while optical observations were initiated after the oscillations had ceased. Subsequent observations were obtained well into the coronal stage of development. The *Spitzer* low-resolution spectra are shown in Figure 6.2. The analysis of these data is still in the early stages, however, a brief discussion of the preliminary results is provided here.

Our initial *Spitzer* observations showed a rich hydrogen recombination spectrum superimposed on a declining blue continuum that may be consistent with free-free emission from hot gas. The strongest non-hydrogen emission lines were from [O IV] λ25.91 μm and [Mg V] λ5.61 μm. Multiple ionization states of neon were present but were weak relative to the H, O, and Mg features. Also present was a broad emission structure from $15 - 25$ μm that may indicate the presence of a small amount of dust at this epoch.

By second epoch of *Spitzer* data, only 18 days later, the magnesium lines had strengthened considerably relative to the hydrogen lines. Multiple ionization states of Mg were present, including [Mg V], [Mg VI], and [Mg VII]. Also evident was a shoulder on the blended Pfund α+Humphreys β line due to [Ne VI] λ7.64

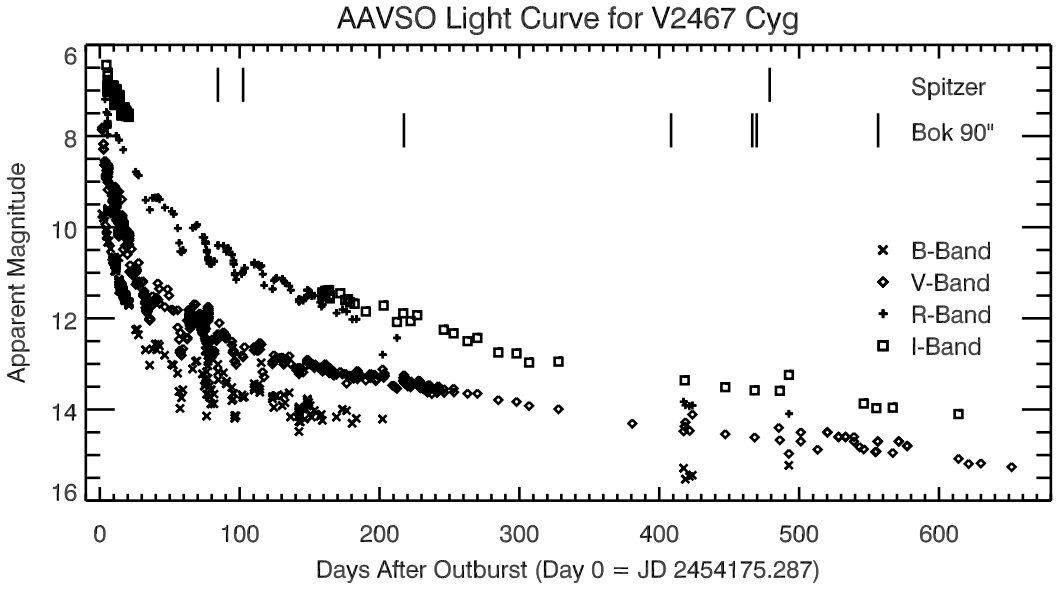

Figure 6.1: AAVSO light curve of V2467 Cyg. Vertical tick marks indicate the epochs of *Spitzer* and Bok 90" optical observations.

μm emission. This neon feature was much stronger than any feature of [Ne II], [Ne III], or [Ne V]. These observations are all consistent with the exceptionally high state of ionization in the ejecta observed at other wavelengths.

Our optical observations obtained on 2007 Nov 19 (day 249) are shown in Figure 6.3. These spectra were dominated by the [O III] doublet at $\lambda\lambda$4959, 5007 Å with additional strong features of [O III] λ4363 Å and [N II] λ5755 Å. Numerous other nitrogen lines were present as were highly ionized species of iron, including [Fe VI] and [Fe VII]. Neon was present at a very low level.

At this stage, there was only a very weak indication of [Fe X] λ6375 Å apparent as an emission shoulder enhancing the strength of [O I] λ6364. Unfortunately, the first *Swift* observations of V2467 Cyg were obtained nearly 240 days after these optical observations preventing us from determining whether the rise in [Fe X] λ6375 Å coincided with the onset of the SSS stage of X-ray emission.

The next epoch of *Spitzer* observations was obtained nearly 480 days after outburst. By this epoch, the hydrogen recombination spectrum had declined

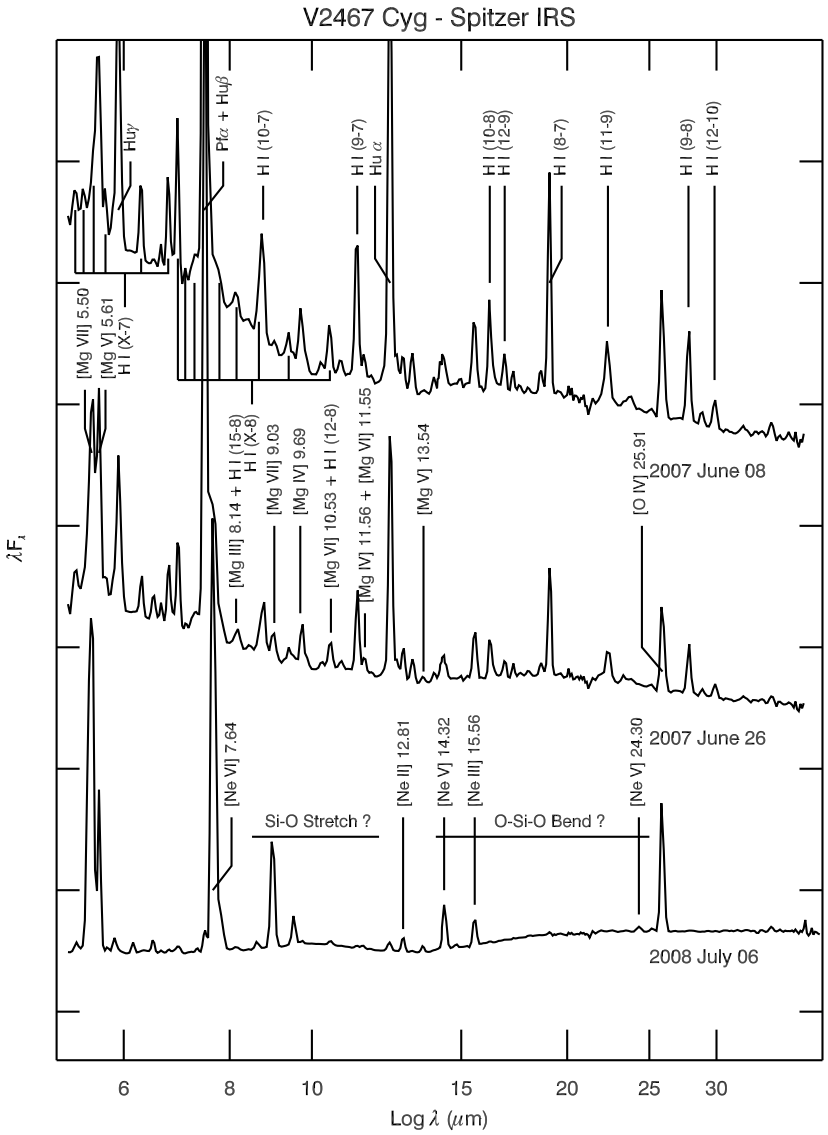

Figure 6.2: Three epochs of *Spitzer* spectra of V2467 Cyg obtained during the nebular and coronal stages of development. Prominent emission lines are labeled, as are possible solid-state emission features.

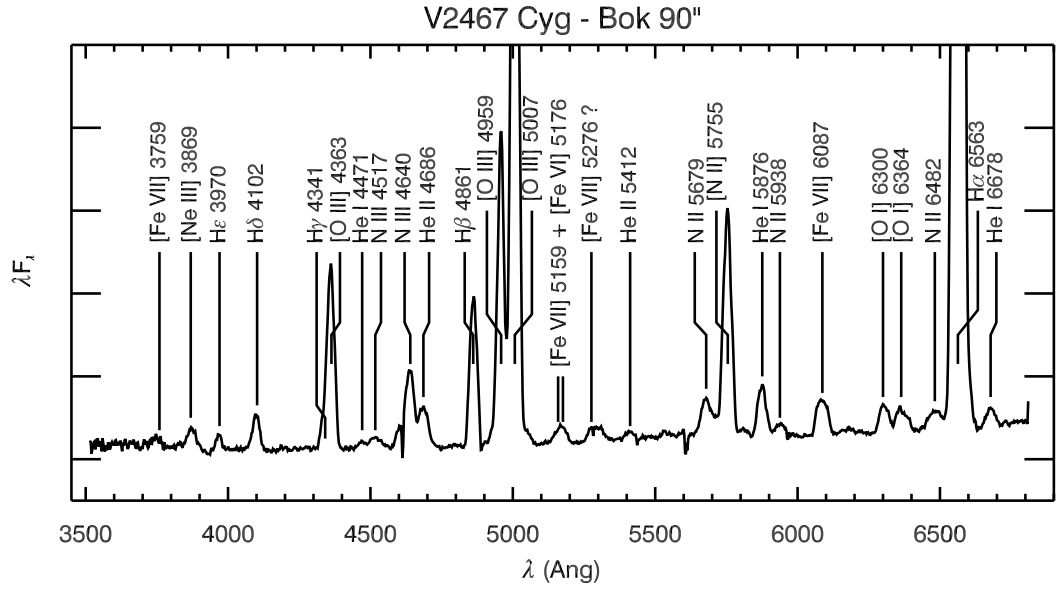

Figure 6.3: Optical spectra of V2467 Cyg obtained on 2007 November 19. Prominent emission lines are labeled.

substantially. The strongest emission line observed was due to [Ne VI] λ7.64 μm, but the Mg lines were also exceptionally strong. At this stage of development, the near-IR data were dominated by [Mg VII] λ3.03 μm (Lynch et al. 2008a). These data represent the most extensive array of magnesium lines observed in our monitoring program to date. Based upon the relative emission line strengths, we hypothesize that this system is highly overabundant in Mg relative to Ne and O.

The optical spectra of V2467 Cyg were not unlike the spectra of other fast, "Fe II"-type novae (e.g., V1065 Cen; Helton et al. 2010b). Indeed, Mg emission is also a common feature of CNe. However, the IR spectra revealed a rich magnesium emission spectrum, the strength and complexity of which clearly indicated that V2467 Cyg was a rarity amongst CNe. The interesting IR spectroscopic characteristics observed in this system emphasize the need for panchromatic observations of CNe in outburst. The observations of Mg lines in this object demonstrates that the IR spectra of novae is a rich source of information on elemental species that have few transitions at other wavelengths or that are very sensitive to blending

and contamination by other emission lines. The next step in the analysis of these data is to conduct rigorous photoionization modeling of the ejecta to determine the true elemental abundances, to characterize the development of the system overall, and to place it into the context of our current understanding of CNe.

6.2.3 Dusty Novae - Continuing Observations

Future dusty novae need to be followed carefully from the onset of dust formation through the late stages of evolution in the mid-IR both photometrically and spectroscopically. Photometric observations with high temporal cadence will enable the characterization of the light curve to examine the "isothermal" behavior observed in some CNe (see Section 5.6.3), while contemporaneous spectroscopic observations will enable a direct comparison of this behavior to the dust emission features. The spectral coverage must include the 3-4 μm band in order to help constrain the aromatic to aliphatic bond ratio, which helps to isolate the molecular carrier of the UIR emission. Spectra in the 6-10 and 15-20 μm windows are necessary to understand fully characterize the emission features and compare them to UIR emission in other astronomical environments. Observations with SOFIA may play a major role in this effort since it will provide access to the mid-IR regime and allow rapid response observations to be made with high spectral resolution and sufficient temporal coverage. Additionally, observations must be obtained in the sub-millimeter and microwave regimes to try to detect the rotational transitions of SCMs.

Bibliography

Allamandola, L. J., Tielens, A. G. G. M., & Barker, J. R. 1985, ApJL, 290, L25

Allamandola, L. J., Tielens, A. G. G. M., & Barker, J. R. 1989, ApJS, 71, 733

Amari, S., Gao, X., Nittler, L. R., Zinner, E., José, J., Hernanz, M., & Lewis, R. S. 2001, ApJ, 551, 1065

Anupama, G. C., Sahu, D. K., & Mayya, Y. D. 2001, Bulletin of the Astronomical Society of India, 29, 375

Ashok, N. M., & Banerjee, D. P. K. 2004, IAU Circular, 8447, 4

Asplund, M., Grevesse, N., Sauval, A. J., & Scott, P. 2009, ARAA, 47, 481

Austin, S. J., Wagner, R. M., Starrfield, S., Shore, S. N., Sonneborn, G., & Bertram, R. 1996, ApJ, 111, 869

Ayani, K. 2007, IAU Circular, 8821, 2

Ayani, K. 2004, IAU Circular, 8443, 2

Barger, A. J., Gallagher, J. S., Bjorkman, K. S., Johansen, K. A., & Nordsieck, K. H. 1993, ApJL, 419, L85

Barker, J. R., Allamandola, L. J., & Tielens, A. G. G. M. 1987, ApJL, 315, L61

Baruffolo, A., Rafanelli, P., & Rosino, L. 1992, IAU Circular, 5471

Bernstein, L. S., & Lynch, D. K. 2009, ApJ, 704, 226

Bevington, P. R., & Robinson, D. K. 1992, *Data Reduction and Error Analysis for the Physical Sciences*, (McGraw-Hill: New York)

Blum, R. D., & Pradhan, A. K. 1992, ApJS, 80, 425

Bode, M. F. 2010, Astronomische Nachrichten, 331, 160

Bode, M. F., & Evans, A. 2008, *Classical Novae,* 2^{nd} *Edition*, Cambridge Univ.

Press: Cambridge

Bode, M., Zamanov, R., Marchant, J., & O'Brien, T. J. 2005, IAU Circular, 8511, 3

Boersma, C., Bauschlicher, C. W., Allamandola, L. J., Ricca, A., Peeters, E., & Tielens, A. G. G. M. 2010, A&A, 511, A32

Bonifacio, P., Selvelli, P. L., & Caffau, E. 2000, A&A, 356, L53

Bowen, I. S. 1947, PASP, 59, 196

Cardelli, J. A., Clayton, G. C., & Mathis, J. S. 1989, ApJ, 345, 245

Cassatella, A., Lamers, H.J.G.L.M., Rossi, C., Altamore, A., & González-Riestra, R. 2004, A&A, 420, 571

Challis, P., Kirshner, R. P., & Garnavich, P. 2008, IAU Circular, 8971, 3

Chesneau, O., et al. 2008, A&A, 487, 223

Chochol, D., & Pribulla, T. 1997, Contributions of the Astronomical Observatory Skalnate Pleso, 27, 53

Chochol, D., Grygar, J., Pribulla, T., Komžík, R., Hric, L., & Elkin, V. 1997 A&A, 318, 908

Chochol, D., Hric, L., Urban, Z., Komžík, R., Grygar, J., & Papoušek, J. 1993, A&A, 277, 103

Ciroi, S., di Mille, F., & Rafanelli, P. 2005, IAU Circular, 8487, 2

Clegg, P. E., et al. 1996, A&A, 315, L38

Collins, P. 1992, IAU Circular, 5454

Collins, P., et al. 1984, IAU Circular, 4023, 1

Darnley, M. J., et al. 2006, MNRAS, 369, 257

Das, R. K., Ashok, N. M., & Banerjee, D. P. K. 2007c, Central Bureau Electronic Telegrams, 925, 1

de Graauw, T., et al. 1996, A&A, 315, L49

Del Pozzo, W. 2005, Ph.D. Thesis, Università di Pisa

Della Valle, M., Hutsemekers, D., Saviane, I., Wenderoth, E., & Bond, H. E. 2003, IAU Circular, 8185, 2

Della Valle, M. & Livio, M. 1995, ApJ, 452, 704

Della Valle, M., Pasquini, L., Daou, D., & Williams, R.E. 2002, A&A, 390, 155

Della Valle, M., Pasquini, L., & Williams, R. 1999, IAU Circular,7193

DePoy, D. L., & Shields, J. C. 1994, ApJ, 422, 187

Draine, B. T. & Lee, H. M. 1984, ApJ, 285, 89

Drake, J. J., et al. 2003, ApJ, 584, 448

Duerbeck, H. W. 2008, in *Classical Novae, 2nd Edition*, eds.: M. F. Bode & A. Evans, (Cambridge Univ. Press: Cambridge)

Duley, W. W. 1987, MNRAS, 229, 203

Duley, W. W., & Jones, A. P. 1990, ApJL, 351, L49

Duley, W. W., & Williams, D. A. 1981, MNRAS, 196, 269

Duley, W. W., & Williams, D. A. 1983, MNRAS, 205, 67P

Ebel, D. S. 2000, J. Geophys. Res., 105, 10363

Elias, J. H., Joyce, R. R., Liang, M., Muller, G. P., Hileman, E. A., & George, J. R., 2006, SPIE, 6269, 138

Elias II, N. M. 1993, Inf. Bull. Var. Stars, No. 3860

Ennis, E., et al. 1977, ApJ, 214, 478

Evans, A., Geballe, T. R., Rawlings, J. M. C., Eyres, S. P. S., & Davies, J. K. 1997, MNRAS, 292, 192

Evans, A., Geballe, T. R., Rawlings, J. M. C., & Scott, A. D. 1996, MNRAS, 282, 1049

Evans, A., & Rawlings, J. M. C. 1994, MNRAS, 269, 427

Evans, A., & Rawlings, J. M. C. 2008, in *Classical Novae, 2nd Edition*, eds.: M. F. Bode & A. Evans, (Cambridge Univ. Press: Cambridge)

Evans, A., Tyne, V. H., Smith, O., Geballe, T. R., Rawlings, J. M. C., & Eyres, S. P. S. 2005, MNRAS, 360, 1483

Evans, A., et al. 2003, AJ, 126, 1981

Evans, A., et al. 2007a, ApJL, 663, L29

Evans, A., et al. 2007b, ApJL, 671, L157

Evans, A., et al. 2010b, MNRAS, 406, L85

Evans, P. A., Renz, W., Krimm, H. A., Bortle, J., Henden, A., van Ballegoij, E.,

& Pickard, R. 2010a, The Astronomer's Telegram, 2466, 1

Eyres, S. P. S., Heywood, I., O'Brien, T. J., Ivison, R. J., Muxlow, T. W. B., & Elkin, V. G. 2005, MNRAS, 358, 1019

Ferland, G. J. 1977, ApJ, 215, 873

Ferland, G. J., Korista, K. T., Verner, D. A., Ferguson, J. W., Kingdon, J. B., & Verner, E. M. 1998, PASP, 110, 761

Ferland, G. J., Williams, R. E., Lambert, D. L., Slovak, M., Gondhalekar, P. M., Truran, J. W., & Shields, G. A. 1984, ApJ, 281, 194

Fitzpatrick, E. L. 1999, PASP, 111, 63

Fleischer, A. J., Gauger, A., & Sedlmayr, E. 1992, A&A, 266, 321

Fujii, M. 1999, IAU Circular, 7324, 1

Gaggero, D., Martire, I., Poggiani, R., Puccetti, V., Shore, S. N., Tognelli, E., & Bernabei, S. 2005, IAU Circular, 8529, 1

Gaposchkin, C. H. P. 1957, Amsterdam, North-Holland Pub. Co.; New York, Interscience Publishers, 1957

Garnavich, P. 1992, IAU Circular, 5461

Geballe, T. R. 1997, From Stardust to Planetesimals, 122, 119

Gehrz, R. D. 1988, ARA&A, 26, 377

Gehrz, R. D. 1990, IAU Colloq. 122: Physics of Classical Novae, 369, 138

Gehrz, R. D. 1998a, Wild Stars in the Old West, 137, 146

Gehrz, R. D. 2008b, in *Classical Novae,* 2^{nd} *Edition*, eds.: M. F. Bode & A. Evans, (Cambridge Univ. Press: Cambridge)

Gehrz, R. D., Grasdalen, G. L., Greenhouse, M. A., Hackwell, J. A., Hayward, T., & Bentley, A. F. 1986, ApJ, 308, L63

Gehrz, R. D., Greenhouse, M. A., Hayward, T. L., Houck, J. R., Mason, C. G., & Woodward, C. E. 1995, ApJL, 448, L119

Gehrz, R. D., Hackwell, J. A., Grasdalen, G. I., Ney, E. P., Neugebauer, G., & Sellgren, K. 1980, ApJ, 239, 570

Gehrz, R. D., Jones, T. J., Lawrence, G., Hayward, T., Hauck, J., & Miles, J. 1992b, IAU Circular, 5497

Gehrz, R. D., Jones, T. J., Woodward, C. E., Greenhouse, M. A., Wagner, R. M., Harrison, T. E., Hayward, T. L., & Benson, J. 1992c, ApJ, 400, 671

Gehrz, R. D., Lawrence, G., & Jones, T. J. 1992a, IAU Circular, 5463

Gehrz, R. D., Salama, A., & Woodward, C. E. 1997, The first ISO workshop on Analytical Spectroscopy, 419, 173

Gehrz, R. D., Truran, J. W., Williams, R. E., & Starrfield, S. G. 1998b, PASP, 110, 3

Gehrz, R. D. et al. 1994, ApJ, 421, 762

Gehrz, R. D. et al. 2007, Rev. Sci. Instrum., 78, 011302.

Gehrz, R. D., et al. 2008a, ApJ, 672, 1167

Gill, C. D., & O'Brien, T. J. 1999, MNRAS, 307, 677

Gilmore, A. C. 1999, IAU Circular, 7179, 1

Gilmore, A. C., & Kilmartin, P. M. 2005, IAU Circular, 8559, 2

Glasner, S. A., & Truran, J. W. 2009, ApJL, 692, L58

Gonzalez-Riestra, R. 1992, A&A, 265, 71

Gonzalez-Riestra, R., Shore, S. N., Starrfield, S., & Krautter, J. 1996, IAU Circular, 6295, 1

Greenhouse, M. A., Feldman, U., Smith, H. A., Klapisch, M., Bhatia, A. K., & Bar-Shalom, A. 1993, ApJS, 88, 23

Greenhouse, M. A., Grasdalen, G. L., Woodward, C. E., Benson, J., Gehrz, R. D., Rosenthal, E., & Skrutskie, M. F. 1990, ApJ, 352, 307

Hachisu, I., & Kato, M. 2001, ApJ, 558, 323

Hachisu, I., & Kato, M. 2006, ApJ, 167, 59

Hachisu, I., & Kato, M. 2007, ApJ, 662, 552

Hachisu, I., & Kato, M. 2009, ApJL, 694, L103

Hachisu, I., Kato, M., & Kato, T. 2004, ApJL, 606, L139

Hachisu, I., Kato, M., Kiyota, S., & Maehara, H. 2009, arXiv:0912.5056

Hack, M., Selvelli, P., & Duerbeck, H. W. 1993, NASA Special Publication, 507 (Washington, D.C., NASA), 261

Hanner, M. 1988, Infrared Observations of Comets Halley and Wilson and Properties of the Grains, 22

Haseda, K., West, D., Yamaoka, H., & Masi, G. 2002, IAU Circular, 7975, 1

Harker, D. E., Wooden, D. H., Woodward, C. E., & Lisse, C. M. 2002, ApJ, 580, 579

Harrison, T. E., Johnson, J. J., & Spyromilio, J. 1993, AJ, 105, 320

Hauschildt, P. H., Starrfield, S., Shore, S. N., Gonzalez-Riestra, R., Sonneborn, G., & Allard, F. 1994, AJ, 108, 1008

Heck, P. R., Marhas, K. K., Hoppe, P., Gallino, R., Baur, H., & Wieler, R. 2007, ApJ, 656, 1208

Helton, L. A., Vonderharr, T., Woodward, C. E., & Schwarz, G. J. 2010a, IAU Circular, 9140, 2

Helton, L. A., Woodward, C. E., Vanlandingham, K., & Schwarz, G. J. 2008a, Central Bureau Electronic Telegrams, 1379, 1

Helton, L. A., Woodward, C. E., Vanlandingham, K., & Schwarz, G. J. 2008b, Central Bureau Electronic Telegrams, 1448, 1

Helton, L. A., Woodward, C. E., Vanlandingham, K., & Schwarz, G. J. 2008c, Central Bureau Electronic Telegrams, 1449, 1

Helton, L. A., Woodward, C. E., Vanlandingham, K., & Schwarz, G. J. 2008d, IAU Circular, 8989, 2

Helton, L. A., et al. 2010b, AJ, 140, 1347

Henden, A., & Munari, U. 2007, Information Bulletin on Variable Stars, 5771, 1

Henden, A., Shears, J., Poyner, G., Dvorak, S., & Krajci, T. 2008, Central Bureau Electronic Telegrams, 1582, 1

Hernanz, M., & Sala, G. 2010, Astronomische Nachrichten, 331, 169

Hernanz, M., & Sala, G. 2002, Science, 298, 393

Hirosawa, K., Yamamoto, M., Nakano, S., Kojima, T., Iida, M., Sugie, A., Takahashi, S., & Williams, G. V. 1995, IAU Circular, 6213, 1

Honda, M., et al. 1975, IAU Circular, 2826, 1

Houck, J., et al. 2004, ApJS, 154, 10

Hounsell, R., Darnley, M. J., Bode, M. F., Harman, D. J., Helton, L. A., & Schwarz, G. J. 2010b, A&A, in preparation

Hounsell, R., et al. 2010a, ApJ, 724, 480

Hric, L., Kundra, E., Niarchos, P., Manimanis, V. N., Liakos, A., & Gális, R. 2008, Astronomical Society of the Pacific Conference Series, 401, 215

Hudson, C. E., Ramsbottom, C. A., Norrington, P. H., & Scott, M. P. 2009, A&A, 494, 729

Hummer, D. G. & Storey, P. J. 1987, MNRAS, 224, 801

Humphreys, R. M., et al. 2010, ApJL, 718, L43

Hyland, A. R., & McGregor, P. J. 1989, Interstellar Dust, 135, 101P

Iben Jr., I. & Fujimoto, M. Y. 2008, in *Classical Novae,* 2^{nd} *Edition*, eds.: M. F. Bode & A. Evans, (Cambridge Univ. Press: Cambridge)

Iijima, T., & Esenoğlu, H. H. 2003, A&A, 404, 997

Iliadis, C., Champagne, A., José, J., Starrfield, S., & Tupper, P. 2002, ApJS, 142, 105

Ivezić, Ž., Nenkova, M., & Elitzer, M. 1999, arXiv:astro-ph/9910475

Iyudin, A. F., et al. 2001, Exploring the Gamma-Ray Universe, 459, 41

José, J., Hernanz, M., Amari, S., Lodders, K., & Zinner, E. 2004, ApJ, 612, 414

José, J. & Shore, S. N. 2008, in *Classical Novae,* 2^{nd} *Edition*, eds.: M. F. Bode & A. Evans, (Cambridge Univ. Press: Cambridge)

Kabashima, F., Corelli, P., Guido, E., & Sostero, G. 2009, IAU Circular, 9089, 1

Kahabka, P., & van den Heuvel, E. P. J. 1997, ARA&A, 35, 69

Kamath, U. S., Anupama, G. C., Ashok, N. M., Mayya, Y. D., & Sahu, D. K. 2005, MNRAS, 361, 1165

Kato, M. 2002, in "The Physics of Cataclysmic Variables and Related Objects", eds. B. T. Gänsicke, K. Beuermann & K. Reinsch, ASP Conf. Proc., 261, 595

Keller, L. D., et al. 2008, ApJ, 684, 411

Kenyon, S. J., Oliversen, N. A., Mikolajewska, J., Mikolajewski, M., Stencel, R. E., Garcia, M. R., & Anderson, C. M. 1991, AJ, 101, 637

Kessler, M. F., et al. 1996, A&A, 315, L27

Kilmartin, P., Gilmore, A., Jones, A. F., & Pearce, A. 1990, IAU Circular, 5002, 1

Kinugasa, K., Honda, S., Hashimoto, O., & Takeda, Y. 2009b, Central Bureau Electronic Telegrams, 1816, 3

Kinugasa, K., Nishiyama, K., Kabashima, F., Honda, S., Hashimoto, O., & Yamaoka, H. 2009a, IAU Circular, 9041, 1

Kiss, L. L., & Thomson, J. R. 2000, A&A, 355, L9

Kiyota, S. 2010, Central Bureau Electronic Telegrams, 2264, 4

Kiyota, S., Vollmann, W., Koberger, H., Nishiyama, K., Kabashima, F., Maehara, H., Kazarovets, E., & Samus, N. N. 2010, IAU Circular, 9112, 1

Klare, G., & Wolf, B. 1978, A&AS, 33, 327

Kolotilov, E. A. 1980, Soviet Astronomy Letters, 6, 268

Krautter, J., Woodward, C. E., et al. 2002, AJ, 124, 2888

Kwok, S. 2007, *Physics and Chemistry of the Interstellar Medium*, (University Science Books: Sausalito, CA), p. 330

Leach, S. 1989, Interstellar Dust, 135, 155

Lee, H., McCall, M. L., Kingsburgh, R. L., Ross, R., & Stevenson, C. C. 2003, AJ, 125, 146

Lee, S., Pearce, A., Gilmore, C., Pollard, K. R., McSaveney, J. A., Kilmartin, P. M., & Caldwell, P. 1999, IAU Circular, 7176, 1

Lennon, D. J., & Burke, V. M. 1994, A&AS, 103, 273

Liller, W. 1989, IAU Circular, 4820, 1

Liller, W. 2005, IAU Circular, 8559, 1

Liller, W. 2008, IAU Circular, 9004, 1

Liller, W., Addiego, G., & Fonseca, W. 2007b, IAU Circular, 8801

Liller, W., Heathcote, B., Schmeer, P., Waagen, E. O., Nelson, P., Stockdale, C., Amorim, A., & Pearce, A. 2007a, IAU Circular, 8800, 1

Liller, W., & Jones, A. 1999, Information Bulletin on Variable Stars, 4774, 1

Liller, W. & Jones, A. F. 2000, IBVS 5004

Livio, M., & Truran, J. W. 1994, ApJ, 425, 797

Luhman, K. L., Engelbracht, C. W., & Luhman, M. L. 1998, ApJ, 499, 799

Lyke, J. E. 2003b, Ph.D. Thesis, University of Minnesota

Lyke, J. E., et al. 2001, AJ, 122, 3305

Lyke, J. E., et al. 2003a, AJ, 126, 993

Lynch, D. K., Rudy, R. J., Mazuk, S., & Puetter, R. C. 2000, ApJ, 541, 791

Lynch, D. K., Rudy, R. J., Venturini, C. C., Mazuk, S., Puetter, R. C., & Perry, R. B. 2006b, IAU Circular, 8730, 5

Lynch, D. K., Russell, R. W., Kellogg, R. C., Mazuk, A. L., & Hanner, M. S. 1997, AJ, 113, 1391

Lynch, D. K., Russell, R. W., Rudy, R. J., & Woodward, C. E. 2007, IAU Circular, 8883, 1

Lynch, D. K., Russell, R. W., Rudy, R. J., & Woodward, C. E. 2008a, IAU Circular, 8955, 1

Lynch, D. K., et al. 2006a, ApJ, 638, 987

Lynch, D. K., et al. 2008b, AJ, 136, 1815

Mainzer, A. K., Young, E. T., Greene, T. P., Acu, N., Jamieson, T. H., Mora, H., Sarfati, S., & van Bezooijen, R. W. 1998, Proc. SPIE, 3356, 1095

Mallama, A. D., & Skillman, D. R. 1979, PASP, 91, 99

Małek, K., et al. 2010, Advances in Astronomy, 2010, 9

Mason, E., Diaz, M., Williams, R. E., Preston, G., & Bensby, T. 2010, A&A, 516, A108

Mason, C. G., Gehrz, R. D., Woodward, C. E., Smilowitz, J. B., Hayward, T. L., & Houck, J. R. 1998, ApJ, 494, 783

Mathis, J. S., Rumpl, W., & Nordsieck, K. H. 1977, ApJ, 217, 425

Mattei, J. A. 1978, JRASC, 72, 178

Mazuk, S., Lynch, D. K., Rudy, R. J., Russell, R. W., Pearson, R. L., Woodward, C. E., Puetter, R. C., & Perry, R. B. 2007, IAU Circular, 8848, 1

Mazuk, S., Rudy, R. J., Lynch, D. K., Venturini, C., Puetter, R. C., & Armstrong, T. 2000, IAU Circular, 7490, 3

McLaughlin, B. M. & Bell, K. L. 2000, J. Phys. B., 33. 597

McLaughlin, D. B. 1960, in *Stellar Atmospheres*, ed. B. L. Greenstein, (Univ. of Chicago Press: Chicago), p. 608

Milbourn, S. W., Alcock, G. E. D., Harlan, E. A., & Phillips, M. 1976, IAU Circular, 2997, 1

Moraes, M., & Diaz, M. 2009, AJ, 138, 1541

Morgan, G. E., Ringwald, F. A., & Prigge, J. W. 2003, MNRAS, 344, 521

Moro, D., Pizzella, A., & Munari, U. 1999, IAU Circular, 7325, 1

Morrison, W., Beckman, K., Baroni, S., & Cavagna, N. 1978, IAU Circular, 3264, 3

Munari, U., Dalla Via, G., Valisa, P., Dallaporta, S., & Castellani, F. 2007a, Central Bureau Electronic Telegrams, 897, 1

Munari, U., & Dallaporta, S. 2010, Information Bulletin on Variable Stars, 5932, 1

Munari, U., Dallaporta, S., & Ochner, P. 2010, Information Bulletin on Variable Stars, 5944, 1

Munari, U., Henden, A., Valentini, M., Siviero, A., Dallaporta, S., Ochner, P., & Tomasoni, S. 2008b, MNRAS, 387, 344

Munari, U., Saguner, T., Siviero, A., Valisa, P., Dallaporta, S., & Graziani, M. 2009a, Central Bureau Electronic Telegrams, 1999, 1

Munari, U., Siviero, A., Cherini, G., Tomaselli, S., Graziani, M., Tozzi, F., & Moretti, S. 2008d, Central Bureau Electronic Telegrams, 1487, 1

Munari, U., Siviero, A., Dallaporta, S., Valisa, P., & Iijima, T. 2007b, Central Bureau Electronic Telegrams, 965, 1

Munari, U., Siviero, A., Moretti, S., Graziani, M., Tomaselli, S., Baldinelli, L., & Maitan, A. 2006, Central Bureau Electronic Telegrams, 596, 1

Munari, U., Siviero, A., Valisa, P., Dallaporta, S., & Baldinelli, L. 2009b, Central Bureau Electronic Telegrams, 2034, 1

Munari, U., Siviero, A., Valisa, P., Frigo, A., Dallaporta, S., Cherini, G., & Dalla Via, G. 2007d, Central Bureau Electronic Telegrams, 1183, 1

Munari, U., Siviero, A., Valisa, P., Ochner, P., Dallaporta, S., Vagnozzi, A.,

Moretti, S., & Tomaselli, S. 2008e, Central Bureau Electronic Telegrams, 1504, 1

Munari, U. & Zwitter, T. 1997, A&A, 318, 269

Munari, U., et al. 2007c, Central Bureau Electronic Telegrams, 1010, 1

Munari, U., et al. 2008a, Central Bureau Electronic Telegrams, 1251, 1

Munari, U., et al. 2008c, Central Bureau Electronic Telegrams, 1431, 1

Munoz Burgos, J. M., Loch, S. D., Ballance, C. P., & Boivin, R. F. 2009, A&A, 500, 1253

Naik, S., Das, M., Jain, C., & Paul, B. 2010, MNRAS, 404, 2056

Naito, H., & Sakamoto, M. 2007, IAU Circular, 8821, 3

Naito, H., Tokimasa, N., & Yamaoka, H. 2005, IAU Circular, 8484, 1

Nakano, S., Kadota, K., Waagen, E., Swierczynski, S., Komorous, M., King, R., & Bortle, J. 2007d, IAU Circular, 8861, 2

Nakano, S., Kanatsu, K., Kawanishi, K., Tago, A., Otomo, S., Urata, T., & Tomita, K. 1993, IAU Circular, 5902, 1

Nakano, S., Kaneda, H., & Kadota, K. 2008a, IAU Circular, 8927, 2

Nakano, S., Nishimura, H., Guido, E., Sostero, G., & Kazarovets, E. V. 2009, IAU Circular, 9093, 1

Nakano, S., Nishimura, H., Kadota, K., Itagaki, K., Yamaoka, H., Nakamura, Y., & Tago, A. 2007b, IAU Circular, 8824, 1

Nakano, S., Nishimura, H., Miles, R., & Yamaoka, H. 2006, IAU Circular, 8697, 1

Nakano, S., Nishimura, H., Wakuda, S., & Kadota, K. 2005, IAU Circular, 8483, 1

Nakano, S., Sakurai, Y., Itagaki, K., & Koff, R. 2007c, IAU Circular, 8832, 1

Nakano, S., Tago, A., Itagaki, K., Kadota, K., Yamaoka, H., Munari, U., & Pereira, A. 2008b, IAU Circular, 8907, 1

Nakano, S., Tago, A., Nishiyama, K., & Sakamoto, T. 2007a, IAU Circular, 8821, 1

Nakano, S., Tago, A., Sakurai, Y., Kushida, R., & Kadota, K. 2004, IAU Circular, 8443, 1

Nakano, S., Takamizawa, K., Kushida, Y., & Kato, T. 1998, IAU Circular, 6941, 1

Nakano, S., et al. 2008c, IAU Circular, 8934, 1

Nakano, S., et al. 2008d, IAU Circular, 8937, 1

Nakano, S., et al. 2008e, IAU Circular, 8950, 1

Nakano, S., et al. 2008f, IAU Circular, 8972, 1

Nakano, S., et al. 2010a, IAU Circular, 9111, 2

Nakano, S., et al. 2010b, IAU Circular, 9119, 1

Narumi, H., Hirosawa, K., Kanai, K., Renz, W., Pereira, A., Nakano, S., Nakamura, Y., & Pojmanski, G. 2006, IAU Circular, 8671, 2

Ness, J.-U., Schwarz, G. J., Retter, A., Starrfield, S., Schmitt, J. H. M. M., Gehrels, N., Burrows, D., & Osborne, J. P. 2007a, ApJ, 663, 505

Ness, J.-U., Schwarz, G., Osborne, J. P., Page, K., Drake, J. J., & Krautter, J. 2008c, The Astronomer's Telegram, 1747, 1

Ness, J.-U., Schwarz, G., Starrfield, S., Osborne, J. P., Page, K. L., Beardmore, A. P., Wagner, R. M., & Woodward, C. E. 2008b, AJ, 135, 1328

Ness, J.-U., et al. 2007b, ApJ, 665, 1334

Ness, J.-U., et al. 2009, The Astronomer's Telegram, 2063, 1

Nielbock, M., & Schmidtobreick, L. 2003, A&A, 400, L5

Nishiyama, K., Kabashima, F., Kiyota, S., Guido, E., Sostero, G., Vollmann, W., & Koberger, H. 2010a, IAU Circular, 9120, 1

Nishiyama, K., Kabashima, F., Liller, W., Yusa, T., & Maehara, H. 2010b, IAU Circular, 9140, 1

Nishiyama, K., et al. 2008, IAU Circular, 8947, 1

Nishiyama, K., et al. 2009a, IAU Circular, 9061, 1

Nishiyama, K., et al. 2009b, IAU Circular, 9100, 1

Nishiyama, K., et al. 2010c, IAU Circular, 9142, 1

Nittler, L. R., & Hoppe, P. 2005, ApJL, 631, L89

Nuth, J. A., III, & Hecht, J. H. 1990, Ap&SS, 163, 79

Orio, M., Covington, J., Ögelman, H. 2001, A&A, 373, 542

Orio, M., Parmar, A. N., Capalbi, M., Piro, L., & Mineo, T. 1999b, IAU Circular, 7325, 3

Orio, M., Torroni, V., & Ricci, R. 1999a, IAU Circular, 7196, 2

Ossenkopf, V., Henning, Th. & Mathis, J. S. 1992, A&A, 261, 567

Osterbrock, D. E., & Ferland, G. J. 2006, Astrophysics of gaseous nebulae and active galactic nuclei, 2nd. ed. by D.E. Osterbrock and G.J. Ferland. Sausalito, CA: University Science Books, 2006

Paresce, F., Livio, M., Hack, W., & Korista, K. 1995, A&A, 299, 823

Patterson, J. 1994, PASP, 106, 209

Peeters, E., et al. 2002, A&A, 390, 1089

Pejcha, O., Prieto, J. L., & Denney, K. 2008, The Astronomer's Telegram, 1825, 1

Pepin, R.O, Gehrz, R.D., et al. 2010, in preparation

Pereira, A., di Cicco, D., Vitorino, C., & Green, D. W. E. 1999, IAU Circular, 7323, 1

Pettit, E. 1946, PASP, 58, 153

Poggiani, R. 2008, Ap&SS, 315, 79

Poggiani, R. 2009, Ap&SS, 323, 319

Pojmanski, G., Masi, G., & Wilcox, R. 2005, IAU Circular, 8505, 1

Pojmanski, G., Yamaoka, H., Kiyota, S., Maehara, H., Ayani, K., Naito, H., Narusawa, S., & Fujii, M. 2006, IAU Circular, 8671, 1

Pojmanski, G., et al. 2004, IAU Circular, 8369, 1

Pontefract, M., & Rawlings, J. M. C. 2004, MNRAS, 347, 1294

Prieto, J. L., Pejcha, O., & Wagner, R. M. 2008, The Astronomer's Telegram, 1835, 1

Quirrenbach, A., Elias II, N. M., Mozurkewich, D., Armstrong, J. T., Buscher, D. F., & Hummel, C. A. 1993, AJ, 106, 1118

Rafanelli, P., Rosino, L., & Radovich, M. 1995, A&A, 294, 488

Rawlings, J. M. C. 1988, MNRAS, 232, 507

Rawlings, J. M. C., & Williams, D. A. 1989, MNRAS, 240, 729

Rayner, J. T., Toomey, D. W., Onaka, P. M., Denault, A. J., Stahlberger, W. E., Watanabe, D. Y., & Wang, S.-I. 1998, Proc. SPIE, 3354, 468

Retter, A. 2004, ApJL, 615, L125

Rho, J., et al. 2008, ApJ, 673, 271

Rohrbach, J. G., Ness, J.-U., & Starrfield, S. 2009, AJ, 137, 4627

Rudy, R. J., Dimpfl, W. L., Lynch, D. K., Mazuk, S., Venturini, C. C., Wilson, J. C., Puetter, R. C., & Perry, R. B. 2003, ApJ, 596, 1229

Rudy, R. J., Erwin, P., Rossano, G. S., & Puetter, R. C. 1991, ApJ, 383, 344

Rudy, R. J., Mazuk, S., Venturini, C., Lynch, D. K., Puetter, R. C., & Mortfield, P. 2001, IAU Circular, 7674, 3

Rudy, R. J., Lynch, D. K., Mazuk, S., Venturini, C. C., Puetter, R. C., Perry, R. B., & Walp, B. 2005, IAU Circular, 8643, 2

Rudy, R. J., Lynch, D. K., Russell, R. W., Kaneshiro, B., Sitko, M., & Hammel, H. 2008c, IAU Circular, 8976, 1

Rudy, R. J., Lynch, D. K., Russell, R. W., & Woodward, C. E. 2007, IAU Circular, 8884, 2

Rudy, R. J., Lynch, D. K., Russell, R. W., Woodward, C. E., & Covey, K. 2008b, IAU Circular, 8938, 2

Rudy, R. J., Lynch, D. K., Russell, R. W., Sitko, M., Woodward, C. E., & Aspin, C. 2008d, IAU Circular, 8997, 2

Rudy, R. J., Lynch, D. K., Venturini, C. C., Mazuk, S., Broadwater, D., Cowan, M., Puetter, R. C., & Perry, R. B. 2006a, IAU Circular, 8728, 1

Rudy, R. J., Prater, T. R., Puetter, R. C., Perry, R. B., & Baker, K. 2009, IAU Circular, 9099, 1

Rudy, R. J., Rossano, G. S., & Puetter, R. C. 1989, ApJ, 346, 799

Rudy, R. J., Russell, R. W., Lynch, D. K., & Woodward, C. E. 2008a, IAU Circular, 8936, 2

Rudy, R. J., Venturini, C. C., Lynch, D. K., Mazuk, S., & Puetter, R. C. 2002, ApJ, 573, 794

Rudy, R. J., et al. 2006b, Bulletin of the American Astronomical Society, 38, 907

Rushton, M. T., Evans, A., Eyres, S. P. S., van Loon, J. T., & Smalley, B. 2008, MNRAS, 386, 289

Russell, R. W., Laag, E. A., Rudy, R. J., Skinner, M. A., & Gregory, S. A. 2010, IAU Circular, 9118, 2

Russell, R. W., Lynch, D. K., & Rudy, R. J. 2005b, IAU Circular, 8527, 1

Russell, R. W., Lynch, D. K., & Rudy, R. J. 2005c, IAU Circular, 8579, 3

Russell, R. W., Lynch, D. K., Rudy, R. J., & Woodward, C. E. 2008a, IAU Circular, 8936, 3

Russell, R. W., Rudy, R. J., Lynch, D. K., Gilbert, A. M., & Woodward, C. E. 2008c, IAU Circular, 8956, 1

Russell, R. W., Rudy, R. J., Lynch, D. K., & Golisch, W. 2005a, IAU Circular, 8524, 2

Russell, R. W., Rudy, R. J., Lynch, D. K., Mazuk, S., Pearson, R. L., Woodward, C. E., Puetter, R. C., & Perry, R. B. 2007a, IAU Circular, 8846, 1

Russell, R. W., Rudy, R. J., Lynch, D. K., & Woodward, C. E. 2006, IAU Circular, 8710, 2

Russell, R. J., Rudy, R. J., Lynch, D. K., & Woodward, C. E. 2007b, IAU Circular, 8888, 1

Russell, R. W., Rudy, R. J., Lynch, D. K., Woodward, C. E., Marion, H., & Griep, D. 2008b, IAU Circular, 8948, 1

Russell, R. W., Soifer, B. T., & Willner, S. P. 1977, ApJL, 217, L149

Saizar, P. et al. 1992, ApJ, 398, 651

Salama, A., Evans, A., Eyres, S. P. S., Leech, K., Barr, P., & Kessler, M. F. 1996, A&A, 315, L209

Salama, A., et al. 1998, Ap&SS, 255, 227

Samus, N. N., Santangelo, M. M. M., Hornoch, K., Souza, W., & Fidrich, R. 2008, IAU Circular, 8940, 2

Saraph, H. E. & Tully, J. A. 1994, A&AS, 107, 29

Sarkar, G., & Sahai, R. 2006, ApJ, 644, 1171

Schirrmacher, V., Woitke, P., & Sedlmayr, E. 2003, A&A, 404, 267

Schlegel, D. J., Finkbeiner, D. P., & Davis, M. 1998, ApJ, 500, 525

Schmeer, P. 1992, IAU Circ. 5455

Schutte, W. A., Tielens, A. G. G. M., Allamandola, L. J., Wooden, D. H., & Cohen, M. 1990, ApJ, 360, 577

Schwarz, G. J., Shore, S. N., Starrfield, S., & Vanlandingham, K. M. 2007a, ApJ, 657, 453

Schwarz, G. J., et al. 2007b, AJ, 134, 516

Schwarz, G. J., et al. 2009, The Astronomer's Telegram, 2157, 1

Scott, A. D., Evans, A., & Rawlings, J. M. C. 1994b, MNRAS, 269, L21

Scott, A. D., Evans, A., Rawlings, S., & Eales, S. 1994a, IAU Circular, 5916, 1

Sekiguchi, K., et al. 1990, MNRAS, 246, 78

Serra Díaz-Cano, L., & Jones, A. P. 2008, A&A, 492, 127

Shafter, A. W. 2008, in *Classical Novae,* 2^{nd} *Edition*, eds.: M. F. Bode & A. Evans, (Cambridge Univ. Press: Cambridge)

Shears, J., et al. 2009, arXiv:0905.1866

Shields, J. C. 1993, ApJ, 419, 181

Shore, S. N., & Gehrz, R. D. 2004, A&A, 417, 695

Shore, S. N., Sonneborn, G., Starrfield, S., Gonzalez-Riestra, R., & Ake, T. B. 1993, AJ, 106, 2408

Shore, S. N., Sonneborn, G., Starrfield, S., González-Riestra, R., & Polidan, R. S. 1994, ApJ, 421, 344

Shore, S. N., Starrfield, S., Ake, T. B., & Hauschildt, P. H. 1997, ApJ, 940, 393

Shore, S. N., Starrfield, S. G., Austin, S. J., Gonzales-Riestra, R., Sonneborn, G., & Wagner, R. M. 1992, IAU Circular, 5523, 1

Shore, S. N. et al. 2003, AJ, 125, 1507

Sitko, M. L., & Lynch, D. K. 2009, IAU Circular, 9054, 1

Sitko, M., Lynch, D. K., Russell, R. W., Rudy, R. J., & Woodward, C. E. 2008, IAU Circular, 8998, 3

Siviero, A., Munari, U., & Jones, A. F. 2005, Information Bulletin on Variable Stars, 5638, 1

Skiff, B., Abe, H., & Bengtsson, H. 1993, IAU Circular, 5904, 2

Slavin, A. J., O'Brien, T. J., & Dunlop, J. S. 1995, MNRAS, 276, 353

Sloan, G. C., Bregman, J. D., Geballe, T. R., Allamandola, L. J., & Woodward, C. E. 1997, ApJ, 474, 735

Sloan, G. C., et al. 2007, ApJ, 664, 1144

Smith, C. H., Aitken, D. K., & Roche, P. F. 1994, MNRAS, 267, 225

Smith, C. H., Aitken, D. K., Roche, P. F., & Wright, C. M. 1995, MNRAS, 277, 259

Smith, F. W. 1984, Journal of Applied Physics, 55, 764

Sostero, G., Yamaoka, H., Kiyota, S., Nakajima, K., & Maehara, H. 2004, IAU Circular, 8445, 3

Starrfield, S., Iliadis, C., & Hix, W. R. 2008, in *Classical Novae,* 2^{nd} *Edition*, eds.: M. F. Bode & A. Evans, (Cambridge Univ. Press: Cambridge)

Starrfield, S., Sparks, W. M., Truran, J. W., & Wiescher, M. C. 2000, ApJS, 127, 485

Starrfield, S., Truran, J. W., Wiescher, M. C., & Sparks, W. M. 1998, MNRAS, 296, 502

Steiner, J. E., Campos, R., & Cieslinski, D. 1999, IAU Circular, 7185, 2

Sun, G., & Gao, X. 2009, IAU Circular, 9049, 1

Swierczynski, E., Ragan, E., Galan, C., & Mikolajewski, M. 2008, The Astronomer's Telegram, 1723, 1

Swierczynski, E., et al. 2009, arXiv:0909.5149

Tabur, V., Monard, L. A. G., & Africa, S. 2003, IAU Circular, 8184, 1

Tamor, M. A., Wu, C. H., Carter, R. O., III, & Lindsay, N. E. 1989, Applied Physics Letters, 55, 1388

Tayal, S. S. 2000, ApJ, 530, 1091

Tokunaga, A. T. 1997, Diffuse Infrared Radiation and the IRTS, 124, 149

Tomov, T., Mikolajewski, M., Brozek, T., Ragan, E., Swierczynski, E., Wychudzki, P., & Galan, C. 2008, The Astronomer's Telegram, 1485, 1

Townsley, D. M., & Bildsten, L. 2004, ApJ, 600, 390

Truran, J. W., & Livio, M. 1986, ApJ, 308, 721

van den Bergh, S., & Younger, P. F. 1987, A&AS, 70, 125

van Diedenhoven, B., et al. 2004, ApJ, 611, 928

Vanlandingham, K. M., Schwarz, G. J., Shore, S. N., Starrfield, S., & Wagner, R. M. 2005, ApJ, 624, 914

Venturini, C. C., Rudy, R. J., Lynch, D. K., Mazuk, S., & Puetter, R. C. 2004, AJ, 128, 405

Venturini, C. C., Rudy, R. J., Lynch, D. K., Mazuk, S., Puetter, R. C., Perry, R. B., & Walp, B. 2005, IAU Circular, 8641, 2

Vollmann, W. 2010, Central Bureau Electronic Telegrams, 2139, 3

Voshchinnikov, N. V., & Henning, T. 2008, A&A, 483, L9

Waagen, E., Bedient, J., Linnolt, M., Monard, B., James, R., & Axelson, R. 2004, IAU Circular, 8371, 2

Warner, B. 2008, in *Classical Novae,* 2^{nd} *Edition*, eds.: M. F. Bode & A. Evans, (Cambridge Univ. Press: Cambridge)

Werner, M. W., et al. 2004, ApJS, 154, 1

Williams, P., Waagen, E. O., Krajci, T., & Schmeer, P. 2006, IAU Circular, 8700, 1

Williams, R. E. 1992, AJ, 104, 725

Williams, R. E. 1994, ApJ, 426, 279

Williams, R. E., Phillips, M. M., & Hamuy, M. 1994, ApJS, 90, 297

Williams, R. E., Hamuy, M., Phillips, M. M., Heathcote, S. R., Wells, L., & Navarrete, M. 1991, ApJ, 376, 721

Wilson, O. C., & Merrill, P. W. 1935, PASP, 47, 53

Woodward, C. E., Gehrz, R. D., Jones, T. J., & Lawrence, G. F. 1992, ApJ, 384, L41

Woodward, C. E., Gehrz, R. D., Jones, T. J., Lawrence, G. F., & Skrutskie, M. F. 1997, ApJ, 477, 817

Woodward, C. E., Wooden, D. H., Pina, R. K., & Fisher, R. S. 1999, IAU Circular, 7220

Woodward, C. E., et al. 1995, ApJ, 438, 921

Woudt, P. A., et al. 2009, ApJ, 706, 738

Yamaoka, H. 2004, IAU Circular, 8380, 1

Yamaoka, H., Itagaki, K., Korotkiy, S., & Samus, N. N. 2008a, IAU Circular, 8971, 2

Yamaoka, H., Nakamura, Y., Itagaki, K., Nakano, S., & Nishimura, H. 2007, IAU Circular, 8810, 1

Yamaoka, H., et al. 2008b, IAU Circular, 8989, 1

Yaron, O., Prialnik, D., Shara, M. M., & Kovetz, A. 2005, ApJ, 623, 398

Young, P. J., Corwin, H. G., Jr., Bryan, J., & de Vaucouleurs, G. 1976, ApJ, 209, 882

Zhang, H. L., Graziani, M., & Pradhan, A. K. 1994, A&A, 283, 319

Appendix A

Glossary and Acronyms

Care has been taken in this thesis to minimize the use of jargon and acronyms, but this cannot always be achieved. This appendix defines jargon terms in a glossary, and contains a table of acronyms and their meaning.

A.1 Glossary

Carbon-Oxygen White Dwarf (**CO WD**) – A white dwarf composed primarily of carbon and oxygen.

Chandrasekhar Mass Limit – This is the terminal mass that a non-rotating, non-magnetic white dwarf can reach before the force of gravitational contraction exceeds the electron degeneracy pressure, equivalent to $1.38M_{\odot}$. Growth beyond this mass results in the collapse of the object into either a neutron star (held up by neutron degeneracy pressure) or a black hole.

Classical Nova (**CN - singular; CNe - plural**) – An explosion arising on the surface of a white dwarf in a mass accreting binary system.

Carbon-Nitrogen-Oxygen Cycle (**CNO Cycle**) – The primary sequence of fusion reactions converting hydrogen into helium in stars $> 1.3M_{\odot}$, in which C, N, and O act as catalysts.

Electron Degeneracy Pressure – This is the force opposing gravitational

collapse in a white dwarf that arises due to the resistance of electrons against occupying the same quantum mechanical energy state, i.e., the Pauli exclusion principle.

Interstellar Medium (**ISM**) – This term generally refers to the environment within a single galaxy between the stars. It also includes all of the gas, dust, and molecules within that environment.

Main Sequence (**MS**) – This is the stage of stellar evolution in which the primary source of energy for a star is through the fusion of hydrogen into helium in its core. The majority of a star's life is spent in this stage of evolution.

Metals – In this context, "metals" refers to any element heavier than helium.

Oxygen-Neon White Dwarf (**ONe WD; formerly ONeMg WD**) – A white dwarf composed primarily of oxygen and neon; formerly called an oxygen-neon-magnesium white dwarf due to theoretical prediction of high fraction of magnesium in the white dwarf.

Proton-Proton Chain (**pp-chain**) – The primary sequence of fusion reactions in low mass stars in which four hydrogen atoms join to produce one helium atom plus energy.

Roche-lobe Overflow – This is the primary process through which mass transfer is realized in classical novae systems. In this process, the outer envelope of the binary companion to the white dwarf fills its Roche-lobe allowing the transfer of material onto the WD primary through the inner Lagrangian point.

Thermonuclear Runaway (**TNR**) – The process of non-equilibrium nuclear burning in the accreted envelope of a WD in a binary system giving rise to a nova outburst.

White Dwarf (**WD**) – A degenerate core of a star with no ongoing nuclear fusion, left behind after the star has run out of nuclear fuel.

A.2 Acronyms

Table A.1: Acronyms

AAVSO	American Association of Variable Star Observers
AC	Amorphous carbon
AOR	Astronomical Observation Request
CN	Classical nova
CNe	Classical novae
CNO	Carbon-nitrogen-oxygen
CO	Carbon-oxygen
CP	Cyclopropenylidene (c-C_3H_2
CTIO	Cerro Tololo Interamerican Observatory
EO	Ethylene oxide (c-C_2H_4O)
FWHM	Full width at half maximum
FWZI	Full width-zero intensity
HAC	Hydrogenated amorphous carbon
HWHM	Half width at half maximum
HWZI	Half width-zero intensity
ISM	Interstellar medium
IR	Infrared
JD	Julian date
JPL	Jet Propulsion Laboratory
LTE	Local thermodynamic equilibrium
MIR	Mid-infrared
MMRD	Maximum magnitude-rate of decline relationship
MRN	Mathis, Rumpl, & Nordsieck
MS	Main sequence
NASA	National Aeronautics and Space Administration
NIR	Near-infrared
NSF	National Science Foundation
ONe	Oxygen-neon
ONeMg	Oxygen-neon-magnesium

PAC	Polycyclic aromatic carbon
PAH	Polycyclic aromatic hydrocarbon
PID	Program Identification Number
RN	Recurrent nova
RNe	Recurrent novae
SCM	Small carbonaceous molecules
SMARTS	Small and Moderate Aperture Research Telescope System
SN	Supernova
SNe	Supernovae
SSS	Super soft X-ray source
TNR	Thermonuclear runaway
UIR	Unidentified infrared feature
UV	Ultraviolet
WD	White Dwarf

A.3 List of Symbols

Table A.2: Symbols

Physical and Astronomical Constants

c	Velocity of light, 2.998×10^{10} cm s^{-1}
G	Gravitational constant, 6.673×10^{-8} dyne cm^2 g^{-2}
h	Planck's constant, 6.626×10^{-27} erg s
k	Boltzmann's constant, 1.381×10^{-16} erg K^{-1}
$L_\odot$	Solar luminosity, 3.826×10^{33} erg s^{-1}
m_H	Mass of hydrogen, 1.674×10^{-24} g
$M_\odot$	Solar mass, 1.989×10^{33} g
σ	Stefan-Boltzmann constant, 5.671×10^{-5} erg cm^{-2} s^{-1} K^{-4}

Other Symbols: Roman Characters

Symbols: Continued

a	Grain radius
a_{avg}	Average grain radius
a_{max}	Maximum grain radius
a_{min}	Minimum grain radius
A_V	Visual extinction in magnitudes
$A_1(\lambda)$	Extinction at a given wavelength λ assuming E(B-V) = 1.0
b	Galactic latitude
B	Apparent B magnitude
c_s	Speed of sound in a plasma
D	Distance to nova
E(B-V)	Color excess due to dust extinction, i.e., reddening
F	Flux
F_λ	Flux density, i.e., flux in a unit wavelength interval
F_ν	Flux density, i.e., flux in a unit frequency interval
I	Apparent I magnitude
J	Angular momentum quantum number
l	Galactic longitude
L	Luminosity
L_{bol}	Bolometric luminosity
L_{Edd}	Eddington luminosity
L_{IR}	Infrared luminosity
m_V	Apparent visual (V) magnitude
$m_{V,\max}$	Maximum apparent V magnitude
M	Mass
M_d	Dust mass in the ejecta
M_{ej}	Total mass of the ejecta
M_g	Gas mass in the ejecta
M_i	Modeled ratio of line flux to H β flux

Symbols: Continued

M_V	Absolute visual (V) magnitude
M_{WD}	White Dwarf mass
$\dot{M}$	Mass accretion rate
n	Number density;
	Number of observed emission lines
n_e	Electron number density
n_H	Hydrogen number density
n_p	Number of free parameters
O_i	Observed ratio of line flux to H β flux
q	Power law index of grain size distribution
Q_{abs}	Absorption coefficient
$\langle Q_a \rangle$	Planck mean absorptivity
$\langle Q_e \rangle$	Planck mean emissivity
r	Radial coordinate
$r_\star$	Stellar radius
R	Apparent R magnitude;
	Spectral resolution;
	Observed flux ratio of Hα to Hβ
R_{cond}	Dust condensation radius
R_{in}	Inner ejecta shell radius
R_{out}	Outer ejecta shell radius
R_0	Intrinsic intensity ratio of Hα to Hβ for Case B approximation
t	Time
t_{cond}	Dust grain condensation time
t_{max}	Date of light curve maximum
t_0	Date of discovery or date of light curve maximum
t_2	Time for the light curve to decay two magnitudes from maximum
t_3	Time for the light curve to decay three magnitudes from maximum

Symbols: Continued

T	Temperature
T_{BB}	Blackbody temperature
T_{cond}	Dust grain condensation temperature
T_d	Dust grain temperature
T_e	Electron temperature
v	Velocity
v_{exp}	Expansion velocity
y	Scaled radius of the ejecta shell
Y	Relative shell ejecta shell thickness

Other Symbols: Greek Characters

α	Power law exponent of grain size distribution
	Power law exponent of light curve decline rate
	Power law exponent of ejecta density distribution
$\Delta\lambda$	Wavelength resolution element
Δr	Shell thickness
η	Dimensionless profile function
θ	Angular size
κ	Mass absorption coefficient
λ	Wavelength
λ_0	Central wavelength
ν	Frequency
	Degrees of Freedom
ρ	Mass density
ρ_{gr}	Grain density
σ	Standard deviation from the mean
σ_i	Error in the observed flux ratio of line flux to H β flux
τ	Optical depth

Symbols: Continued

χ^2	Chi-squared goodness of fit
χ^2_{red}	Reduced chi-squared goodness of fit, i.e., the chi-squared value divided by the number of free parameters